Journal of Nanomaterials

Advanced Nanotechnology for Biomedical and Healthcare Applications

Lead Guest Editor: Weiguo Li
Guest Editors: Xuncai Chen and Isaac Acquah

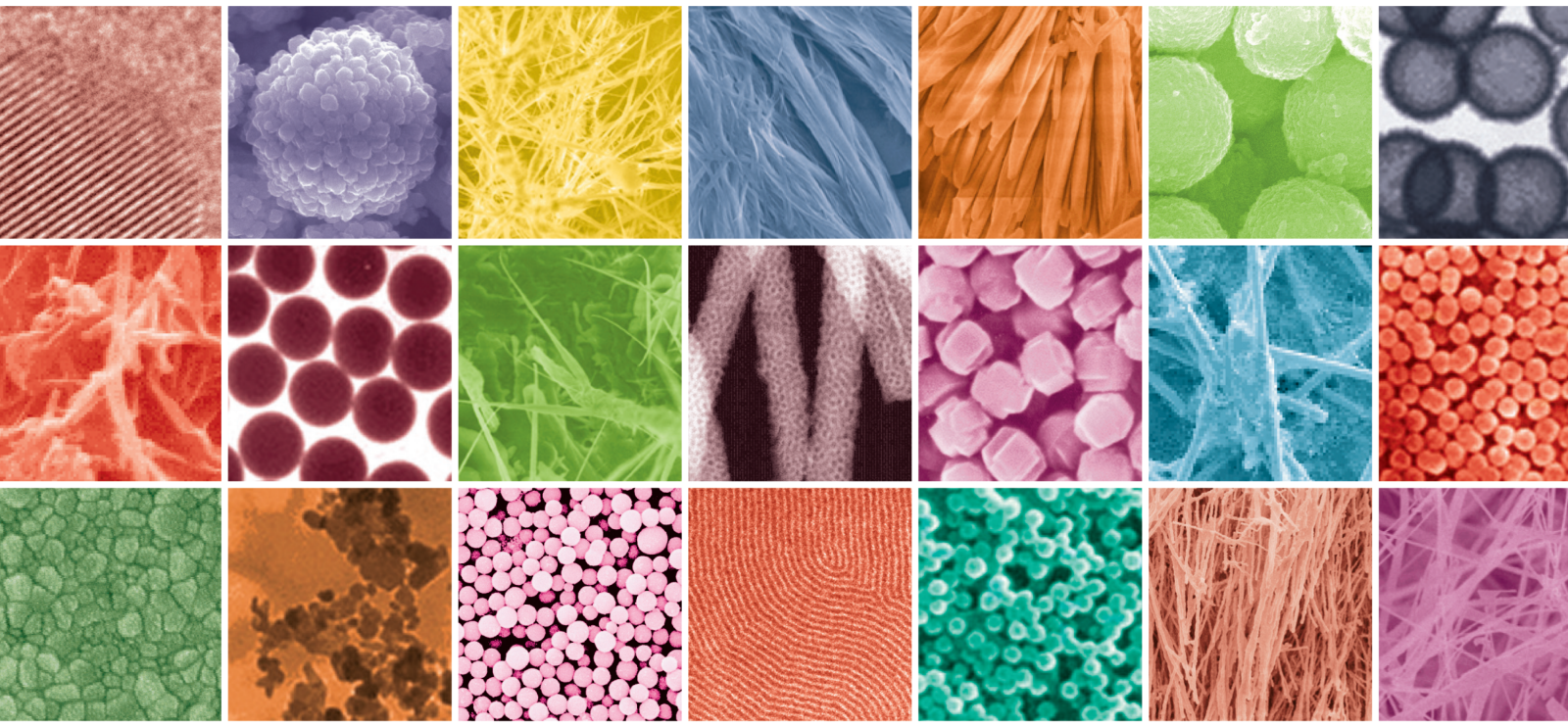

Advanced Nanotechnology for Biomedical and Healthcare Applications

Journal of Nanomaterials

Advanced Nanotechnology for Biomedical and Healthcare Applications

Lead Guest Editor: Weiguo Li
Guest Editors: Xuncai Chen and Isaac Acquah

Contents

Hindawi
Journal of Nanomaterials
Volume 2022, Article ID 1967606, 19 pages
https://doi.org/10.1155/2022/1967606

Research Article

Application of Factorial Design and Response Surface Methodology in the Optimization of Clindamycin Nanocomposites

Yousef Rezek Almahamid,[1] Samer Hasan Hussein-Al-Ali,[1] and Mike Kh. Haddad[2]

[1]*Department of Basic Pharmaceutical Sciences, Faculty of Pharmacy, Isra University, P.O. Box 22, Amman 11622, Jordan*
[2]*Department of Renewable Energy Engineering, Faculty of Engineering, Isra University, P.O. Box 22, Amman 11622, Jordan*

Correspondence should be addressed to Samer Hasan Hussein-Al-Ali; sameralali72@yahoo.com

Received 22 February 2022; Accepted 27 July 2022; Published 31 August 2022

Academic Editor: Isaac Acquah

This study is aimed at achieving the optimized preparation of a new extended-release formulation of clindamycin (CLD) via loading of the CLD onto chitosan-chondroitin sulfate (CS-Chondro). The CS-Chondro-CLD nanocomposites were prepared by mixing different masses of CS (50, 100, and 200 mg) with Chondro (50, 100, and 200 mg) and different masses of CLD (75, 150, and 300 mg). The prepared nanocomposites were characterized by different techniques including loading efficiency (LE), X-ray powder diffraction (XRD), scanning electron microscopy (SEM), Fourier-transform infrared spectroscopy (FTIR), and release study. The XRD spectra of CS-Chondro-CLD nanocomposites showed two peaks at $2\theta = 22.5^{\circ}$ and 40.7°, indicating amorphous forms. The FTIR data shows incorporation of CLD into the CS-Chondro polymers. An *in vitro* release study of CLD from nanocomposites was carried out using PBS at pH 7.4. The result showed that the release rate was completed after 25 hours. This study showed that the CS-Chondro-CLD nanocomposites have promising applications in the delivery of CLD drug.

1. Introduction

A new advanced topic in pharmaceutical studies known as "pharmaceutical nanotechnology" focuses on pharmaceutical development. Nanoparticles are solid colloidal particles ranging in size from 10 nm to 1 μm [1]. The physical and chemical properties of materials change when prepared in nanoscale, leading to a noticeably different surface chemistry of nanoparticles compared to that of the original material [2, 3]. Major advantages of nanoparticles include increased rate of dissolution, solubility, oral bioavailability, therapeutic action, and lower amount of dose required [4].

Nanotechnology and nanoparticles are helping to considerably improve many technologies and industries such as information technology, photocatalytic applications, medicine, energy, food safety, and environmental sciences [5–8].

Polymeric nanoparticles are popular due to their ease in preparation with required characteristics for drug delivery systems. They provide an intelligent alternative for the conventional dosage form of therapeutic agents for chronic administration [9]. In addition, nanoparticles protect loaded bioactive substances against degeneration by enzymes [10]. Polymeric nanoparticles were used to overcome gastrointestinal challenge by interaction between the drug and epithelial cells in the gastrointestinal tract [11].

Chondroitin sulfate is a water-soluble component of cells, tissues, and organs. It is a major constituent of the extracellular structure [12, 13].

Chondroitin and other polymers such as albumin and chitosan have been a material of choice for the delivery of oligonucleotides, DNA, protein, and drugs [14, 15]. Chondroitin sulfate in tissues undergoes natural conversion in the physiological environment to provide controlled release of the drug [16]. The reaction of chondroitin with the drug to obtain the novel substances is carried out in a manner dependent on the functional groups involved. Chondroitin

is the most extensively studied encapsulating material for the controlled release of drugs [16].

Clindamycin (CLD) drug was approved by the US Food and Drug Administration for treatment of anaerobic infections. It is used alone or in combination with other therapies for treating several cases such as infections of the head and neck, respiratory system, babesiosis which causes flow out of red or blackish urine, acne vulgaris, vagina, bone and soft tissue, and abdomen. CLD can be bactericidal or bacteriostatic depending on its concentration and site of infection [17]. Common side effects of CLD use include rash and diarrhea which could be resolved through a strategy to prevent antibiotic-associated diarrhea and mainly probiotic administration for short time [18]. In spite of the comparatively short half-life of CLD, in which it is administered every 8 hours for 5-7 days, it is considered an appropriate treatment for most contagions. In patients with normal renal function, the half-life is 2.4 hours [19].

Clindamycin was used as a hydrophilic cationic drug loaded with dextran sulphate or sodium alginate as an anionic polymer. The results showed that these properties for polymers had a significant effect on drug loading, as the presence of dextran sulphate increased from 1.32 to 18.19%, as well as an effect on reducing the release for the drug. This improved performance of CLD was due to the novel properties of small particle size and increase surface area [20].

An attempt to study the effect of transfersomal (TRSS) on the delivery of CLD through the skin showed an enhanced penetration of the drug. The characteristics of the particles such as entrapment efficiency, particle size, surface charge, and morphology were evaluated. TRSS showed higher entrapment efficiency (EE) of 93.3%, which led to a higher *in vitro* release of CLD [21].

Rauta et al. focused on increasing the efficacy of CLD loaded on PLA/PLGA polymer as novel nanoparticle delivery system by oral administration. The results confirmed that CLD-PLA/PLGA polymers significantly increased the bioavailability and drug activity [22].

In another study that prepared CLD-alginate and chitosan composites as mucoadhesive drug delivery system for periodontal therapy, the results showed that concentration of sodium alginate and the molecular weight of chitosan affected the characteristics of the composites such as thickness, encapsulation, structure, tumescence, adhesion, and *in vitro* drug release [23].

The aim of the present study is to prepare a novel nanocomposite, which contains CLD loaded onto chitosan-chondroitin to enhance the release properties.

2. Experimental

2.1. Materials. The chemicals used in this study are clindamycin hydrochloride monohydrate ($C_{18}H_{34}Cl_2N_2O_5S.H_2O$, Sigma-Aldrich), low molecular weight chitosan (10-120 kDa, Sigma-Aldrich), chondroitin sulphate ($C_{13}H_{21}NO_{15}S$, Sigma-Aldrich), and phosphate-buffered saline tablets (PBS) (Sigma-Aldrich). The acetic acid was purchased from Chem CO (England).

Table 1: Levels of CS, Chondro and CLD factors.

Factors	Unit	Low level	Middle level	High level
CS	mg	50	100	200
Chondro	mg	50	100	200
CLD	mg	75	150	300

2.2. Instrumentation. All the prepared samples (CS-Chondro and CS-Chondro-CLD) and standard CLD samples were studied using several instruments, which are detailed as follows:

(1) X-ray diffraction (XRD) was studied using CuK radiation at 30 kV and 30 mA (GBC Scientific Equipment, USA) at the Institute of Functional Nanosystems, UIM University (Germany)

(2) Fourier transform infrared spectroscopy (FTIR) data spectra were measured by a Thermo Nicolet Nexus, Smart Orbit spectrometer

(3) The scanning electron microscope (SEM) images were obtained at 10 kV, Hitachi High-Tech Global

(4) The UV-Vis spectra were measured using Shimadzu UV-1601

(5) Zeta potential and particle size of formulations were analyzed through dynamic light scattering (DLS) with Zetasizer Nano S (Malvern UK)

3. Methods

3.1. Design of Experiment. Full factorial design was used to study the %LE, zeta potential, and particle size as responses of the CS, Chondro and CLD preparations. The ranges of values used in the design are described in Table 1, and all the experimental run results are presented in Table 2.

3.2. Data Analysis of the Factorial Design. A plot of residuals versus corresponding predicted values, a response surface plot, a normal probability plot of the residuals, and interaction plots were used as graphical tools for the analysis of the factorial design.

A regression analysis was also used to study the relationship between the independent variables (CS, Chondro, and CLD) and the response (LE, size, and zeta potential). The experimental data were processed by using Minitab software version 18 [24].

3.3. Preparation of CS-Chondro Nanoparticles and CS-Chondro-CLD Nanocomposites. CS-Chondro nanoparticles were prepared by ionic gelation technique [25]. The CS (50, 100, 200 mg) was dissolved in 1% (*w*/*v*) acetic acid. Chondro solutions with masses of 50, 100, and 200 mg were added to CS solution, and the pH was controlled at 5, with stirring for 18 hours [26]. The product was collected at 11000 rpm.

CS-Chondro-CLD nanocomposites were formed by a drop-wise method of the aqueous solution of Chondro with

Table 2: Matrix for 3^3 full factorial designs.

Std. order	Sample code	CS	Chondro	CLD	%LE	Size	Potential
50	1	200	100	150	*	*	10.8
67	2	100	100	75	*	130	-14.3
69	3	100	100	300	71.3	181	*
22	4	200	100	75	31.3	*	*
63	5	50	200	300	75.2	*	-9.9
51	6	200	100	300	75.7	304	5.7
7	7	50	200	75	19.1	150	-7.6
47	8	200	50	150	52.2	*	14.9
16	9	100	200	75	6.3	*	-18.2
11	10	100	50	150	66.0	185	-8.4
38	11	100	50	150	62.7	*	-6.3
74	12	200	50	150	54.5	*	14.9
70	13	100	200	75	5.5	171	-18.6
42	14	100	100	300	68.5	244	*
40	15	100	100	75	*	150	-15.9
79	16	200	200	75	33.6	300	12.3
14	17	100	100	150	50.8	164	-7.3
2	18	50	50	150	*	176	-2.0
3	19	50	50	300	86.9	240	-6.2
43	20	100	200	75	7.8	190	-19.1
77	21	200	100	150	*	*	10.9
33	22	50	100	300	*	182	*
26	23	200	200	150	26.8	275	12.4
56	24	50	50	150	*	*	-6.4
61	25	50	200	75	15.2	111	-7.4
8	26	50	200	150	23.3	151	-8.5
71	27	100	200	150	22.2	152	-8.8
32	28	50	100	150	69.3	*	*
19	29	200	50	75	27.9	460	19.2
5	30	50	100	150	52.3	*	*
73	31	200	50	75	28.5	450	19.6
4	32	50	100	75	32.9	*	*
46	33	200	50	75	26.2	445	20.0
20	34	200	50	150	57.2	*	14.9
76	35	200	100	75	33.2	340	*
34	36	50	200	75	14.3	147	-7.8
27	37	200	200	300	71.1	200	13.4
25	38	200	200	75	23.8	297	12.0
58	39	50	100	75	36.2	*	*
60	40	50	100	300	*	180	*
75	41	200	50	300	71.5	308	8.0
53	42	200	200	150	30.5	252	12.4
24	43	200	100	300	78.0	*	3.6
72	44	100	200	300	56.0	261	-12.6
31	45	50	100	75	24.6	*	*

Table 2: Continued.

Std. order	Sample code	CS	Chondro	CLD	%LE	Size	Potential
12	46	100	50	300	64.8	*	-19.4
23	47	200	100	150	*	328	11.0
59	48	50	100	150	62.3	*	*
62	49	50	200	150	26.5	201	-7.8
6	50	50	100	300	*	185	*
64	51	100	50	75	*	177	-10.6
17	52	100	200	150	23.0	203	-18.7
55	53	50	50	75	60.5	*	-6.8
49	54	200	100	75	31.7	379	*
57	55	50	50	300	86.4	230	-6.1
45	56	100	200	300	58.0	225	-12.6
66	57	100	50	300	61.7	238	-18.9
80	58	200	200	150	34.9	302	12.3
1	59	50	50	75	61.4	*	-8.7
36	60	50	200	300	76.2	*	-7.9
44	61	100	200	150	23.6	206	-13.8
9	62	50	200	300	87.7	*	-5.9
30	63	50	50	300	88.4	244	-6.3
52	64	200	200	75	27.7	302	12.7
41	65	100	100	150	62.8	185	-10.3
78	66	200	100	300	79.9	298	7.8
15	67	100	100	300	72.2	*	*
68	68	100	100	150	60.1	150	-8.8
54	69	200	200	300	75.0	192	14.2
28	70	50	50	75	61.0	*	-7.7
37	71	100	50	75	*	158	-11.4
81	72	200	200	300	74.0	191	12.6
29	73	50	50	150	*	*	-7.2
48	74	200	50	300	71.0	*	8.6
13	75	100	100	75	*	132	-17.5
21	76	200	50	300	76.3	303	7.5
65	77	100	50	150	*	150	-10.5
39	78	100	50	300	55.0	229	-18.4
10	79	100	50	75	*	149	-9.8
35	80	50	200	150	29.6	190	-9.1
18	81	100	200	300	55.5	250	-12.6

*The deleted sample during processing with data.

50, 100, and 200 mg into 50, 100, and 200 mg solution of CS, containing 75, 150, and 300 mg of CLD, with constant stirring. The resulting nanocomposites were collected by centrifugation at 11000 rpm [26].

3.4. The CLD Loading Efficiency. The procedure for calculating loading efficiency (%LE) was as follows: 2.0 ml of suspension was centrifuged at 11000 rpm; then the free drug was measured by UV-Vis at λ_{max} of 300 nm.

$$\%\text{LE} = \frac{Q_T - Q_{un}}{\text{mass of nanocomposite}} \times 100, \quad (1)$$

where Q_T is the total CLD used during preparation and Q_{un} is the free CLD in the supernatant.

3.5. In Vitro Release Study of CLD from CS-Chondro-CLD Nanocomposites. An in vitro release study of CLD from CS-Chondro-CLD nanocomposites was carried out in PBS

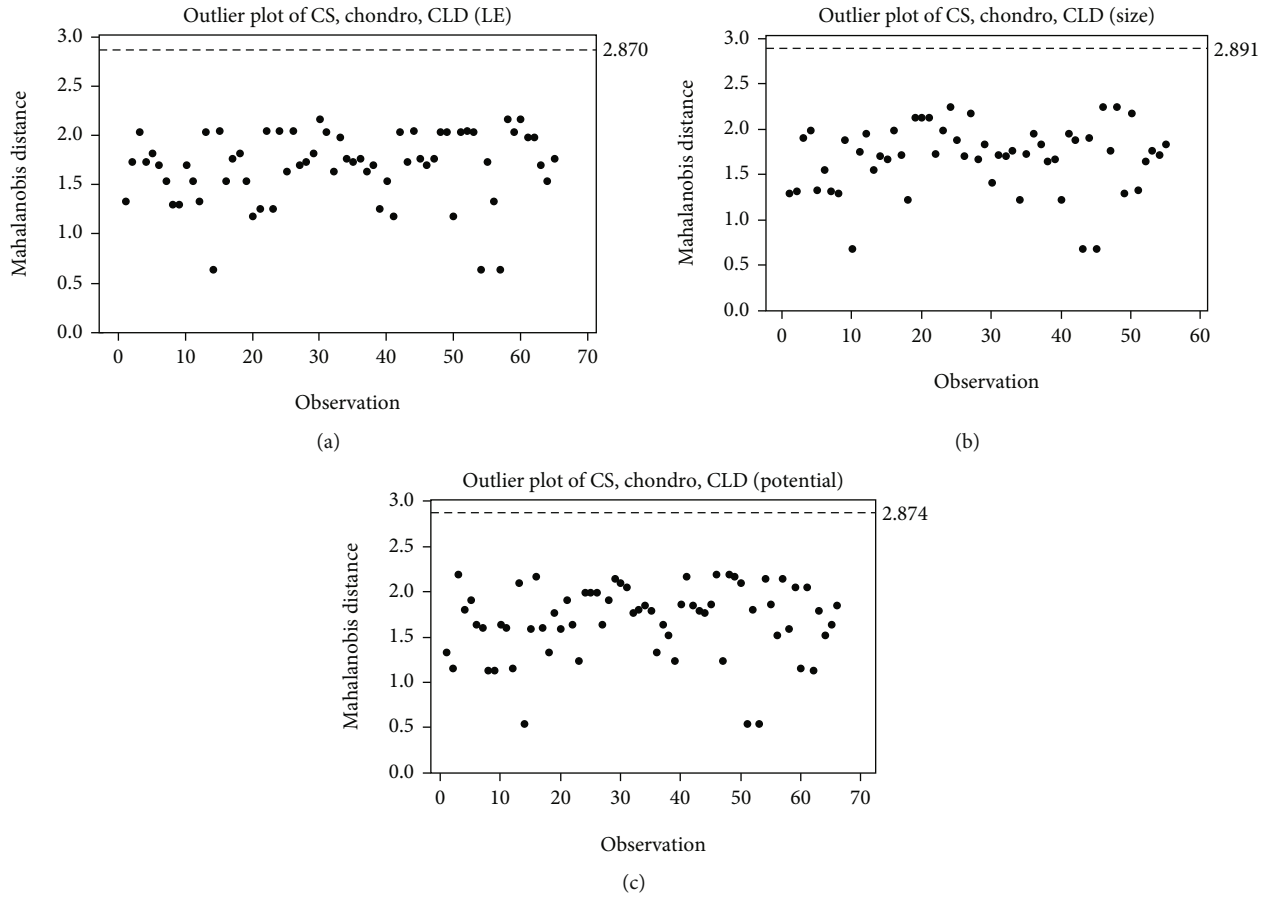

Figure 1: Dj model value for independent variables values for %LE (a), particle size (b), and zeta potential (c).

at pH 7.4, at λ_{max} of 300 nm. A suitable amount of nanocomposite was added to the release media. The cumulative amount of CLD released into the media was measured at different time intervals [27]. The percentage release of CLD was calculated using the following equation:

$$\%\text{Release} = \frac{\text{Concentration of CLD time } t}{\text{Concentration of CLD in the nano Formulations}} \times 100. \quad (2)$$

4. Results and Discussion

4.1. Detection Outlier Reading. An outlier is a reading which deviates from other data. For univariate data, familiar Euclidean distance and rarity are used in the data analysis, but for multivariate data, the Mahalanobis distance method was used. It enables detecting multivariate outliers that need to be eliminated from future analysis to enhance a model.

Mahalanobis distance (Dj) can be defined as the distance between a data point and overall mean. It is based on the vector of data (x) and the vector of mean values of independent variables (m) [28].

The formula used for Mahanabolis distance [29] is as follows:

$$Dj = (x - m)^T C^{-1} (x - m), \quad (3)$$

where T indicates the vector should be transposed and C^{-1} is the inverse covariance matrix of independent variables.

From the Dj standard formula, the values of the outliers are identified for the independent variables values which are dependent on the concentration of CS, Chondro, and CLD.

In the Dj value, threshold values are assigned to the multivariate data. The list of the threshold values assigned for different variants is given in Figure 1.

As in the current work, the critical value is for three independent variables (threshold is 2.858) (Figure 1(a)); the Dj values found above 2.858 are outliers. Fortunately, there are no outlier values suspected as spam to all responses. With regard to %LE, particle size, and zeta potential data analysis, the amount of data was deleted to increase the R^2 value. Therefore, the Dj values become 2.870 (%LE) (Figure 1(b)), 2.891 (particle size) (Figure 1(c)), and 2.874 (zeta potential) (Figure 1(d)), without any outlier values for all experiments being recorded.

Table 3: ANOVA data for %LE, particle size, and zeta potential models.

	LE model						Particle size model						Zeta potential model				
	t value	Coef	*F* value	*p* value	VIF		*t* value	Coef	*F* value	*p* value	VIF		*t* value	Coef	*F* value	*p* value	VIF
Model	19.83	44.23	72.61	0.00	—	Model	23.24		86.72	0.00		Model	-11.79	-12.47	164.29	0.00	
Linear	—	—	130.09	0.00	—	Linear			97.67	0.00		Linear			183.40	0.00	
CS	-2.57	-3.26	6.63	0.00	1.06	CS	16.54	71.43	273.56	0.00	1.16	CS	23.33	9.873	544.36	0.00	1.18
Chondro	-7.95	-9.68	63.28	0.00	1.02	Chondro	-4.39	-17.42	19.26	0.00	1.15	Chondro	-1.87	-0.666	3.48	0.00	1.04
CLD	17.35	21.82	300.85	0.00	1.05	CLD	2.87	11.27	8.23	0.00	1.12	CLD	-2.71	-1.099	7.33	0.00	1.06
Square			14.46	0.00	—	Square			16.36	0.00		Square			121.54	0.00	
CS* CS	3.80	10.22	14.46	0.00	1.11	CS* CS	3.52	27.91	12.38	0.00	1.20	CS* CS	17.94	14.371	321.76	0.00	1.14
Chondro* Chondro						Chondro* Chondro	4.08	33.78	16.67	0.00	1.10	Chondro* Chondro	2.34	2.37	5.49	0.00	1.17
CLD* CLD													-2.82	-2.184	7.95	0.00	1.07
2-way interaction	—	—	17.34	0.00	—	2-way interaction			97.75	0.00		2-way interaction			18.45	0.00	
CS* Chondro	4.13	5.84	17.07	0.00	1.00	CS* Chondro	-9.74	-48.29	94.77	0.00	1.18	CS* Chondro					
Chondro* CLD	4.34	6.18	18.83	0.00	1.02	Chondro* CLD						Chondro* CLD	5.17	-1.467	26.71	0.00	1.02
CS* CLD						CS* CLD	-12.5	-62.33	155.92	0.00	1.19	CS* CLD	-3.03	2.187	9.16	0.00	1.05

Table 4: K-S and A-P tests for goodness-of-fit models.

	%LE model	Particle size model	Zeta potential model
D_n (calculated value for K-S test)	0.143	0.156	0.107
D_{crit} (critical value for K-S test)	0.170	0.183	0.167
$D_{Agostino\text{-}Pearson}$ (A-P test)	0.084	0.006	0.072

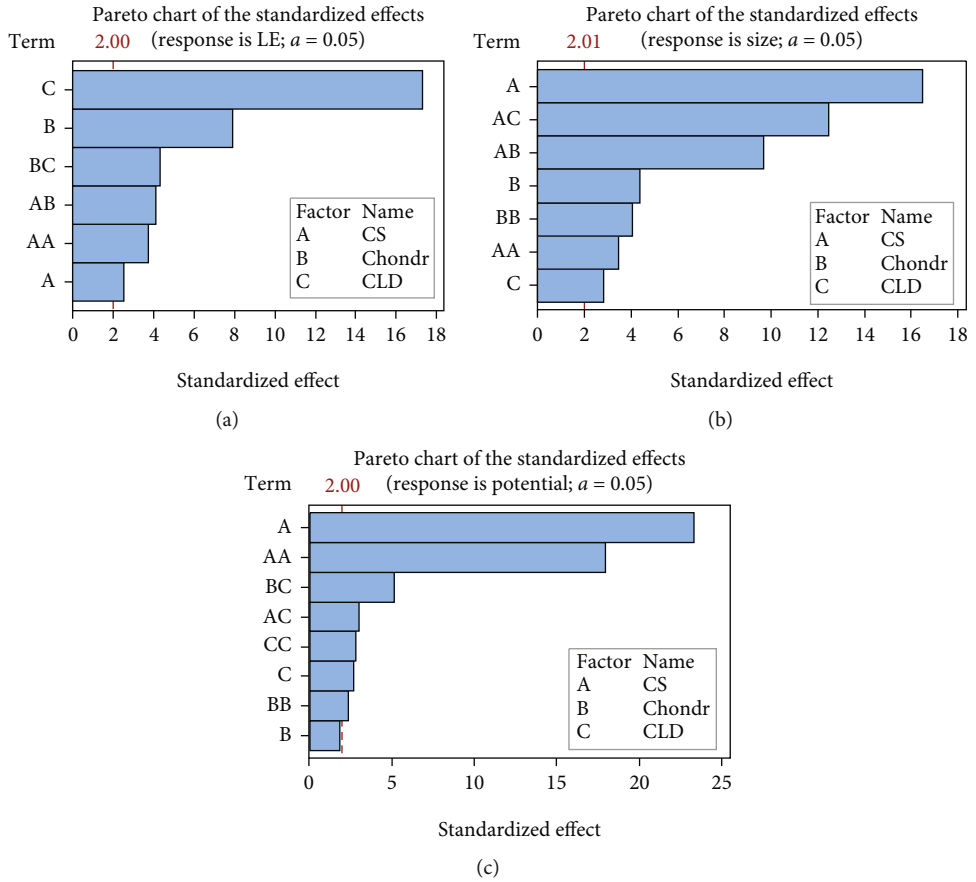

Figure 2: Pareto chart of the %LE (a), particle size (b), and zeta potential (c).

4.2. Statistical Data Analysis. The variance inflation factor (VIF) is one of the methods used to assess the multicollinearity properties, i.e., if the predictors are correlated. If no factors are correlated, the VIFs will all be <5 [30]. Due to absence of multicollinearity in this work, the data was analyzed using the multivariate regression model.

Multiple regressions is a method used to predict the value of a variable based on the value of two or more other variables [31].

4.2.1. ANOVA Data. From ANOVA data for the %LE model in Table 3, we estimated the individual factors (CS, Chondro and CLD) and their combinations on the response (CS ∗ CS, CS ∗ Chondro, and Chondro ∗ CLD). The significant effect on the %LE can be seen with a p value less than 0.05 and a high F value. From Table 3, we noted the following important characteristics: (i) the average p value for the model, individual factors, and their combinations are much less than 0.05, which means that the conditions in the model have a high significance [32]; (ii) the F values for individual factors (CLD, Chondro, and CS) were 300.85, 63.28, and 6.63, respectively, whereas the F value for combinations (Chondro ∗ CLD, CS ∗ Chondro, and CS ∗ CS) was 18.83, 17.07, and 14.46, respectively.

Table 3 shows ANOVA data for the particle size model. The results of the statistical evaluation and variance analysis of the data show that all of the variables and their interactions had significant effects except CLD ∗ CLD and CLD ∗ Chondro. Also, the F value of the model was 86.72; this large value could occur due to noise [33, 34].

Table 3 also shows the F value and p value for zeta potential model. From the data in Table 3, the F values for individual factors (CLD, Chondro, and CS) were 7.33, 3.48, and 544.36, respectively, whereas the F value for combinations

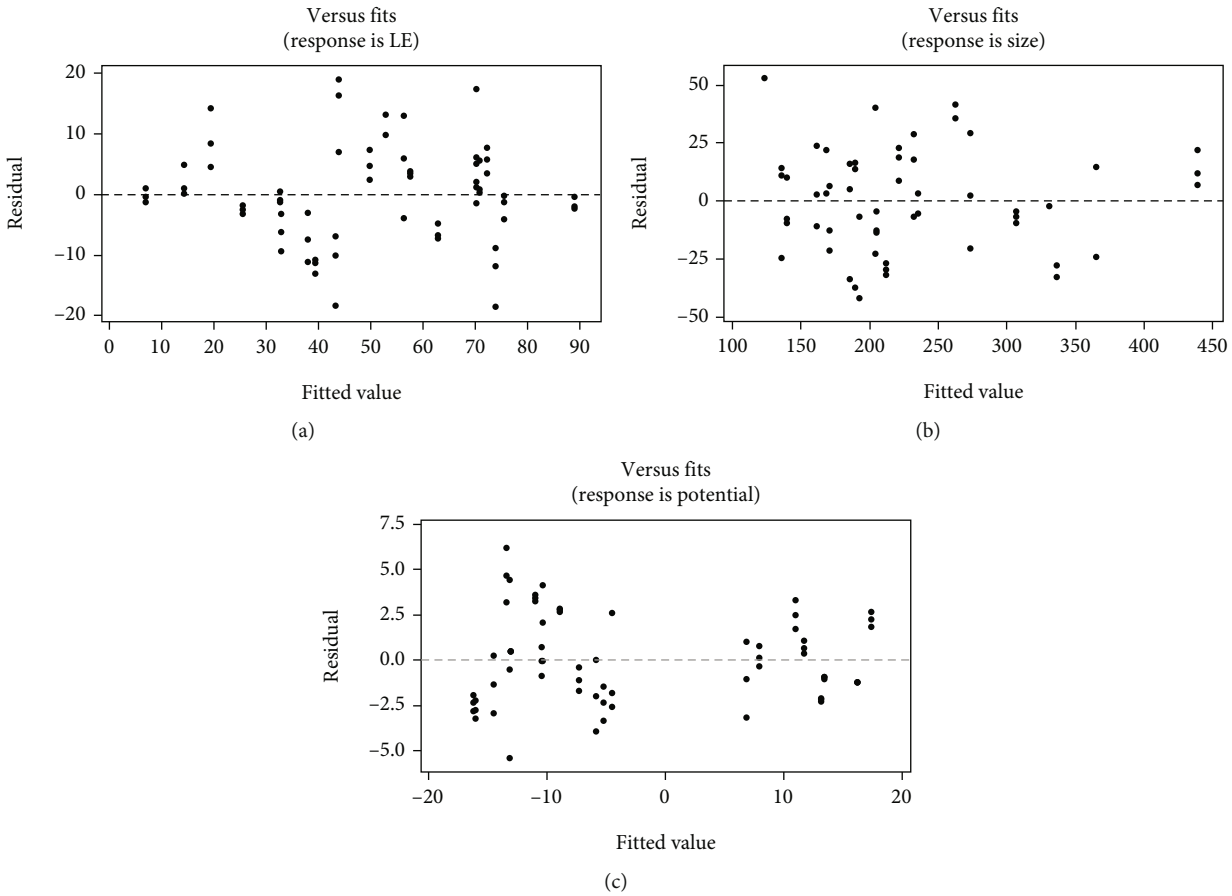

Figure 3: The residuals plot versus the fitted values for %LE (a), particle size (b), and zeta potential (c).

(CS ∗ CS, Chondro ∗ Chondro, CLD ∗ CLD, Chondro ∗ CLD, and CS ∗ CLD) was 321.76, 5.49, 7.95, 26.71, and 9.16, respectively.

In statistics, the coefficient of determination (R^2) is the proportion of the variation in the dependent variable which is predictable from the independent variable(s). The R^2 for the %LE model was 88.25%, and the R^2_{adj} is 87.04%. In addition, the value of R^2 for particle size model was 92.81%, and the R^2_{adj} is 91.74%. Finally, the R^2 for the zeta potential model was 95.84%, and the R^2_{adj} is 95.26%. There is no difference between the R^2 and R^2_{adj} values, which indicate the significant conditions in the three models.

4.3. Goodness-Of-Fit Test for the Normal Distribution for Three Models

4.3.1. The Kolmogorov-Smirnov (K-S) Test for Goodness-Of-Fit. The K-S test is a nonparametric test of the equality of continuity, and it contains one and two samples. At the one-sample test, one-dimensional probability distributions are used to compare a sample with a reference probability distribution (hypothesized distribution), whereas a two-sample test is one of the most useful and general nonparametric methods for comparing two samples [35, 36].

The K-S test null hypothesis is defined as [37] follows:

H_o: the sample data are not significantly different than a normal population.

H_a: the sample data are significantly different than a normal population.

The D_n calculated value can be determined by the following equation:

$$D_n = \max_{1\le i\le N}\left(F(Y_i) - \frac{i-1}{N}, \frac{i}{N} - F(Y_i)\right), \quad (4)$$

where F is the theoretical cumulative distribution.

The critical value of the K-S test can be calculated by the following equation [38]:

$$D_{\text{crit},0.05} = \frac{1.36}{\sqrt{n}}. \quad (5)$$

4.3.2. The D'Agostino-Pearson (A-P) Test. The D'Agostino-Pearson test is a very powerful test for assessing departures from normality [39]. The null hypothesis is defined as follows:

H_o: the sample data are not significantly different than a normal population.

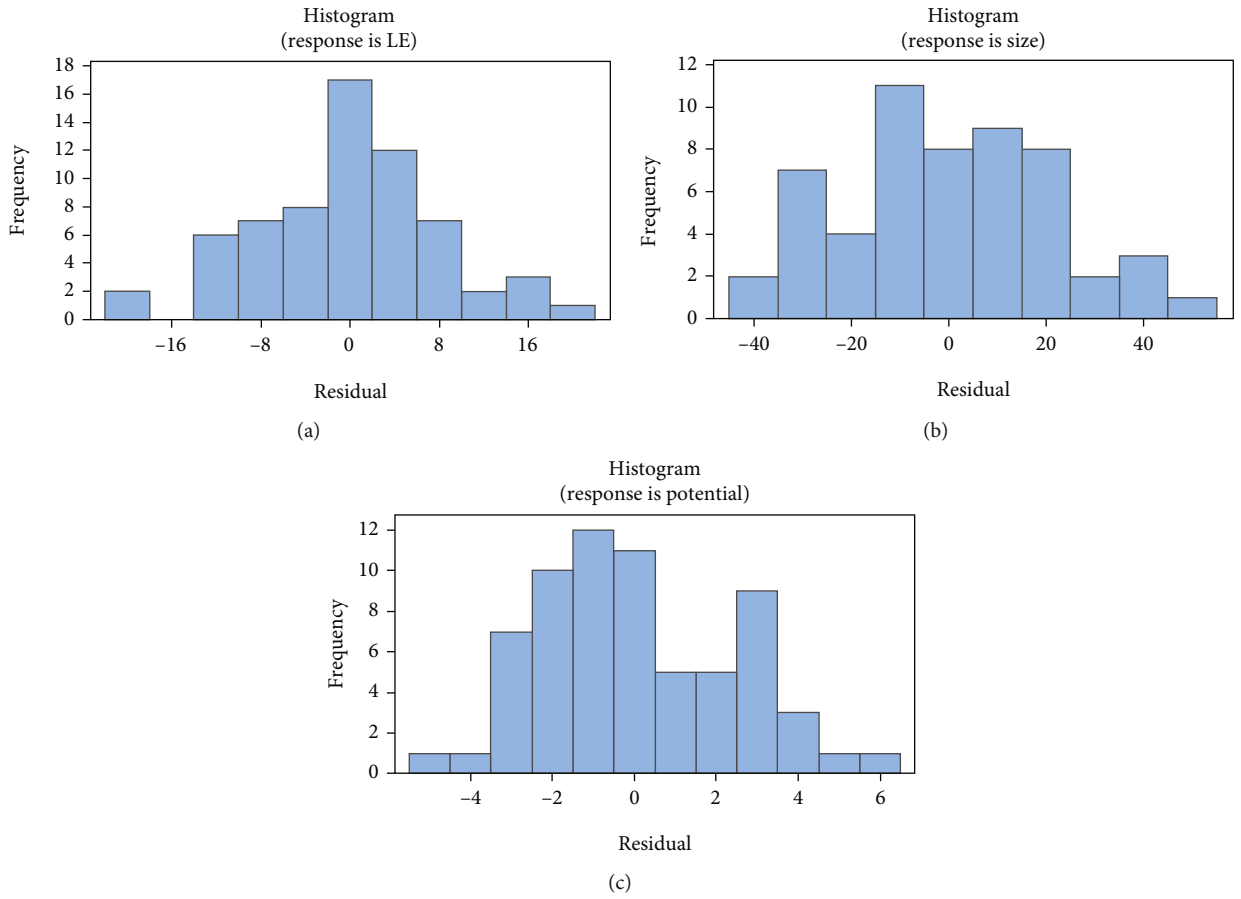

Figure 4: Histogram of the standardized residuals for %LE (a), particle size (b), and zeta potential (c).

H_a: the sample data are significantly different than a normal population.

The D is a test that can statistically calculate the value by the following equation:

$$D = \frac{T}{\sqrt{n^3 \mathrm{SS}}}, \tag{6}$$

where "SS" is the sum of squares of the data and "n" is the sample size.

$$T = \sum \left(i - \frac{n+1}{2} \right) X_i, \tag{7}$$

where "i" is the order or rank of observation.

From the results in Table 4, D_{crit} (critical value) for %LE, particle size, and zeta potential are bigger than D_n (calculated value); therefore, the null hypothesis is not rejected (for the normally distributed data). In addition, the $D_{\text{Agostino-Pearson}}$ value for %LE and zeta potential is bigger than 0.05 ($D > p$), indicating that the model set is not significantly different than normal.

4.4. Pareto Chart of the Standardized Effects of the Three Models. A Pareto chart is normally used as a graphical representation for evaluating the effects of the main variables and their interactions on the response. Figure 2 shows the bars of the main f variables and their interactions, arranged in a descending order according to the t values. The vertical line is the statistical threshold for a level of significance.

From the results in Figure 2(a), it can be seen that three main factors have a statistically significant effect on the %LE. In a descending order, according to their effect estimates, the three factors are CLD, Chondro, and CS, and the interactions Chondro ∗ CLD (BC), CS ∗ Chondro (AB), and CS ∗ CS (AA).

In addition, in the Pareto chart in Figure 2(b) which is related to particle size model, bars that cross the reference line (2.01) are statistically significant with the following order: A>AC>AB>B>BB>AA>C.

Figure 2(c) plots the effects in the decreasing order of their absolute values with reference line at 2 values calculated by Lenth's method [40]. In these results, the two main effects (CS and CLD) are statistically significant ($\alpha = 0.05$). In addition, the two square effects (CS ∗ CS (AA), Chondro ∗ Chondro (BB), and CLD ∗ CLD (CC)) are statistically significant ($\alpha = 0.05$). The two-way interaction (Chondro ∗ CLD (BC) and CS ∗ Chondro (AB)) can also be seen, which also shows significant results.

4.5. Residual Plot. Figure 3 shows the correlation between residuals with predicted responses of the three models. The

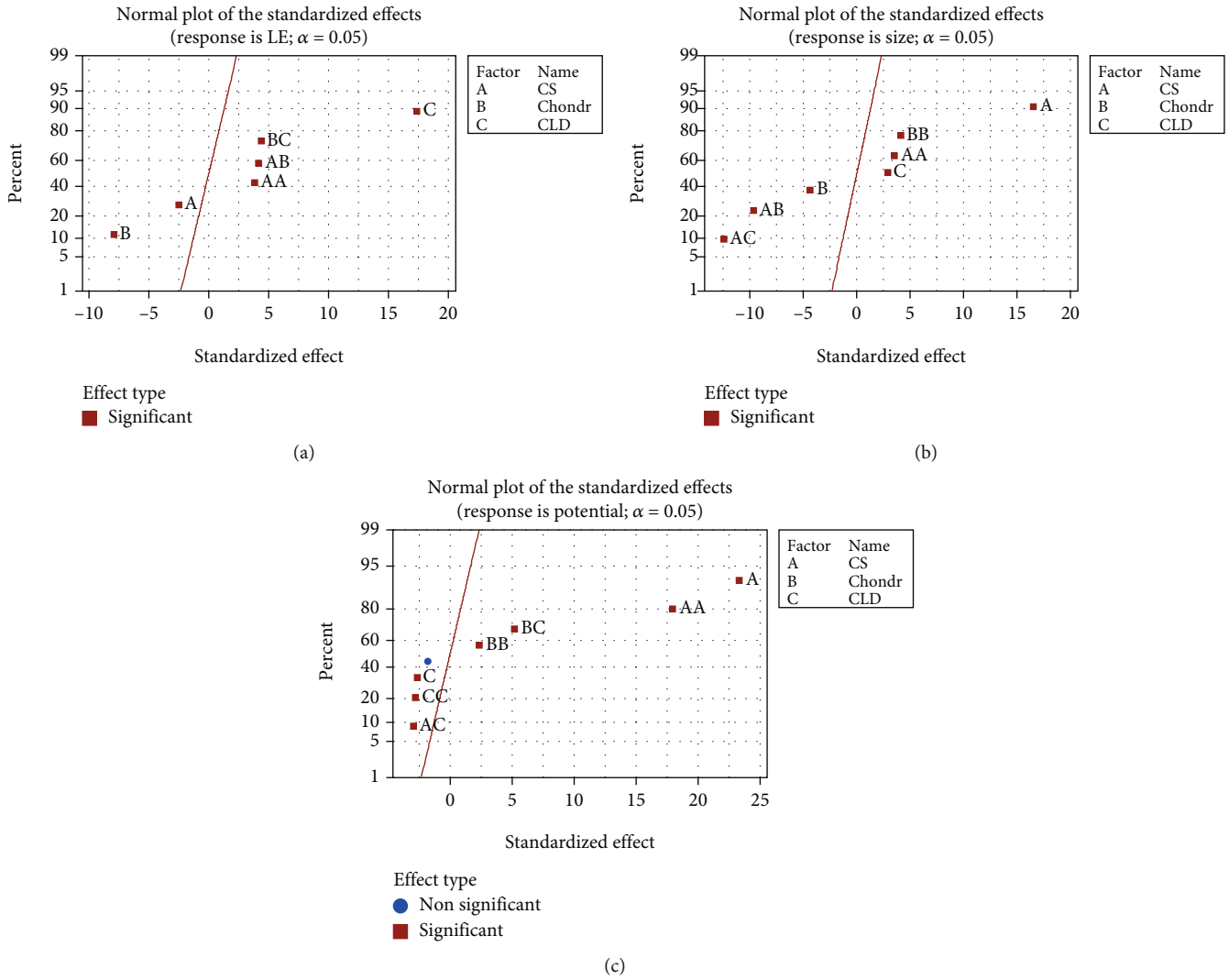

Figure 5: Normal probability plot of the effects for %LE (a), particle size (b), and zeta potential (c).

residuals of three models are scattered randomly about zero. These results indicate that the errors have a constant variance and the experiment does not contain any possibility of systematic errors.

4.6. Histogram Plot. The histogram plot of residuals are used to determine whether the data are skewed or outliers exist in the data. Figures 4(a)–4(c) show the %LE, particle size, and zeta potential histogram residual plots, respectively. Results show symmetric bell-shaped curves, indicating that the data are complete residual normality assumption.

4.7. Normal Probability Plot of the Standard Effects. Figures 5(a)–5(c) shows the normal probability plot of the effects for %LE, particle size, and zeta potential, respectively.

From Figure 5(a), it could be seen that there are no factors or combinations on a line which lies close to zero. Three of the individual factors show deviation of varying degrees—A and B (negative direction) and C (positive direction). In addition, three of the combinations at level two—AA, AB, and BC—showed a significant result toward %LE response with positive direction. From Figure 5(b), it can be seen that three of the factors show negative direction (B, AB, and AC) and four of the factors show positive direction (A, C, AA, and BB). In addition, Figure 5(c) shows significant positive direction for A, AA, BB, and AB factors, whereas the factors C, CC, and AC show significant negative direction.

4.8. Contour Plot and Surface Plot of Responses against Different Factors. Figure 6(a) shows the contour plot of %LE. The %LE with a value higher than 60% corresponds with high values of CLD and Chondro, but varies from 50 mg to 200 mg, and the surface is maximum (Figure 6(b)).

Figure 6(c) shows the dependence of %LE on CS and CLD. When CS concentrations are at their minimum and maximum levels and at same time the CLD is at maximum level, the %LE was found to be maximum surface (Figure 6(d)). However, the contour of CS against Chondro concentrations (Figure 6(e)) showed the highest %LE in the lower left of the plot, which corresponds with low values of CS and Chondro, and the surface is maximum (Figure 6(f)).

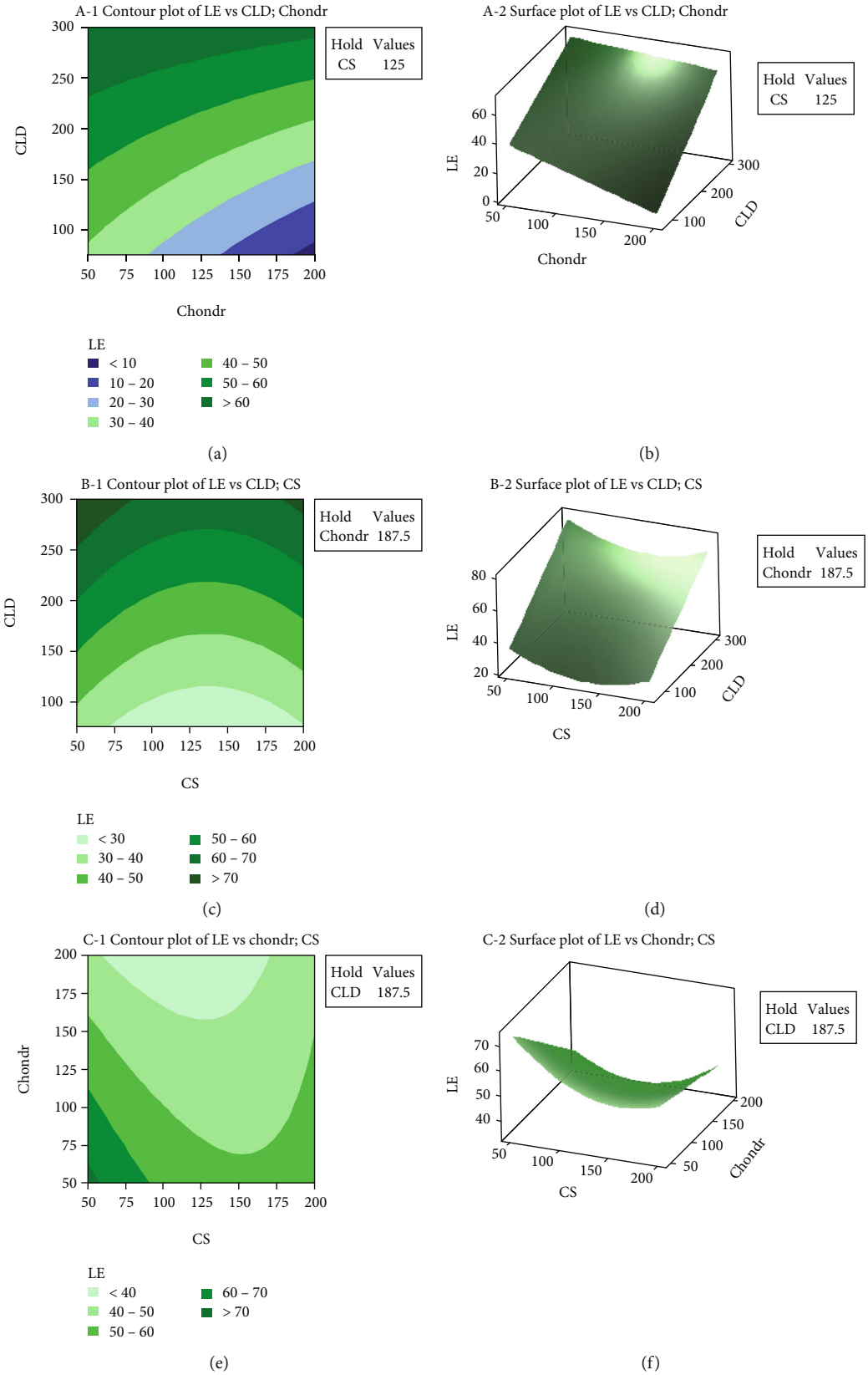

Figure 6: Contour plots and surface plots of %LE.

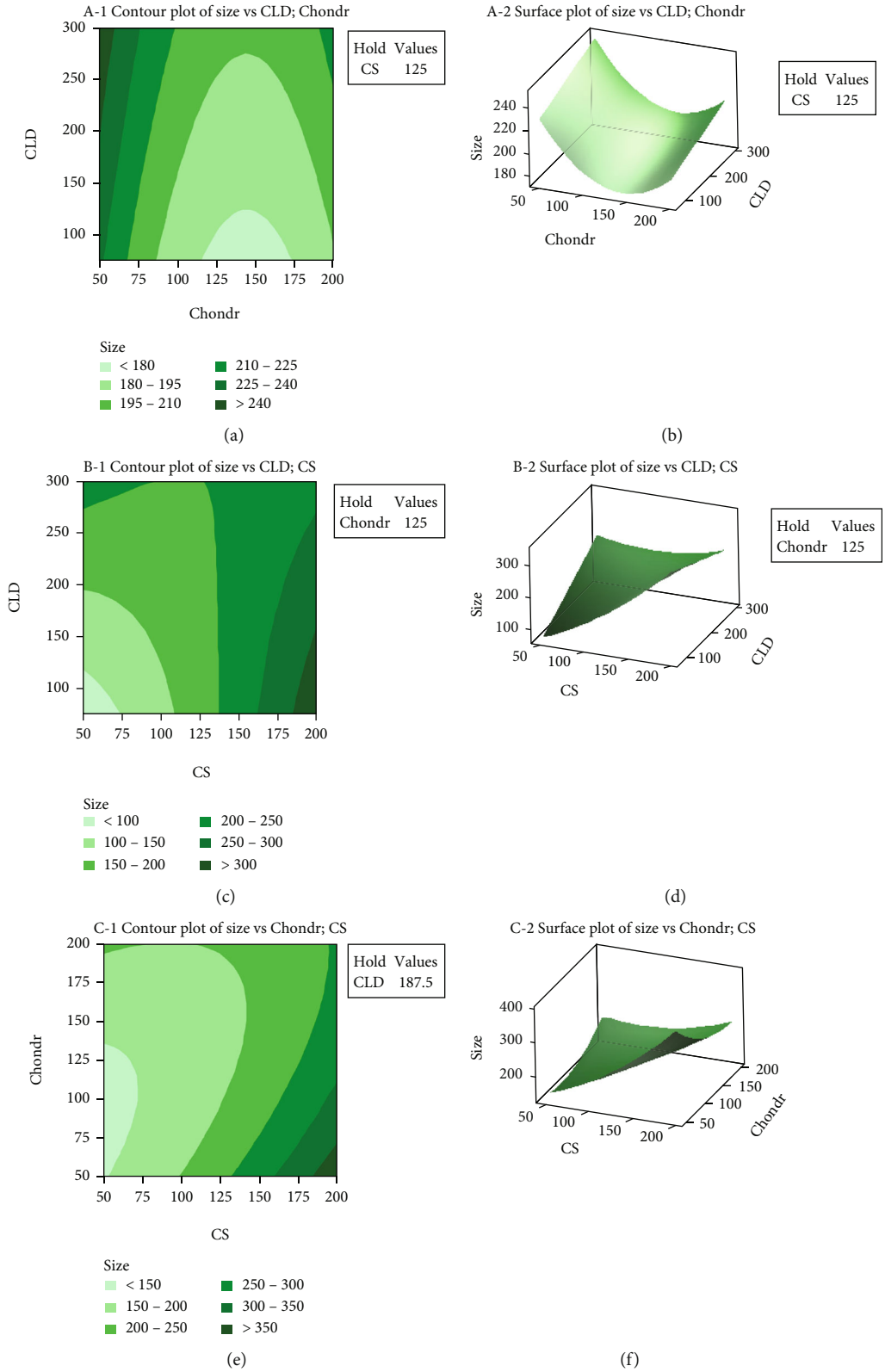

Figure 7: The contour plots and surface plots of size against different factors.

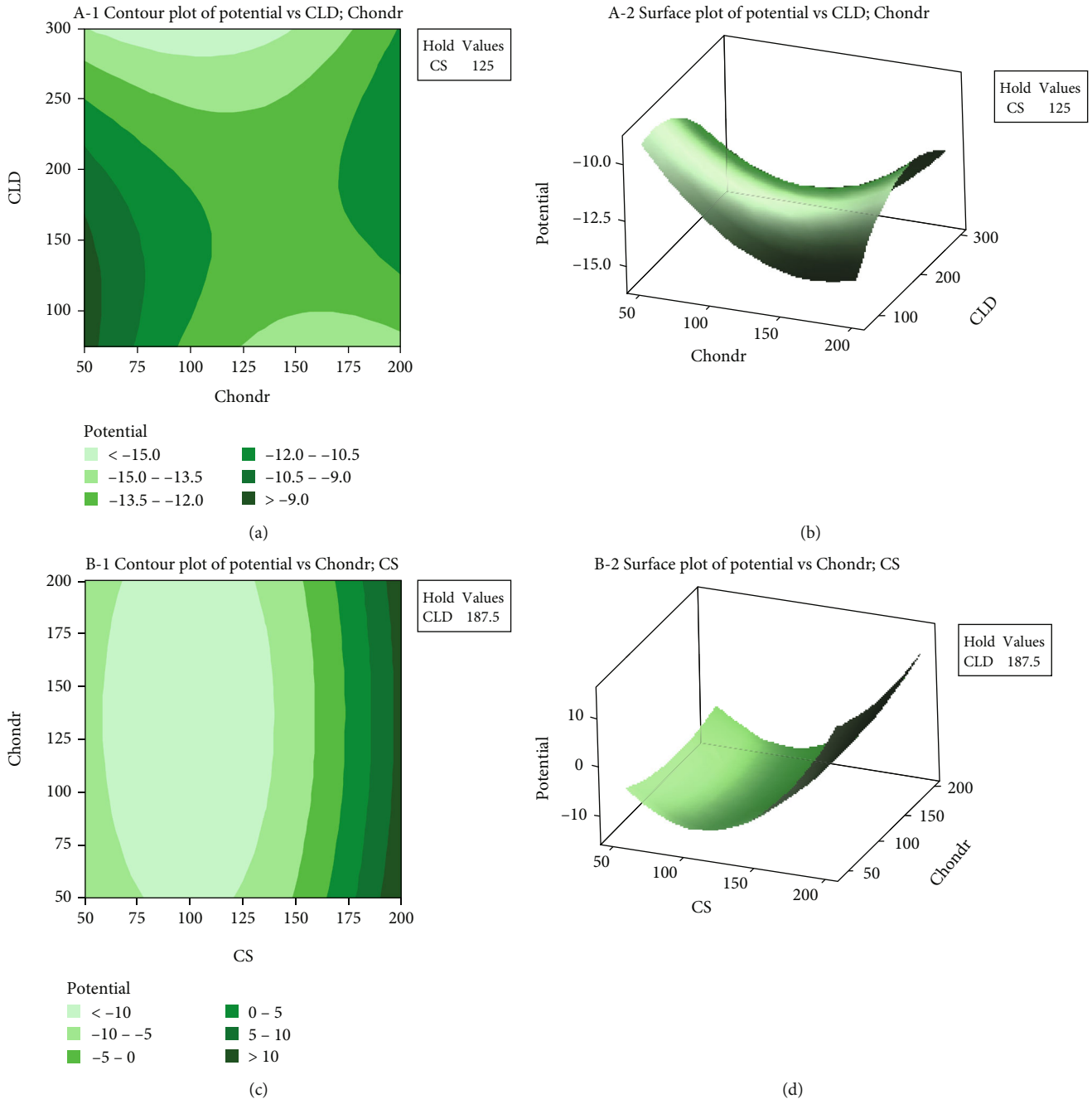

Figure 8: Continued.

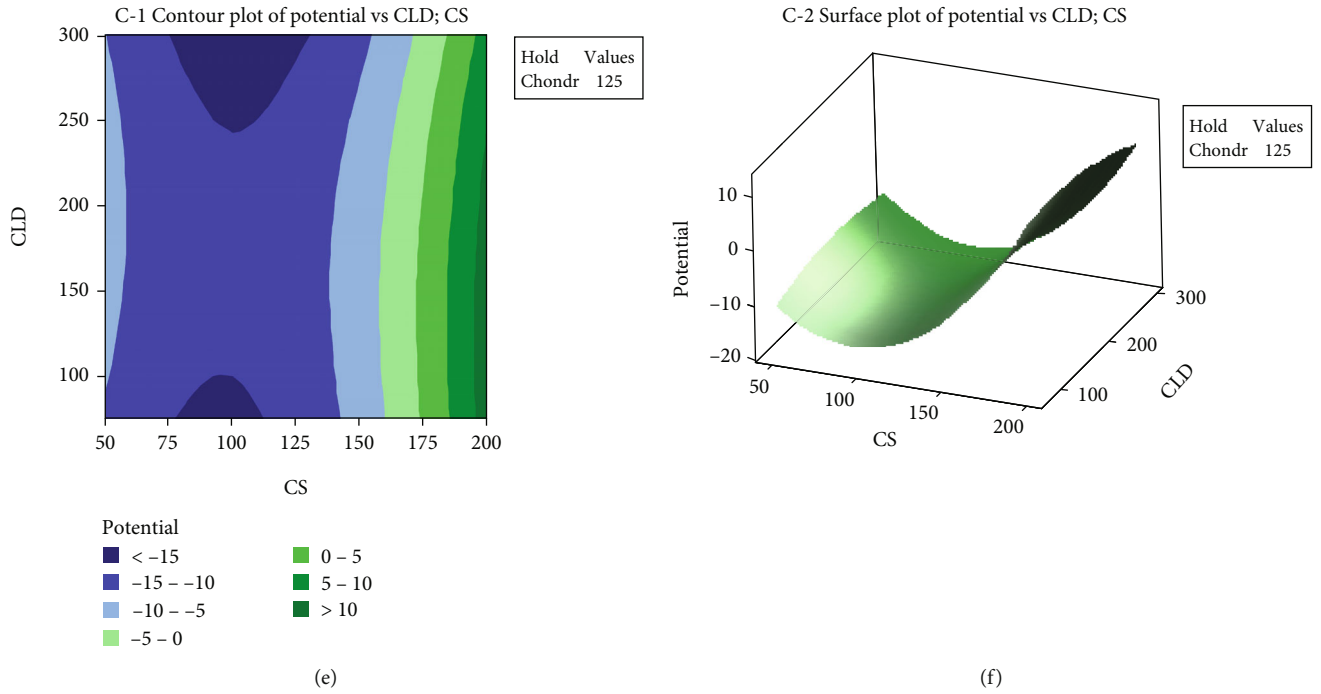

Figure 8: The contour plot and surface plot of zeta potential against different factors.

Table 5: Comparison of the observed and predicted values of the response variables of optimized formulation.

Concentrations	Experimental response	Predicted values	Observed values	Bias (%)
CS = 200 mg Chondro = 138 mg CLD = 254 mg	LE (%)	64.1	61.2	-4.5
	Particle size (nm)	271.0	253.4	-6.5
	Zeta potential (mV)	11.7	11.3	-3.4
CS = 128 mg Chondro = 138 mg CLD = 254 mg	LE (%)	56.0	52.4	-6.4
	Particle size (nm)	220.0	220.7	0.3
	Zeta potential (mV)	-11.3	-10.9	-3.5
CS = 160 mg Chondro = 112 mg CLD = 149 mg	LE (%)	35.0	39.0	11.4
	Particle size (nm)	263.4	259.1	-1.6
	Zeta potential (mV)	-13.9	-14.5	5.4

Bias was calculated as (observed value – predicted value/predicted value) × 100%.

Figure 7(a) shows the contour plot of size against the Chondro and CLD. The smallest values of particle size are at the bottom of the plot, which corresponds with 50 mg of CLD, and Chondro varies from 115 mg to 175 mg; the surface is minimum (Figure 7(b)).

In Figure 7(c), the contour plot shows that the minimum particle size occurs at low concentrations of CS and CLD; the surface is minimum (Figure 7(d)). In addition, Figure 7(e) shows the contour plot of size against the Chondro and CS. The smallest values of particle size are at the bottom left of the plot, which corresponds with 50 mg of CS, and Chondro and varies from 50 mg to 175 mg; the surface is minimum (Figure 7(f)).

Figures 8(a) and 8(b) shows the contour plot of zeta potential against the Chondro and CLD. The -15 mV zeta potential can be collected at Chondro concentration range of 50-200 mg and CLD at 300 mg. The -9 mV zeta potential can be collected at Chondro concentration below 60 mg and CLD ranging between 50 and 160 mg.

Figure 8(c) shows that the zeta potential was dependent on CS and Chondro. When CS was more than 190 mg and at the same time the Chondro was between 50 and 200 mg, the zeta potential was found to be +10 mV (Figure 8(d)). In addition, when CS variables were in the range 75-125 mg and the Chondro was between 50 and 200 mg, the zeta potential was found to be -10 mV (Figure 8(d)). The contour of CS vs. CLD concentrations is shown in Figure 8(e). When CS variables were between 50 and 190 mg and at same time the CLD was between 50 and 300 mg, the zeta potential was found to be -15 mV (Figures 8(e) and 8(f)). Finally, when the CS concentrations were more than 160 mg, they produced a positive value of zeta potential.

4.9. Prediction, Optimization, and Validation of Three Models. Taking into account the main factors in our work (A, B, and C) and their combinations (A ∗ A, B ∗ B, C ∗ C, A ∗ B, A ∗ C, and B ∗ C), a general equation can be obtained with regard to the real values by a response surface method. For predicting %LE, particle size, and zeta potential, the following equations were derived:

$$\begin{aligned}
\%\text{LE} &= 91.21 - 0.627\,\text{CS} - 0.3962\,\text{Chondro} \\
&\quad + 0.1023\,\text{CLD} + 0.001816\,\text{CS} * \text{CS} \\
&\quad + 0.001038\,\text{CS} * \text{Chondro} \\
&\quad + 0.000733\,\text{Chondro} * \text{CLD}. \\
\text{Particle size} &= -56.3 + 2.170\,\text{CS} - 0.661\,\text{Chondro} \\
&\quad + 1.0236\,\text{CLD} + 0.00496\,\text{CS} * \text{CS} \\
&\quad + 0.00601\,\text{Chondro} * \text{Chondro} \\
&\quad - 0.008586\,\text{CS} * \text{Chondro}0.007388\,\text{CS} \\
&\quad * \text{CLD}. \\
\text{Zeta potential} &= 16.44 - 0.4745\,\text{CS} - 0.1626\,\text{Chondro} \\
&\quad + 0.0443\,\text{CLD} + 0.002555\,\text{CS} * \text{CS} \\
&\quad + 0.000421\,\text{Chondr} * \text{Chondr} \\
&\quad - 0.000173\,\text{CLD} * \text{CLD} - 0.000174\,\text{CS} \\
&\quad * \text{CLD} + 0.000259\,\text{Chondr} * \text{CLD}.
\end{aligned} \tag{8}$$

According to our criteria for higher %LE (88.86%), the concentrations under canonical analysis were selected at 50 mg, 50 mg, and 300 mg, of CS, Chondro, and CLD, respectively. In addition, to prepare nanoparticles with a size of 64 nm, 50 mg CS, 91 mg Chondro, and 75 mg CLD were used. Furthermore, the zeta potential with -17 mV value can be obtained by using 103.3 mg CS, 101.5 mg Chondro, and 300 mg CLD.

A bias formula under optimized factors was applied to compare with the predicted values. As shown in Table 5, the bias was around −4.5%, −6.5%, and 3.4% for the first formula (CS = 200 mg, Chondro = 138 mg, and CLD = 254 mg). In addition, the bias was around −6.4%, 0.3%, and -3.5% for the second formula (CS = 128 mg, Chondro = 138 mg, and CLD = 254 mg) and around 11.4%, -1.6%, and 15.4% for the third formula (CS = 160 mg, Chondro = 112 mg, and CLD = 149 mg), respectively. These results indicate the validity of the generated models with no statistically significant difference and good correlation between predicted and experimental values.

The zeta potential (mV) of nanocarriers represents the surface charge. It depends on the dispersing medium as well as the composition of the particles. The nanoparticles that possess zeta potentials between +30 mV and −30 mV are considered a stable system that prevents nanoparticle aggregation. From Table 5, the observed zeta potential values of nanocomposites are 11.3, -10.9, and -14.5 mV. These values indicate that the nanocomposites were stable.

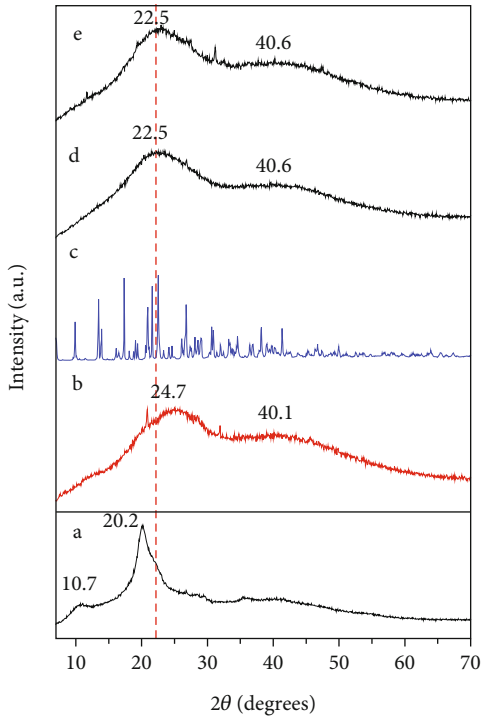

Figure 9: Powder X-ray diffraction patterns of the CS (a), Chondro (b), CLD (c), CS-Chondro (d), and CS-Chondro-CLD nanocomposites (e).

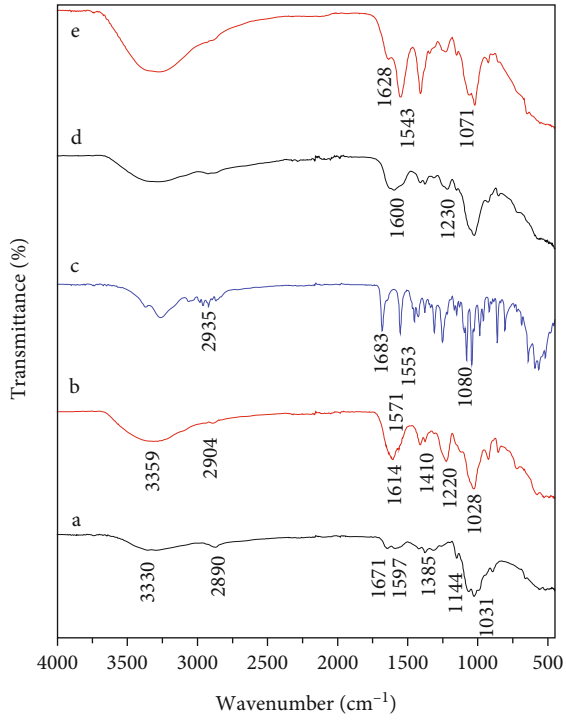

Figure 10: FT-IR spectrum of CS (a), Chondro (b), CLD (c), CS-Chondro (d), and CS-Chondro-CLD nanocomposites (e).

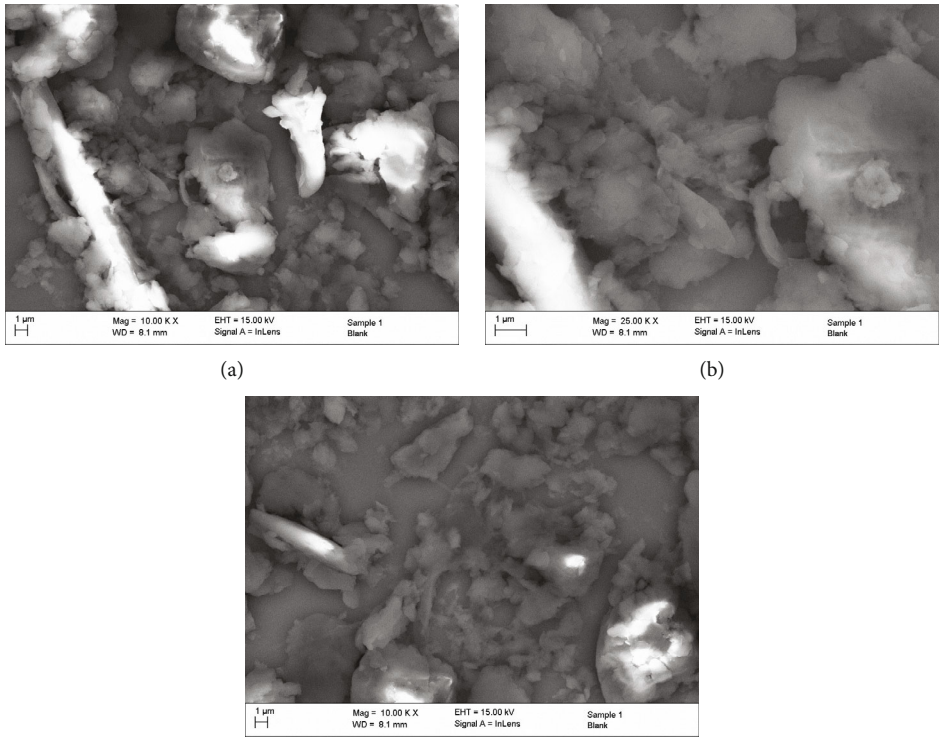

Figure 11: SEM images of Chondro-CS (a, b) and Chondro-CS-CLD (c).

5. Characterization of Formulations

5.1. X-Ray Diffraction (XRD). Figures 9 (a), (b), (c), (d), and (e) shows the XRD patterns of CS, Chondro, CLD, CS-Chondro, and CS-Chondro-CLD nanocomposites, respectively. From Figure 9(a), CS showed strong diffraction peaks at $2\theta = 10.7$ and 20.2°, indicating a high degree of crystallinity [41, 42].

Diffraction broad bands similar to Chondro were seen for CS-Chondro and CS-Chondro-CLD due to amorphous behavior of the polymer. The diffraction peaks of Chondro were observed at 24.7 and 40.1° (Figure 9(b)), whereas the diffraction peaks with maximum intensity were observed at 22.5 for CS-Chondro and CS-Chondro-CLD as seen in Figures 9(d) and (e). These diffraction peaks in Chondro, CS-Chondro, and CS-Chondro-CLD were very broad which is indicative of their highly amorphous nature with low crystallinity [43].

5.2. Infrared Spectroscopy (FTIR). The IR spectra of CS (a), Chondro (b), CLD (c), CS-Chondro (d), and CS-Chondro-CLD nanocomposites (e), respectively, are shown in Figure 10. IR spectrum of CS showed vibration at 3330 cm^{-1} due to overlapped –OH and N–H stretching; the C–H stretching of CH_3 or CH_2 groups of CS is at 2890 cm^{-1}. The peaks at 1671 and 1597 cm^{-1} correspond to the amide bonds and NH_2 group, respectively. The peak at 1385 cm^{-1} due to stretching of C=N bond and the stretching of C–O bond are shown at 1,079 and 1,030 cm^{-1} [44].

The IR spectrum of Chondro in Figure 10(b) showed the –OH and N–H stretching at 3359 cm^{-1}. The peak at 2904 cm^{-1} was due to C–H stretching of CH_3 or CH_2 groups. The peak at 1614 cm^{-1} was due to the amide bands, whereas the peaks at 1413 and 1380 cm^{-1} are due to the C–O stretch vibration, indicating the presence of a free carboxyl group. The peak at 1220 cm^{-1} was due to the stretching of S=O bond of SO_4^{2-} [44].

The IR spectrum of CS-Chondro is shown in Figure 10(c). The peak at 1671 cm^{-1} for amide in CS was shifted to 1600 cm^{-1}, whereas the peak of NH_2 group disappeared, and this leads to cross-linking of NH_2 of CS with Chondro [44]. The peak at 1220 cm^{-1} of S=O turned weaker and shifted to 1230 cm^{-1}, which indicates cross-linking of SO_4^{2-} group of CS with Chondro.

The FT-IR spectrum of CLD in Figure 10(c) showed characteristics of peaks at 1683 cm^{-1} (C=O stretching), 1080 cm^{-1} (C-O stretching), 1553 cm^{-1} (C=C stretching), and 2935 cm^{-1}(C-H stretching) [45].

Comparing the FT-IR spectrum of CS-Chondro-CLD in Figure 10(e) with the FT-IR spectrum of the CS-Chondro in Figure 10(d), two specific peaks of CLD can be seen to have appeared at 1683 $cm^{-1}$and 1553 cm^{-1}, indicating the incorporation of CLD into the CS-Chondro-CLD.

5.3. Scanning Electron Microscopy. SEM images are widely used to examine the surface morphology of polysaccharides [46]. The morphological analysis of Chondro-CS and Chondro-CS-CLD in this study was carried out using SEM.

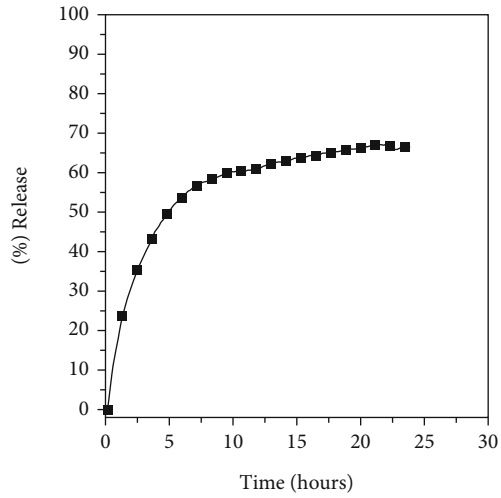

Figure 12: *In vitro* release profiles of CLD from nanocomposite at pH 7.4.

Figure 11 shows the SEM images of Chondro-CS and Chondro-CS-CLD with magnifications of 10000x and 25000x. It could be seen that the morphological properties of both Chondro-CS and Chondro-CS-CLD were similar (Figure 11(a)–11(c)). The Chondro-CS and Chondro-CS-CLD had a smooth homogeneous surface with lots of particle layers stacked together.

5.4. In Vitro Release Study. The release profiles of CLD from the optimized sample at pH 7.4 are illustrated in Figure 12.

It was noticed that the release rate of CLD at pH 7.4 was significantly very slow, where it started after 1 hour. This result can be explained based on the swelling term [47, 48]. The last results suggest that the CLD release profile was prominently prolonged by the encapsulation.

6. Conclusion

The aim of this work was to study the factors affecting the %LE, zeta potential, and particle size using response surface methodology model. The results indicated that for %LE, the square (Chondro ∗ Chondro and CLD ∗ CLD) and two-way interaction (CS ∗ CLD) was excluded from the final equation, whereas at size response, two-way interaction (Chondro ∗ CLD) only was excluded from the final equation. In addition, at zeta potential response, two-way interaction (CS ∗ Chondro) was excluded from the final equation. The developed multiple linear regression models provided the best fits to the data set. The XRD spectra of nanocomposites showed amorphous forms. The FT-IR data shows the functional group of CLD in nanocomposites, indicating incorporation of CLD into the nanocomposites. In addition, the prepared formulation shows sustained release, which may increase the chance for the patient to respond to the medication, since formulations are generally characterized by one daily given dose.

Data Availability

The original data can collected from Prof Samer AlAli by contact in his email sameralali72@yahoo.com or samer.alali@iu.edu.jo.

Conflicts of Interest

The authors report no conflicts of interest in this work.

Acknowledgments

The authors would like to thank the Faculty of Pharmacy at Isra University for provided funding for this research 2017/2018/19 (6/9/2018). Furthermore, the authors would like to acknowledge the Institute of Functional Nanosystems for the permission to use their advanced facilities in UIM University (Germany).

References

[1] D. K. Robinson, A. Rip, and V. Mangematin, "Technological agglomeration and the emergence of clusters and networks in nanotechnology," *Research Policy*, vol. 36, no. 6, pp. 871–879, 2007.

[2] P. Christian, F. von der Kammer, M. Baalousha, and T. Hofmann, "Nanoparticles: structure, properties, preparation and behaviour in environmental media," *Ecotoxicology*, vol. 17, no. 5, pp. 326–343, 2008.

[3] P. Homayonpour, H. Jalali, N. Shariatifar, and M. Amanlou, "Effects of nano-chitosan coatings incorporating with free /nano-encapsulated cumin (_Cuminum cyminum_ L.) essential oil on quality characteristics of sardine fillet," *International Journal of Food Microbiology*, vol. 341, article 109047, 2021.

[4] B. Vigani, S. Rossi, G. Sandri, M. C. Bonferoni, C. M. Caramella, and F. Ferrari, "Hyaluronic acid and chitosan-based nanosystems: a new dressing generation for wound care," *Expert Opinion on Drug Delivery*, vol. 16, no. 7, pp. 715–740, 2019.

[5] M. Yeganeh, E. Charkhloo, H. R. Sobhi, A. Esrafili, and M. Gholami, "Photocatalytic processes associated with degradation of pesticides in aqueous solutions: systematic review and _meta_ -analysis," *Chemical Engineering Journal*, vol. 428, article 130081, 2022.

[6] R. Noroozi, M. Gholami, M. Farzadkia, and A. Jonidi Jafari, "Degradation of ciprofloxacin by $CuFe_2O_4$/GO activated PMS process in aqueous solution: performance, mechanism and degradation pathway," *International Journal of Environmental Analytical Chemistry*, vol. 102, no. 1, pp. 174–195, 2022.

[7] N. M. Mahmoodi and M. Arami, "Modeling and sensitivity analysis of dyes adsorption onto natural adsorbent from colored textile wastewater," *Journal of Applied Polymer Science*, vol. 109, no. 6, pp. 4043–4048, 2008.

[8] D. Asefi, N. M. Mahmoodi, and M. Arami, "Effect of nonionic co-surfactants on corrosion inhibition effect of cationic gemini surfactant," *Colloids and Surfaces A: Physicochemical and Engineering Aspects*, vol. 355, no. 1-3, pp. 183–186, 2010.

[9] S. Bhatia and S. Bhatia, "Nanoparticles types, classification, characterization, fabrication methods and drug delivery applications," in *Natural Polymer Drug Delivery Systems*, pp. 33–93, Springer, 2016.

[10] B. Mishra, B. B. Patel, and S. Tiwari, "Colloidal nanocarriers: a review on formulation technology, types and applications toward targeted drug delivery," *Nanomedicine: Nanotechnology, Biology and Medicine*, vol. 6, no. 1, pp. 9–24, 2010.

[11] C. Dussaubat, J. L. Brunet, M. Higes et al., "Gut pathology and responses to the microsporidium Nosema ceranae in the honey bee Apis mellifera," *PLoS One*, vol. 7, no. 5, article e37017, 2012.

[12] J. N. Hathcock and A. Shao, "Risk assessment for glucosamine and chondroitin sulfate," *Regulatory Toxicology and Pharmacology*, vol. 47, no. 1, pp. 78–83, 2007.

[13] O. Bukalo, M. Schachner, and A. Dityatev, "Modification of extracellular matrix by enzymatic removal of chondroitin sulfate and by lack of tenascin-R differentially affects several forms of synaptic plasticity in the hippocampus," *Neuroscience*, vol. 104, no. 2, pp. 359–369, 2001.

[14] A.-M. Anton, I. Rau, F. Kajzar, A. M. Simion, and C. Simion, "Third order nonlinear optical properties of DNA-based biopolymers thin films doped with selected natural chromophores," *Optical Materials*, vol. 88, pp. 181–186, 2019.

[15] P. Homayonpour, H. Jalali, N. Shariatifar, and M. Amanlou, "Performance investigation of Zeolitic Imidazolate Framework - 8 (ZIF-8) in the removal of trichloroethylene from aqueous solutions," *Microchemical Journal*, vol. 150, article 104185, 2019.

[16] R. Duncan and J. Kopeček, "Soluble synthetic polymers as potential drug carriers," in *Polymers in Medicine*, Springer, Berlin, Heidelberg, 1984.

[17] M. Smieja, "Current indications for the use of clindamycin: a critical review," *Canadian Journal of Infectious Diseases and Medical Microbiology*, vol. 9, 28 pages, 1998.

[18] M. Seminario-Amez, J. López-López, A. Estrugo-Devesa, R. Ayuso-Montero, and E. Jané-Salas, "Probiotics and oral health: a systematic review," *Medicina Oral, Patología Oral y Cirugía Bucal*, vol. 22, article e282, e288 pages, 2017.

[19] M. J. Kasten, "Clindamycin, metronidazole, and chloramphenicol," *Mayo Clinic Proceedings*, vol. 74, no. 8, pp. 825–833, 1999.

[20] M. Abbaspour, B. S. Makhmalzadeh, Z. Arastoo, A. Jahangiri, and R. Shiralipour, "Effect of anionic polymers on drug loading and release from clindamycin phosphate solid lipid nanoparticles," *Tropical Journal of Pharmaceutical Research*, vol. 12, no. 4, pp. 477–482, 2013.

[21] A. A. Abdellatif and H. M. Tawfeek, "Transfersomal nanoparticles for enhanced transdermal delivery of clindamycin," *AAPS PharmSciTech*, vol. 17, no. 5, pp. 1067–1074, 2016.

[22] P. R. Rauta, N. M. das, D. Nayak, S. Ashe, and B. Nayak, "Enhanced efficacy of clindamycin hydrochloride encapsulated in PLA/PLGA based nanoparticle system for oral delivery," *IET Nanobiotechnology*, vol. 10, no. 4, pp. 254–261, 2016.

[23] M. Kilicarslan, M. Ilhan, O. Inal, and K. Orhan, "Preparation and evaluation of clindamycin phosphate loaded chitosan/alginate polyelectrolyte complex film as mucoadhesive drug delivery system for periodontal therapy," *European Journal of Pharmaceutical Sciences*, vol. 123, pp. 441–451, 2018.

[24] O. Borges, G. Borchard, J. C. Verhoef, A. de Sousa, and H. E. Junginger, "Preparation of coated nanoparticles for a new mucosal vaccine delivery system," *International Journal of Pharmaceutics*, vol. 299, no. 1-2, pp. 155–166, 2005.

[25] M. K. Yeh, K. M. Cheng, C. S. Hu, Y. C. Huang, and J. J. Young, "Novel protein-loaded chondroitin sulfate-chitosan nanoparticles: preparation and characterization," *Acta Biomaterialia*, vol. 7, no. 10, pp. 3804–3812, 2011.

[26] T. A. Abdullah, N. J. Ibrahim, and M. H. Warsi, "Chondroitin sulfate-chitosan nanoparticles for ocular delivery of bromfenac sodium: improved permeation, retention, and penetration," *International journal of pharmaceutical investigation*, vol. 6, no. 2, pp. 96–105, 2016.

[27] B. Saifullah, M. Z. Hussein, S. H. Hussein-Al-Ali, P. Arulselvan, and S. Fakurazi, "Antituberculosis nanodelivery system with controlled-release properties based on para-amino salicylate–zinc aluminum-layered double-hydroxide nanocomposites," *Drug Design, Development and Therapy*, vol. 7, p. 1365, 2013.

[28] M. J. Anderson, "Distance-based tests for homogeneity of multivariate dispersions," *Biometrics*, vol. 62, no. 1, pp. 245–253, 2006.

[29] G. J. McLachlan, "Mahalanobis distance," *Resonance*, vol. 4, no. 6, pp. 20–26, 1999.

[30] L. Murray, H. Nguyen, Y. F. Lee, M. D. Remmenga, and D. W. Smith, *Variance Inflation Factors in Regression Models with Dummy Variables*, 2012.

[31] S. Sinharay, "An overview of statistics in education," in *International Encyclopedia of Education (Third Edition)*, P. Peterson, E. Baker, and B. McGaw, Eds., pp. 1–11, Elsevier, Oxford, 2010.

[32] K. Nishimura, S. I. Nishimura, H. Seo, N. Nishi, S. Tokura, and I. Azuma, "Macrophage activation with multi-porous beads prepared from partially deacetylated chitin," *Journal of Biomedical Materials Research Part A*, vol. 20, no. 9, pp. 1359–1372, 1986.

[33] A. Jain and S. K. Jain, "Formulation and optimization of temozolomide nanoparticles by 3 factor 2 level factorial design," *Biomatter*, vol. 3, no. 2, article e25102, 2013.

[34] G. Khairnar, J. Naik, and V. Mokale, "A statistical study on the development of micro particulate sustained drug delivery system for losartan potassium by 3^2 factorial design approach," *Bulletin of Faculty of Pharmacy, Cairo University*, vol. 55, no. 1, pp. 19–29, 2017.

[35] F. J. Massey, "The Kolmogorov-Smirnov test for goodness of fit," *Journal of the American Statistical Association*, vol. 46, no. 253, pp. 68–78, 1951.

[36] G. Fasano and A. Franceschini, "A multidimensional version of the Kolmogorov–Smirnov test," *Monthly Notices of the Royal Astronomical Society*, vol. 225, no. 1, pp. 155–170, 1987.

[37] A. Justel, D. Peña, and R. Zamar, "A multivariate Kolmogorov-Smirnov test of goodness of fit," *Statistics & Probability Letters*, vol. 35, no. 3, pp. 251–259, 1997.

[38] P. O'Connor and A. Kleyner, *Practical reliability engineering*, John Wiley & Sons, 2012.

[39] R. D'Agostino and M. Stephens, *Tests for Normal Distribution in Goodness-Of-Fit Techniques, Statistics: Textbooks and Monographs*, R. B. D'Agostino and M. A. Stephens, Eds., Dekker, New York, 1986.

[40] "Quick and easy analysis of Unreplicated factorials," *Technometrics*, vol. 31, no. 4, pp. 469–473, 1989.

[41] L. Qi, Z. Xu, X. Jiang, C. Hu, and X. Zou, "Preparation and antibacterial activity of chitosan nanoparticles," *Carbohydrate Research*, vol. 339, no. 16, pp. 2693–2700, 2004.

[42] C. Radhakumary, P. D. Nair, S. Mathew, and C. R. Nair, "Biopolymer composite of chitosan and methyl methacrylate for

medical applications," *Biomaterials and Artificial Organs*, vol. 18, no. 2, pp. 117–124, 2005.

[43] J. Venkatesan, R. Pallela, I. Bhatnagar, and S. K. Kim, "Chitosan-amylopectin/hydroxyapatite and chitosan-chondroitin sulphate/hydroxyapatite composite scaffolds for bone tissue engineering," *International Journal of Biological Macromolecules*, vol. 51, no. 5, pp. 1033–1042, 2012.

[44] J. R. Amrutkar and S. G. Gattani, "Chitosan–chondroitin sulfate based matrix tablets for colon specific delivery of indomethacin," *AAPS PharmSciTech*, vol. 10, no. 2, pp. 670–677, 2009.

[45] P. Patel and P. Patel, "Formulation and evaluation of clindamycin HCL in situ gel for vaginal application," *International journal of pharmaceutical investigation*, vol. 5, no. 1, pp. 50–56, 2015.

[46] D. A. Brant, "Novel approaches to the analysis of polysaccharide structures," *Current Opinion in Structural Biology*, vol. 9, no. 5, pp. 556–562, 1999.

[47] C. S. Nunes, K. B. Rufato, P. R. Souza et al., "Chitosan/chondroitin sulfate hydrogels prepared in [Hmim][HSO_4] ionic liquid," *Carbohydrate Polymers*, vol. 170, pp. 99–106, 2017.

[48] S. Nanda, N. Sood, B. V. K. Reddy, and T. S. Markandeywar, "Preparation and characterization of poly(vinyl alcohol)-chondroitin sulphate hydrogel as scaffolds for articular cartilage regeneration," *Indian Journal of Materials Science*, vol. 2013, Article ID 516021, 8 pages, 2013.

Hindawi
Journal of Nanomaterials
Volume 2022, Article ID 6405772, 8 pages
https://doi.org/10.1155/2022/6405772

Research Article

An *In Vitro* Study on the Antibacterial Effects of Chlorhexidine-Loaded Positively Charged Silver Nanoparticles on *Enterococcus faecalis*

Ahmad Gholami,[1,2,3] **Keyvan Ghezelbash**,[4] **Bahar Asheghi**,[4] **Abbas Abbaszadegan**,[4] **and Abbas Amini**[5]

[1]*Biotechnology Research Center, Shiraz University of Medical Sciences, Shiraz, Iran*
[2]*Pharmaceutical Sciences Research Center, Shiraz University of Medical Sciences, Shiraz, Iran*
[3]*Department of Pharmaceutical Biotechnology, School of Pharmacy, Shiraz University of Medical Sciences, Shiraz, Iran*
[4]*Department of Endodontics, Shiraz Dental School, Shiraz University of Medical Sciences, Shiraz, Iran*
[5]*Centre for Infrastructure of Engineering, Western Sydney University, Penrith, NSW 2751, Australia*

Correspondence should be addressed to Bahar Asheghi; asheghib@sums.ac.ir
and Abbas Abbaszadegan; dr.abbaszadegan@gmail.com

Received 6 January 2022; Revised 25 April 2022; Accepted 26 June 2022; Published 25 July 2022

Academic Editor: Isaac Acquah

This study successfully developed a positively charged silver nanocomplex as a nanocarrier for chlorhexidine (CHX) using ionic liquids. This nanocomplex can interestingly deliver the antibacterial agent with a synergistic effect. In this study, we synthetized and characterized a positively charged silver nanocomplex ($AgNPs^+$) and CHX-loaded positively charged silver nanoparticles ($CHX@AgNPs^+$) using UV-visible spectroscopy, transmission electron microscopy, X-ray diffractometer, Fourier transform infrared spectroscopy, and Zetasizer. Then, the loading efficiency and release profile of XHX from nanocomplex were evaluated. The antibacterial activity was evaluated by employing two standard microdilution tests to obtain the minimum bactericidal and inhibitory concentrations. The average sizes of 27.43 nm and 29.66 nm were obtained for $AgNPs^+$ and $CHX@AgNPs^+$, respectively. The $CHX@AgNPs^+$ showed a constant release of CHX, making them a more effective antibacterial agent against *Enterococcus faecalis* (*E. faecalis*) than CHX or $AgNPs^+$ alone. Antibacterial assays showed that $CHX@AgNPs^+$ significantly reduced the viability of the bacterial strain compared to CHX as the standard irrigant. $AgNPs^+$ had an antibacterial effect similar to CHX only at intermediate concentrations (12 and 25 μg/mL), and their effects were significantly less than those of CHX at other concentrations (3, 6, 50, and 100 μg/mL). The effects of $CHX@AgNPs^+$ were statistically greater than those of $AgNPs^+$ at all concentrations tested. The MIC values of $CHX@AgNPs^+$ and CHX were 50 and 100 μg/mL. However, $AgNPs^+$ were not showed MIC value at tested concentrations. Therefore, the designed nanocomplex can be regarded as a potential root canal disinfectant with clinical applications for bacterial infections.

1. Introduction

Bacterial elimination in infected root canal systems is performed using mechanical debridement and chemical elimination of intraradicular microorganisms [1]. As a very resistant microorganism in infected root canals, *Enterococcus faecalis* (*E. faecalis*) can stubbornly survive lethal challenges and invade dentinal tubules, making it the most persistent pathogen in root canal treatment [2].

For the chemomechanical preparation of the root canal system, one or more antibacterial irrigants may be used to enhance intracanal disinfection. Ethylenediaminetetraacetic

acid (EDTA), chlorhexidine (CHX), and sodium hypochlorite (NaOCl) are the most frequently used root canal irrigation solutions for removing bacteria from infected canals. NaOCl and EDTA remove the smear layer from the infected canals. NaOCl also has a tissue dissolution capability [3, 4]. The principal downside of NaOCl is its nasty odor and taste along with its caustic effect particularly when it is extruded from the apical region. Although CHX is an interesting irrigant with an effective antibacterial activity, previous studies have demonstrated that it has a toxic effect on some eukaryotic cells [5]. Besides, its activity is pH sensitive and it should be prescribed with care due to the risk of bacterial resistance [6]. Although many studies have been conducted on intracanal preparation and canal irrigants, no ideal endodontic irrigant has been found yet [7].

Silver nanoparticles (AgNPs) have a strong and broad-spectrum antibacterial activity. As a result, they have been employed in several fields including dentistry [8]. It has been speculated that AgNPs interfere with oxygen uptake and bacterial cell wall integrity due to their ability to bind with enzymes and proteins [9]. Furthermore, many studies have demonstrated that Ag particles at the nanoscale are compatible with human cells in minute concentrations [10]. In addition, the surface charge of AgNPs and their magnitude play a significant role in the level of their antibacterial activity [11].

One of the most significant global threats is antibacterial resistance [12]. To counter antibacterial resistance, it is required that new drug development strategies such as combination therapies be implemented. One technique to improve the efficacy of antibacterial agents is to combine them in order to counter the rising rates of resistance to conventional antibacterial agents [13]. Combination therapies are different in terms of the number of their components and the targeted pathways [14].

Previous studies have shown the synergistic effects of antibacterial agents in dental treatments. Lu et al. demonstrated the synergistic effects of CHX and AgNPs against peri-implantitis pathogens [15]. Moreover, another study showed that the mixture of calcium and nanosilver can have good and residual antibacterial properties after one week compared with the other groups [16]. Combining CHX and silver ions can increase their effectiveness and improve the quality of endodontic treatment [17].

A suitable nanocarrier for antibacterial compounds that can target infection foci in the root canal microenvironment is one of the necessities of modern endodontic treatment [18].

This *in vitro* study was designed to (i) synthesize and characterize AgNPs with a positive charge and a CHX molecule loaded on them (CHX@$AgNPs^+$) and (ii) to evaluate their antibacterial efficacy by determining their minimum bactericidal concentration (MBC) and minimum inhibitory concentration (MIC) against *E. faecalis* and comparing them with those of CHX and $AgNPs^+$ alone.

2. Materials and Methods

2.1. Synthesis and Characterization. In order to synthesize the positively charged NPs, 1.0 mL of an aqueous solution of $AgNO_3$ (Sigma-Aldrich Co., St. Louis, MO, USA, 0.01 M) was mixed and stirred with 6.2 mM 1-dodecyl-3-methylimidazolium chloride (Sigma-Aldrich Co., USA) according to our previous study [19]. The prepared 0.4 M $NaBH_4$ aqueous solution was next instantly added dropwise to the stirred solutions till a golden color was resulted. Afterward, to remove the remaining ionic liquids, the colloidal solutions were centrifuged for approximately 20 min.

An alcoholic solution of CHX (Sigma-Aldrich Co., USA, 1.5 mg/mL) was prepared and poured on the alcoholic suspension of $AgNPs^+$ (2 mg/mL) and stirred for 24 h at room temperature using a magnetic stirrer. Finally, the obtained suspension was dried at 40°C in the oven and kept in a dark container in the refrigerator for antibacterial studies. Before the antibacterial studies, the powder was suspended in sterile distilled water.

Several analytical instruments were used in order to characterize the synthesized nanoparticles. UV-visible spectroscopy is a simple and common technique to verify the formation of nanoparticles. In the current research, distilled water was used as a reference. A UV-1800 UV-visible spectrometer (Shimadzu Corporation, Kyoto, Japan) was employed to obtain the absorbance spectrum of the colloidal sample which was found to range from 200 to 800 nm.

The transmission electron microscopy (TEM) analysis was performed in order to determine the morphology, shape, and size of AgNPs. The TEM measurements were performed using a HITACHI H-800 microscope which operated at 200 kV. In order to prepare the TEM grid, a drop of the diluted solution was placed on a carbon-coated copper grid and then dried under a lamp.

A Siemens D5000 diffractometer (Karlsruhe, Germany) was employed for the X-ray diffraction (XRD) analysis using monochromatic Cu kα radiation ($\lambda = 1.5406$ Å) which operated at 40 kV and 30 mA at a 2θ angle pattern. The scanning range was from 20° to 80°. A comparison was performed between the obtained images and the database of Joint Committee on Powder Diffraction Standards (JCPDS) so that the crystalline structure could be explained.

The Fourier transform infrared spectroscopy (FT-IR spectroscopy) analysis was conducted to classify the compounds responsible both for the stabilization of nanoparticles and the reduction of metals. A Vertex 70 (Bruker, Germany) in the wavelength range of 400-4000 cm^{-1} was employed to analyze the functional group at the surface of AgNPs.

Using a Zetasizer (Nano ZS-90, Malvern Instruments, UK), the zeta potentials of the nanoparticles were determined. 700 μL AgNP suspensions were freshly prepared and analyzed at 25°C with a scattering angle of 90°.

2.2. CHX Loading Efficiency. UV/VIS was used to evaluate the loading efficiency of CHX on $AgNPs^+$ at the wavelength of 254 nm. Accordingly, the amount of unloaded CHX after the loading procedure was calculated and the CHX loading percentage was presented using the following equation from the study of Gholami et al. [20]:

$$\text{Loading efficiency}\ (\%) = \frac{(\text{total concentration of CHX} - \text{concentration of unloaded CHX})}{\text{concentration of CHX}}. \quad (1)$$

2.3. CHX Release Profile. Based on the study of Gholami et al. [20], UV/VIS at 254 nm was used to assess the release behavior of CHX on $AgNPs^+$. 20 mg of CHX@$AgNPs^+$ in a dialysis bag (with a cutoff of 100 kDa) was placed in PBS (50 mL) for 7 days at 37°C, and the rate of drug release was measured at predetermined time points. At these time points, 1 mL PBS was taken from the container and the released CHX was reported.

2.4. Antibacterial Study through the Determination of MIC and MBC. The MBC and MIC of each experimental solution against planktonic *E. faecalis* were obtained three times by a microdilution broth method. The tested solutions were 0.2% CHX, $AgNPs^+$, and synthesized CHX@$AgNPs^+$. All the tests were conducted according to the instructions of the Clinical and Laboratory Standards Institute (CLSI). In order to obtain the MIC, 2-fold serial dilutions (up to seven times) of the experimental solutions and the control group were prepared using Mueller-Hinton broth (MHB) in 96-well microplates. To obtain a volume of 90 μL, *E. faecalis* was cultured in BHI broth and the turbidity was set to 0.11-0.13 at an optical density (OD) of 600, resulting in 1.5×10^8 colony forming units per milliliter (CFU/mL) of bacteria. Then, the suspension was diluted 1 : 20 with broth culture. Eventually, 10 μL of *E. faecalis* suspension was added to each microplate and incubated at 37°C. After 24 hours, a microplate reader was used to record the absorbance at a wavelength of 600 nm to evaluate the inhibitory effects of the test solutions. The positive control group consisted of *E. faecalis* inoculated culture media, while the negative control group was composed of culture media without microorganisms. The least concentration of each experimental solution inhibiting 90% of *E. faecalis* growth compared with the negative control group was defined as the MIC value.

To quantify the level of MBC for the test irrigants, the experimental solutions with equal and higher concentrations than the MICs were placed on tryptic soy agar plates and incubated at 37°C. The colonies were counted after 24 hours. The MBC value was defined as the least concentration leading to the almost complete elimination of the microorganisms in the primary inocula. This happened when less than 4 visible colonies were detectable in the agar plates after 24 h of incubation at 37°C.

2.5. Statistical Analysis. The one-way ANOVA was used to compare the antibacterial agents. Tukey's post hoc test was utilized to analyze the data. In addition, the SPSS statistical software (IBM, version: 19.0) was employed to evaluate the results. The P value of <0.05 was assumed a significant difference, and the test was repeated thrice.

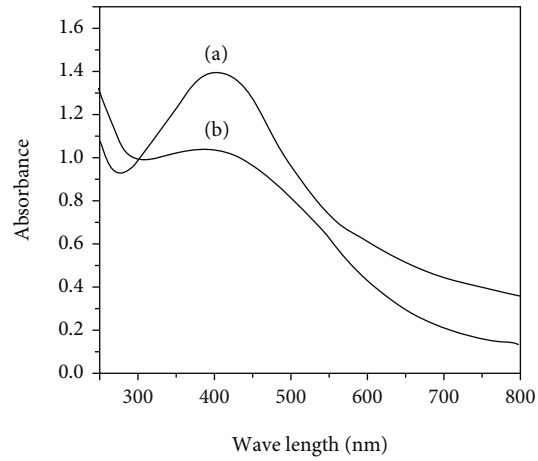

Figure 1: UV-visible spectroscopy of (a) $AgNPs^+$ and (b) CHX@$AgNPs^+$.

3. Results

3.1. Synthesis and Characterization of the Nanostructures. Positively charged silver nanoparticles with a relatively uniform spherical morphology were synthesized according to Gholami et al. [19]. The UV-visible spectroscopy of $AgNPs^+$ and CHX@$AgNPs^+$ is shown in Figure 1. A UV-vis spectrophotometer was employed to observe and record the synthesis process of AgNPs from 300 to 800 nm. During the reduction process, a characteristic absorption peak at around 400-450 nm resulted from the surface plasmon resonance (SPR) marked the formation of AgNPs [21]. The intensity of this peak was strongly correlated with the three factors of particle size, solvent dielectric constant, and chemical structure. AgNPs possess free electrons that result in a SPR absorption band that can be observed by a UV-vis spectrophotometer because of the mutual vibration of electrons in resonance with the light wave [22]. In this study, in the graphs of both $AgNPs^+$ and CHX@$AgNPs^+$, this characteristic peak appears in regions with a wavelength of about 450 nm. This wavelength range is in accordance with several previous studies [10, 19, 23].

As shown in Figure 2, the TEM micrographs of $AgNPs^+$ and CHX@$AgNPs^+$ represent spherical particles. To obtain the average sizes of the nanoparticles, 30 isolated nanoparticles in each figure were measured. The average sizes of 27.43 nm and 29.66 nm were obtained for $AgNPs^+$ and CHX@$AgNPs^+$, respectively. The TEM images revealed that the average sizes of $AgNPs^+$ and CHX@$AgNPs^+$ were approximately equal.

CHX was loaded on the surface of $AgNPs^+$ probably by introducing the cationic groups of ionic liquid into the CHX solution. The surface functionalization of positively charged CHX on $AgNPs^+$ may be due to the weak van der Waals forces such as lipophilic (between the alkyl chain of the CHX structures and the poly alkyl chain of the ionic liquid on $AgNPs^+$) and/or electrostatic interactions (between the Cl^- groups in the CHX molecule and the NH_3^+ groups in the imidazolium structure). Further studies are needed

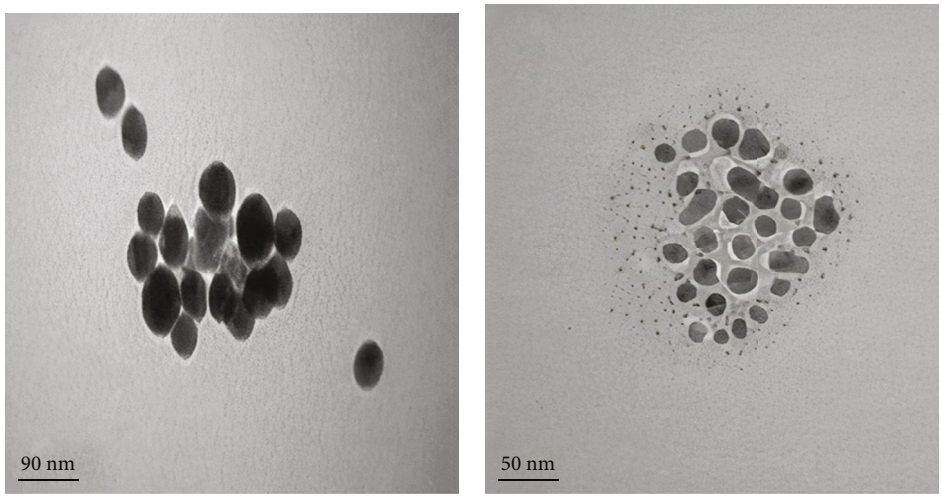

(a) (b)

Figure 2: The TEM images of (a) $AgNPs^+$ and (b) $CHX@AgNPs^+$.

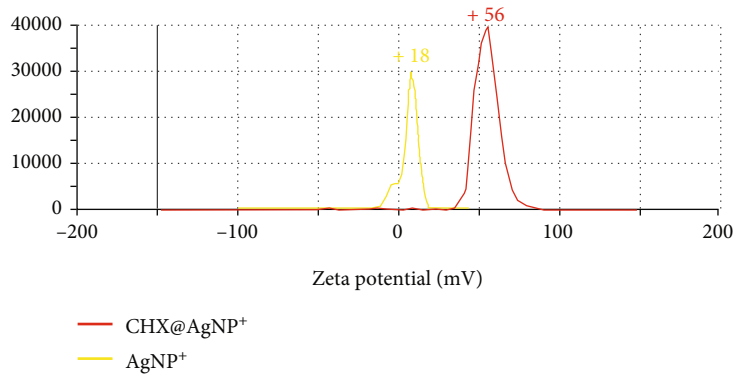

Figure 3: The zeta potentials of the $AgNPs^+$ and $CHX@AgNPs^+$.

to prove and accurately determine these interactions. However, the increase of the zeta potential after the functionalization of $AgNPs^+$ with CHX may partially confirm this claim.

In fact, using a DLS device, the zeta potentials of $AgNPs^+$ and $CHX@AgNPs^+$ were obtained as +18 mV and +56 mV, respectively. By adding CHX to $AgNPs^+$, the zeta potential increased from +18 mV to +56 mV due to the interaction between the cations of $AgNPs^+$ and CHX (with two cationic centers) containing 10 N atoms. The amplification of the zeta potential could also show that CHX intercalated within the alkylated AgNPs and altered their surfaces (Figure 3).

The wide-angle XRD pattern of the resulted AgNPs at a 2θ range of 20°-80° at room temperature revealed the intensity diffraction peaks at 38°, 44°, 65°, and 78° which corresponded to (111), (200), (220, 311) planes, respectively (Figure 4).

The functional groups involved in the stabilization, capping, surface, and reduction of AgNPs were confirmed by FT-IR analysis (Figure 5). As shown in graph 4a, there are characteristic peaks for $AgNPs^+$ at 3402, 2920, and 1644 cm^{-1}. The peak at 3402 cm^{-1} in the $AgNPs^+$ is associated with the N-H bond of amide and the O-H bond of

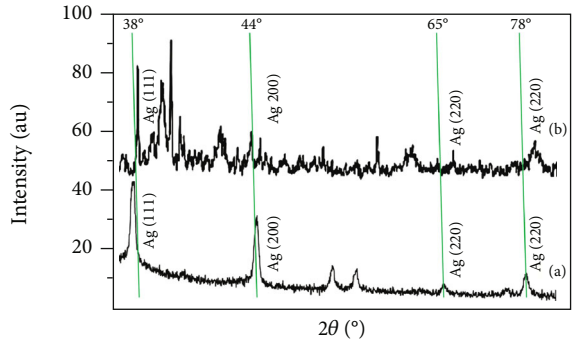

Figure 4: The XRD patterns of (a) $AgNPs^+$ and (b) $CHX@AgNPs^+$.

the hydroxy groups which extend to the surface imidazolium groups. Furthermore, the vibrations at around 2920 cm^{-1} can be associated with the stretching aliphatic CH bands which exist in the cationic aliphatic side chain. The peak that appears at about 1644 cm^{-1} also confirms the presence of an acrylic carbonyl group of $AgNPs^+$. This peak also appears in the graph of $CHX@AgNPs^+$.

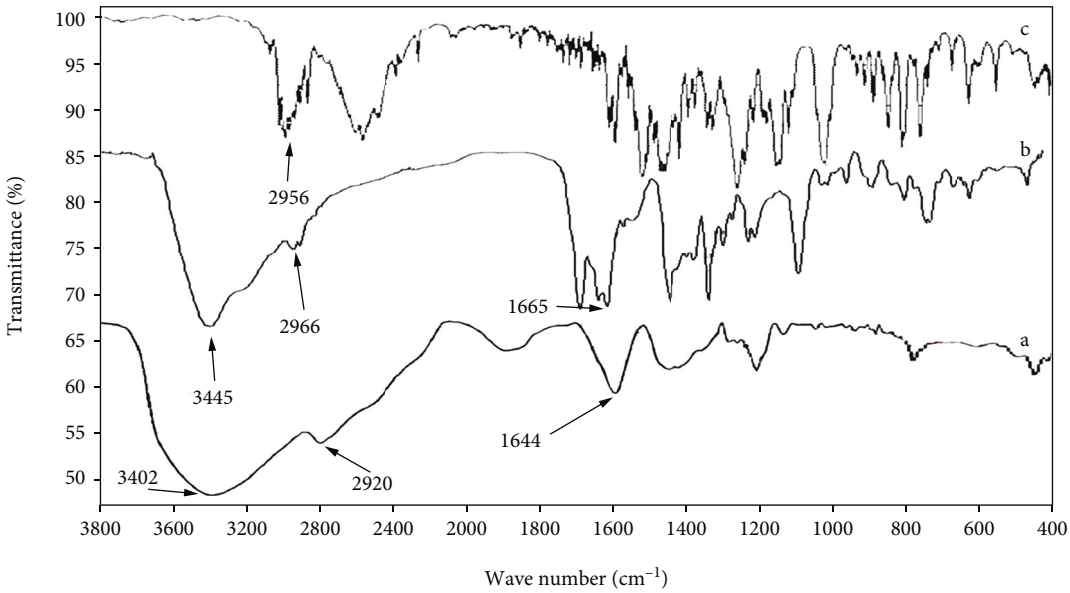

Figure 5: The FT-IR spectra of (a) AgNPs$^+$, (b) CHX@AgNPs$^+$, and (c) CHX with a KBr tablet in the region of 400-4000 cm^{-1}.

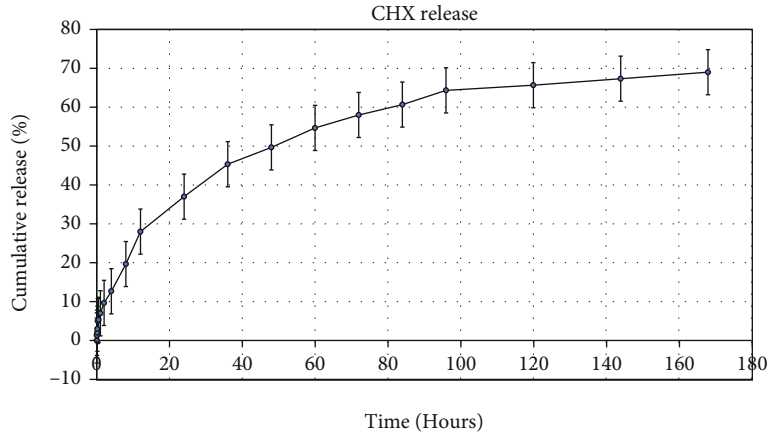

Figure 6: The release profile of CHX from CHX@AgNPs$^+$ during 180 hours.

3.2. The Loading Efficiency and Release Profile of CHX. Ideal drug carriers efficiently attach to the microbial cell membrane and adequately release the antibacterial agent. To achieve sufficient release of CHX, the aliphatic ionic liquid was introduced to the surface of AgNPs$^+$ to load CHX through electrostatic interaction. The UV-vis measurement revealed that the loading efficiency of CHX on AgNPs$^+$ was 86.7 ± 13.2.

The release profile of CHX from CHX@AgNPs$^+$ is interesting. As shown in Figure 6, an initial rapid release pattern occurred for CHX during the first 8 hours. About 20% of CHX was cumulatively released after 8 hours, whereas 37% of CHX was released after 24 hours. This fast release may be due to the dissociation and protonation of the carboxyl functional groups, resulting in the preferential release of CHX.

3.3. The Assessment of Antibacterial Activity. Based on the results of the broth microdilution test, the three experimental solutions all inhibited the growth of *E. faecalis* significantly in comparison with the control group. The MIC values of all the tested solutions were similar to their MBC values. The smallest MIC and MBC values belonged to CHX@AgNPs$^+$ (50 μg/mL), followed by CHX (100 μg/mL) and AgNPs$^+$ (N/A). In their initial concentration, AgNPs$^+$ could not inhibit 90% of *E. faecalis*. Thus, the exact MBC and MIC values for AgNPs$^+$ could not be determined. The statistical analysis showed that in most concentrations (except for 100 μg/mL), CHX@AgNPs$^+$ significantly reduced the viability of the bacterial strain compared to CHX as the standard irrigant. On the other hand, AgNPs$^+$ had an antibacterial effect similar to CHX only at intermediate concentrations (12 and 25 μg/mL) and their

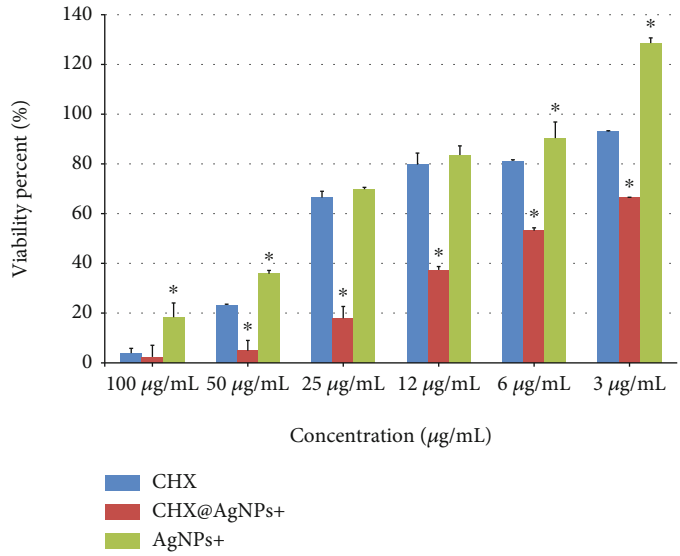

Figure 7: The viability of *E. faecalis* when treated with different concentrations of experimental solutions. *Statistically significant difference between the CHX (as the standard antibacterial irrigant) and other groups.

effects were significantly less than those of CHX at other concentrations (3, 6, 50, and 100 μg/mL). The effects of CHX@AgNPs$^+$ were statistically greater than those of AgNPs$^+$ at all concentrations tested. Figure 7 summarizes the details.

4. Discussion

In endodontics, the use of intracanal disinfectant solutions with adequate efficacy and acceptable biocompatibility will lead to the eradication of resistant microorganisms within the root canal and periapical areas and will consequently decrease the failure rate of root canal treatment [17].

The use of AgNPs has increased in many fields including dentistry. It is speculated that the antibacterial nanoscale structures do not allow the bacteria to resist [24]. Therefore, many studies have mentioned AgNPs as an effective and appropriate medication for endodontic purposes [25]. In the present preliminary *in vitro* study, the possible synergistic impacts of AgNPs$^+$ and CHX were investigated since both of these substances have a strong antibacterial activity. Lu et al. showed that CHX-loaded silver-decorated mesoporous silica nanoparticles (Ag-MSNs@CHX) had a pH-responsive release of silver ions and CHX simultaneously. This resulted in synergistically antibacterial effects against both Gram-negative *Escherichia coli* and Gram-positive *Staphylococcus aureus* [15]. Another study demonstrated the effective antibacterial activity of a novel CHX-AgNP solution which could be an effective antibacterial agent against endodontic flora [26].

This study used positively charged AgNPs and synthesized a new structure with a spherical shape and size of 20-30 nm. Recent studies have confirmed that the physicochemical characteristics of AgNPs$^+$ (including crystal structure, shape, surface morphology, zeta potential, size, and surface charge) are significant factors that affect their antibacterial activity [23, 27–29]. Besides, it was demonstrated that positively charged AgNPs could have a greater antibacterial efficacy against *E. faecalis* and have an outstanding level of biocompatibility [25].

In this study, CHX was also loaded on AgNPs$^+$ due to its strong antibacterial and synergistic effect. CHX@AgNPs$^+$ was synthesized and characterized, and then, the antibacterial effect of this solution on *E. faecalis* was assessed in order to determine its MIC and MBC values compared to those of CHX and AgNPs$^+$ alone. *E. faecalis* was selected based on previous studies that associated this microorganism with recurrent infections after root canal treatments [30].

Our results revealed that the MBC and MIC values of CHX@AgNPs$^+$ were less than those of CHX and AgNPs$^+$ alone. The MBC and MIC values of CHX@AgNP$^+$s were similar (50 μg/mL), while CHX was less effective with the MBC and MIC values of 100 μg/mL. For the AgNPs$^+$, we were not able to determine the exact MIC and MBC values during the serial dilutions. This means that this agent, even at its initial concentration, was not enough in inhibiting the growth of 90% of the bacteria.

The greater effectiveness of the CHX@AgNPs$^+$ solution on the microorganism compared to the other tested irrigants might be attributed to the electrostatic repulsion between CHX and AgNPs$^+$ due to their total electrical surface charge that may result in a lower aggregation of particles, more surface area, and minimization of the interaction time, destroying the microorganism with optimal effectiveness [31]. Additionally, the negatively charged components in the structure of Gram-positive bacterial cell walls and cell membrane (including teichoic acid, lipoteichoic acid, carboxyl, and phosphate groups) [9, 32] act as a target for the positive charge of the synthesized particle, leading to the disturbance of cell wall permeability, formation of proteinaceous pores, and destruction of the bacterial organism due to the leakage of intracellular contents. These findings

were in agreement with those of former studies focusing on the effect of surface charge on the bactericidal efficacy of NPs [9, 19, 27].

Suitable nanocarriers bind to bacterial surfaces and quickly release antibiotics or antiseptics in reaction to any stimulus. Based on the release profile of CHX, a new antibacterial solution was made to irrigate the root canal during the treatment process. The solution was expected to have rapid antibacterial properties. Since time is limited in clinical work, a fast release can be beneficial and more CHX can come in contact with the root canal system.

To sum up, the current study demonstrated that CHX@AgNPs^{+} had an excellent antibacterial effect on *E. faecalis*. In the current in vitro study, we tried to integrate nanoscience, chemistry, and bacteriology to obtain a new disinfectant for endodontic purposes. However, since the root canal ecosystem is a complex environment, further studies on the effect of CHX@AgNPs^{+} on infected *ex vivo* models and other bacterial species as well as cytocompatibility assessments of CHX@AgNPs^{+} against human cells are needed to evaluate its application as a new disinfectant in endodontics adequately.

5. Conclusion

Within the limitations of the present research, we can state that CHX@AgNPs^{+}, whose MBC and MIC values are significantly lower than those of CHX and AgNPs^{+} alone, can be regarded as a potential root canal disinfectant. Further studies are needed to confirm the results of the present study regarding this agent when it is used in *ex vivo* models and against bacterial biofilm.

Data Availability

All data used to support the findings of this study are included within the article.

Conflicts of Interest

The authors declare that they have no conflicts of interest.

Acknowledgments

The authors of this paper would like to appreciate the Vice-Chancellery of Shiraz University of Medical Sciences for supporting this study (Ethics Committee Approval: #IR.SUMS.DENTAL.REC.1399.071; Grant: #20450).

References

[1] F. Mohammadi, A. Abbaszadegan, and A. Gholami, "Recent advances in nanodentistry: a special focus on endodontics," *Micro & Nano Letters*, vol. 15, no. 12, pp. 812–816, 2020.

[2] A. Abbaszadegan, S. Sahebi, A. Gholami et al., "Time-dependent antibacterial effects of Aloe vera and Zataria multiflora plant essential oils compared to calcium hydroxide in teeth infected with Enterococcus faecalis," *Journal of Investigative and Clinical Dentistry*, vol. 7, no. 1, pp. 93–101, 2016.

[3] M. Nabavizadeh, A. Abbaszadegan, A. Gholami et al., "Chemical constituent and antimicrobial effect of essential oil from Myrtus communis leaves on microorganisms involved in persistent endodontic infection compared to two common endodontic irrigants: an in vitro study," *Journal of conservative dentistry: JCD*, vol. 17, no. 5, pp. 449–453, 2014.

[4] M. Sedigh-Shams, A. Gholami, A. Abbaszadegan et al., "Antimicrobial efficacy and cytocompatibility of calcium hypochlorite solution as a root canal irrigant: an in vitro investigation," *Iranian endodontic journal*, vol. 11, no. 3, pp. 169–174, 2016.

[5] A. Abbaszadegan, A. Gholami, Y. Ghahramani et al., "Antimicrobial and cytotoxic activity of Cuminum cyminum as an intracanal medicament compared to chlorhexidine gel," *Iranian endodontic journal*, vol. 11, no. 1, pp. 44–50, 2016.

[6] F. Cieplik, N. S. Jakubovics, W. Buchalla, T. Maisch, E. Hellwig, and A. al-Ahmad, "Resistance toward chlorhexidine in oral bacteria–is there cause for concern?," *Frontiers in Microbiology*, vol. 10, p. 587, 2019.

[7] A. Abbaszadegan, Y. Ghahramani, M. Farshad, M. Sedigh-Shams, A. Ghomali, and A. Jamshidzadeh, "In vitro evaluation of dynamic viscosity, surface tension and dentin wettability of silver nanoparticles as an irrigation solution," *Iranian Endodontic Journal*, vol. 14, no. 1, pp. 23–27, 2019.

[8] N. Ebrahimi, S. Rasoul-Amini, A. Ebrahiminezhad, Y. Ghasemi, A. Gholami, and H. Seradj, "Comparative study on characteristics and cytotoxicity of bifunctional magnetic-silver nanostructures: synthesized using three different reducing agents," *Acta Metallurgica Sinica (English Letters)*, vol. 29, no. 4, pp. 326–334, 2016.

[9] A. Abbaszadegan, A. Gholami, S. Abbaszadegan et al., "The effects of different ionic liquid coatings and the length of alkyl chain on antimicrobial and cytotoxic properties of silver nanoparticles," *Iranian endodontic journal*, vol. 12, no. 4, pp. 481–487, 2017.

[10] S. N. Abootalebi, S. M. Mousavi, S. A. Hashemi, E. Shorafa, N. Omidifar, and A. Gholami, "Antibacterial effects of green-synthesized silver nanoparticles using ferula asafoetida against Acinetobacter baumannii isolated from the hospital environment and assessment of their cytotoxicity on the human cell lines," *Journal of Nanomaterials*, vol. 2021, 12 pages, 2021.

[11] A. Abbaszadegan, Y. Ghahramani, A. Gholami et al., "The effect of charge at the surface of silver nanoparticles on antimicrobial activity against gram-positive and gram-negative bacteria: a preliminary study," *Journal of Nanomaterials*, vol. 2015, article 720654, 2015.

[12] P. Fan, Z. Ma, A. J. Partow et al., "A novel combination therapy for multidrug resistant pathogens using chitosan nanoparticles loaded with β-lactam antibiotics and β-lactamase inhibitors," *International Journal of Biological Macromolecules*, vol. 195, pp. 506–514, 2022.

[13] A. Gholami, A. Ebrahiminezhad, N. Abootalebi, and Y. Ghasemi, "Synergistic evaluation of functionalized magnetic nanoparticles and antibiotics against Staphylococcus aureus and Escherichia coli," *Pharmaceutical nanotechnology*, vol. 6, no. 4, pp. 276–286, 2018.

[14] M. A. Fischbach, "Combination therapies for combating antimicrobial resistance," *Current Opinion in Microbiology*, vol. 14, no. 5, pp. 519–523, 2011.

[15] M. Lu, Y. Ge, and C. Tang, "Synergistically antibacterial effect of chlorhexidine-loaded, silver-decorated mesoporous silica nanoparticles against peri-implantitis pathogens," *Clinical Oral Implants Research*, vol. 29, no. S17, pp. 53–53, 2018.

[16] F. Afkhami, G. Rostami, S. Batebi, and A. Bahador, "Residual antibacterial effects of a mixture of silver nanoparticles/calcium hydroxide and other root canal medicaments against Enterococcus faecalis," *Journal of Dental Sciences*, vol. 17, no. 3, pp. 1260–1265, 2021.

[17] K. Yousefi, H. D. Manesh, A. R. Khalifeh, and A. Gholami, "Fabrication and characterization of a nanofast cement for dental restorations," *International*, vol. 2021, pp. 1–12, 2021.

[18] W. Zakrzewski, M. Dobrzyński, A. Zawadzka-Knefel et al., "Nanomaterials Application in Endodontics," *Materials (Basel)*, vol. 14, no. 18, p. 5296, 2021.

[19] A. Gholami, M. S. Shams, A. Abbaszadegan, and M. Nabavizadeh, "Ionic liquids as capping agents of silver nanoparticles. Part II: antimicrobial and cytotoxic study," *Green Processing and Synthesis*, vol. 10, no. 1, pp. 585–593, 2021.

[20] A. Gholami, F. Emadi, M. Nazem et al., "Expression of key apoptotic genes in hepatocellular carcinoma cell line treated with etoposide-loaded graphene oxide," *Journal of Drug Delivery Science and Technology*, vol. 57, article 101725, 2020.

[21] K. Anandalakshmi, J. Venugobal, and V. Ramasamy, "Characterization of silver nanoparticles by green synthesis method using Pedalium murex leaf extract and their antibacterial activity," *Applied Nanoscience*, vol. 6, no. 3, pp. 399–408, 2016.

[22] R. Das, S. S. Nath, D. Chakdar, G. Gope, and R. Bhattacharjee, "Synthesis of silver nanoparticles and their optical properties," *Journal of Experimental Nanoscience*, vol. 5, no. 4, pp. 357–362, 2010.

[23] M. Nabavizadeh, A. Abbaszadegan, A. Gholami et al., "Antibiofilm efficacy of positively charged imidazolium-based silver nanoparticles in enterococcus faecalis using quantitative real-time PCR," *Journal of Microbiology*, vol. 10, no. 10, 2017.

[24] M. K. Rai, S. D. Deshmukh, A. P. Ingle, and A. K. Gade, "Silver nanoparticles: the powerful nanoweapon against multidrug-resistant bacteria," *Journal of Applied Microbiology*, vol. 112, no. 5, pp. 841–852, 2012.

[25] A. Adl, A. Abbaszadegan, A. Gholami, F. Parvizi, and Y. Ghahramani, "Effect of a new imidazolium-based silver nanoparticle irrigant on the bond strength of epoxy resin sealer to root canal dentine," *Iranian Endodontic Journal*, vol. 14, no. 2, pp. 122–125, 2019.

[26] S. Charannya, D. Duraivel, K. Padminee, S. Poorni, C. Nishanthine, and M. R. Srinivasan, "Comparative evaluation of antimicrobial efficacy of silver nanoparticles and 2% chlorhexidine gluconate when used alone and in combination assessed using agar diffusion method: an in vitro study," *Contemporary clinical dentistry*, vol. 9, Suppl 2, pp. S204–S209, 2018.

[27] A. Abbaszadegan, M. Nabavizadeh, A. Gholami et al., "Positively charged imidazolium-based ionic liquid-protected silver nanoparticles: a promising disinfectant in root canal treatment," *International Endodontic Journal*, vol. 48, no. 8, pp. 790–800, 2015.

[28] M. Guzman, J. Dille, and S. Godet, "Synthesis and antibacterial activity of silver nanoparticles against gram- positive and gram-negative bacteria," *Nanomedicine: Nanotechnology, Biology and Medicine*, vol. 8, no. 1, pp. 37–45, 2012.

[29] C. V. Restrepo and C. C. Villa, "Synthesis of silver nanoparticles, influence of capping agents, and dependence on size and shape: a review," *Environmental Nanotechnology, Monitoring & Management*, vol. 15, article 100428, 2021.

[30] Y. Ghahramani, N. Mohammadi, A. Gholami, and D. Ghaffaripour, "Antimicrobial efficacy of intracanal medicaments against E. faecalis bacteria in infected primary molars by using real-time PCR: a randomized clinical trial," *International Journal of Dentistry*, vol. 2020, 6 pages, 2020.

[31] S. Zargarnezhad, A. Gholami, M. Khoshneviszadeh, S. N. Abootalebi, and Y. Ghasemi, "Antimicrobial activity of isoniazid in conjugation with surface-modified magnetic nanoparticles against Mycobacterium tuberculosis and nonmycobacterial microorganisms," *Journal of Nanomaterials*, vol. 2020, 9 pages, 2020.

[32] B. Bechinger and S.-U. Gorr, "Antimicrobial peptides: mechanisms of action and resistance," *Journal of Dental Research*, vol. 96, no. 3, pp. 254–260, 2017.

Hindawi
Journal of Nanomaterials
Volume 2022, Article ID 5351611, 12 pages
https://doi.org/10.1155/2022/5351611

Research Article

Astragalus Polysaccharides Inhibit Pancreatic Cancer Progression by Downregulation of TLR4/NF-κB Signaling Pathway

Jingjing Fang, Zongyang Wu, Jinbo Wang, Jiye Feng, and Liping Ying

Department of Hepatobiliary and Pancreatic Surgery, The Affiliated People's Hospital of Ningbo University, Ningbo 315040, China

Correspondence should be addressed to Jingjing Fang; nbyzfjj@163.com

Received 16 February 2022; Accepted 30 June 2022; Published 12 July 2022

Academic Editor: Xuncai Chen

Background. Pancreatic cancer (PC) leads to high human malignancy mortality worldwide. This study explored the role of Astragalus polysaccharide (APS) on human PC PANC-1 cells and its underlying mechanisms. *Method*. Cell viability, proliferation, apoptosis, invasion, and migration were measured by CCK-8, EdU incorporation, flow cytometry, Transwell, and wound healing assay, respectively. ELISA assay was utilized to detect the IL-1α, IL-4, IL-6, IL-8, and TNF-α levels. The western blot assay was performed to measure the level changes of cell function-related proteins. The transportation of NF-κB P65 protein was detected through immunofluorescence assay. *Results*. Compared with the control group, APS treatment could significantly inhibit cell proliferation. APS treatment could also suppress cell migration and invasion ability and induce apoptosis and inflammation in PANC-1 cells. Furthermore, APS inhibited the activation of TLR4/NF-κB signaling pathway via suppressing the phosphorylation and transportation of NF-κB P65 into the PANC-1 cell nucleus. *Conclusion*. APS suppresses PANC-1 cell viability, proliferation, migration, and invasion while inducing inflammation and apoptosis. APS might regulate PC cell motility via downregulating TLR4/NF-κB signaling pathway.

1. Introduction

Pancreatic cancer (PC) has the characteristic of rapid progression, insidious onset, and low survival rate [1], thus resulting in high human malignancies mortality worldwide [2]. Nowadays, the survival rate of PC has been reduced with the development of surgical removal and target therapy [3]. However, the PC survival rate has a minor progression since PC metastasis often develops dramatically, and surgical removal cannot cure [4]. The prognosis of PC remains poor since around 50% of the PC patient recurrence in the following year after their first surgery [5]. Therefore, a specific and effective therapeutic agent is required to improve the prognosis of PC patients.

Astragalus polysaccharides (APS) is isolated from the root of A. membranaceus and serves as a traditional medicine. Many recent studies indicated that APS promotes various bioactivities including immunomodulation, anti-inflammation, and anticancer [6]. Furthermore, ASP possesses immunomodulatory properties and promotes the production of antibodies [7]. The early stages of obstructive pancreatitis apoptosis results in cell death of pancreatic acinar cells [8]. The apoptosis process is implemented through multiple pathways and intersected and has three major biological pathways, including the death receptor, the mitochondrial, and the endoplasmic reticulum pathway. The cascade reaction is the central link for both the death receptor pathway and the mitochondrial pathway, in which caspase-3 acts as the ultimate executor of apoptosis. Recent studies reported that APS could reduce cell viability and promote cell apoptosis, indicating a strong anticancer effect of APS treatment [9, 10]. However, the role and underlying mechanisms of APS in PC still need more research.

In this study, we aimed to investigate the roles of APS in PC cells' viability, proliferation, migration, invasion, inflammation, and apoptosis and its association with the TLR4/NF-κB signaling pathway.

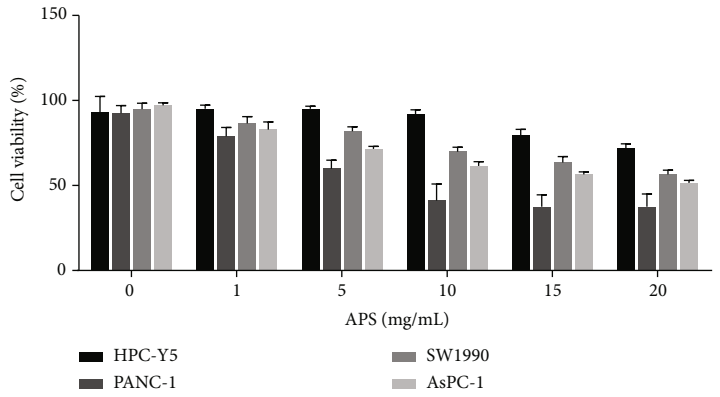

(a)

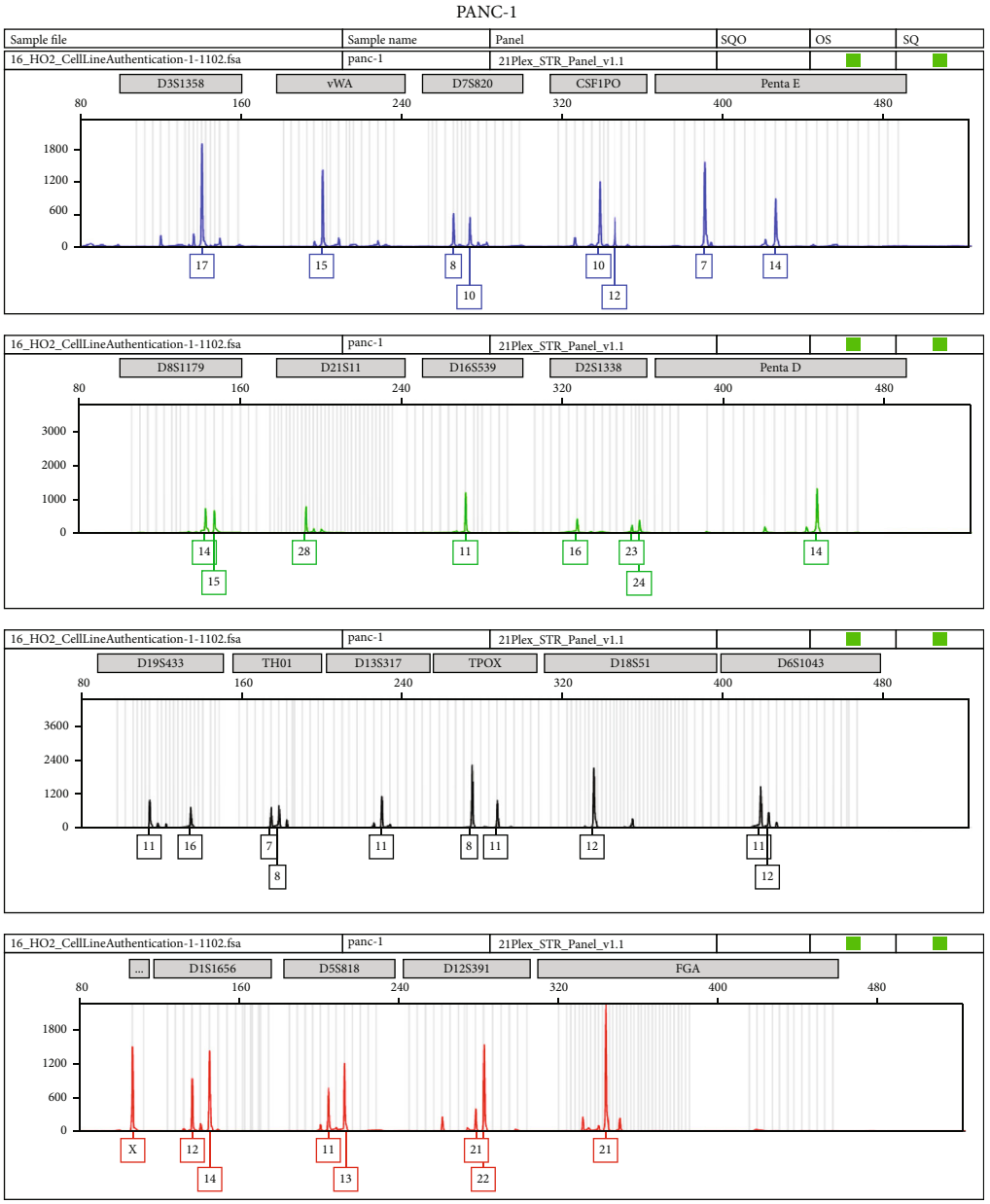

(b)

Figure 1: Continued.

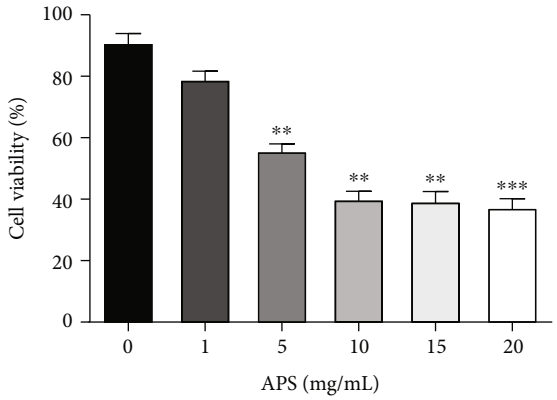

(c)

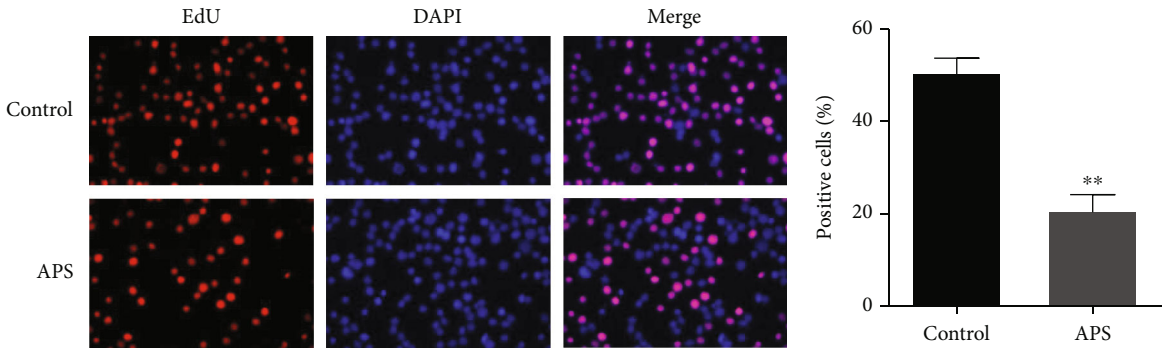

(d)

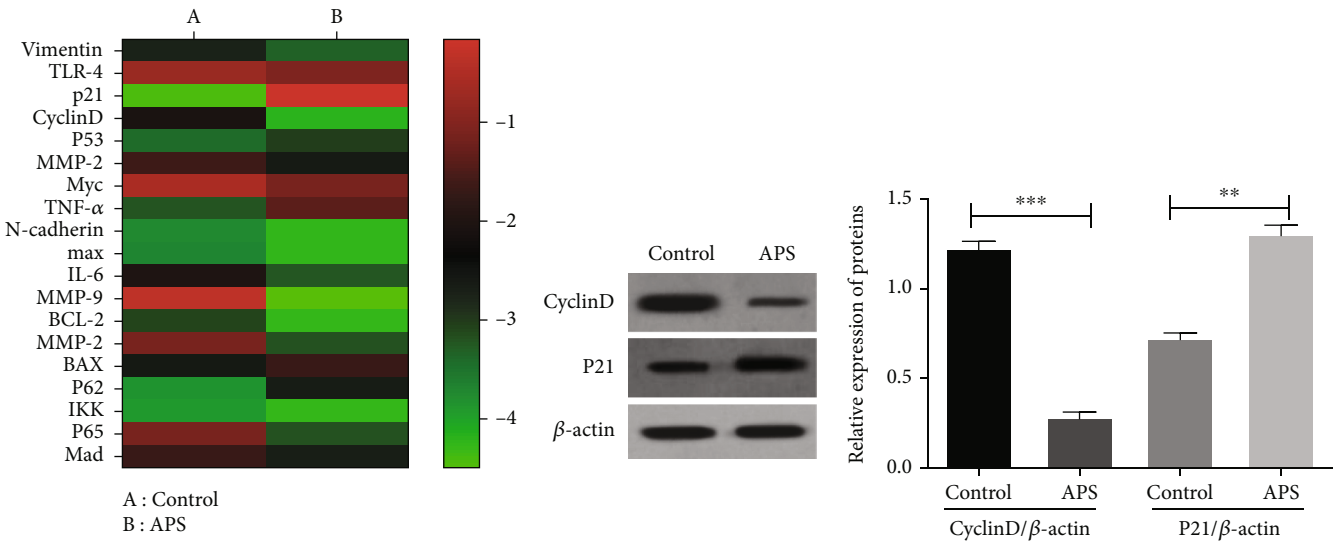

(e) (f)

Figure 1: Continued.

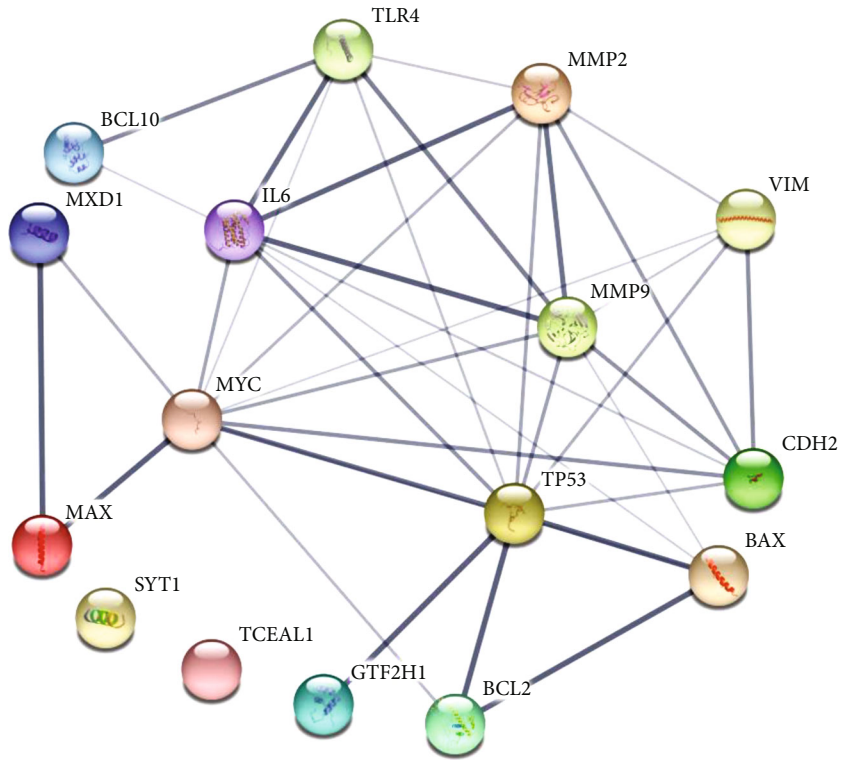

(g)

Figure 1: APS inhibited viability and proliferation of PANC-1 cells. (a) CCK-8 assay was used to detect the effects of Astragalus polysaccharides (APS) on cell viability and proliferation in human normal pancreatic cell line HPC-Y5 and pancreatic cancer cell lines including PANC-1, SW1990, and AsPC-1. Various doses of APS (0, 1, 5, 10, 15, and 20 mg/mL) were treated to the cells and cultured for 24 h. (b) PANC-1 cell line STR identification. (c) CCK-8 assay was applied to explore the cell viability of different concentrations (0 (control), 1, 5, 10, 15, and 20 mg/mL) of APS treatment in PANC-1 cells. (d) EdU assay was used to examine the proliferation of APS on PANC-1 cells. (e) RNA-Seq analysis was used to detect the differentially expressed genes in PANC-1 cells treated with APS. (f) Western blot assay was performed to detect the expression of proliferation related proteins. (g) Protein interaction network of differentially expressed genes after APS treatment. The thicker the line, the stronger the interaction. $^{*}P < 0.05$, $^{**}P < 0.01$, and $^{***}P < 0.001$, compared with the control group. Scale bar = 100 μm.

2. Material and Methods

2.1. Cell Culture. The pancreatic cancer cell line PANC-1 was obtained from Shanghai Fuheng Biotechnology (China). The PANC-1 cells were cultured in Dulbecco's modified Eagle's medium (DMEM, Gibco, USA) containing 10% fetal bovine serum (FBS) (Gibco, USA) and 1% penicillin-streptomycin (Gibco, USA). The cells were cultured in a humidified incubator (Thermo Fisher, USA) with 5% CO_2 at 37°C.

2.2. Cell Viability Assay. The PANC-1 cells were seeded in the 96-well plates (2×10^3 cells/well). Then, 200 μL normal culture medium containing various doses of APS (0, 1, 5, 10, 15, and 20 mg/mL) was added to PANC-1 cells for 24 h [11]. Then, 10 μL of CCK-8 (Dojindo, Japan) was added, and the cells were cultured for another 1 h. Subsequently, a microplate reader (Bio-Rad, USA) was used to detect the absorbance at the wavelength of 450 nm.

2.3. Cell Proliferation Assay. 5-Ethynyl-2′-deoxyuridine (EdU) incorporation assay (Beyotime Biotechnology, China) was utilized to examine cell proliferation. The cells were seeded and treated according to the instruction. The staining was captured by a fluorescence microscope.

2.4. Migration and Invasion Assay. To measure the cell migration ability, PANC-1 cells were cultured in the top chamber; the normal medium was added into the lower compartment. The plates were cultured in a humidified incubator for 24 h. After fixing, the cell was stained in crystal violet. To detect the cell invasion ability, the Transwell membranes were procoated with Matrigel (BD Biosciences, USA).

2.5. Wound Healing Assay. After seeding cells for 24 h, a pipette tip was utilized to scratch three parallel lines on the bottom of plates, and cell debris was rinsed with DMEM. After the corresponding treatment for 24 h, a light microscope was used to assess the ability of the cells to migrate into a cell-free area.

2.6. Flow Cytometric Analysis of Cell Apoptosis. The annexin V-FITC/PI double-stained kit (Invitrogen, USA) was utilized

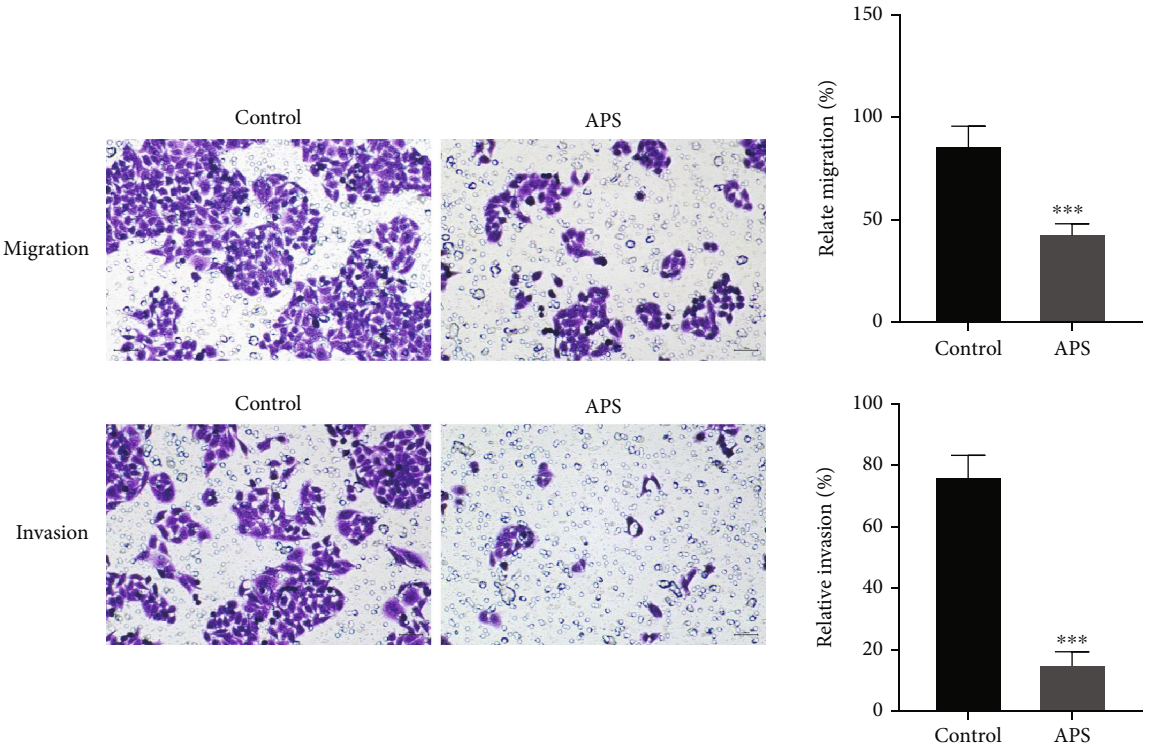

(a)

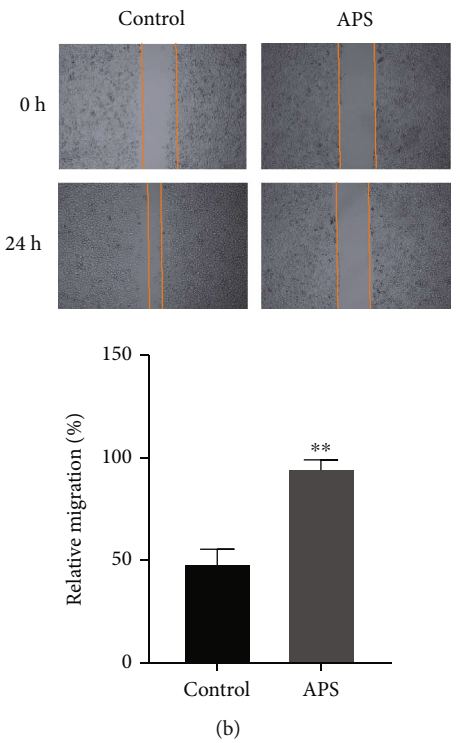

(b)

Figure 2: Continued.

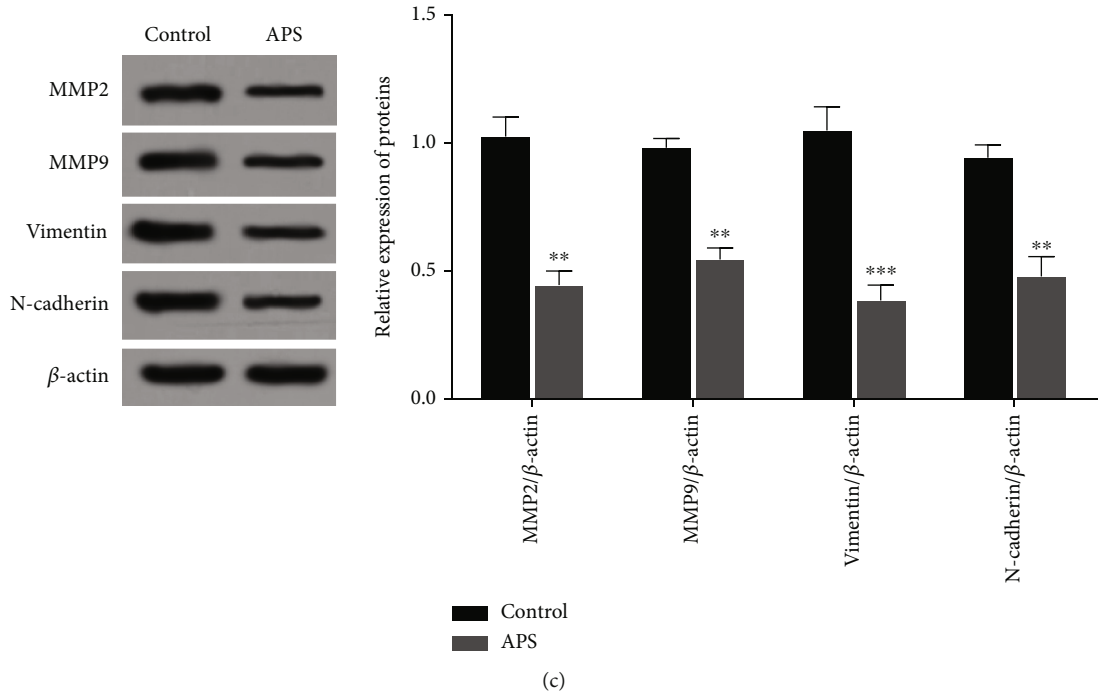

Figure 2: APS inhibited migration and invasion of PANC-1 cells. (a) Transwell experiment was conducted to study the effects of APS on cell migration and invasion. (b) Wound healing assay was used to study the effects of APS on cell migration. (c) Western blot assay was used to measure the protein levels of migration- and invasion-related proteins including MMP2, MMP9, vimentin, and N-cadherin. $^{*}P < 0.05$, $^{**}P < 0.01$, and $^{***}P < 0.001$, compared with the control group.

to detect cell apoptosis. After resuspending in binding buffer, the cells were stained with the fluorescent dye for 15 min at temperature without light. The treated cells were detected through flow cytometry. FlowJo software (Tree Star, USA) was utilized to analyze the portion of apoptotic cells.

2.7. ELISA Analysis. IL-1α, IL-4, IL-6, IL-8, and TNF-α were detected using enzyme-linked immunosorbent assay kits (Boster Biological Technology, China) at a wavelength of 405 nm.

2.8. Real-Time Quantitative PCR. TRIzol reagent was used to extract the total cell RNA (Thermo Fisher, USA). After synthesizing cDNA, real-time PCR was performed with the SYBR Green master mix (Takara, Japan).

2.9. Western Blot. RIPA (Thermo Fisher, USA) was utilized to extract total cell proteins. After running a 12% SDS-PAGE electrophoresis (Beyotime Biotechnology, China), the proteins were transferred to a PVDF membrane (Millipore, USA). The primary antibodies against CyclinD1 (1 : 1000, ab134175, Abcam, UK), P21 (1 : 1000, ab109520, Abcam, UK), MMP2 (1 : 2000, ab92536, Abcam, UK), MMP9 (1 : 2000, ab76003, Abcam, UK), vimentin (1 : 1000, ab92547, Abcam, UK), N-cadherin (1 : 1000, AB76001, Abcam, UK), Bcl-2 (1 : 1000, ab196495, Abcam, UK), Bax (1 : 2000, ab182733, Abcam, UK), P62 (1 : 2000, ab109012, Abcam, UK), TLR4 (1 : 2000, ab13556, Abcam, UK), Myd88 (1 : 2000, ab133739, Abcam, UK), phosphorylated NF-κB P65 (p-P65, 1 : 1000, ab76302, Abcam, UK), P65 (1 : 2000, ab32536, Abcam, UK), and β-actin (1 : 3000, ab8226, Abcam, UK) were used. After being cultured with the corresponding second antibodies (Beyotime Biotechnology, China), the signal of the protein band was detected in a ChemiDoc XRS^{+} system (Bio-Rad, Berkeley, CA, USA).

2.10. Immunofluorescence (IF) Experiment. The TLR4/NF-κB signaling pathway agonist, human tumor necrosis factor-α (TNF-α), was purchased from the Cell Signaling Technology Company (USA). 24 h before the experiment, PANC-1 cells were paved with Cellvis board (Shanghai Kaveson Biotech, no. D29-20-1 N, China). Once the cell density reached 80%, the corresponding drugs, TNF-α and APS, were treated for 4 h, followed by 24 h cell culture after the liquid change. The cells were then fixed at room temperature with 4% polyformaldehyde for 30 min, followed by washing with PBS three times, 10 min at a time. The cells were then incubated at 0.1% Triton-100 (Beyotime Biotechnology, China) at room temperature for 30 min. PBS (Solarbio, China) was added to wash the cells three times, 10 min each time. An antidilution solution of p65 antibodies (1 : 200) was added and incubated throughout the night. The antibody was collected, and the cells were washed three times by PBS. After 1 h incubation with goat anti-rabbit fluorescent secondary antibody (Invitrogen, China) at room temperature at the concentration of 1 : 200, the cells were washed three times with PBS, 15 min each. The distribution of p65 was then observed under the Leica fluorescence microscope (Germany).

2.11. Statistical Analysis. All quantitative data were expressed as mean ± standard deviation (SD). SPSS 17.0

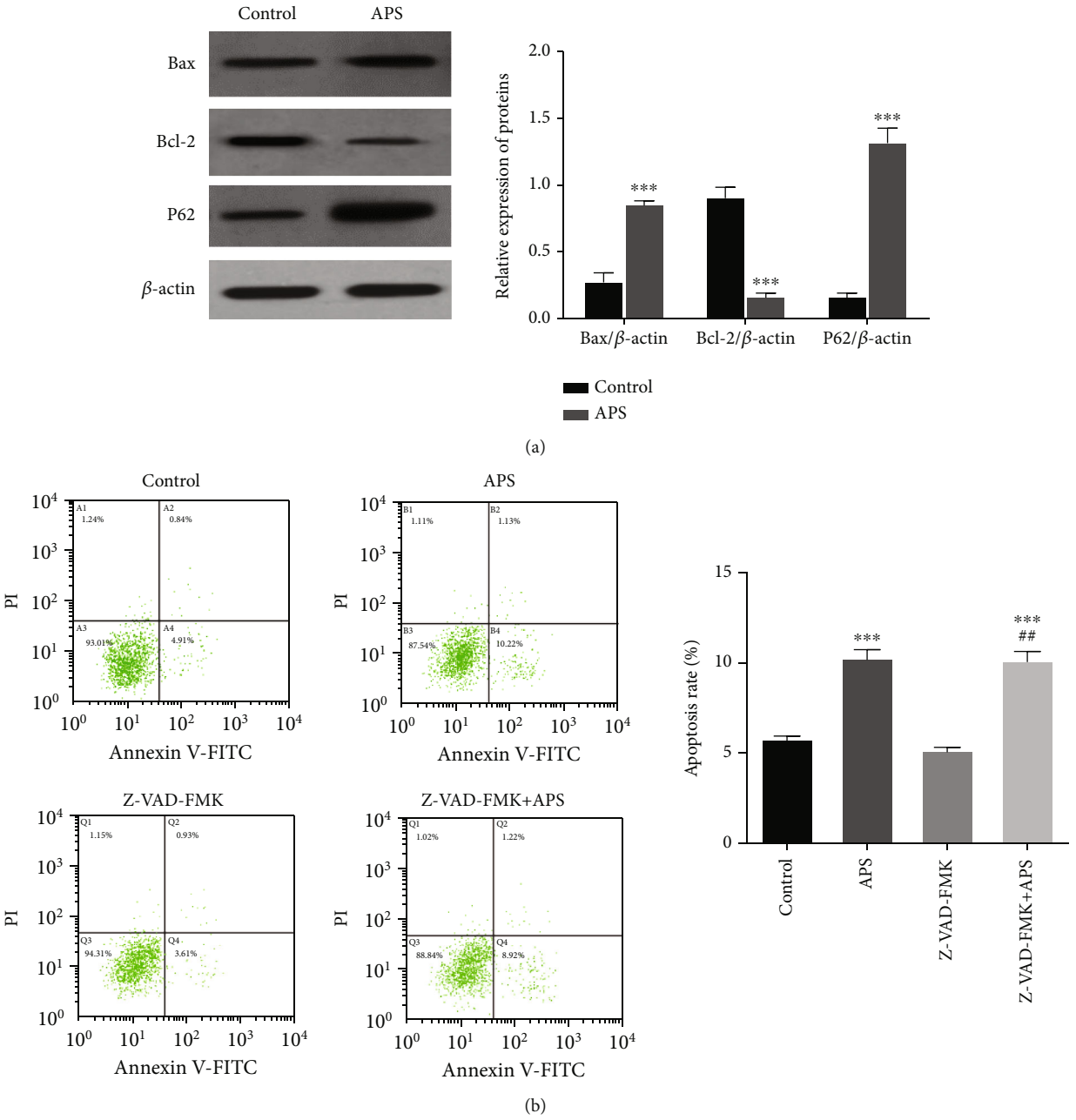

Figure 3: APS induced the apoptosis of PANC-1 cells. (a) Western blot assay was used to detect the apoptosis-related protein expression including Bax, Bcl-2, and P62. (b) Flow cytometry assay was performed to detect cell apoptosis rate. $^{***}P < 0.001$, compared with the control group; $^{\#\#}P < 0.01$, compared with the Z-VAD-FMK group.

software (SPSS, USA) was used to analyze the data. One-way analysis of variance (ANOVA) was applied for the significant differences between the groups by Tukey's multiple range test. The $P < 0.05$ was considered statistically significant.

3. Results

3.1. APS Inhibited Viability and Proliferation of PANC-1 Cells. As shown in Figure 1(a), we chose several PC cell lines including PANC-1, SW1990, and AsPC-1 and human normal pancreatic cell line HPC-Y5 to detect the cytotoxicity of APS treatment during the preexperiments. We found that PANC-1 cells were the most sensitive cell line; thus, we used PANC-1 cells in the following formal experiment. The PANC-1 cell line verification was shown in Figure 1(b). In Figure 1(c), APS treatment inhibited cell viability and proliferation in a dose-dependent manner (all $P < 0.05$). In the following APS treatment experiments, 10 mg/mL APS was selected. Compared with the control group, the EdU assay showed that APS treatment significantly suppressed cell proliferation ($P < 0.05$, Figure 1(d)). As shown in Figure 1(e), the intracellular transcription factors CyclinD, p21, p65, and MMP-2 changed significantly after APS treatment. As

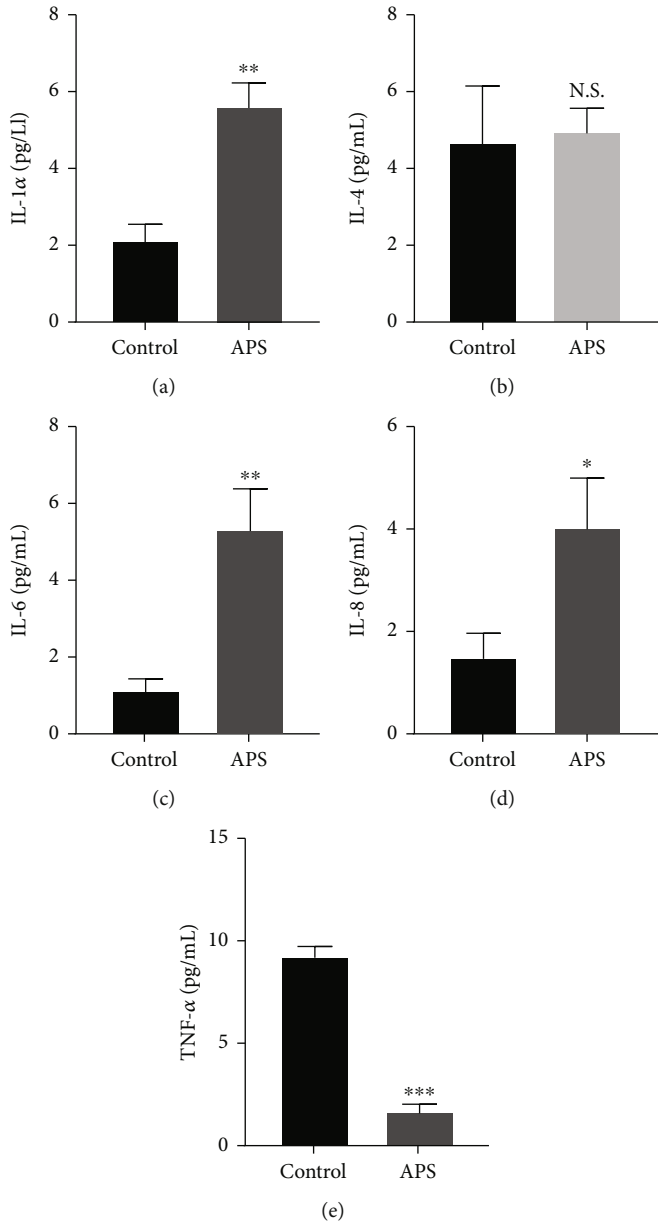

Figure 4: Effects of APS on inflammatory cytokines expression in PANC-1 cells. (a–e) The expression levels of IL-1α, IL-4, IL-6, IL-8, and TNF-α were measured by ELISA assay. $^{*}P < 0.05$, $^{**}P < 0.01$, and $^{***}P < 0.001$, compared with the control group.

shown in Figure 1(f), western blot assay illustrated that APS treatment could decrease the protein levels of CyclinD1 ($P < 0.05$) and increase the P21 protein expression ($P < 0.05$). These results suggested that APS inhibited viability and proliferation of PANC-1 cells. Additionally, we also constructed the protein interaction network of APS downstream genes. According to the number of interacting genes, IL-6, Myc, TP53, and MMP9 interact most widely and are at the core of the network (Figure 1(g)). These genes may be the key link of APS downstream mechanism.

3.2. APS Suppressed Migration and Invasion of PANC-1 Cells. In Figure 2(a), the migration and invasion of cells were significantly inhibited after APS treatment ($P < 0.05$). Besides, wound healing assay showed consistent results ($P < 0.05$, Figure 2(b)). We also detected the migration- and invasion-related proteins including MMP-2, MMP-9, vimentin, and N-cadherin. In Figure 2(c), APS treatment significantly decreased the protein levels of MMP-2, MMP-9, vimentin, and N-cadherin (all $P < 0.05$), which indicated that APS could suppress migration and invasion in PANC-1 cells.

3.3. APS Induced Apoptosis of PANC-1 Cells. We measure the protein levels of apoptosis-related proteins including Bax, Bcl-2, and P62. As shown in Figure 3(a), APS treatment obviously downregulated the expression levels of Bcl-2 ($P < 0.05$) and upregulated the levels of Bax and P62 (all $P < 0.05$). Furthermore, as shown in Figure 3(b), compared with the control group, cell apoptosis rate in the APS group

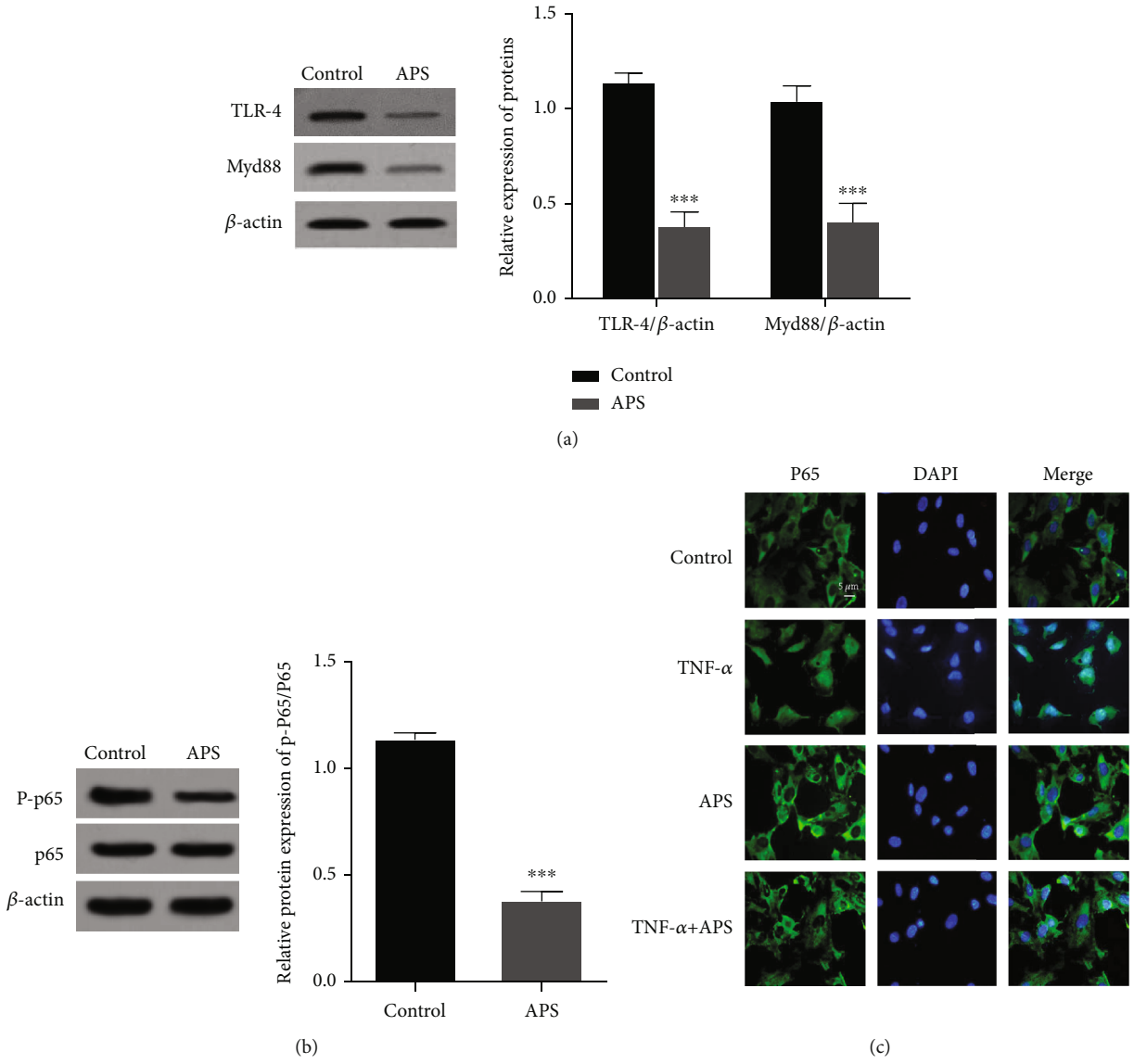

Figure 5: APS suppressed the activation of TLR4/NF-κB signaling pathway in PANC-1 cells. (a and b) The protein expression of TLR4, Myd88, nuclear phosphorylated p65 (P-p65), and p65 was measured by western blot assay. (c) The distribution of p65 was detected by IF experiment. $^{***}P < 0.001$, compared with the control group. Scale bar = 5 μm.

was significantly higher ($P < 0.05$). Meanwhile, after treating cells with apoptosis inhibitors, Z-VAD-FMK, we found that APS could still induce apoptosis, but its induction efficiency was inhibited ($P < 0.05$). The above results suggested that APS could induce PANC-1 cell apoptosis.

3.4. APS Induced Inflammation in PANC-1 Cells. To explore the roles of APS in the PANC-1 cell inflammatory injury, we examined the effects of APS on the concentrations of IL-1α, IL-4, IL-6, IL-8, and TNF-α using ELISA kit in PANC-1 cells. As shown in Figures 4(a)–4(e), we found that compared to the control group, APS significantly increased the levels of IL-1α, IL-6, and IL-8 (all $P < 0.05$). However, we found an inverse change of TNF-α ($P < 0.05$) and did not observe any significant change of IL-4 in both groups. These results suggested that APS could induce PANC-1 cells inflammatory injury.

3.5. APS Suppressed TLR4/NF-κB Signaling Pathway in PANC-1 Cells. To study the underlying mechanism of APS on cell motility, we further detected the effects of APS on TLR4/NF-κB signaling pathway in PANC-1 cells. In Figures 5(a) and 5(b), we found that APS decreased the protein levels of TLR4, Myd88, and phosphorylation p65 (all $P < 0.05$), which suggested that APS suppressed the activation of the TLR4/NF-κB pathway. In Figure 5(c), IF experiments showed that the transcription factor P65 could be activated and enter the nucleus, thus enhancing the expression of downstream target genes in the presence of TLR4/NF-κB signaling pathway agonist TNF-α. When both TNF-α and APS were presented, p65 remained in the cytoplasm and could not activate the TLR4/NF-κB signaling pathway (Figure 5(b)). Besides, we also found that APS downregulated the levels of TNF-α, which could further inhibit the

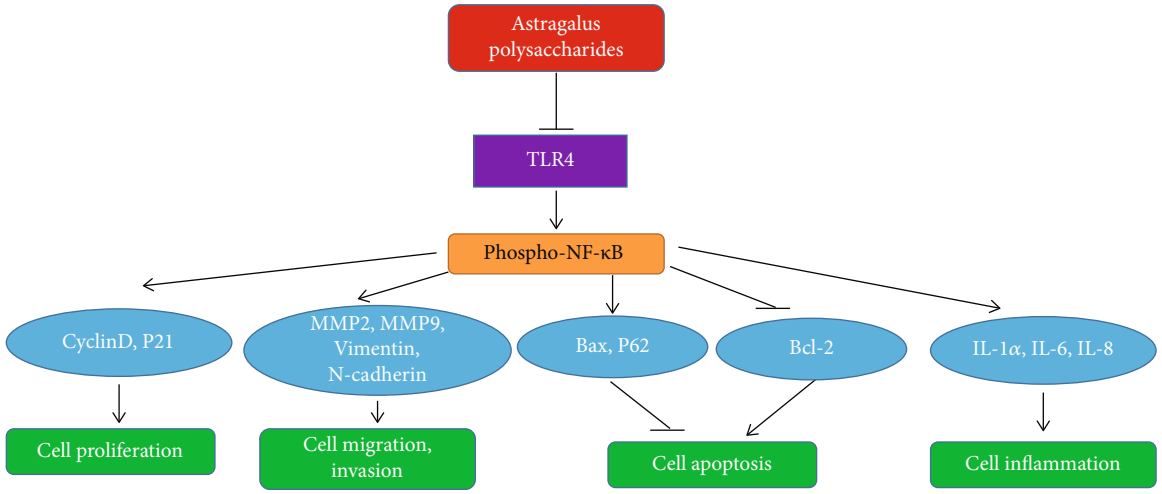

Figure 6: Schematic diagram of signaling pathway.

transportation of p65 and then inhibit the activation of TLR4/NF-κB signaling pathway. These results suggested that APS suppressed the activation of TLR4/NF-κB signaling pathway in PANC-1 cells.

4. Discussion

Characteristics of tumor cells promote proliferation and suppress apoptosis in the occurrence and development of cancer [12–14]. In this study, the decrease in EdU-positive portion in APS-treated group suggested that APS could inhibit PANC-1 cell proliferation. CyclinD1 and P21 are the key cell cycle proteins that promote mitosis [15, 16]. We found that APS treatment could downregulate the protein levels of CyclinD1 and P21. Furthermore, the results of flow cytometry and ELISA assay suggested the proapoptotic and proinflammatory roles of APS. After using antiapoptotic agent Z-VAD-FMK (anticaspase), we found that APS could still induce apoptosis, but its induction efficiency was inhibited. The above results suggested that APS could induce apoptosis via caspase-dependent pathways.

The metastatic potential and metastasis of PC usually cause adverse outcomes [17, 18]. However, APS on invasion and migration of PANC-1 cells was unexplored [19]. It is known that extracellular matrix (ECM) contributes to EMT since cancer cells begin to invade and migrate [20, 21] by first degrading ECM. MMP-2 and MMP-9 can damage ECM and basement membrane [22]. In this study, APS inhibited the migration and invasion of PANC-1 cells and reduced MMP-2 expression in PANC-1 cells. Besides, APS also downregulated the migration- and invasion-related proteins including vimentin and N-cadherin protein levels, which was consistent with the results of MMPs.

TLR is a key receptor to initiate inflammation process. Some studies have found that TLR4 can activate SIRS. TLR4 plays a vital role in the pathophysiology and severity of acute biliary pancreatitis [23]. However, whether TLR4 is related to human PC and the role it plays in PC is not clear. TLR is a specific product of innate immune system that recognizes invading pathogenic microorganisms and destroys tissue or cell degradation products and reacts to them. TLR4 is a member of the TLR family [24, 25]. In addition to the identification of specific product bacteria/viral pathogen-associated molecular patterns (PAMP), TLR4 also can identify the damage tissue or cell matrix after degradation product of small molecules, such as heat shock protein 60, 70, Gp96, polysaccharide hyaluronic acid low molecular fragments, fibrinogen, and HMGB1 [26]. Activation of TLR4 signaling pathways will activate an important regulatory factor, NF-κB, to activate inflammatory response genes and ultimately lead to the synthesis and secretion of IL-6 and IL-8 in inflammatory cells [27–29]. Furthermore, TLR4 had a suppressive effect in the regulatory T cells via activating the NF-κB pathway [30]. This study showed that APS treatment could upregulate the levels of IL-1α, IL-6, and IL-8, which suggested that APS might induce inflammation in PC cells. However, we did not observe significant change of IL-4, and the levels of TNF-α were even decreased. Based on bioinformatics analysis, TLR4 may be involved in the APS downstream signaling, and we found that APS decreased the expression of TLR4 and nuclear p-p65, suggesting that APS suppressed the NF-κB signaling pathway. IF experiment showed that APS treatment inhibited the transportation of p65 into cell nucleus. The downregulation of TNF-α could enhance this inhibitory effect as an agonist of the TLR4/NF-κB signaling pathway. The above results suggested that APS could regulate the suppressed activation of TLR4/NF-κB pathway in PANC-1 cells (Figure 6).

There are some limitations in our study. At first, we did not use multiple cell lines in our experiments. However, we have verified that APS treatments could significantly induce cell damage in some PC cell lines including PANC-1, SW1990, and AsPC-1 and human normal pancreatic cell line HPC-Y5. Among those cells, PANC-1 cells were the most sensitive. Thus, we used this cell lines to perform the following experiments. Besides, although we found that APS could inhibited cancer cell functions and promote apoptosis and inflammation through TLR4/NF-κB pathway, the underlying mechanism and related functional consequences still need further investigation in animal models.

To summarize, we found that APS showed a suppressive activity in PC cells via decreasing cell viability, proliferation, invasion, and migration and inducing cell apoptosis and inflammation in PANC-1 cells. Furthermore, APS could inhibit the activation of TLR4/NF-κB signaling pathway through the p65 phosphorylation and transportation into cell nucleus. This study suggested a cell experiment basis for developing the clinical application of APS-related therapy for PC patients.

Data Availability

The data used to support the findings of this study are included within the article.

Conflicts of Interest

The authors declare that there are no conflicts of interest regarding the publication of this paper.

Acknowledgments

This work was supported by the Agricultural and Social Development Science and Technology Project in Yinzhou District of Ningbo City (Grant No. 20191YZQ010004).

References

[1] L. Xia, M. Song, M. Sun, W. Chen, and C. Yang, "miR-486 promotes Capan-2 pancreatic cancer cell proliferation by targeting phosphatase and tensin homolog deleted on chromosome 10 (PTEN)," *Frontiers in Genetics*, vol. 10, no. 10, p. 541, 2019.

[2] X. Bai, D. Lu, Y. Lin, Y. Lv, and L. He, "A seven-miRNA expression-based prognostic signature and its corresponding potential competing endogenous RNA network in early pancreatic cancer," *Experimental and Therapeutic Medicine*, vol. 18, no. 3, pp. 1601–1608, 2019.

[3] M. T. Roth, D. B. Cardin, and J. D. Berlin, "Recent advances in the treatment of pancreatic cancer," *F1000Research*, vol. 9, p. 131, 2020.

[4] S. Saxena, A. Purohit, M. L. Varney, Y. Hayashi, and R. K. Singh, "Semaphorin-5A maintains epithelial phenotype of malignant pancreatic cancer cells," *BMC Cancer*, vol. 18, no. 1, p. 1283, 2018.

[5] H. G. Beger, F. C. Thorab, Z. Liu, N. Harada, and B. M. Rau, "Pathogenesis and treatment of neoplastic diseases of the papilla of Vater: Kausch-Whipple procedure with lymph node dissection in cancer of the papilla of Vater," *Journal of Hepato-Biliary-Pancreatic Surgery*, vol. 11, no. 4, pp. 232–238, 2004.

[6] L. Zhao, S. Tan, H. Zhang et al., "Astragalus polysaccharides exerts anti-infective activity by inducing human cathelicidin antimicrobial peptide LL-37 in respiratory epithelial cells," *Phytotherapy Research*, vol. 32, no. 8, pp. 1521–1529, 2018.

[7] L. Ren, X. Wang, S. Li et al., "Effect of gamma irradiation on structure, physicochemical and immunomodulatory properties of Astragalus polysaccharides," *International Journal of Biological Macromolecules*, vol. 120, Part A, pp. 641–649, 2018.

[8] R. Zhu, Y. Zhao, X. Li et al., "Effects of penehyclidine hydrochloride on severe acute pancreatitis-associated acute lung injury in rats," *Biomedicine & Pharmacotherapy*, vol. 97, pp. 1689–1693, 2018.

[9] B. Yang, B. Xiao, and T. Sun, "Antitumor and immunomodulatory activity of Astragalus membranaceus polysaccharides in H22 tumor-bearing mice," *International Journal of Biological Macromolecules*, vol. 62, pp. 287–290, 2013.

[10] W. H. Huang, W. R. Liao, and R. X. Sun, "Astragalus polysaccharide induces the apoptosis of human hepatocellular carcinoma cells by decreasing the expression of notch 1," *International Journal of Molecular Medicine*, vol. 38, no. 2, pp. 551–557, 2016.

[11] C. Y. Wu, Y. Ke, Y. F. Zeng, Y. W. Zhang, and H. J. Yu, "Anticancer activity of Astragalus polysaccharide in human non-small cell lung cancer cells," *Cancer Cell International*, vol. 17, no. 1, p. 115, 2017.

[12] Y. Wang, L. Sun, Y. Luo, and S. He, "Knockdown of KDM1B inhibits cell proliferation and induces apoptosis of pancreatic cancer cells," *Pathology, Research and Practice*, vol. 215, no. 5, pp. 1054–1060, 2019.

[13] B. J. Thompson, "YAP/TAZ: drivers of tumor growth, metastasis, and resistance to therapy," *BioEssays*, vol. 42, no. 5, article e1900162, 2020.

[14] J. H. Zhu, R. A. De Mello, Q. L. Yan et al., "MiR-139-5p/SLC7A11 inhibits the proliferation, invasion and metastasis of pancreatic carcinoma via PI3K/Akt signaling pathway," *Biochimica et Biophysica Acta - Molecular Basis of Disease*, vol. 1866, no. 6, article 165747, 2020.

[15] S. Du, H. Wang, J. Cai et al., "Apolipoprotein E2 modulates cell cycle function to promote proliferation in pancreatic cancer cells via regulation of the c-Myc–p21Waf1signalling pathway," *Biochemistry and Cell Biology*, vol. 98, no. 2, pp. 191–202, 2020.

[16] Z. Li, K. Jiang, X. Zhu et al., "Encorafenib (LGX818), a potent BRAF inhibitor, induces senescence accompanied by autophagy in BRAFV600E melanoma cells," *Cancer Letters*, vol. 370, no. 2, pp. 332–344, 2016.

[17] W. Luo, G. Yang, W. Luo et al., "Novel therapeutic strategies and perspectives for metastatic pancreatic cancer: vaccine therapy is more than just a theory," *Cancer Cell International*, vol. 20, no. 1, p. 66, 2020.

[18] Q. Liu, R. Zhang, C. W. Michalski, B. Liu, Q. Liao, and J. Kleeff, "Surgery for synchronous and metachronous single-organ metastasis of pancreatic cancer: a SEER database analysis and systematic literature review," *Scientific Reports*, vol. 10, no. 1, article 4444, 2020.

[19] K. Ogawa, Q. Lin, L. Li et al., "Prometastatic secretome trafficking via exosomes initiates pancreatic cancer pulmonary metastasis," *Cancer Letters*, vol. 481, no. 481, pp. 63–75, 2020.

[20] G. R. Rossi, E. S. Trindade, and F. Souza-Fonseca-Guimaraes, "Tumor microenvironment-associated extracellular matrix components regulate NK cell function," *Frontiers in Immunology*, vol. 11, no. 11, p. 73, 2020.

[21] A. M. Moreira, J. Pereira, S. Melo et al., "The extracellular matrix: an accomplice in gastric cancer development and progression," *Cell*, vol. 9, no. 2, p. 394, 2020.

[22] N. Singh, P. Das, S. Datta Gupta et al., "Prognostic significance of extracellular matrix degrading enzymes-cathepsin L and matrix metalloproteases-2 [MMP-2] in human pancreatic cancer," *Cancer Investigation*, vol. 31, no. 7, pp. 461–471, 2013.

[23] E. Anılır, F. Özen, İ. A. Özemir, İ. H. Yıldırım, Ç. Bilgiç, and O. Alimoğlu, "TLR4 Asp299Gly and Thr399Ile and TLR2 intron 2 microsatellite gene polymorphism in patients with acute biliary pancreatitis: does it cause the disease?," *Turkish Journal of Surgery*, vol. 34, no. 3, pp. 191–197, 2018.

[24] J. Torres-Ruiz, D. A. Carrillo-Vazquez, D. M. Padilla-Ortiz et al., "TLR expression in peripheral monocyte subsets of patients with idiopathic inflammatory myopathies: association with clinical and immunological features," *Journal of Translational Medicine*, vol. 18, no. 1, p. 125, 2020.

[25] Y. N. Paudel, E. Angelopoulou, C. Piperi, I. Othman, K. Aamir, and M. F. Shaikh, "Impact of HMGB1, RAGE, and TLR4 in Alzheimer's disease (AD): from risk factors to therapeutic targeting," *Cell*, vol. 9, no. 2, p. 383, 2020.

[26] B. M. Famakin, O. Tsymbalyuk, N. Tsymbalyuk et al., "HMGB1 is a potential mediator of astrocytic TLR4 signaling activation following acute and chronic focal cerebral ischemia," *Neurology Research International*, vol. 2020, Article ID 3929438, 9 pages, 2020.

[27] B. Jiang, M. Xue, D. Xu, Y. Song, and S. Zhu, "Retracted article: upregulation of microRNA-204 improves insulin resistance of polycystic ovarian syndrome via inhibition of HMGB1 and the inactivation of the TLR4/NF-κB pathway," *Cell Cycle*, vol. 19, no. 6, pp. 697–710, 2020.

[28] G. Wan, Y. An, J. Tao et al., "MicroRNA-129-5p alleviates spinal cord injury in mice via suppressing the apoptosis and inflammatory response through HMGB1/TLR4/NF-κB pathway," *Bioscience Reports*, vol. 40, no. 3, article BSR20193315, 2020.

[29] L. Pan, L. Yu, L. Wang et al., "Inflammatory stimuli promote oxidative stress in pancreatic acinar cells via toll-like receptor 4/nuclear factor-κB pathway," *International Journal of Molecular Medicine*, vol. 42, no. 6, pp. 3582–3590, 2018.

[30] C. Luo, H. Liu, H. Wang, and J. Wang, "Toll-like receptor 4 signaling in high mobility group box-1 protein 1 mediated the suppression of regulatory T-cells," *Medical Science Monitor*, vol. 23, no. 23, pp. 300–308, 2017.

Hindawi
Journal of Nanomaterials
Volume 2022, Article ID 2137188, 7 pages
https://doi.org/10.1155/2022/2137188

Research Article

Solubilization and In Vitro Physical and Chemical Properties of the Amorphous Spray-Dried Lactose-Luteolin System

Liping Dong[1,2] **Bo Wang**[1] **Lin Chen**[1] **and Min Luo**[3,4]

[1]*Xiangya School of Pharmaceutical Sciences, Central South University, Changsha 410013, China*
[2]*Academician Workstation, Changsha Medical University, Changsha 410219, China*
[3]*Department of Nephrology, The Second Xiangya Hospital, Central South University, Changsha, 410011 Hunan Province, China*
[4]*Department of Rehabilitation Medicine and Health Care, Hunan University of Medicine, Huaihua, 418000 Hunan Province, China*

Correspondence should be addressed to Bo Wang; 197211030@csu.edu.cn and Min Luo; xyluomin@csu.edu.cn

Received 21 February 2022; Revised 11 March 2022; Accepted 14 March 2022; Published 12 April 2022

Academic Editor: Weiguo Li

Luteolin is a hydrophobic drug with low solubility, which has many limitations in practical use. To improve solubility, a spray drying technique was used to prepare complexes with lactose to promote the solubility and bioavailability of luteolin. The solution samples were spray dried using different ratios of water and ethanol as different dissolution media. By characterizing the spray-dried powders obtained, we found that the solubility of the different groups of samples obtained by spray drying was improved, and similarly, their dissolution rates were also increased to different degrees. By comparison, both luteolin and the cofactor lactose were able to achieve high dissolution rates at suitable solution ratios and formed amorphous eutectic crystals after the spray drying process, which contributed well to the increased solubility and altered dissolution efficiency of luteolin.

1. Introduction

Many food-derived phytochemicals and their derivatives, such as curcumin, resveratrol, and luteolin, have great potential in the treatment of cancer. Luteolin (3,4,5,7-tetrahydroxyflavones) is a common phytochemical flavonoid found in a variety of plants such as celery chrysanthemums, bell peppers, carrots, onion leaves, and broccoli and has a variety of biological effects such as anti-inflammatory, antiallergic, and anticancer [1, 2]. Various lignan-rich plants have long been used in traditional Chinese, Iranian, and Brazilian medicine to treat many diseases such as inflammation, cardiovascular disease, and cancer. Their pharmacologically active anti-inflammatory effects may be related to their anticancer properties [3].

Inflammation is a complex biochemical response in which immune and nonimmune cells are highly coordinated. Inflammation is a natural response to harmful stimuli, such as tissue stress, injury, and microbial invasion, in order to maintain a state of homeostasis in the body [4–6]. The main aim of the inflammatory response is to eliminate harmful stimuli, and during the inflammatory response, immune cells secrete several types of mediators, including cytokines (e.g., interferon-like, interleukin, and tumor necrosis factor-α) and chemokines (e.g., monocyte chemotactic protein 1), produced tumor necrosis factor-alpha interferon beta and granulocyte-macrophage colony-stimulating factor (all proinflammatory cytokines), and increased levels of IL-10 [7–9]. Luteolin exerts their effects by altering these signaling pathways (including nuclear factor-κB) [10–12]. Cancer is a large group of diseases characterized by evasion of apoptosis, unlimited replicative potential, ongoing angiogenesis, tissue invasion and metastasis, and evasion of immune surveillance [13]. Luteolin is known to inhibit kinases, regulate the cell cycle, induce apoptosis, and reduce transcription factors through various mechanisms. The anticancer properties of luteolin are associated with the induction of apoptosis, which involves redox regulation, deoxyribonucleic acid damage, and inhibition of cancer cell proliferation by protein kinases, as well as

inhibition of metastasis and angiogenesis. In addition, luteolins can sensitize various cancer cells to treatment-induced cytotoxicity by inhibiting cell survival pathways and stimulating apoptotic pathways, while luteolin acts by altering a number of signaling pathways and exerts inhibitory and therapeutic effects on cancers such as breast, colon, pancreatic, prostate, and oral cancers through a variety of mechanisms [1, 10, 14–16].

However, luteolin is a refractory bioactive compound, and its inherent low water solubility (1.93×10^{-5} mol/l) and low oral bioavailability hinder its clinical application. Therefore, the aim of this study was to prepare and study various solid dispersions of luteolin by high solubility in ethanol in order to improve its solubility and bioactivity [17–20]. Spray drying technology is one of the best ways to prepare solid dispersions because of its proven technology and ease of operation [21]. The commonly used excipient lactose is used as a carrier, and different solvents are used as dispersion media. In the preparation process, lactose was codispersed with luteolins in the dispersion medium and prepared in the same spray drying condition. The powder samples obtained were characterized by differential scanning calorimetry (DSC), X-ray diffraction (XRD), and scanning electron microscopy (SEM), and the in vitro solubility and powder properties of luteolin were evaluated.

2. Materials and Methods

2.1. Chemical Materials. Luteolin (≥98.0%) was purchased from Xi'an Ruidi-Bio Technology Co., Ltd. Lactose (≥99.9%) was accessed from Dawning Pharmaceutical Co., Ltd., China. Absolute ethanol (purity ≥ 99.7%) for luteolin dissolution was purchased from Shanghai Titan Technology Co., Ltd.; the purified water was made from our own laboratory in fresh. All the chemical materials used in this experiment are of analytical/pharmaceutical grade with high purity.

2.2. Preparation of Physical Mixture. The lactose crystals were accurately weighed with luteolin, and the pharmaceutical grade lactose and luteolins were mixed at a mass ratio of 9 : 1 using the physical mixing method to obtain a homogeneous mixture. The physical mixture obtained was properly sieved using a no. 60 sieve to remove potentially larger particles and stored in a desiccator pending further characterization.

2.3. Preparation of Sample Solutions/Suspensions. Lactose crystals and luteolin were accurately weighed and then sieved separately to avoid potential slow dissolution problems and then kept separately in a desiccator for backup. Suspension A was prepared using pure water by first dissolving 9.0 g of pharmaceutical grade lactose in water and adding 1.0 g of luteolin under stirring to obtain suspension A, which was then stirred continuously under sealed conditions.

Lactose and luteolin were weighed separately according to the same method, and then, lactose and luteolin were dissolved in different solvents, where lactose was dissolved in pure water and luteolin in anhydrous ethanol. Both solutions were sonicated simultaneously at 40.0 kHz for 10.0 minutes, and after the two components were completely dissolved, the ethanol solution of luteolin was slowly poured into the aqueous solution of lactose along a glass rod and stirred thoroughly at low speed (30.0 rpm/min) to mix well while avoiding crystallization of the two substances as much as possible to obtain solution B.

2.4. Setting of Spray Dryer Parameters. The experimental process was carried out using a small spray dryer BYC-015. The spray drying process was protected by a nitrogen flow rate of 28.0 kg/h to prevent the organic phase ethanol from exploding in contact with oxygen in a high-temperature environment. The solution flow rate was 15.0 ml/min and was carried out using a nozzle with a diameter of 1.0 mm. The two solutions were sprayed separately under identical conditions and completed continuously. The parameters of the spray drying process were kept constant during the spray drying process: fan frequency 50.0 ± 0.5 Hz, inlet gas temperature 140.0 ± 1.0°C, outlet gas temperature 130.0 ± 3.0°C, and spray pressure 0.20 ± 0.01 MPa. After the spraying process, each sample was obtained separately in the collection hopper, sealed, and stored, respectively.

2.5. Characterization of Samples

2.5.1. Solubilization Experiments. In order to investigate the solubilizing effect of the spray drying process on luteolin and the effect on its dissolution state, a physical mixture of luteolin and the excipient lactose was prepared according to the formulation, and two spray-dried samples A and B were pressed into tablets at the same pressure, 0.30 g each, and prepared in triplicate to obtain disintegration solubility data. Dissolution data were obtained from an RC1210G Dissolution Analyzer (Xinzhi, China) with a paddle method of extraction at 75.0 rpm/min, 37.0 ± 0.1°C, and a sampling height of 750.0 ml. During the dissolution process, 1.0 ml of each sample was taken at different time intervals using a sampling needle and the standard solution was replenished promptly until the dissolution process was completed.

2.5.2. Ultraviolet-Visible Spectrophotometer (UV-Vis). The solution obtained from the dissolution experiment was filtered through a microporous membrane and diluted in the same multiples to configure the required test sample. The diluted solutions were poured individually into quartz dishes, the absorbance was measured using a UV-Vis spectrophotometer, and the solubility curve was plotted against the absorbance. The instrument used for this experiment was a UV-2401pc spectrophotometer (Shimadzu, Kyoto, Japan).

2.5.3. Differential Scanning Calorimetry (DSC). To check the physical crystalline state of the samples, thermodynamic analyses of lactose, xylitol, physical mixtures, and spray-dried samples were carried out using a differential scanning calorimeter (HSC-4 DSC, Henven, China). Samples for DSC determination were prepared in sealed, crimped aluminum pans according to standard procedures. Approximately 9.5 ± 0.3 mg of each specimen was used for analysis at a temperature range of 35.0-400.0°C and a slope of 5.0°C/min.

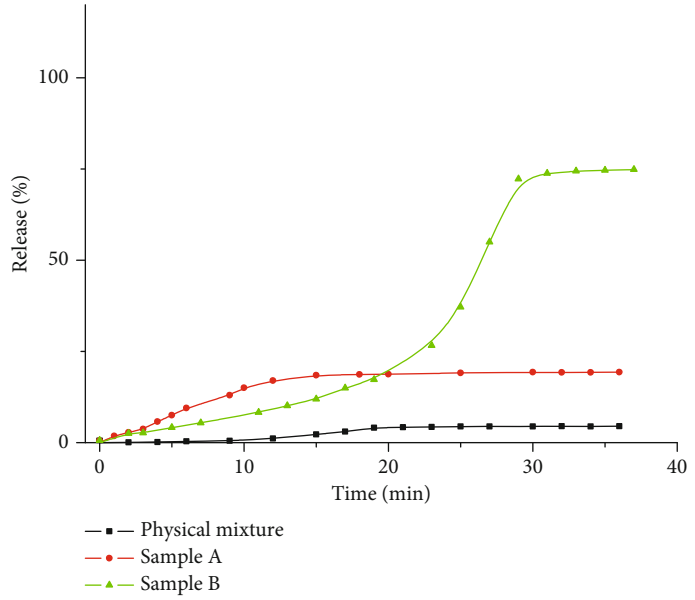

Figure 1: Release spectra of luteolin tablets in two samples and physical mixture of the same formulation.

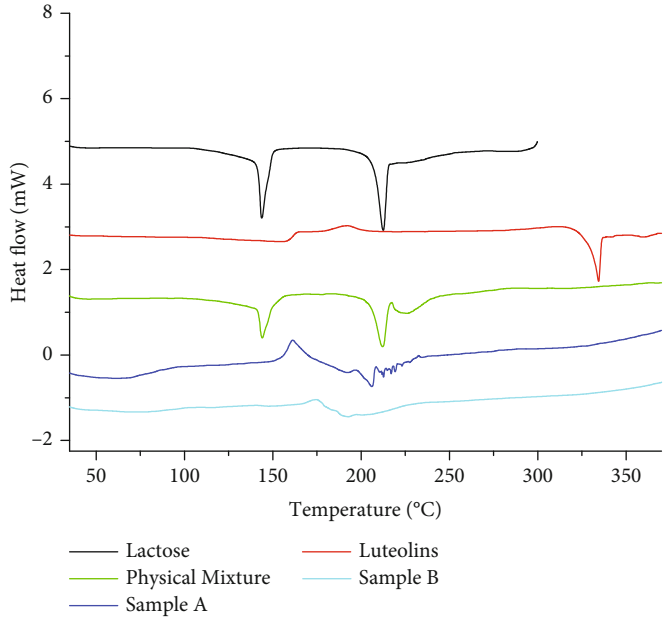

Figure 2: DSC plots of raw materials, physical mixtures of the same formulation, and samples from the experiments.

2.5.4. Thermogravimetric Analyzer (TGA). Samples were analyzed using a thermogravimetric analyzer (TGA Q5000 V3.17 Build 265). N_2 was used as the equilibrium gas during this process. The temperature during thermogravimetric analysis is 35.0-400.0°C, and the heating rate is 5.0°C/min. Samples are also examined in an alumina pan.

2.5.5. Scanning Electron Microscopy (SEM). In order to observe the surface morphology of the specimen powders, the specimen powders were uniformly plated with gold and subsequently placed on aluminum specimen stakes with carbon strips. The gold-plated specimens were examined using a JSM-7200F Scanning Electron Microscope (SEM, JEOL Ltd.).

2.5.6. N_2 Adsorption. Separate mesoporous adsorption experiments were carried out on powder samples to assess the differences in pore size distribution, surface area, and pore volume of different samples to determine the effect of different dissolution states of solutes in different spray feedstocks on their powder state.

2.5.7. X-Ray Diffraction (XRD). XRD analysis is used to study the crystalline behavior of samples. Solid samples were mounted on a powder holder, and samples were analyzed using

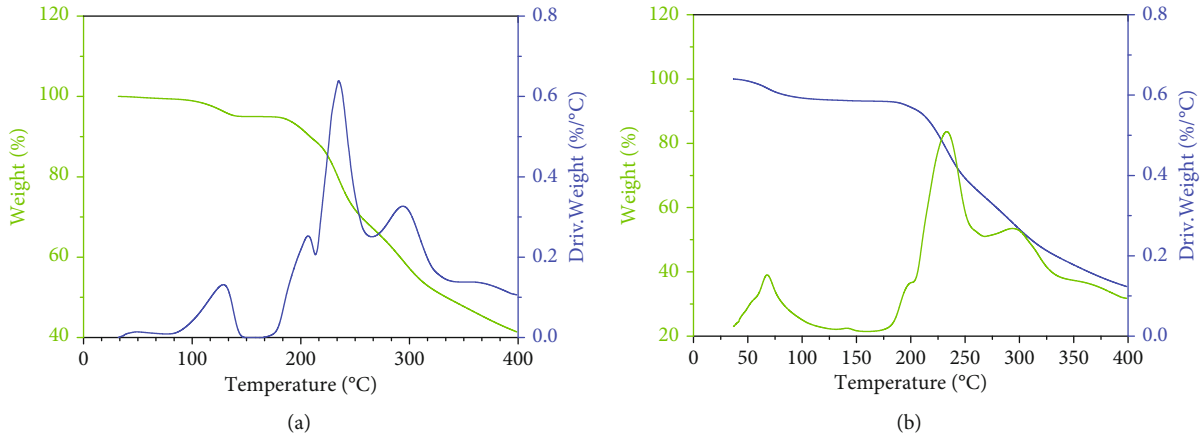

Figure 3: TGA curves of two spray-dried samples from the experiment: sample A (a) and sample B (b).

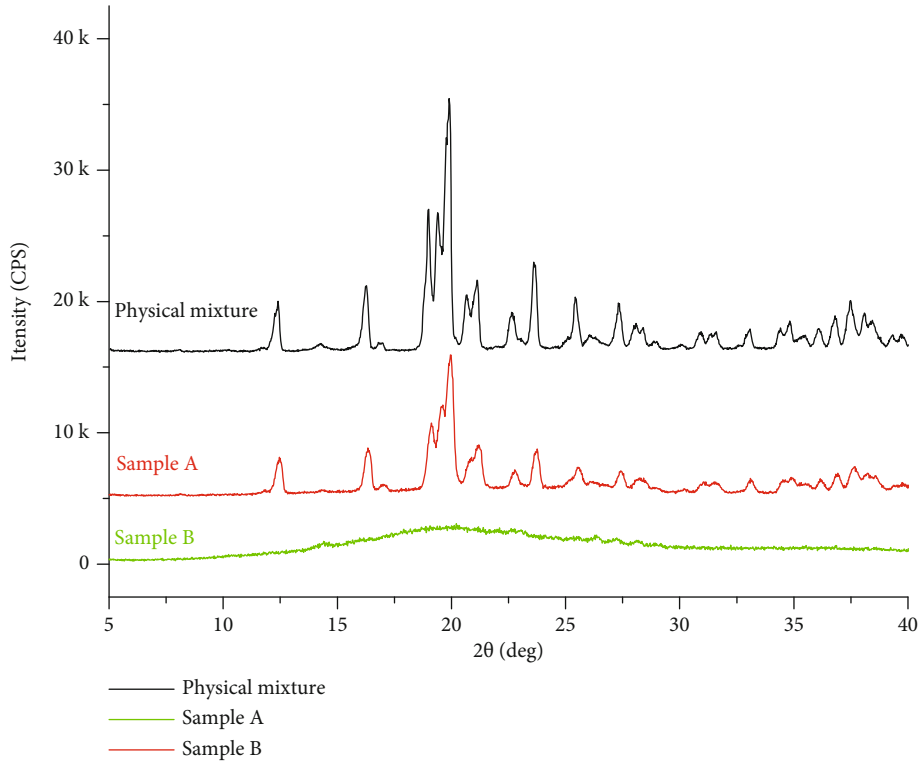

Figure 4: XRD curves of the physical mixture of the same formulation and of the two spray-dried samples from the experiment.

a Siemens D5000 diffractometer with a scan rate of 0.02°/s, a scan current of 30.0 mA, and a scan voltage of 40.0 kV.

3. Results and Discussion

Dissolution curves were plotted based on the absorbance of the sample solutions obtained by sampling at different stages of the dissolution process, as shown in Figure 1. For the physical mixture, luteolin was less water soluble and less than 5.0% of the drug was released during this dissolution process. In contrast, the release rate of both sample powders increased significantly after the complete disintegration of the drug following the spray drying process. Sample B showed a significant increase in release rate. Comparing sample A and sample B, we found that the percentage release was significantly higher for sample B, but the dissolution rate was relatively smaller than that of sample A, and it took more time to reach dissolution equilibrium. It is possible that this is due to the fact that a higher proportion of ethanol in the same solution makes luteolin more soluble, resulting in the analytical release of more luteolin molecules from the lattice and destroying the crystalline structure of luteolin during the spray drying process, resulting in more amorphous luteolin being formed, leading to a significant increase in its solubility. Similarly, in this process, due to the lower solubility of lactose in ethanol, more lactose crystals

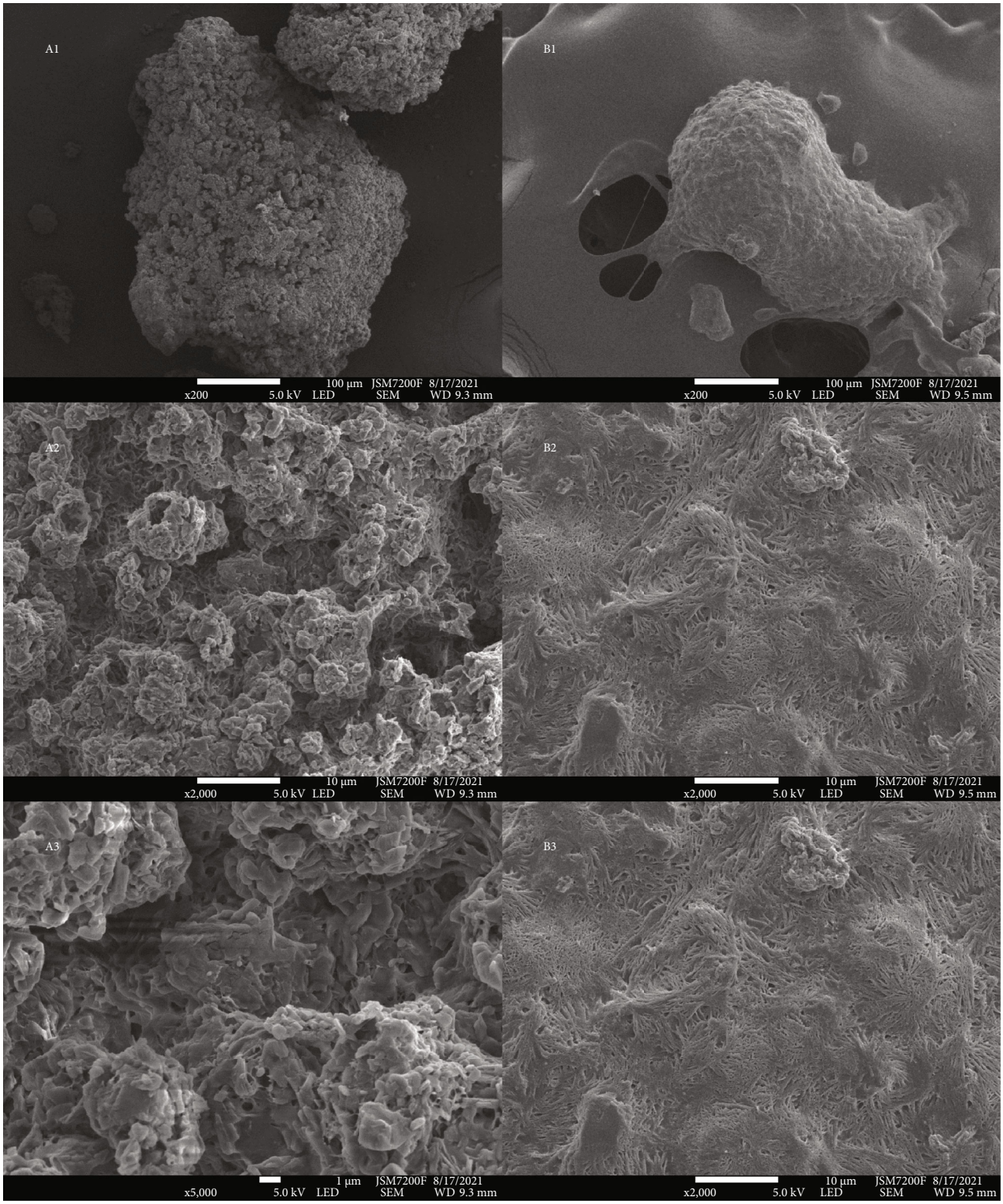

Figure 5: SEM images of spray-dried samples obtained in two experiments at 200x, 2000x, and 5000x (A1-3 for sample A; B1-3 for sample B).

precipitated prior to the high-temperature drying process, the proportion of amorphous lactose was reduced, and the crystalline form of the powder in the tablets pressed from the sample B powder was more complex, making the overall system more difficult to disintegrate.

We carried out thermal analysis of the constituent materials in the experiment. By analyzing the DSC curves of the samples (Figure 2), the water of crystallization and heat absorption peaks of lactose monohydrate and the melting peak of lactose crystals occurred at 144.3°C and 213.4°C,

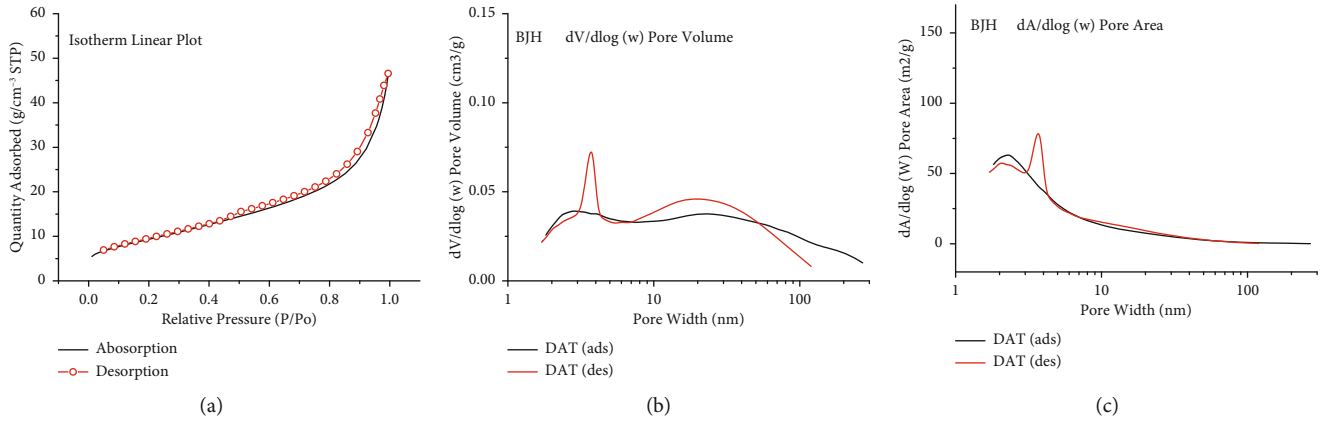

Figure 6: Nitrogen adsorption curves for sample B obtained from the experiments: isotherm linear plot (a), BJH adsorption/desorption $dV/d\log(w)$ pore volume (b); BJH adsorption/desorption $dA/d\log(w)$ pore (c).

respectively, while the maximum heat absorption peak of xylitol occurred at 334.4°C. For the physical mixture, the heat absorption peak of lactose shifted towards the lower-temperature region with the maximum heat absorption occurring at 212.1°C, while the heat absorption peak of xylitol disappeared near 334.0°C and a broad and blunt heat absorption peak appeared near the lactose heat absorption peak with its peak shifted to 226.1°C, which may be related to the slower heat transfer rate of the solid mixture. In contrast, for the spray-dried sample, the overall peak pattern changed dramatically, with the disappearance of the crystalline water peak for lactose, a reduction in the crystalline melting peak for lactose and luteolin, and an upward exothermic peak acting towards the lower temperature region, indicating the possible appearance of an amorphous product. By comparing sample A and sample B, the amorphous exothermic peak of sample A appeared at 160.8°C with a larger heat absorption peak at 205.8°C. In addition, a complex and fine heat absorption peak appears during sustained heating, which may be due to differences in the enthalpy of melting due to polycrystal formation, suggesting that a more complex crystal composition may be present. In contrast, for sample B, the exothermic peak shifted towards the high-temperature region, reaching 175.5°C. During heating, no small peaks similar to those of sample A appear and the heat flow curve is flat throughout. This indicates that in sample B, the crystalline form is relatively homogeneous and a relatively pure amorphous product, suggesting that both luteolin and lactose are well soluble in the appropriate proportions of ethanol solution and that both can exist as free molecules in spray drying under high-temperature conditions, rapidly losing water to form an amorphous product.

Figure 3 shows the thermogravimetric curves of these two groups of samples in order from left to right. These two sets of samples show the same trend of weight loss with increasing temperature. These samples show a trend of weight loss after 50.0°C, reaching a maximum rate at around 260.0°C. A comprehensive analysis of these two sets of samples showed that the physical composition of the spray-dried powders obtained from the different concentrations of solutions was essentially the same, but the proportions of crystalline components showed significant differences and the weight loss trends were approximately the same for both sets of samples; however, there were differences in the weight loss curves at around 200.0°C; samples A and B may have different crystalline compositions.

According to the XRD curves (Figure 4), the α-lactose peaks at 2θ were 12.5°, 19.1°, 19.6°, and 19.9° in the two samples, respectively, while the β-lactose peak at $2\theta = 10.5°$ was absent in both samples, indicating that no lactose swirling occurred during the dissolution and spray drying process or it occurred in a very small proportion. The diffraction pattern showed that the individual diffraction peaks in the physical mixture were sharp and steep and that the individual diffraction peaks in sample A became relatively short and flat compared to the physical mixture, indicating a possible reduction in crystalline material, while the diffraction peaks at different positions in sample B disappeared and were replaced by a large blunt and flat amorphous peak at around $2\theta = 20.0°$. This suggests that the proportion of crystalline material in the sample was reduced during the spray drying process, particularly in sample B, where the whole composition was able to transform into an amorphous state after dissolution in a suitable solution and after the spray drying process.

tBased on electron microscopic observations, sample A and sample B exhibited completely different states in the SEM field of view (Figure 5). Sample A exhibits a porous aggregate of various fine crystal particles with relatively smooth solid bridges wrapped between the crystal particles, indicating the presence of some amorphous components in the powder of sample A. During the spray drying process, the undissolved solid components in solution were dried together with the solution, and the dissolved molecules in solution partially crystallized and partially wrapped around the surface of the crystals in an amorphous state, forming a rough aggregate of solid particles. On the other hand, sample B shows a different crystalline/noncrystalline state. Unlike sample A, the surface of sample B is very smooth and porous with no apparent granular structure, indicating that most of the components in sample A are probably in a noncrystalline state.

For sample B, which was in a porous state, nitrogen adsorption experiments were carried out to calculate and evaluate its pore structure (Figure 6). Its BET adsorption and

desorption curves visually represent its porosity. Its average pore size was calculated by analysis to be approximately 7.4 nm, with a cumulative volume of pores with widths between 1.7000 nm and 300.0000 nm: 0.069187 cm^3/g. The BET surface area (33.8243 m^2/g), whose large pore volume may provide better compressibility, confirms the trend of the solubility curve.

4. Conclusion

To improve the solubility of luteolin, a complex with lactose was prepared by the spray drying technique to promote the solubility and bioavailability of luteolin. The experimental results showed that the solubility and dissolution efficiency of the spray-dried drug were significantly higher compared to those of the solid mixture. The spray drying resulted in a higher proportion of amorphous products in the drug product powder. The amorphous content of the product could be significantly altered by changing the ratio of the components in the dissolution medium to form a porous eutectic product with a smooth surface, which could contribute to the enhancement of the solubility of luteolin and its clinical application.

Data Availability

All data used to support the findings of this study are included within the article.

Disclosure

Liping Dong is a postdoctor under the supervision of Professor Wenhu Zhou in Xiangya School of Pharmaceutical Sciences, Central South University.

Conflicts of Interest

There is no conflict of interest regarding the publication of this paper.

Acknowledgments

The work is supported by the Postdoctoral Start-up Fund from Central South University. This work is also supported by the Foundation of the Second Xiangya Hospital (XYEYY20200812).

References

[1] Y. Lin, R. Shi, X. Wang, and H. M. Shen, "Luteolin, a flavonoid with potential for cancer prevention and therapy," *Current Cancer Drug Targets*, vol. 8, no. 7, pp. 634–646, 2008.

[2] S. F. Nabavi, N. Braidy, O. Gortzi et al., "Luteolin as an anti-inflammatory and neuroprotective agent: a brief review," *Brain Research Bulletin*, vol. 119, Part A, pp. 1–11, 2015.

[3] N. Aziz, M. Y. Kim, and J. Y. Cho, "Anti-inflammatory effects of luteolin: a review of in vitro, in vivo, and in silico studies," *Journal of Ethnopharmacology*, vol. 225, pp. 342–358, 2018.

[4] K. Roe, "An inflammation classification system using cytokine parameters," *Scandinavian Journal of Immunology*, vol. 93, no. 2, article e12970, 2021.

[5] N. Singh, D. Baby, J. P. Rajguru, P. B. Patil, S. S. Thakkannavar, and V. B. Pujari, "Inflammation and cancer," *Annals of African Medicine*, vol. 18, no. 3, pp. 121–126, 2019.

[6] R. Medzhitov, "Origin and physiological roles of inflammation," *Nature*, vol. 454, no. 7203, pp. 428–435, 2008.

[7] J. Iype and M. Fux, "Basophils orchestrating eosinophils' chemotaxis and function in allergic inflammation," *Cell*, vol. 10, no. 4, p. 895, 2021.

[8] A. Sgambato and A. Cittadini, "Inflammation and cancer: a multifaceted link," *European Review for Medical and Pharmacological Sciences*, vol. 14, no. 4, pp. 263–268, 2010.

[9] D. Wallach, T. B. Kang, and A. Kovalenko, "Concepts of tissue injury and cell death in inflammation: a historical perspective," *Nature Reviews. Immunology*, vol. 14, no. 1, pp. 51–59, 2014.

[10] M. Imran, A. Rauf, T. Abu-Izneid et al., "Luteolin, a flavonoid, as an anticancer agent: a review," *Biomedicine & Pharmacotherapy*, vol. 112, 2019.

[11] F. Ali and Y. H. Siddique, "Bioavailability and pharmacotherapeutic potential of luteolin in overcoming Alzheimer's disease," *CNS & Neurological Disorders Drug Targets*, vol. 18, no. 5, pp. 352–365, 2019.

[12] W. C. Huang, C. J. Liou, S. C. Shen, S. Hu, C. Y. Hsiao, and S. J. Wu, "Luteolin attenuates IL-1β-induced THP-1 adhesion to ARPE-19 cells via suppression of NF-κB and MAPK pathways," *Mediators of Inflammation*, vol. 2020, Article ID 9421340, 15 pages, 2020.

[13] G. Kroemer and J. Pouyssegur, "Tumor cell metabolism: cancer's Achilles' heel," *Cancer Cell*, vol. 13, no. 6, pp. 472–482, 2008.

[14] C. J. Wruck, M. Claussen, G. Fuhrmann et al., "Luteolin protects rat PC12 and C6 cells against MPP+ induced toxicity via an ERK dependent Keapl-Nrf2-ARE pathway," *Journal of Neural Transmission. Supplementum*, vol. 72, pp. 57–67, 2007.

[15] S. Ahmed, H. Khan, D. Fratantonio et al., "Apoptosis induced by luteolin in breast cancer: mechanistic and therapeutic perspectives," *Phytomedicine*, vol. 59, 2019.

[16] R. K. Ambasta, R. Gupta, D. Kumar, S. Bhattacharya, A. Sarkar, and P. Kumar, "Can luteolin be a therapeutic molecule for both colon cancer and diabetes?," *Briefings in Functional Genomics*, vol. 18, no. 4, pp. 230–239, 2018.

[17] S. Alshehri, S. S. Imam, M. A. Altamimi et al., "Enhanced dissolution of luteolin by solid dispersion prepared by different methods: physicochemical characterization and antioxidant activity," *ACS Omega*, vol. 5, no. 12, pp. 6461–6471, 2020.

[18] G. Wu, J. Li, J. Yue, S. Zhang, and K. Yunusi, "Liposome encapsulated luteolin showed enhanced antitumor efficacy to colorectal carcinoma," *Molecular Medicine Reports*, vol. 17, no. 2, pp. 2456–2464, 2018.

[19] M. Mahin, A. Ali, K. Elahe et al., "Synthesis of a copolymer carrier for anticancer drug luteolin for targeting human breast cancer cells," *Journal of Traditional Chinese Medicine*, vol. 39, no. 4, pp. 474–481, 2019.

[20] M. Imran, R. Mehmood, U. R. Mughal, B. Ali, and A. Malik, "Vicarin, a new isoflavone from Eremostachys vicaryi," *Journal of Asian Natural Products Research*, vol. 14, no. 3, pp. 293–296, 2012.

[21] B. Wang, F. Liu, J. Xiang et al., "A critical review of spray-dried amorphous pharmaceuticals: synthesis, analysis and application," *International Journal of Pharmaceutics*, vol. 594, 2021.

Hindawi
Journal of Nanomaterials
Volume 2022, Article ID 4642477, 10 pages
https://doi.org/10.1155/2022/4642477

Research Article

A Prognostic Model for Patients with Hepatocellular Carcinoma Based on Hypoxia-Related Long Noncoding RNAs

Lan Jiang,[1] Huacheng Li,[2] and Deqing Zhao[1]

[1]*Department of Oncology, Huangshi Central Hospital, Affiliated Hospital of Hubei Polytechnic University, China*
[2]*Hubei University of Chinese Medicine, China*

Correspondence should be addressed to Deqing Zhao; jlpc2009@stmail.hbtcm.edu.cn

Received 23 February 2022; Accepted 22 March 2022; Published 1 April 2022

Academic Editor: Weiguo Li

Objective. The prognosis of patients with hepatocellular carcinoma (HCC) varies greatly due to the hypoxic environment and multiple factors driving metastasis progress. In this study, we aimed to correlate the expression of hypoxia-related long noncoding RNAs (lncRNAs) with the survival of patients with HCC to develop a prognostic model for HCC. *Methods*. The Pearson correlation analysis was used to screen hypoxia-related lncRNAs between differentially expressed lncRNAs by analyzing lncRNA expression profiles in The Cancer Genome Atlas (TCGA) database and 200 hypoxia genes downloaded from the Molecular Signatures Database (M5891). The univariate and multivariate Cox regression analyses were used to identify significantly predictive hypoxia-related lncRNAs, and a prognostic model based on these factors was constructed to predict the survival of HCC. The Kaplan-Meier (K-M) survival analysis and receiver operating characteristic curve (ROC) were performed to evaluate the performance of the model. *Results*. A total of 490 hypoxia-related lncRNAs were screened out. A prognostic model comprising 10 significantly predictive hypoxia-related lncRNAs was constructed by the multivariate Cox regression analysis. The hypoxia-related risk scores were calculated and were divided into high-risk and low-risk groups. The K-M survival analysis showed a lower overall survival rate of patients in the high-risk group ($P < 0.05$). ROC analysis showed that the AUC value of hypoxia-related risk score was 0.799, demonstrating that the hypoxia-related risk score was an independent prognosis factor of HCC. *Conclusion*. Our study indicates that identified 10 key hypoxia-related lncRNAs have potential prognostic values for HCC patients and may provide new targets for the treatment of HCC.

1. Introduction

Hepatocellular carcinoma (HCC) is the main type of liver cancer, accounting for 85%-90% of the primary liver cancers, and the global disease burden caused by HCC is also increasing [1]. Although some new advances have been made in the treatment of HCC in recent years, the rate of 5-year overall survival in patients with HCC is still no more than 20% [2]. Nowadays, molecular mechanism research based on bioinformatics analysis has become one of the important tools in cancer research [3, 4]. Therefore, using bioinformatics technique to explore new molecular markers for predicting the survival of HCC is of great significance for individualized and precision therapy of HCC.

Hypoxia, which manifested as a decrease in the level of available oxygen in the tissues, often occurs in patients with acute and chronic vascular diseases, lung diseases, and cancer [5]. Due to the imbalance between tumor cell proliferation speed and vascular nutrient supply, hypoxia is a common phenomenon in solid tumors [6]. Many studies had recognized the important role of hypoxia in tumor angiogenesis, cell proliferation, cell differentiation, and apoptosis [7, 8]. The liver is one of the three most vulnerable organs to hypoxia, and HCC is a hypermetabolic tumor that consumes more oxygen than its surrounding normal tissues. Previous studies have found that hypoxia was related to HCC metastasis, poor prognosis, and treatment resistance [9, 10]. A recent study found that an increased expression of hypoxia-inducible factor-1α (HIF-1α) in HCC tissues may contribute to the invasion and metastasis of HCC and poor prognosis [11]. Besides, HIF-1α is also the main reason for the resistance of HCC to sorafenib [12].

Long noncoding RNAs (lncRNAs) are noncoding RNAs with a length of more than 200 nucleotides [13]. Recently, lncRNAs are gaining increasing attention from researchers because they are involved in several key molecular and biological processes of the body, such as they affect the occurrence and development of tumors [14]. Besides, studies have shown that various lncRNAs responding to hypoxia environment played an important role in the occurrence and development of tumors [15]. Based on this, we speculate that hypoxia-related lncRNAs may be served as prognostic markers for HCC patients. Therefore, this study was aimed at exploring prognostic markers of HCC based on hypoxia-related lncRNAs by a bioinformatics approach and constructing a prognostic model for predicting the survival outcomes in HCC.

2. Materials and Methods

2.1. Data Acquisition and Processing. The gene expression profiles and clinical data of HCC patients were downloaded from The Cancer Genome Atlas (TCGA) database (https://portal.gdc.cancer.gov/repository) on August 10, 2021. We excluded those with an overall survival period of ≤30 days (because these patients may die from unpredictable factors such as infection or bleeding) and those with unknown survival time and survival status. A total of 350 HCC patients (cancerous liver tissues and adjacent noncancerous liver tissues) were included in this study.

2.2. Screening Hypoxia-Related lncRNAs. The transcriptome data of 350 HCC patients were annotated into mRNAs and lncRNAs. Differentially expressed lncRNAs between cancerous liver tissues and adjacent noncancerous liver tissues were screened by analyzing raw data of gene expression profiles using the Limma package from the R/Bioconductor software in accordance with $|\log 2(\text{fold change [FC]})| > 0$ and adjusted $P \leq 0.05$. A total of 200 iconic hypoxia genes on the hypoxia-related pathway (HALLMARK-HYPOXIA) were downloaded from the Molecular Signatures Database V7.4 (http://www.gseahttp://msigdb.org/gsea/msigdb/index.jsp). Then Pearson correlation analysis was used to analyze the correlation between the hypoxia score and the expression of lncRNAs, and the hypoxia-related lncRNAs were screened out according to the criteria of correlation coefficient $(|r|) > 0.4$ and $P < 0.001$.

2.3. Identifying Key Hypoxia-Related lncRNAs Associated with the Prognosis of HCC. The univariable Cox regression was used to identify the key hypoxia-related lncRNAs associated with the prognosis of HCC. Hypoxia-related lncRNAs with significant prognostic value ($P < 0.001$) were defined as key hypoxia-related lncRNAs and were screened out for subsequent research.

2.4. Constructing the Hypoxia-Related Prognostic Model. The multivariate Cox regression analysis was used to construct the hypoxia-related prognostic model, and the risk score of each sample was calculated by the following algorithm: $\text{Risk score} = \text{Expression}_{\text{lncRNA1}} \times \text{Coefficient}_{\text{lncRNA1}} + \text{Expression}_{\text{lncRNA2}} \times \text{Coefficient}_{\text{lncRNA2}} + \cdots + \text{Expression}_{\text{lncRNAn}} \times \text{Coefficient}_{\text{lncRNAn}}$ (Expression $_{\text{lncRNA}}$ refers to the expression level of hypoxia-related lncRNA; Coefficient $_{\text{lncRNA}}$ is the regression coefficient of lncRNA obtained by multivariate Cox regression analysis). Then, patients were divided into low-risk group and high-risk group according to their median value of the risk score.

2.5. Bioinformatics Analysis. Receiver operating characteristic (ROC) curve was used to evaluate the performance of the prognostic model. Principal component analysis (PCA) and gene set enrichment analysis (GSEA) (http://www.gsea-msigdb.org/gsea/msigdb/index.jsp) were performed to determine whether the hypoxia-related lncRNA set is statistically significantly enriched in some distribution pattern and some functional pathways between high-risk group and low-risk group.

2.6. Statistical Analysis. The Pearson correlation analysis was used to identify the hypoxia-related lncRNAs. The Kaplan-Meier (K-M) analysis was used to draw survival curve, and log-rank test was used to compare the survival rate of patients in high-risk and low-risk groups. The univariate and multivariate Cox regression analyses were used to determine the prognostic hypoxia-related lncRNAs of HCC. All statistical analysis was performed by R software (Version 4.0.2; https://mirror.lzu.edu.cn/CRAN/). $P < 0.05$ indicated that the difference is statistically significant.

3. Results

3.1. Identification of Hypoxia-Related lncRNAs. After downloading the transcriptome data and clinical data of HCC samples from the TACG database, converting the ID of the data into the gene name, we annotated the transcriptome data into lncRNAs and mRNAs. The iconic hypoxia genes including 200 genes were downloaded from the Molecular Signatures Database. By constructing a hypoxia lncRNA-mRNA coexpression network, a total of 490 hypoxia-related lncRNAs were screened out following the selection criteria of $|r| > 0.4$ and $P < 0.001$.

3.2. Construction of the Hypoxia-Related Prognostic Model. Among the 490 hypoxia-related lncRNAs screened out above, a total of 37 hypoxia-related lncRNAs were associated with the prognosis of HCC by the univariate Cox regression analysis (Figure 1). The multivariate Cox regression identified 10 key hypoxia-related lncRNAs to construct the prognostic model, including AL365203.2, AC015908.3, MSC-AS1, AC145207.5, AL117336.3, TMEM220-AS1, AL031985.3, AC009005.1, THUMPD3-AS1, and PRRT3-AS1 (Table 1). Based on the expression levels of 10 hypoxia-related lncRNAs and their coefficients from the multivariable Cox regression, we then calculated the risk score of each patient by using the following algorithm: $\text{Risk score} = (0.254 \times \text{the expression level of AL365203.2}) + (-1.420 \times \text{the expression level of AC015908.3}) + (0.334 \times \text{the expression level of MSC} - \text{AS1}) + (0.445 \times \text{the expression level of AC145207.5}) + (0.482 \times \text{the expression level of AL117336.3}) + (1.117 \times \text{the expression level of TMEM220} - \text{AS1}) + (0.433 \times \text{the expression level of AL031985.3}) + (0.363 \times$

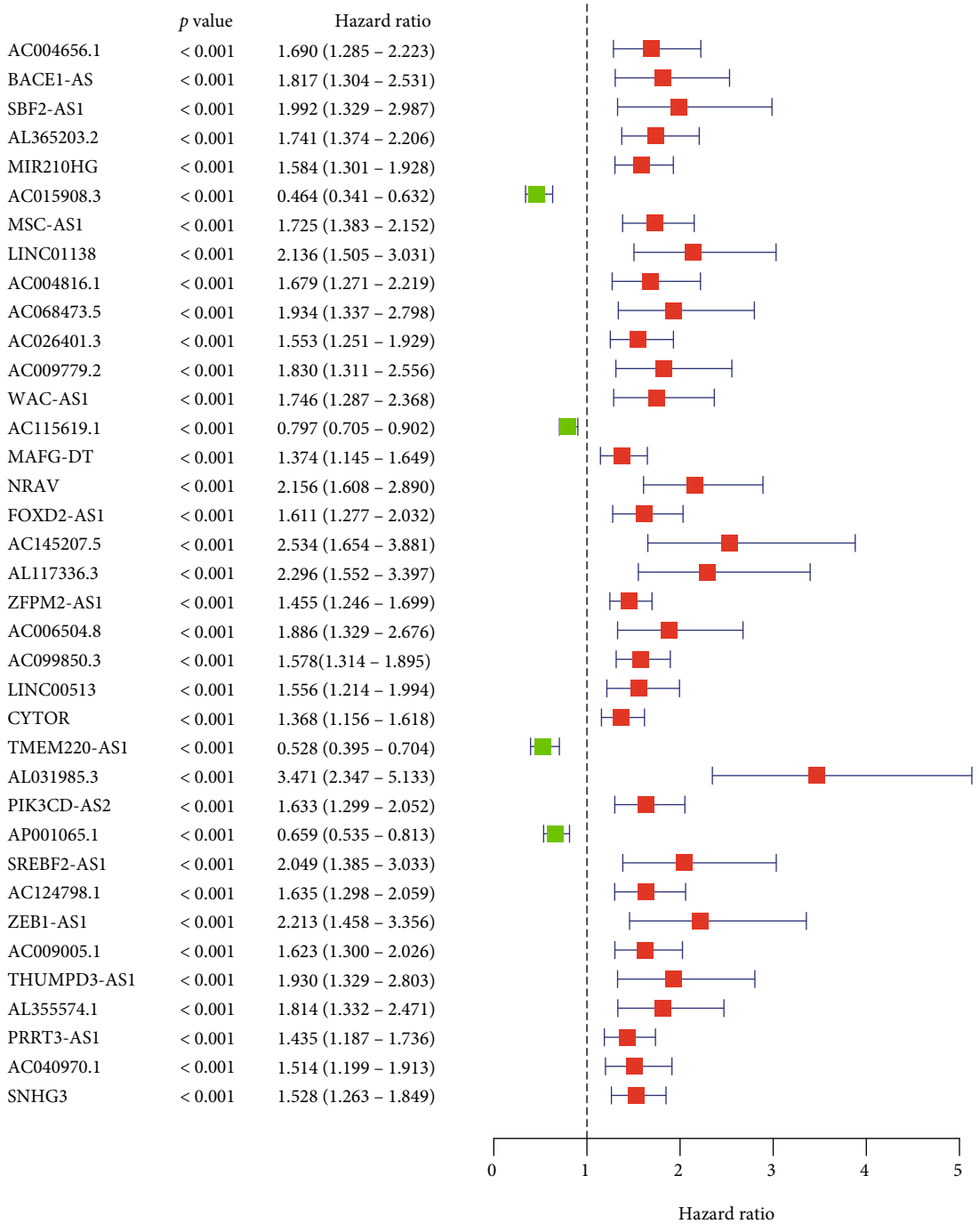

Figure 1: A forest map showed that 37 hypoxia-related lncRNAs identified by the univariate Cox regression analysis were associated with the prognosis of HCC.

the expression level of AC009005.1) + (−0.596 × the expression level of THUMPD3 − AS1) + (0.267 × the expression level of PRRT3 − AS1). The details of the 10 hypoxia-related lncRNAs are shown in Table 1.

3.3. Clinical Characteristics of HCC Patients in High-Risk and Low-Risk Groups. Based on the above risk score calculation formula, 350 HCC patients were divided into high-risk and low-risk groups according to the median value of risk score. The survival status, risk score distribution, and key gene expression are shown in Figure 2, from which we can see that the low-risk group had significantly lower hypoxia-related risk score (Figure 2(a)) and higher survival rate (Figure 2(b)). Furthermore, as the hypoxia-related risk score increased, the expression levels of AL365203.2, MSC-AS1, AC145207.5, AL117336.3, AL031985.3, AC009005.1, THUMPD3-AS1, and PRRT3-AS1 were increased, while the expression levels of AC015908.3 and TMEM220-AS1

Table 1: 10 key hypoxia-related lncRNAs selected as prognosis-associated factors in HCC.

lncRNA	Coef	HR	HR.95L	HR.95H	*P* value
AL365203.2	0.254	1.289	0.971	1.712	0.048
AC015908.3	-1.420	0.242	0.088	0.663	0.006
MSC-AS1	0.334	1.396	1.063	1.834	0.016
AC145207.5	0.445	1.560	0.925	2.632	0.010
AL117336.3	0.482	1.620	0.999	2.625	0.009
TMEM220-AS1	1.117	3.056	1.174	7.953	0.002
AL031985.3	0.433	1.541	0.914	2.598	0.014
AC009005.1	0.363	1.437	1.098	1.880	0.008
THUMPD3-AS1	-0.596	0.551	0.314	0.965	0.037
PRRT3-AS1	0.267	1.306	1.041	1.639	0.021

were decreased (Figure 2(c)). In addition, the K-M survival analysis showed that the overall survival rate of the high-risk group was significantly lower than that of the low-risk group ($P < 0.05$) (Figure 2(d)).

3.4. Correlation between Hypoxia-Related Risk Scores and Clinical Characteristics. We analyzed the correlation between the hypoxia-related risk scores and clinical and demographic characteristics such as age, gender, grade, T stage, N stage, and M stage. The results showed that C009005.1, AC015908.3, AC145207.5, AL031985.3, THUMPD3-AS1, and TMEM220-AS1 were correlated with T stage (all $P < 0.05$). AC145207.5, AL031985.3, AC009005.1, and THUMPD3-AS1 have low expression in stage T1 and high expression in stages T2-T4, while TMEM220-AS1 and AC015908.3 have low expression in stages T2 and T3 but high expression in stages T1 and T4 (Figure 3). In addition, both univariate and multivariate Cox regression analysis results showed that only hypoxia-related risk scores were significantly related to the prognosis of HCC patients (all $P < 0.001$) (Table 2). ROC analysis showed that the AUC values of hypoxia-related risk score, age, gender, classification, staging, T stage, N stage, and M stage were 0.799, 0.454, 0.506, 0.475, 0.743, 0.752, 0.508, and 0.508, respectively (Figure 4), demonstrating that the hypoxia-related risk score was an independent prognosis factor of HCC.

3.5. Analysis of Hypoxia Characteristics of Patients in High-Risk and Low-Risk Groups. Based on the key hypoxia-related lncRNAs for constructing the prognostic model and all hypoxia-related lncRNAs, we used PCA to explore the different distribution patterns between the high-risk and low-risk groups. The results showed that the distribution of hypoxia-related lncRNAs in the high-risk and low-risk groups was significantly different, showing two separate parts (Figures 5(a) and 5(b)). The GSEA analysis further indicated that hypoxia-related phenotypes were significantly enriched in the high-risk group (Figure 6).

4. Discussion

HCC is a highly invasive malignant tumor of the digestive system [16, 17]. Despite some progress has been made in the diagnosis and treatment of HCC in recent years, the prognosis of HCC is still poor [18]. Therefore, identifying new prognostic markers to optimize treatment is a great challenge in the field of tumor research. Studies have shown that the occurrence and development of HCC is a complex process affected by many factors [19, 20].

Hypoxia is an important feature of the microenvironment of most malignant tumors, especially HCC, and it is closely related to the poor prognosis of patients [21]. Several studies have shown that hypoxia is associated with the aggressive development of HCC [5, 8]. Recently, lncRNA-related signatures have received more and more attention due to their higher prediction accuracy compared with standard benchmarks [22–24]. Previous studies have also demonstrated that lncRNAs are involved in the occurrence, development, and metastasis of HCC [25, 26]. Hypoxia can affect the expression of some lncRNAs [27]. In view of the role of lncRNAs in the biological process of cancer and their correlation with hypoxia, it is of great clinical significance to explore the predictive value of hypoxia-related lncRNAs in the prognosis of HCC. However, prognostic markers based on the hypoxia-related lncRNA expression profile have not been studied in HCC.

In this study, we focused on hypoxia-related lncRNA signatures with the prognosis value of HCC. We analyzed the transcriptome information and clinical data of HCC patients in TCGA database, and found a group of hypoxia-related lncRNAs by coexpression analysis. A total of 37 hypoxia-related lncRNAs were found to be associated with the prognosis of HCC by the univariate Cox regression analysis, indicating that these hypoxia-related lncRNAs were involved in the development of HCC. In further analysis of the data by the multivariate Cox regression, we identified 10 key hypoxia-related lncRNAs (AL365203.2, AC015908.3, MSC-AS1, AC145207.5, AL117336.3, TMEM220-AS1, AL031985.3, AC009005.1, THUMPD3-AS1, and PRRT3-AS1) which were associated with the prognosis of HCC. A prognostic model of HCC was constructed based on these10 key hypoxia-related lncRNAs. The prognosis of patients in the high-risk group was worse than those in the low-risk group. Besides, we also found that the hypoxia-related risk score was significantly correlated with T stage. Therefore, these results further

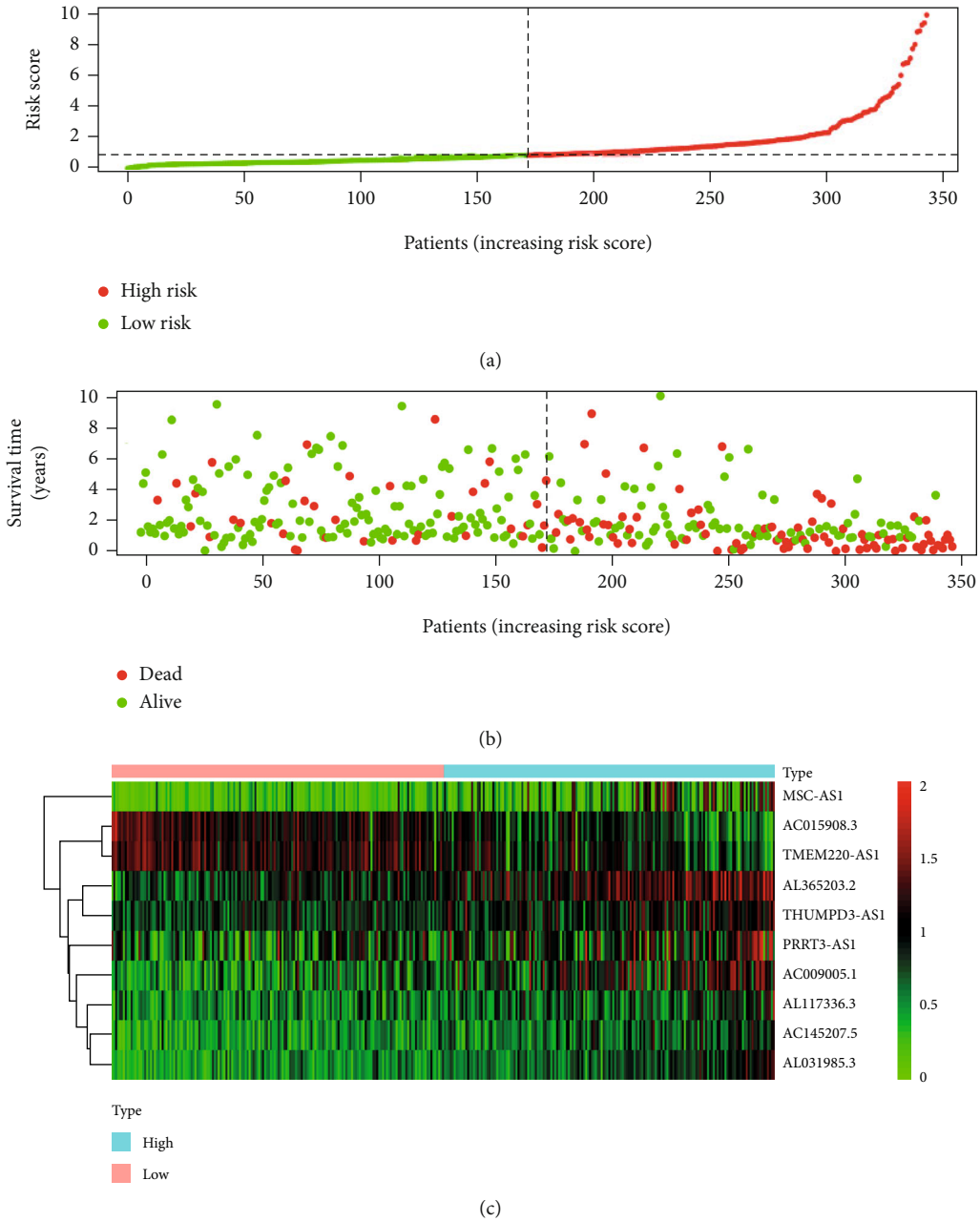

Figure 2: Continued.

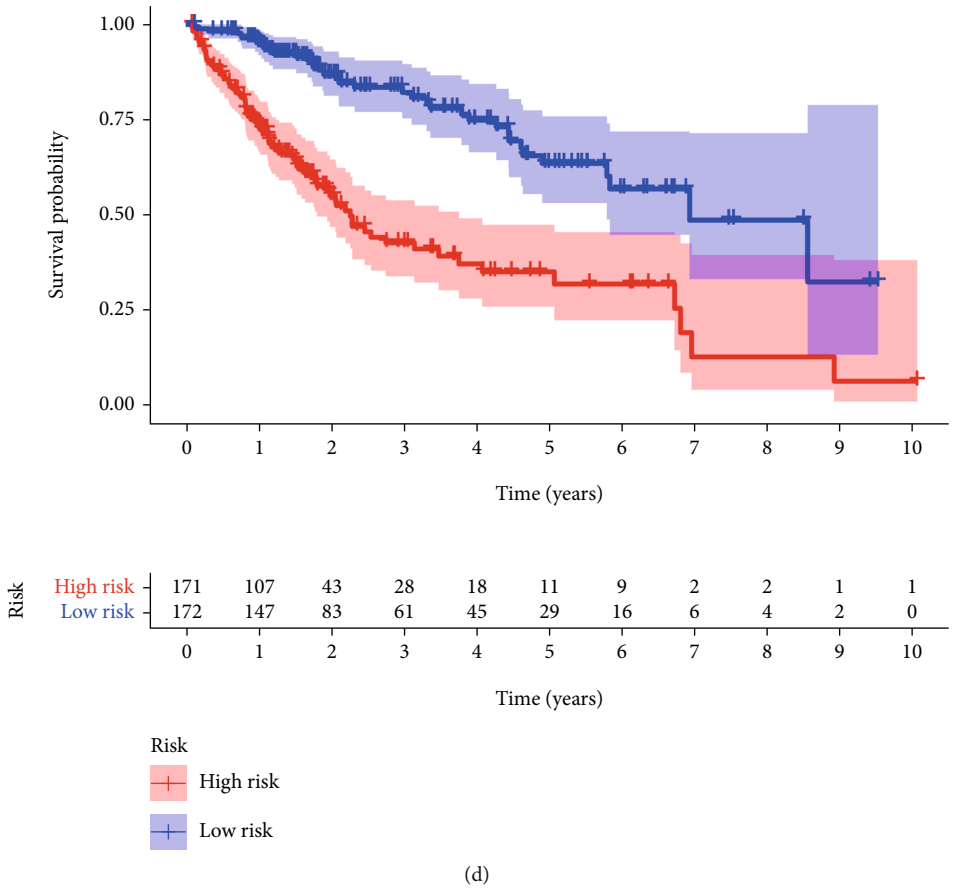

(d)

Figure 2: The prognostic model constructed based on 10 key hypoxia-related lncRNAs. (a) Distribution of high-risk and low-risk groups of patients. (b) Survival status of high-risk and low-risk groups of patients. (c) Heat map of the expression of the 10 key hypoxia-related lncRNAs in HCC. (d) Kaplan-Meier curves for the OS of patients in the high-risk and low-risk groups.

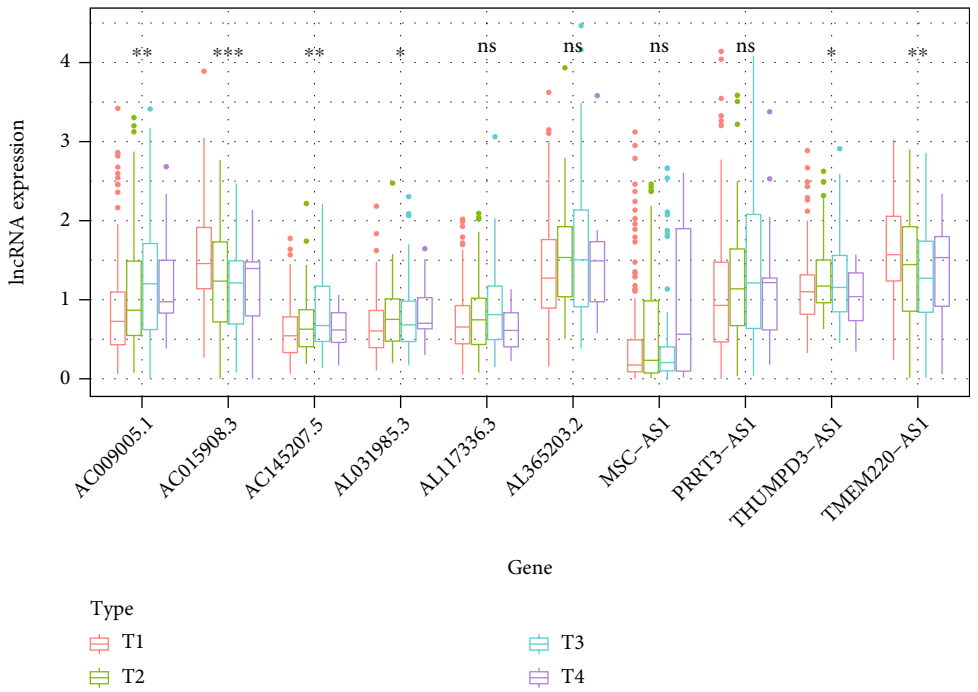

Figure 3: Correlation analysis of the10 key hypoxia-related lncRNAs and clinical T staging of HCC (∗ represents $P < 0.05$, ∗∗ represents $P < 0.01$, ∗∗∗ represents $P < 0.001$, and ns represents $P > 0.05$).

Table 2: Univariate and multivariate independent prognostic analysis of HCC.

Variables	Univariate analysis				Multivariate analysis			
	HR	HR 95% low	HR 95% high	*P* value	HR	HR 95% low	HR 95% high	*P* value
Age	0.996	0.978	1.015	0.678	1.001	0.982	1.019	0.940
Gender	0.770	0.471	1.257	0.296	0.830	0.476	1.449	0.513
Grade	1.023	0.739	1.415	0.892	1.069	0.744	1.537	0.719
Stage	2.077	1.599	2.696	0.000	0.970	0.349	2.699	0.954
T	1.990	1.564	2.532	0.000	1.847	0.735	4.638	0.192
M	4.294	1.342	13.742	0.014	1.263	0.331	4.821	0.732
N	2.246	0.547	9.219	0.261	2.339	0.393	13.906	0.350
Risk score	1.372	1.267	1.486	6.38E-15	1.332	1.219	1.455	2.16E-10

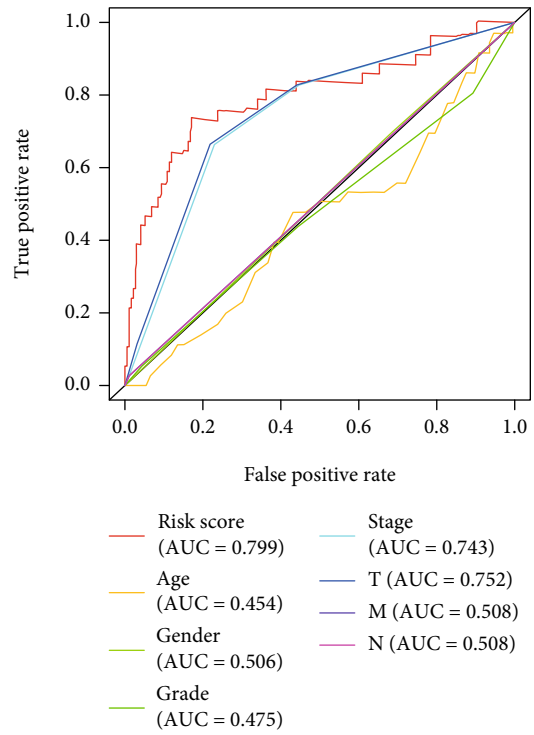

Figure 4: ROC curves evaluated the prognostic performance of the HCC prognostic model.

confirmed that these key hypoxia-related lncRNAs were associated with the progress of HCC. ROC analysis indicated that the 10 key hypoxia-related lncRNA signatures can be a good indicator for the prognosis of HCC.

Among the 10 key hypoxia-related lncRNAs found in HCC, AL365203.2 has been reported in previous studies as autophagy-related lncRNA, epithelial-mesenchymal transition-related lncRNA, and immune-related lncRNA to participate in the progress of HCC [28–30]. It was reported that AC015908.3 was also involved in the regulation of HCC cells' stemness, which was closely related to drug resistance and poor prognosis of HCC [28–30]. MSC-AS1 can promote HCC oncogenesis via inducing the expression of phosphoglycerate kinase1 [31]. AC145207.5, AL031985.3, and PRRT3-AS1 participated in the infiltration of immune cells, which was associated with immunotherapy response in patients with HCC [30, 32]. AL117336.3 and AC009005.1 can also regulate the process of autophagy and participate in the occurrence and development of HCC [28, 32]. TMEM220-AS1 has been demonstrated to suppress HCC by regulating the miR-484/MAGI1 axis as a competing endogenous RNA [28, 33]. THUMPD3-AS1 has been reported to be associated with the prognosis of non-small-cell lung cancer and HBV-related HCC [34, 35].

In addition, we also used PCA to study the different distribution patterns between the high-risk and low-risk groups based on the expression sets of key hypoxia-related lncRNAs for constructing the risk scoring model and all hypoxia-related lncRNAs. According to the gene sets of the two hypoxia-related lncRNAs, patients in the high-risk and low-risk groups were clearly divided into two parts, and the hypoxia risk score of the low-risk group

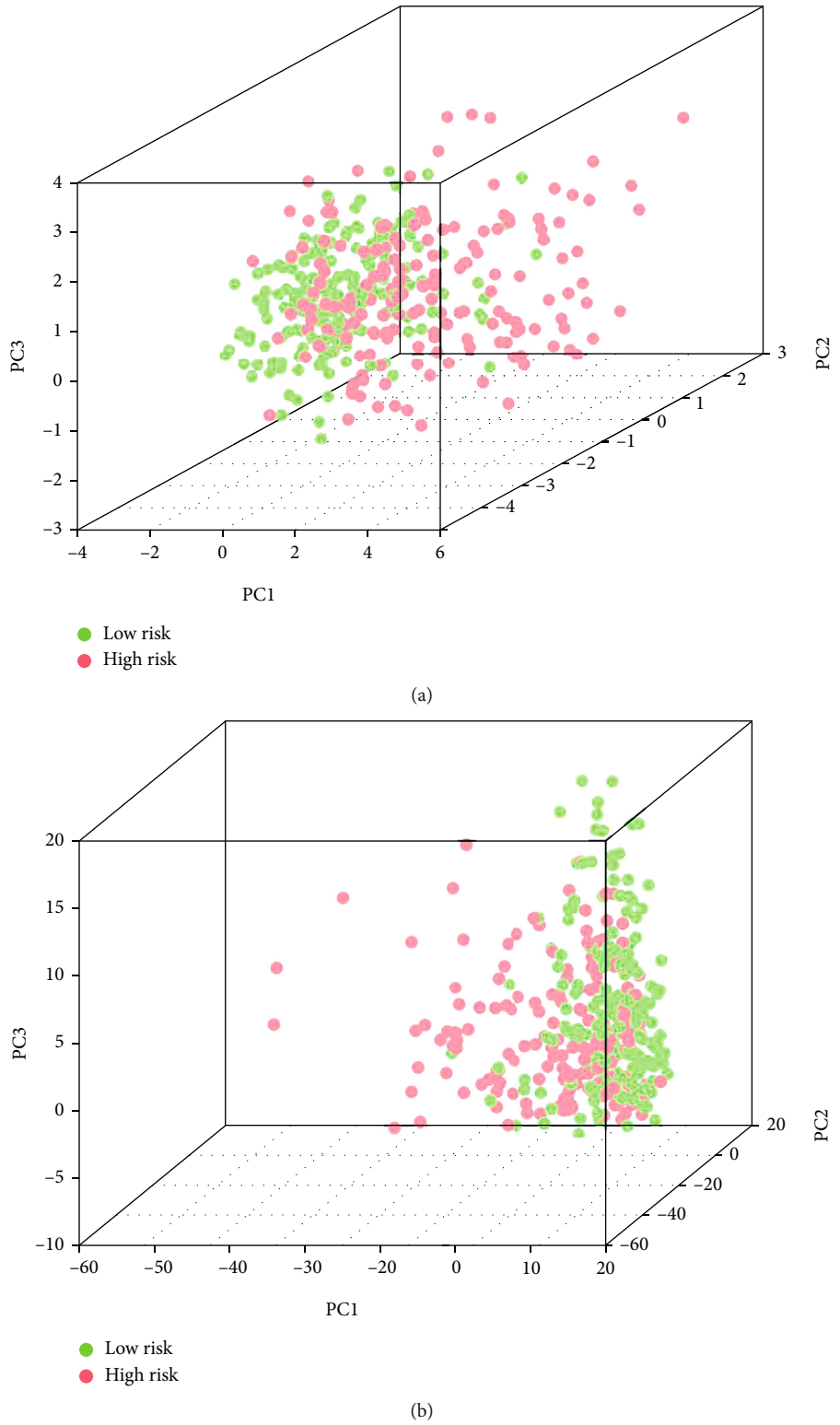

Figure 5: Principal component analysis (PCA). (a) The PCA of high-risk and low-risk groups based on the 10 key hypoxia-related lncRNAs constructed the prognostic model. (b) The PCA of high-risk and low-risk groups based on all hypoxia-related lncRNAs.

was lower than that of the high-risk group. GSEA showed that hypoxia-related phenotypes were abundant in high-risk patients. These results suggest that the prognostic model based on the 10 key hypoxia-related lncRNAs can help identify high-risk patients from patients with the same clinical or molecular characteristics, make accurate judgments on the prognosis of patients, and thus achieve individualized treatment.

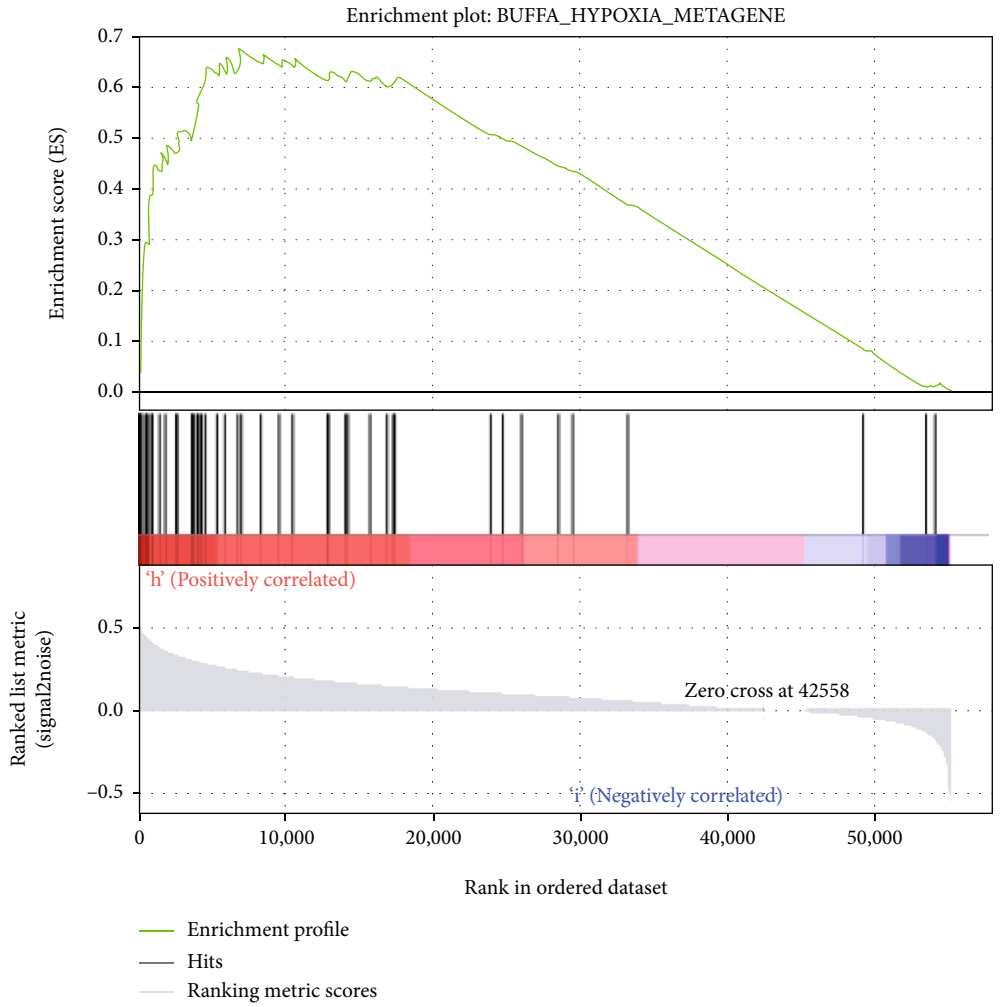

Figure 6: Gene set enrichment analysis (GSEA) of the hypoxia-related lncRNAs.

However, the current study has the following limitations that need to be acknowledged. Firstly, we failed to find an available independent lncRNA dataset to verify the usefulness of the prognostic model. Secondly, the samples in this study mainly come from international databases, lacking our own samples to verify the model. Thirdly, we just screened out 10 hypoxia-related lncRNAs that were associated with the prognosis of HCC by a series of bioinformatics method; further in vivo and in vitro experiments are needed to explore their potential mechanisms affecting the prognosis of HCC.

In conclusion, this study identified 10 key hypoxia-related lncRNAs that were associated with the prognosis of HCC by a series of bioinformatics methods based on the TCGA database, indicating that hypoxia-related lncRNAs have potential prognostic value for HCC patients and it may provide a new target for the treatment of HCC.

Data Availability

The data used to support the findings of this study are included in the article.

Conflicts of Interest

No potential conflicts of interest need to be declared.

Authors' Contributions

Lan Jiang and Huacheng Li equally contributed to the work.

References

[1] J. M. Llovet, F. Castet, M. Heikenwalder et al., "Immunotherapies for hepatocellular carcinoma," *Nature Reviews. Clinical Oncology*, vol. 19, no. 3, pp. 151–172, 2022.

[2] J. C. Nault and A. Villanueva, "Biomarkers for hepatobiliary cancers," *Hepatology*, vol. 73, Suppl 1, pp. 115–127, 2021.

[3] I. D. Kyrochristos, D. E. Ziogas, and D. H. Roukos, "Dynamic genome and transcriptional network-based biomarkers and drugs: precision in breast cancer therapy," *Medicinal Research Reviews*, vol. 39, no. 3, pp. 1205–1227, 2019.

[4] F. Yin, L. Shu, X. Liu et al., "Microarray-based identification of genes associated with cancer progression and prognosis in hepatocellular carcinoma," *Journal of Experimental & Clinical Cancer Research*, vol. 35, no. 1, p. 127, 2016.

[5] X. X. Xiong, X. Y. Qiu, D. X. Hu, and X. Q. Chen, "Advances in hypoxia-mediated mechanisms in hepatocellular carcinoma," *Molecular Pharmacology*, vol. 92, no. 3, pp. 246–255, 2017.

[6] L. H. Gray, A. D. Conger, M. Ebert, S. Hornsey, and O. C. Scott, "The concentration of oxygen dissolved in tissues at the time of irradiation as a factor in radiotherapy," *The British Journal of Radiology*, vol. 26, no. 312, pp. 638–648, 1953.

[7] N. Nishida and M. Kudo, "Oxidative stress and epigenetic instability in human hepatocarcinogenesis," *Digestive Diseases*, vol. 31, no. 5-6, pp. 447–453, 2013.

[8] X. Z. Wu, G. R. Xie, and D. Chen, "Hypoxia and hepatocellular carcinoma: the therapeutic target for hepatocellular carcinoma," *Journal of Gastroenterology and Hepatology*, vol. 22, no. 8, pp. 1178–1182, 2007.

[9] K. Graham and E. Unger, "Overcoming tumor hypoxia as a barrier to radiotherapy, chemotherapy and immunotherapy in cancer treatment," *International Journal of Nanomedicine*, vol. Volume 13, pp. 6049–6058, 2018.

[10] J. T. Erler and A. J. Giaccia, "Lysyl oxidase mediates hypoxic control of metastasis," *Cancer Research*, vol. 66, no. 21, pp. 10238–10241, 2006.

[11] S. S. Zheng, X. H. Chen, X. Yin, and B. H. Zhang, "Prognostic significance of HIF-1alpha expression in hepatocellular carcinoma: a meta-analysis," *PLoS One*, vol. 8, no. 6, article e65753, 2013.

[12] C. Mendez-Blanco, F. Fondevila, A. Garcia-Palomo, J. Gonzalez-Gallego, and J. L. Mauriz, "Sorafenib resistance in hepatocarcinoma: role of hypoxia-inducible factors," *Experimental & Molecular Medicine*, vol. 50, no. 10, pp. 1–9, 2018.

[13] A. Fatica and I. Bozzoni, "Long non-coding RNAs: new players in cell differentiation and development," *Nature Reviews. Genetics*, vol. 15, no. 1, pp. 7–21, 2014.

[14] A. Bhan, M. Soleimani, and S. S. Mandal, "Long noncoding RNA and cancer: a new paradigm," *Cancer Research*, vol. 77, no. 15, pp. 3965–3981, 2017.

[15] Y. N. Chang, K. Zhang, Z. M. Hu et al., "Hypoxia-regulated lncRNAs in cancer," *Gene*, vol. 575, no. 1, pp. 1–8, 2016.

[16] M. Huang, H. Wang, X. Hu, and X. Cao, "lncRNA MALAT1 binds chromatin remodeling subunit BRG1 to epigenetically promote inflammation-related hepatocellular carcinoma progression," *Oncoimmunology*, vol. 8, no. 1, article e1518628, 2019.

[17] J. Ahodantin, M. Bou-Nader, C. Cordier et al., "Hepatitis B virus X protein promotes DNA damage propagation through disruption of liver polyploidization and enhances hepatocellular carcinoma initiation," *Oncogene*, vol. 38, no. 14, pp. 2645–2657, 2019.

[18] J. U. Marquardt, P. R. Galle, and A. Teufel, "Molecular diagnosis and therapy of hepatocellular carcinoma (HCC): an emerging field for advanced technologies," *Journal of Hepatology*, vol. 56, no. 1, pp. 267–275, 2012.

[19] H. B. El-Serag and K. L. Rudolph, "Hepatocellular carcinoma: epidemiology and molecular carcinogenesis," *Gastroenterology*, vol. 132, no. 7, pp. 2557–2576, 2007.

[20] T. Couri and A. Pillai, "Goals and targets for personalized therapy for HCC," *Hepatology International*, vol. 13, no. 2, pp. 125–137, 2019.

[21] W. R. Wilson and M. P. Hay, "Targeting hypoxia in cancer therapy," *Nature Reviews. Cancer*, vol. 11, no. 6, pp. 393–410, 2011.

[22] R. Miao, C. Ge, X. Zhang et al., "Combined eight-long noncoding RNA signature: a new risk score predicting prognosis in elderly non-small cell lung cancer patients," *Aging (Albany NY)*, vol. 11, no. 2, pp. 467–479, 2019.

[23] Y. Liu, L. Wang, H. Liu, C. Li, and J. He, "The prognostic significance of metabolic syndrome and a related six-lncRNA signature in esophageal squamous cell carcinoma," *Frontiers in Oncology*, vol. 10, p. 61, 2020.

[24] Y. Shen, X. Peng, and C. Shen, "Identification and validation of immune-related lncRNA prognostic signature for breast cancer," *Genomics*, vol. 112, no. 3, pp. 2640–2646, 2020.

[25] Z. Huang, J. K. Zhou, Y. Peng, W. He, and C. Huang, "The role of long noncoding RNAs in hepatocellular carcinoma," *Mol Cancer*, vol. 19, no. 1, p. 77, 2020.

[26] L. J. Lim, S. Y. S. Wong, F. Huang et al., "Roles and regulation of long noncoding RNAs in hepatocellular carcinoma," *Cancer Research*, vol. 79, no. 20, pp. 5131–5139, 2019.

[27] H. Choudhry, A. L. Harris, and A. McIntyre, "The tumour hypoxia induced non-coding transcriptome," *Molecular Aspects of Medicine*, vol. 47-48, pp. 35–53, 2016.

[28] Y. Jia, Y. Chen, and J. Liu, "Prognosis-predictive signature and nomogram based on autophagy-related long non-coding RNAs for hepatocellular carcinoma," *Frontiers in Genetics*, vol. 11, p. 608668, 2020.

[29] B. H. Xu, J. H. Jiang, T. Luo, Z. J. Jiang, X. Y. Liu, and L. Q. Li, "Signature of prognostic epithelial-mesenchymal transition related long noncoding RNAs (ERLs) in hepatocellular carcinoma," *Medicine Baltimore*, vol. 100, no. 30, article e26762, 2021.

[30] P. Zhou, Y. Lu, Y. Zhang, and L. Wang, "Construction of an immune-related six-lncRNA signature to predict the outcomes, immune cell infiltration, and immunotherapy response in patients with hepatocellular carcinoma," *Frontiers in Oncology*, vol. 11, p. 661758, 2021.

[31] C. Cao, Q. Zhong, L. Lu et al., "Long noncoding RNA MSC-AS1 promotes hepatocellular carcinoma oncogenesis via inducing the expression of phosphoglycerate kinase 1," *Cancer Medicine*, vol. 9, no. 14, pp. 5174–5184, 2020.

[32] W. Kong, X. Wang, X. Zuo, Z. Mao, Y. Cheng, and W. Chen, "Development and validation of an immune-related lncRNA signature for predicting the prognosis of hepatocellular carcinoma," *Frontiers in Genetics*, vol. 11, p. 1037, 2020.

[33] H. Wu, T. Liu, J. Qi, C. Qin, and Q. Zhu, "Four autophagy-related lncRNAs predict the prognosis of HCC through coexpression and ceRNA mechanism," *BioMed Research International*, vol. 2020, Article ID 3801748, 2020.

[34] X. Zhao, Z. Bai, C. Li, C. Sheng, and H. Li, "Identification of a novel eight-lncRNA prognostic signature for HBV-HCC and analysis of their functions based on coexpression and ceRNA networks," *BioMed Research International*, vol. 2020, Article ID 8765461, 2020.

[35] J. Hu, Y. Chen, X. Li et al., "THUMPD3-AS1 is correlated with non-small cell lung cancer and regulates self-renewal through miR-543 and ONECUT2," *Oncotargets and Therapy*, vol. 12, pp. 9849–9860, 2019.

Hindawi
Journal of Nanomaterials
Volume 2022, Article ID 3425297, 10 pages
https://doi.org/10.1155/2022/3425297

Review Article

Nanomaterial-Based Prosthetic Limbs for Disability Mobility Assistance: A Review of Recent Advances

Qiaoyin Tan,[1] Cuicui Wu,[2] Lei Li,[2] Weide Shao ,[2] and Min Luo [3,4]

[1]*College of Teacher Education, Zhejiang Normal University, Jinhua, Zhejiang 321004, China*
[2]*College of Physical Education and Health Sciences, Zhejiang Normal University, Jinhua, Zhejiang 321004, China*
[3]*Department of Nephrology, The Second Xiangya Hospital, Central South University, Changsha, 410011 Hunan Province, China*
[4]*Department of Rehabilitation Medicine and Health Care, Hunan University of Medicine, Huaihua, 418000 Hunan Province, China*

Correspondence should be addressed to Weide Shao; txsh@zjnu.cn and Min Luo; xyluomin@csu.edu.cn

Received 24 February 2022; Revised 8 March 2022; Accepted 9 March 2022; Published 31 March 2022

Academic Editor: Weiguo Li

The emergence of new hybrid nanomaterial has enabled prosthetic devices to have more performance and significantly improved the quality of life of the disabled. Due to the biosensing properties of prosthetic limbs made of nanomaterials, a large number of nanocomposites have been designed, developed, and evaluated for various prosthetic limbs, such as e-skin, e-skin's neurotactility sensing, human prosthetic interface tissue engineering, bones, and biosensors. Nano-based materials are also considered to be the new generation of scientific and technological materials for the preparation of various prosthetic devices for the disabled, which can effectively improve the sense of use of the disabled and achieve functional diversity. The study described various nanomaterials for prosthetic devices, and introduced some basic components of nanocomposites; their applications are in three areas, such as bone, skin, and nerve, and evaluated and summarized the advantages of these applications. The results show that (1) carbon-based nanomaterials as neural materials have been studied most deeply. Due to that strong stability of the carbon-based material and the simple transmission mechanism, the cost can be controlled in manufacturing the artificial limb. Materials with human-computer interaction function are the research focus in the future. (2) Skin nanomaterials are mainly composite materials, generally containing metal- and carbon-based materials. Ionic gels, ionic liquids, hydrogels, and elastomers have become the focus of attention due to the sensitivity, multimodal, and memory properties of their materials. (3) Outstanding nanomaterials for bone are fibrous materials, metallic synthetic materials, and composite materials, with extremely high hardness, weight, and toughness. Of the skeletal materials, the choice of prosthetic socket material is the most important and is typically based on fiber laminate composites. Some of these materials make sensors for durability and performance that can be used for large-scale clinical testing.

1. Introduction

Since the emergence of nanotechnology, the application of nanomaterials in wearing aids and sports prosthetic limbs has been the focus of attention of researchers in the field of disability sports. As nanomaterials have different electrical, magnetic, thermal, mechanical, and other properties from common materials, they are currently used by a large number of scholars in the field of prosthesis manufacturing [1]. Prosthetic limbs used by persons with disabilities to assist movement include mechanical prosthetic limbs (ordinary materials), electric prosthetic limbs (nanomaterials), and myoelectric prosthetic limbs (nanomaterials). According to research, artificial limbs made of traditional materials are stiff, expensive, and not easy to handle [2]. The users of artificial limbs made of traditional materials can only rely on the uncomfortable tactile information between the residual limb and the ground. As a result, the risk of falling is increased, and the activity ability is limited. Artificial limbs are considered to increase cognitive burden of the brain caused by foreign objects in the movement. As a result, many psychological troubles and problems of giving up artificial

Table 1: The generation and use of neural material.

Material name	Generation method	Function	Advantage	Reference
Graphene	3D structure making (1) Template orientation (2) Self-assembly (3) Electrospinning and 3D printing	The piezoresistive sensor made of 3D graphene shows good potential in electronic skin and other aspects	(1) Simple Preparation (2) Simple readout mechanism (3) Low power consumption (4) Convenient signal acquisition	[14]
Carbon-based materials, inorganic nanomaterials	NM	Detectable index (1) Body movements (2) Body temperature (3) Respiratory rate (4) Heart rate and blood pressure (5) Electrophysiological signals	(1) Stretchability (2) Ultrathin and conformal (3) Biocompatibility (4) Biodegradability	[12]
Carbon nanoparticle material	Integrate nano-additive from 0 to 3.5%	Experimental, artificial neural network techniques were used to calculate the strain-time relationships of prosthetic and orthotic composites of carbon nanoparticle materials	For the nanoparticle-reinforced composite, the mechanical properties and creep properties can be up to 5 times	[9]
Carbon nanotube polyester wire	A bionic electronic nerve sensor with high tensile and deformation insensitivity is made of a composite material of polyester wires coated with carbon nanotubes	Bionic electronic exogenous nerve sensor has great potential in some fields, such as human-computer interaction	(1) High stretchability (2) Deformation insensitive (3) Excellent stability (4) Rapid response (5) High robustness (6) Geometric layered sensing (7) Cutability	[13]
Metal polymer carbon material (metal-polymer mixture)	Implantable device	(1) Prosthetic limbs for pain relief (2) Sports prosthesis (3) Cognitive nerve prosthesis	By reducing the difference between the soft tissue and the electrode, the polymer portion can adjust the metal modulus	[8]
NiCo (nickel-cobalt) nanoparticles	Obtaining nickel-cobalt nanoparticles by chemical reduction on multiwalled carbon nanotubes	(1) Make sensor (2) Realize automatic detection (3) Automatic control	(1) High stability (2) High sensitivity (3) Reproducibility (4) Low detection limit	[15]
Proanthocyanidins/reduced graphene oxide (PC/rGO), glycerol-plasticized polyvinyl alcohol-borax (PVA-borax) hydrogel	The proanthocyanidin/reduced graphene oxide (PC/rGO) composite was introduced into glycerol-plasticized polyvinyl alcohol-borax (PVA-borax) hydrogel, and the bionic tactile PC/rGO/PVA hydrogel was obtained	(1) It can imitate and detect skin epidermal movements, such as facial expression changes and finger bending (2) Simulate the tactile ability of natural skin through hydrogel	(1) Stretchability (2) Immediate and complete self-healing (3) High strain sensitivity	[17]
Hydrogel	NM	(1) The human body movement monitoring (2) Artificial tissues or artificial limbs	(1) Biocompatibility and degradability, antibacterial (2) Heat protection and antifreeze (3) Stretchability and compressibility (4) Dynamic durability	[16]
Ion gel gated organic synaptic transistor (IGOST)	Crossbar array simulation Sensor integration	Artificial auditory nerve with short-term attenuation and artificial neural network with long-term memory	Synaptic attenuation of IGOST is relatively easy to regulate	[18]

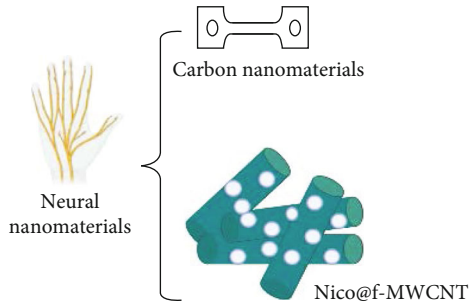

Figure 1

limbs have become the major causes of burden [3]. The combination of biomedicine and material science has led to the emergence of new hybrid nanomaterials that meet the needs of ideal prosthetic limbs. Prosthetic limbs made of nanomaterials can significantly improve the quality of life of the disabled due to their unique and more capabilities.

Due to the biosensing nature of prosthetic limbs made of nanomaterials, there are different components based on the use of polymer nanocomposites in prosthetic limbs. In these components, the functional stretchable composite structures are mainly manufactured by using conductive nanofillers in an insulating or conductive polymer matrix [4]. Conductive polymers such as carbon-based composites and structures include carbon black (CB), carbon nanotubes (CNT), carbon fibers, graphene sheets, and graphene oxides. Other conductive fillers such as metal nanowires, nanoparticles, ionic liquids, and Mxenes are also quite common. In addition, polymers such as polydimethylsiloxane (PDMS), polyurethane (PU), thermoplastic polyurethane (TPU), ecoflex, polyimide (PI), natural rubber, polypropylene, polypyrrole, and polyethylene terephthalate can be used as materials in the flexible matrix to maintain the nanofiller interface. Conductive polymers, such as poly (3, 4-ethylenedioxythiophene):-poly (styrene sulfonate) (PEDOT:PSS) and polyaniline, are also used in functional nanocomposite to support conductive networks [5]. In summary, in functional nanocomposites, the nanofillers impart functional sensing properties, while the polymer matrix supports a conductive network configuration. Some of these materials make sensors for durability and performance that can be used for large-scale clinical testing [6].

In recent years, a large number of nanocomposites have been designed, developed, and evaluated for various prosthetic prostheses, such as e-skin, e-skin's neurotactility sensing, human prosthetic interface tissue engineering, bones, and biosensors. Nano-based materials are also considered to be the new generation of scientific and technological materials for the preparation of various prosthetic devices for the disabled, which can effectively improve the sense of use of the disabled and achieve functional diversity. Prosthetic limbs made of nanocomposites enable patients to engage in more demanding recreational activities such as running [7]. Today, the use of most nanomaterials holds promise for a variety of prosthetic applications. The study described various nanomaterials for prosthetic devices and introduced some basic components of nanocomposites; their applications are in three areas, such as bone, skin, and nerve, and evaluated and summarized the advantages of these applications.

2. Classification and Application of Tissue Material

2.1. Neural Material. As shown in Table 1, nanomaterials used to manufacture prosthetic nerve sensors are carbon-based materials, metal nanomaterials, metal-polymer mixtures, hydrogels, and the like [8]. As shown in Table 1, carbon-based nanomaterials perform well in creep resistance, and nanoparticle-reinforced composites creep more easily than carbon nanoparticle materials, affecting the useful life of prosthetic limbs [9]. Bionic electronic exogenous nerve sensor can achieve monitor physiological indexes [10] and feel the body movements; the role of the transmission of electrophysiological signals [11], such as additional wearable devices, body temperature, respiratory rate, heart rate, and blood pressure, can also be tested [12]. The neural sensor can be applied to the surface layer of the skin and can also be used for nerve signal transmission inside limbs. When used for the nerve signal transmission of the skin's surface layer, the carbon nanotube polyester thread of the carbon-based material is highly stretchable and insensitive to deformation, and has excellent stability (> 15,000 cycles test), rapid response (≤ 15 ms), high robustness, geometric layered sensing, and personalized cuttability [13]. In addition, there are 3D graphene-based piezoresistive sensors, which show good performance in electronic skin. It comes from electrospinning and 3D printing because of its simple preparation and readout. It is considered as a promising flexible sensor due to its simple mechanism, low power consumption, and convenient signal acquisition [14].

The neural sensor can also use metal nanomaterial, such as NiCo nanoparticles (as shown in Figure 1), which are derived from that nickel-cobalt nanoparticles obtained on the functionalized multiwall carbon nanotubes by a chemical reduction method and have higher stability, high sensitivity, repeatability, and low detection limit [15]. In terms of the combination of metal polymers and carbon nanomaterials, the polymer part can adjust the metal modulus, and the material can reduce the difference between soft tissues and electrodes and improve the function of prosthetic limbs. In addition, the emerging hydrogel material is also one of the nerve manufacturing options. As an artificial tissue or artificial limb into which bioelectronics can be implanted, it possesses biocompatibility, biodegradability, and antibacterial property. It also protects against heat and freezing and takes a long time to recover. Tensile, compressive, dynamic durability, and strain sensitivity are stronger than other materials [16]. For example, the proanthocyanidin/reduced graphene oxide (PC/rGO) composite material with a neural-like nanonetwork is introduced into a glycerol-plasticized polyvinyl alcohol-borax (PVA-borax) hydrogel system to obtain a bionic tactile PC/rGO/PVA hydrogel [17]. It can simulate and control some real epidermal movements controlled by nerves, such as finger bending and facial expression changes, and can simulate the tactile ability through the layered design

Table 2: The generation and use of skin material.

Material name	Generation method	Function	Advantage	Reference
Cross-linked gold nanoparticles	Using inkjet printing and scalable microforming technology	Prosthetic artificial skin	(1) Physical flexibility (2) Sensitivity	[20]
Polydimethylsiloxane (PDMS) zinc (ZnO) nanorods	The top and bottom electrode layers are interlocked by zinc oxide (ZnO) nanorods grown vertically on top of the PDMS to improve the sensitivity of the contact force and ambient temperature measurements	(1) A tactile sensor array was successfully fabricated and will be applied to (e-skin) (2) Tactile sensors can be used for flexible interfaces, wearable devices, and bionic robot skin	(1) High sensitivity (2) Flexibility (3) Measurable temperature	[21]
Silver nanowire @ polyurethane scaffold Carbon fiber active composite material	A tactile sensor was made by combining silver nanowires @ polyurethane scaffolds with layered carbon fabrics	The actual fingertip events can be transformed into visual or auditory interactive feedback in virtual reality	(1) Mechanical feeling range can be enhanced > 100% (2) High sensitivity (3) Fast response time 4 Repeatability	[23]
Carbon nanotubes (CNT) Film and polyacrylonitrile (PAN)	Use an electrostatic spinning process	The multimodal sensing capability is developed in the electronic skin for soft robots, intelligent artificial	(1) CNT strong, flexible, stretchable (2) PAN material can withstand thousands of cycles with little effect on the output signal	[25]
Carbon materials (carbon black (CB), carbon nanotubes (CNT), carbon fibers, graphene sheets, and graphene oxide)	Made from conductive nanofillers in an insulating or conductive polymer matrix	(1) Human motion detection (2) Soft robot (3) Smart textiles	(1) This is the most widely studied nanocomposite material (2) Low cost and available volume	[5]
Thermoelectric clays made of carbon nanotubes (CNT) and nonionic surfactants	Reconfigurable thermoelectric clay made of carbon nanotubes and viscous additives create a skin-compatible thermoelectric patch for e-skin	(1) To prevent hammering or even piercing (2) Used for skin adaptive semipermanent power supply with mechanical durability	(1) Skin suitability and mechanical durability (2) Very soft, stretchable, and repairable	[26]
Vertical graphene array (VGA)	A vertical graphene array (VGA) was fabricated directly on the surface of the natural latex film	E-skin can be used in soft robot, artificial limbs, wearable equipment, etc.	The electronic skin has multifunctional tactile perception of object pressure and surface morphology and also has noncontact sensing characteristics for temperature difference between the detected object and the electronic skin, including ultrafast response, elasticity, high sensitivity, and strong cyclicity	[27]
Laser-induced graphene (LIG) on polyimide film	The honeycomb electronic skin with laser-induced graphene (LIG) was prepared by one-step carbonization of polyimide film	(1) Promote carbon-based electronic skin with a large area array pattern (2) The e-skin has great potential for artificial intelligence, the universal touch of robots, and prosthetic limbs	(2) Strain sensitivity (2) It has excellent mechanical properties and high dyeing sensitivity (3) This kind of e-skin shows the perception ability and subtle touch to a wide range of human activities	Wei, Liu [28]
HCl-doped poly (o-methylaniline) (POMANI)-Mn 3O4 thin film nanocomposites	(1) Split using OP-AMP method (2) Shunting by logarithmic amplifier method	(1) Sensing prosthesis temperature (2) For prosthetic applications (3) Manufacture of conformal temperature sensors for prosthetic gloves/hands	(1) This nanocomposite sensor has consistency and flexibility (2) Various linearization methods have been analyzed to find the best output	[31] [30]

Table 2: Continued.

Material name	Generation method	Function	Advantage	Reference
Carrageenan and locust bean gum (hydrogel)	Photo-crosslinking of acrylamide provides an elastomeric matrix that is functionally modified with carrageenan and locust bean gum by physical crosslinking with K2CO3	The hydrogel-based soft controller is used for potential bionic skin of artificial limb human-computer interaction control	(1) The hydrogel has high elasticity (2) Recovers immediately after stretching to 500% or compressing to 10% of its original length (3) It can still maintain its flexibility and conductivity at low temperature	
Ionic gel, ionic liquids, hydrogel, and elastomers ITS	NM	Mimics human skin, such as anisotropic structures, mechanical behavior, and tactile function, and even includes mechanically sensitive ion channels critical for human tactile sensation	It has advantages in sensitivity, response speed, and multimode sensing, especially the development of electrochromism	[29]
Silane and keratin derivatives	A percutaneous bone-integrated prosthesis (POP) consists of a metal post attached to bone that extends outwardly through the skin to connect to an external prosthesis	A coating that mimics the composition of human nails	The purified human keratin biomaterial coating is resistant to degradation	[33]
Folded nanocone cluster	Novel microstructures introduce folded nanoclusters, semi-ellipsoids, and folds in different sensors	(1) Wearable equipment (2) Robots (3) In bionic artificial limb	(1) It can provide more complete and accurate interactive information such as gesture recognition and fine tactile discrimination (2) Real-time recording and mapping of multiple mechanical stimuli can be achieved due to independence, high sensitivity, and rapid response	[32]

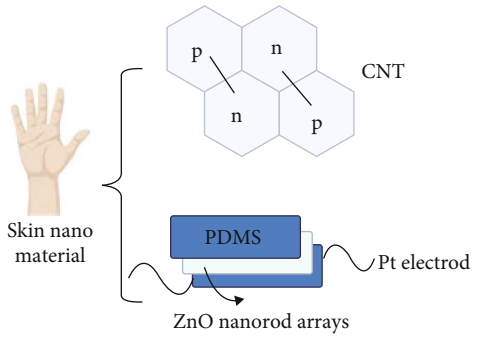

Figure 2

of hydrogel networks. There is also an ion gel gate organic synaptic transistor (IGOST) which can convert biological signals and bet regulate synaptic attenuation to generate an artificial neural network with long-term memory, thus realizing multifunctional neural mimicry application from neural mimicry calculation to neural prosthesis [18].

2.2. Skin Material. As shown in Table 2, nanomaterials for skin are metal materials, carbon-based materials, and other composite materials [5], in general, to make prosthetic limbs more realistic to the touch; air bladders are designed for each nanomaterial layer on the skin surface [19]. Metallic materials generally have advantages in terms of physical flexibility and sensitivity. Cross-linked gold nanoparticles, such as prosthetic skin and using inkjet printing and microforming techniques, can be extended to submillimeter dimensions [20]. Demonstrating high sensitivity, fast response time, and repeatability, in addition to the former, polydimethylsiloxane (PDMS) zinc oxide (ZnO) nanorods also have the ability to measure temperature [21], as shown in Figure 2. The mechanical feel range of smart sensors made of silver nanowire composites can be significantly enhanced > 100% programmatically, translating actual fingertip events into visual or auditory interactive feedback from the electronic device [22]; can be used for designing the intelligent artificial limbs with sensory disability and physical disability; and shows the feasibility and practicability of the design concept with the sense of future science fiction [23].

The research on carbon-based materials is quite extensive and advantageous. Carbon materials (carbon black (CB), carbon nanotubes (CNT), carbon fibers, graphene

Table 3: The generation and use of skeleton material.

Material name	Generation method	Function	Advantage	Reference
Polyester resin (jute, glass, carbon, pearl cotton) fiber	The laminated composite is reinforced with polyester resin as the bonding matrix and with (jute, glass, carbon, pearl cotton) fibers by vacuum bagging technology. The laminate samples were characterized by mechanical tensile tests, such as tensile strength, Young' s modulus, and elongation, and physical tests (density) to measure specific strength and specific modulus	The smoothness of the cross section increases, indicating that the brittle to semiductile transition occurs	Tensile strength reached 162 Mpa and modulus of elasticity reached 3.60 GPa. Specific strength and specific modulus up to 134 MPa. cm^3/gm–2.544 GPa. cm^3/gm	[37]
Composite material made of agave	Cantala fibers (CF) were treated with 6% NaOH and incubated for 0 h (UF), 3 h (AK3), 6 h (AK6), 9 h (AK9), and 12 h (AK12), respectively	Used as prosthetic engineering components to make prosthetic sockets	(1) The best tensile strength was obtained when Kantala fiber was treated with 1 6% NaOH solution (2) Biodegradable, with sufficient strength and power (3) Good mechanical resistance	[35]
Synthetic fibers (carbon, kevlar, and glass)	Made with a constant 5 wt% glass fiber-reinforced epoxy, vinyl ester, and polyester matrix with different jute and jute loading	Widely used as a reinforcing material in the manufacture of artificial limbs	(1) Strength and hardness increase with the increase in the proportion of natural fibers (2) Higher stretching and bending are obtained	[34]
(Carbon, jute, glass, and perlon) fiber-reinforced polyester resin	Different laminated composites, such as fiber-reinforced polymers, are used to make the prosthetic socket	It can be used in prosthetic sockets: devices that connect prosthetic limbs to amputated parts	(1) Bending strength, bending modulus, maximum shear stress, impact strength, fracture toughness (2) Manufacturing prosthetic socket makes wear more comfortable, light weight, high strength, and durable	[36]
MWCNT–(polydimethylsiloxane) PDMS	NM	(1) Development of printable nanocomposite tensile sensor system (2) Low-cost digital method for casting custom prosthetic liners (3) For growth/volume tracking (4) With embedded active cooling system	(1) Cheaper (2) Easier replacement and maintenance	[38]
EBM Ti-6Al-4V implant	The bioactivity and osteogenesis of the 3D-printed Ti-6Al-4V implant were enhanced by constructing layered micro-/nanotopography on the surface	Accelerating 3D printing in the future	NM	[41]
Ti-Ta composites	The Ti-Ta composites with layered structure were prepared by continuous discharge plasma sintering, machining, and annealing. The samples were sintered at 1200°C and then hot rolled at 60% high	Ti-Ta composites can be used in orthopedic applications	The Ti-Ta composite material with bionic structure has high strength, good ductility, low modulus, and good biocompatibility	[40]

Table 3: Continued.

Material name	Generation method	Function	Advantage	Reference
	pressure to exhibit a multiscale-layered microstructure			
Al_2O_3-CaO	It is composed of two materials (Al_2O_3-CaO) and prepared by sol-gel method	These composite materials are used in biological applications such as the manufacture of artificial limbs	(1) Compared with the polymer blend material without adding the nano powder, the mechanical property of the obtained composite material is remarkably improved (2) When different sizes of particles are added, respectively, the tensile property, flexural property and hardness are improved	[42]
High-density polyethylene (HDPE), polyamide (PA) 6 or nylon 6, polyamide (PA) 66	NM	This is the best choice for standing, walking, and running under standard loads	Various loads applied by the patient are supported	[39]

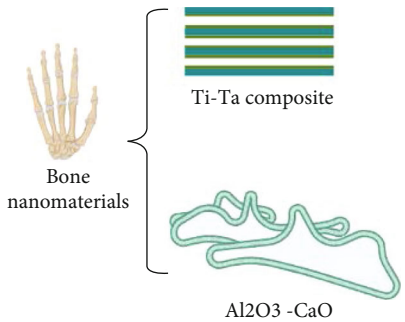

Figure 3

sheets, and graphene oxides) are generally made of conductive nanofillers. In multimode sensing, carbon-based materials have attracted much attention due to their strong sensing ability, durability, and low cost [24]. Synthetic materials such as carbon nanotube (CNT) films and polyacrylonitrile (PAN) are very strong, flexible, and stretchable when used as skin. It can withstand more than 1000 cycles with little effect on the output signal [25]. CNT can also be used with thermoelectric clay made of nonionic surfactant as viscous additive to make skin-adaptive thermoelectric patch for e-skin. It serves as a mechanically durable, skin-compatible, semipermanent power source that prevents hammering and even puncture [26].

Carbon-based nanomaterials are made with films of other materials and have different effects. For example, laser-induced graphene (LIG) was prepared by one-step carbonization of polyimide film [27]. Cellular electronic skin can be made that exhibits strain sensitivity to a wide range of tensile and compressive stimuli. Based on its excellent mechanical properties and high staining sensitivity, this e-skin well demonstrates the perception of a wide range of human activities and subtle tactile sensations. There is also a vertical graphene array (VGA), which is directly fabricated on the surface of a natural latex film using a simple method. It can realize the multifunctional tactile sensation to the pressure, air flow, and surface morphology of the object and can also sense the temperature difference sensing characteristic between the detected object and the electronic skin in a noncontact mode, including ultrafast response (6.7 ms) and elasticity (13.4 ms), wide pressure sensing range (2.5 Pa-1.1 MPa), high sensitivity, and strong cyclicity [28].

With respect to other composite materials, ionic gels, ionic liquids, hydrogels, and elastomers, ITS can mimic human skin, including not only typical anisotropic structures, mechanical behaviors, and tactile functions, but even mechanically sensitive ion channels crucial for human tactile sensation. Breakthrough element advances have been made in the sensitivity, response speed, and multimodal sensing of these materials [29], especially electrochromic breakthrough. Also improved carrageenan and locust bean gum are obtained on an elastic matrix by photo-crosslinking with acrylamide, the hydrogel having high elasticity, a stress of 0.04 MPa at 650% strain, which immediately recovers after stretching to 500%, or compression to 10% of its original length, which still maintains its flexibility and conductivity at a low temperature of -10°C [30]. Cutaneous nerve sensing: HCl-doped poly (o-toluidine) (POMANI)-Mn_3O_4 film nanocomposite material can be used for manufacturing conformal temperature sensors for upper limb hand skin or gloves [31]. In the aspect of receptor fabrication for finer functions, there are novel microstructures that introduce folded nanoclusters, semi-ellipsoids, and folds in different sensors to provide more complete and accurate interactive information to achieve finer functions, such as object manipulation and fine tactile discrimination, and real-time recording and mapping of multiple mechanical stimuli [32]. With respect to prosthetic nails, silane and keratin derivatives can mimic a coating of a human nail component, showing resistance to degradation [33].

2.3. Bone Material. As shown in Table 3, the skeletal material of the prosthetic limb is generally used for support and is therefore required to be particularly rigid. However, due to the need for user experience and the need for light weight, bone nanomaterials used for prosthetic limbs include fiber materials, metal composites, and composites. Fiber materials are generally synthesized by adding natural fibers and other fibers, which can significantly enhance their original properties. They are called reinforced materials. Such as a synthetic fiber made of carbon fiber, Kevlar fiber, and glass fiber, after adding a lot of jute fiber, strength and hardness increase with the increase in the proportion of natural fiber and also get higher tensile and bending ability [34]. This fibrous material is commonly used in prosthetic sockets, which are devices that connect prosthetic limbs to amputated parts. Among the skeletal materials, the choice of prosthetic socket material is of prime importance because it determines the user's experience. The bending strength, maximum shear stress, impact strength, and fracture toughness of the prosthetic socket can be enhanced with different laminated composites (fiber reinforced polymers). Agave fibers have biodegradability, sufficient strength and power, and good mechanical resistance [35], which are generally used as prosthetic engineering components, making prosthetic socket. Fiber-reinforced polyester resin, such as carbon, jute, glass, and perlon, can make prosthetic socket wear more comfortable, light weight, high strength, and durable [36]. Fiber laminate composites are very durable and are reinforced with polyester resin as the bonding matrix and with (jute, glass, carbon, pearl cotton) fibers by vacuum bagging. Upon mechanical stretching, the smoothness of its cross section automatically changes from brittle to semiductile [37].

Prosthetic sockets have cheaper options, such as MWCNT–(polydimethylsiloxane) PDMS, as a composite material that can be used to make prosthetic socket pads for embedded tensile sensors, active cooling systems, and at lower cost [38]. Composites for bones are high-density polyethylene (HDPE), polyamide (PA) 6 or nylon 6, and polyamide (PA) 66, which are the best choice considering standard loads for standing, walking, and running [39].

The metallic material is generally a Ti-Ta composite, sintered at 1200°C, and then hot rolled at a height of 60% reduction, which exhibits a multiscale-layered microstructure [40], as shown in Figure 3. It has a good bearing application prospect in orthopedics, such as EBM Ti-6Al-4V [41]; Ti-Ta composites with bionic structure have high strength, good ductility, low modulus, and good biocompatibility. Other high hardness bone materials include Al_2O_3-CaO composite nanoparticles, which can also significantly improve the tensile properties, flexural properties, and hardness [42].

3. Conclusion

The realization of the vast functions of the intelligent limb cannot be separated from various nanomaterials. When manufacturing an intelligent prosthetic limb, the selection of materials for each part is crucial. The results have shown that (1) carbon-based nanomaterials have been studied most deeply when they are used for neural materials. Because carbon-based material has strong stability and has simple transmission mechanism, the cost can be controlled when being use for manufacturing the artificial limb. Materials with the function of man-machine interaction are the focus of future research. (2) The nanomaterials for skin are mainly composite materials and generally contain metal- and carbon-based materials. Ionic gels, ionic liquids, hydrogels, and elastomers have been the focus of attention due to the sensitivity, multimodal, and memory properties of the materials. (3) Outstanding nanomaterials for bones are fiber materials, metal synthetic materials, and composite materials, with extremely high hardness, weight, and toughness. Of the skeletal materials, the choice of prosthetic socket material is the most important and is generally dominated by fiber laminate composites.

To date, the use of most nanomaterials in the manufacture of prosthetic limbs has been derived from limited experimentation. Due to the extraction process, manufacturing cost, stability, and other reasons, some parts have not yet been put into the actual production of prosthetic limbs. Therefore, the industry needs more relevant research, including specific material update iterations, generation of new functions (not only at the theoretical level), and disability motor function recovery data to finally verify the effectiveness and practicability of these nanomaterials. It is hoped that in the future, more materials can be applied to nanomaterials for artificial limbs, and the nanomaterials are more practical, environment-friendly, and cost-effective.

Conflicts of Interest

The authors declare that the research was conducted in the absence of any commercial or financial relationships that could be construed as a potential conflict of interest.

Authors' Contributions

The manuscript was written through the contributions of all authors. All authors have read and agreed to the published version of the manuscript.

References

[1] M. S. Hasnain, S. A. Ahmad, M. A. Minhaj, T. J. Ara, and A. K. Nayak, "6-Nanocomposite materials for prosthetic devices," in *Applications of Nanocomposite Materials in Orthopedics*, A. M. A. Inamuddin and A. Mohammad, Eds., pp. 127–144, Woodhead Publishing, Cambridge, England, 2019.

[2] E. Gashawtena, B. Sirahbizu, and A. Kidane, "Review on alternate materials for producing low cost lower limb prosthetic socket," *Journal of Material Sciences & Engineering*, vol. 10, no. 6, 2021.

[3] G. Valle, G. Preatoni, and S. Raspopovic, "Chapter 9-Connecting residual nervous system and prosthetic legs for sensorimotor and cognitive rehabilitation," in *Somatosensory Feedback for Neuroprosthetics*, B. Güçlü, Ed., pp. 293–320, Academic Press, Salt Lake City,Utah,USA, 2021.

[4] Y. Chen and T. J. Webster, "9-Nanostructured biomaterials for artificial tissues and organs," in *Biomaterials for Artificial*

Organs, M. Lysaght, Ed., pp. 236–269, Woodhead Publishing, Cambridge, England, 2011.

[5] M. A. U. Khalid and S. H. Chang, "Flexible strain sensors for wearable applications fabricated using novel functional nanocomposites: a review," *Composite Structures*, vol. 284, article 115214, 2022.

[6] E. J. Weathersby, J. C. Cagle, B. G. Larsen, K. M. Henrikson, and J. E. Sanders, "Development of a magnetic composite material for measurement of residual limb displacements in prosthetic sockets," *Journal of Rehabilitation and Assistive Technologies Engineering*, vol. 5, 2018.

[7] H. K. Talla, J. K. Oleiwi, and A. K. F. Hassan, "Performance of athletic prosthetic feet made of various composite materials with PMMA matrix: numerical and theoretical study," *Revue des Composites et des Matériaux Avancés*, vol. 31, no. 4, pp. 257–264, 2021.

[8] P. Zarrintaj, M. R. Saeb, S. Ramakrishna, and M. Mozafari, "Biomaterials selection for neuroprosthetics," *Current Opinion in Biomedical Engineering*, vol. 6, pp. 99–109, 2018.

[9] M. Al-Waily, M. J. Jweeg, Q. H. Jebur, and K. K. Resan, *Creep characterization of various prosthetic and orthotics composite materials with nanoparticles using an experimental program and an artificial neural network*, Materials Today: Proceedings, Amsterdam, Netherlands, 2021.

[10] F. Khoshmanesh, P. Thurgood, E. Pirogova, S. Nahavandi, and S. Baratchi, "Wearable sensors: at the frontier of personalised health monitoring, smart prosthetics and assistive technologies," *Biosensors and Bioelectronics*, vol. 176, article 112946, 2021.

[11] A. Leal-Junior and A. Frizera-Neto, "Soft wearable robots," in *Optical Fiber Sensors for the Next Generation of Rehabilitation Robotics*, A. Leal-Junior and A. Frizera-Neto, Eds., pp. 27–52, Academic Press, 2022.

[12] Z. Lou, L. Wang, K. Jiang, Z. Wei, and G. Shen, "Reviews of wearable healthcare systems: materials, devices and system integration," *Materials Science and Engineering: R: Reports*, vol. 140, article 100523, 2020.

[13] X. Liao, W. Wang, L. Wang et al., "A highly stretchable and deformation-insensitive bionic electronic exteroceptive neural sensor for human-machine interfaces," *Nano Energy*, vol. 80, article 105548, 2021.

[14] M. Cao, J. Su, S. Fan, H. Qiu, D. Su, and L. Li, "Wearable piezoresistive pressure sensors based on 3D graphene," *Chemical Engineering Journal*, vol. 406, article 126777, 2021.

[15] K. Arikan, H. Burhan, R. Bayat, and F. Sen, "Glucose nano biosensor with non-enzymatic excellent sensitivity prepared with nickel–cobalt nanocomposites on f-MWCNT," *Chemosphere*, vol. 291, Part 3, article 132720, 2022.

[16] P. Rahmani and A. Shojaei, "A review on the features, performance and potential applications of hydrogel-based wearable strain/pressure sensors," *Advances in Colloid and Interface Science*, vol. 298, article 102553, 2021.

[17] X. Pan, Q. Wang, P. He et al., "A bionic tactile plastic hydrogel-based electronic skin constructed by a nerve-like nanonetwork combining stretchable, compliant, and self-healing properties," *Chemical Engineering Journal*, vol. 379, article 122271, 2020.

[18] D.-G. Seo, Y. Lee, G. T. Go et al., "Versatile neuromorphic electronics by modulating synaptic decay of single organic synaptic transistor: from artificial neural networks to neuroprosthetics," *Nano Energy*, vol. 65, article 104035, 2019.

[19] M. Buchanan, "Softer skin makes for more realistic touch from artificial limbs," *New Scientist*, vol. 210, no. 2807, p. 14, 2011.

[20] D. Alvares, L. Wieczorek, B. Raguse, F. Ladouceur, and N. H. Lovell, "Development of nanoparticle film-based multi-axial tactile sensors for biomedical applications," *Sensors and Actuators A: Physical*, vol. 196, pp. 38–47, 2013.

[21] M.-S. Suen, Y.-C. Lin, and R. Chen, "A flexible multifunctional tactile sensor using interlocked ZnO nanorod arrays for artificial electronic skin," *Procedia Engineering*, vol. 168, pp. 1044–1047, 2016.

[22] C. Demolder, A. Molina, F. L. Hammond III, and W. H. Yeo, "Recent advances in wearable biosensing gloves and sensory feedback biosystems for enhancing rehabilitation, prostheses, healthcare, and virtual reality," *Biosensors and Bioelectronics*, vol. 190, article 113443, 2021.

[23] X. Liao, W. Song, X. Zhang et al., "Hetero-contact microstructure to program discerning tactile interactions for virtual reality," *Nano Energy*, vol. 60, pp. 127–136, 2019.

[24] Y. Liu, R. Bao, J. Tao, J. Li, M. Dong, and C. Pan, "Recent progress in tactile sensors and their applications in intelligent systems," *Science Bulletin*, vol. 65, no. 1, pp. 70–88, 2020.

[25] J. W. Fastier-Wooller, V. T. Dau, T. Dinh, C. D. Tran, and D. V. Dao, "Pressure and temperature sensitive e-skin for in situ robotic applications," *Materials & Design*, vol. 208, article 109886, 2021.

[26] M. H. Kim, C. H. Cho, J. S. Kim et al., "Thermoelectric energy harvesting electronic skin (e-skin) patch with reconfigurable carbon nanotube clays," *Nano Energy*, vol. 87, article 106156, 2021.

[27] D. Yao, L. Wu, S. A et al., "Stretchable vertical graphene arrays for electronic skin with multifunctional sensing capabilities," *Chemical Engineering Journal*, vol. 431, article 134038, 2022.

[28] S. Wei, Y. Liu, L. Yang et al., "Flexible large e-skin array based on patterned laser-induced graphene for tactile perception," *Sensors and Actuators A: Physical*, vol. 334, article 113308, 2022.

[29] R. Scaffaro, A. Maio, and M. C. Citarrella, "Ionic tactile sensors as promising biomaterials for artificial skin: review of latest advances and future perspectives," *European Polymer Journal*, vol. 151, article 110421, 2021.

[30] Y. Miao, M. Xu, J. Yu, and L. Zhang, "Conductive cold-resistant and elastic hydrogel: a potential bionic skin for human-machine interaction control over artificial limbs," *Sensors and Actuators B: Chemical*, vol. 327, article 128916, 2021.

[31] A. Kumar, M. L. Singla, A. Kumar, and J. K. Rajput, "Fabrication and linearisation of conformable POMANI-Mn3O4 nanocomposite based thermistor for temperature monitoring applications in prosthetic gloves," *Sensors and Actuators A: Physical*, vol. 285, pp. 588–598, 2019.

[32] X. Zeng, Y. Liu, F. Liu et al., "A bioinspired three-dimensional integrated e-skin for multiple mechanical stimuli recognition," *Nano Energy*, vol. 92, article 106777, 2022.

[33] A. Trent and M. E. Van Dyke, "Development and characterization of a biomimetic coating for percutaneous devices," *Colloids and Surfaces B: Biointerfaces*, vol. 182, article 110351, 2019.

[34] J. M. Khare, S. Dahiya, B. Gangil, and L. Ranakoti, "Influence of different resins on physico-mechanical properties of hybrid fiber reinforced polymer composites used in human prosthetics," *Materials Today: Proceedings*, vol. 38, pp. 345–349, 2021.

[35] S. Sakuri, E. Surojo, D. Ariawan, and A. R. Prabowo, "Investigation of Agave cantala-based composite fibers as prosthetic socket materials accounting for a variety of alkali and microcrystalline cellulose treatments," *Theoretical and Applied Mechanics Letters*, vol. 10, no. 6, pp. 405–411, 2020.

[36] J. K. Oleiwi, Q. A. Hamad, and S. A. Abdulrahman, *Flexural, impact and max. shear stress properties of fibers composite for prosthetic socket*, Materials Today: Proceedings, Amsterdam, Netherlands, 2022.

[37] Q. A. Hamad, J. K. Oleiwi, and S. A. Abdulrahman, *Tensile properties of laminated composite prosthetic socket reinforced by different fibers*, Materials Today: Proceedings, Amsterdam, Netherlands, 2021.

[38] B. Oldfrey, A. Tchorzewska, R. Jackson et al., "Additive manufacturing techniques for smart prosthetic liners," *Medical Engineering & Physics*, vol. 87, pp. 45–55, 2021.

[39] S. Sundararaj and G. V. Subramaniyan, "Structural design and economic analysis of prosthetic leg for below and above knee amputation," *Materials Today: Proceedings*, vol. 37, pp. 3450–3460, 2021.

[40] Q. Huang, S. Xu, Z. Ouyang, Y. Yang, and Y. Liu, "Multi-scale nacre-inspired lamella-structured Ti-Ta composites with high strength and low modulus for load-bearing orthopedic and dental applications," *Materials Science and Engineering: C*, vol. 118, article 111458, 2021.

[41] B. Ren, Y. Wan, C. Liu et al., "Improved osseointegration of 3D printed Ti-6Al-4V implant with a hierarchical micro/nano surface topography: an in vitro and in vivo study," *Materials Science and Engineering: C*, vol. 118, article 111505, 2021.

[42] H. A. Sallal, A. A. Abdul-Hamead, and F. M. Othman, "Effect of nano powder (Al2O3-CaO) addition on the mechanical properties of the polymer blend matrix composite," *Defence Technology*, vol. 16, no. 2, pp. 425–431, 2020.

Hindawi
Journal of Nanomaterials
Volume 2022, Article ID 3573005, 12 pages
https://doi.org/10.1155/2022/3573005

Review Article

Stevia rebaudiana, a Versatile Food Ingredient: The Chemical Composition and Medicinal Properties

Ronald Mlambo,[1] Junyan Wang,[2] and Chuanpin Chen[1]

[1]*Xiangya School of Pharmaceutical Sciences, Central South University, Changsha 410013, China*
[2]*Faculty of Engineering, Monash University, 3800 Melbourne, Australia*

Correspondence should be addressed to Junyan Wang; junyan.wang@monash.edu and Chuanpin Chen; ccpin2000@hotmail.com

Received 15 November 2021; Accepted 15 January 2022; Published 29 March 2022

Academic Editor: Weiguo Li

Stevia rebaudiana is a well-known sugar substitute with low calories. Recently, Stevia rebaudiana has been reported with many medicinal properties that could possibly be used in functional foods. The work presents the chemical composition of Stevia rebaudiana. The Stevia is capable of treating renal diseases, liver pathologies, diabetes, hyperglycemia, hypoglycemia, hypertension, tumors, microbial diseases, and obesity. Nonetheless, researches are still going on to understand Stevia. Therefore, the conclusion made is not everything known about Stevia. This work highlights chemical composition of Stevia rebaudiana and its medicinal properties like antioxidant, antidiabetic, anti-inflammatory, antihypoglycaemic, anticancer, renal-healing, cardiac-healing, antilipidemic, and hepatoprotective effects. The information has been discussed from a food and medical perspective. Future works may focus on the development of novel functional foods.

1. Introduction

Nature is full of unveiled scientific inventions, innovations, and discoveries. There are about 1500 years now since *S. rebaudiana* (a food ingredient) had been used by our antique forefathers. Dr. Moises Santiago Bertoni, who was a Director of Agriculture in Asuncion College, discovered *Stevia* in Paraguay in 1888. He first gave the biological description of *Stevia*. Few years down the line in 1905, Dr. Rebaudi, a chemist named the plant (Momtazi et al., 2016). He was the first person to extract and isolate the glycosides in the *Stevia*. Complete characterization of the glycosides was done by 1931. *Stevia rebaudiana* appertains to a genus of *Asteraceae* family. It is one of the 154 known members of this family. It belongs to Kingdom *Plantae*, *Angiosperms* division, *Eudicots* class *Asterals* order, *Stevia* genus, *Eupatoricae* tribe, and *Bertholdii* species (Verma et al., 2019). This green herb has elliptical, sessile leaves which are approximately 3-4 cm long. It can grow up to 1 m in terms of height (Fasiha et al., 2020). Around 1961, cultivation of the herb commenced [1]. The herb is native in Amambay Valley, a junction formed by some regions of Argentina, Brazil, and Paraguay. In Brazil and Paraguay, *Stevia* is found naturally between 22°-24° south and 53°-54° west. Paraguayan Indians are the pioneers in using *S. rebaudiana* leaves as natural sweeteners. *S. rebaudiana* leaves are referred to as candy or honey leaf because of its sweet taste. It is reported that only a handful leaves are enough to increase the sweetness of beverages, for example herbal tea. The use of the leaves became common and popular since the discovery made by the Paraguayan Indians that the *S. rebaudiana* leaves can be used as natural sweeteners. Long back, the herb seemed only to be more medicinal than commercial. *S. rebaudiana* is now known as an important commercial herb. Almost every continent is actually aware of this practice and started *Stevia* agriculture, following the observation that it is a potent medicinal and commercial herb (Zou et al., 2020). These nations include China, Canada, Indonesia, Korea, Brazil, Mexico, Tanzania, and United States of America (Martins et al., 2016; Zou et al., 2020). Approximately 1000000

hectares worldwide of Stevia cultivation were reported, with China having the largest portion (Sharangi et al., 2016).

Among about 200 genus species of Stevia, *S. rebaudiana* has drawn a great portion of attention due to its sweet nature (Ahmed & Mukta, 2017). *Stevia* flourishes in an acidic-neutral (roughly pH 6-7) soil rich in animal or plant remains. Moisture is needed. Researches revealed that *Stevia* grows naturally in low lying sand acidic parts next to swamps. Application of urea fertilizer ought to be done thrice. First application is done at basal. The rest two are done following first and second cutting of leaves. Phosphorus and potassium high levels plus low nitrogen level enhance Stevia flourishment. Borax 6% is sprayed whenever the plant shows boron deficiency ailment symptoms. The disease is known for causing spots on the leaves [1]. Researches are still going on to understand the herb fully and maximize on it. There are several factors that affect the amount of stevia secondary metabolites, including the nutrition and climate. For example, high glycoside percentage is found in Stevia grown in mountainous regions. It is reported that when length of the day is less than twelve hours and when temperatures are below 293 K, the rate of growth diminishes. Increasing day length to approximately sixteen hours and elevating light intensity increases growth and stevioside levels. Nonetheless, a number of varieties have a disposition not to give positive phototropism response. Stevioside content is higher in early flowering stevia but the total yield is lower. Researchers unveiled the observation that stevioside concentration in the leaves increase when the plant is grown under long day conditions. Also, transplanting and planting dates are critical agricultural factors that have a big likelihood to quantity and quality of yield [1]. The purpose of this review is to delve into the distribution, chemical composition, medicinal uses, pharmacology, and commercial aspects of Stevia.

2. Chemical Composition

Momtazi et al. (2016) assert that in some studies and experiments conducted, *Stevia* leaves are loaded with different types of chemicals. Among the chemicals are nine essential amino acids viz. glutamate, aspartate, methionine, tyrosine, proline, alanine, isoleucine, lysine, and serine. Lemus-Mondaca et al. (2012) reported that all essential amino acids are present in the leaves of Stevia with an exception of tryptophan. In addition to that, fatty acids, namely, linoleic acid, linolenic, oleic, stearic, palmitoleic, and palmitic acid, were found present. Moreover, vitamins such as vitamin B_{12}, vitamin C, and folic acid were also present, along with minerals such as calcium, phosphorus, magnesium, iron, sodium, zinc, and potassium. Not only that, phytochemicals, namely, β-carotene, thiamine, steviol, stevioside, riboflavin, rebaudi oxides, nilacin, dulcoside, and austroinullin, were detected in the plant leaves. Needless to say, secondary metabolites are present. Majority of articles and researches report that anthraquinones, reducing compounds, triterpenes, sterols, saponins, cardiac glycosides alkaloids, and tannins are found in the *Stevia* leaves. Terpenes and flavonoids dominate in terms of chemical composition in the *Stevia* leaves (Sharangi et al., 2016). Fasiha et al. (2020) reported the presence of phenols and coumarins in the *Stevia* leaves.

Glycosides found in *Stevia* have a common backbone structure, which are given an umbrella term, steviol glycoside. These chemicals are diterpenes with four rings. The sweet taste is rendered by the C-13 hydroxyl group and C-19 carboxyl group. Stevioside, steviolbioside, isosteviol, and rebaudioside A, B, C, D, E, and F are the major glycosides present in the herb. Stevioside and rebaudioside C and A are 250-300, 50-120, and 250-450 times sweeter than can sugar, respectively. Rebaudioside A and D are convertible to rebaudioside B under alkaline hydrolysis. The duo is highly soluble and can be metabolized in the human body without side effects. The most attractive attributes of the two are that they are thermostable (up to 200°C), highly water soluble, pH stable, and do not ferment (Sharangi et al., 2016). On the next leaf is a backbone structure of glycosides found in Stevia as reported by Lemus-Mondaca et al. (2012). Different group constituent results in different glycosides are shown in Table 1.

3. Methods Employed for Extraction and Identification of a Broad Spectrum of Chemicals in *Stevia*

A lot of different extraction methods had been employed and can be categorized as solvent extraction (Bondarev et al., 2001; Morita et al., 1978), supercritical fluids (Keinle, 1992), selective precipitation (Fuh & Chiang, 1990), ion exchange, and chromatographic adsorption (Herrera et al., 2001; Nathalie *et al*., 2019). Complex compounds extracted from *Stevia* leaves vary in terms of composition. Concentrations of these complex compounds depend on the herb genetic make-up and the region of cultivation [3]. For instance, Khiraoui et al. (2017) reported that the variations are due to geographical locations and cultivars. Gasmalla et al. (2014) contributed other factors which affect *Stevia* chemical composition. The researchers observed that methods of drying and processing affected percentage chemical yield.

3.1. Steviosides. Solvent partition extraction is the refining standard operating procedures for the extraction of stevioside from *Stevia*, which were grouped into water and methanol, by Rank and Midmore (2006). The methods encompassed solvent partition extraction coupled with in situ precipitation with calcium hydroxide-carbon dioxide to get rid of the impurities. The duo seemed to employ the exact purification procedure that is employed in the sugar industry (Lemus-Mondaca et al., 2012). In addition to that, Rank and Midmore (2006) reported other methods of purification like plasmid gel, ion exchange, chromatographic techniques, and adsorption activated by graphite. Hot water was the extraction medium with first preference. The reason being that rebaudiside A was more soluble than stevioside (Liu et al., 1997). Nonetheless, a number of patents highlighted good reasons in using solvents like methanol, ethanol, chloroform, sorbitol, glycerine, and propylene glycol (Lemus-Mondaca et al., 2012). Liu and colleagues (1997) isolated stevioside from *S. rebaudiana* dried leaves using hot methanol. The team went on further to study the

Table 1: The substituents of steviol glycosides.

Steviol glycoside	R1 constituent	R2 constituent
Dulcoside A	β-Glc	β-Glc-α- Rha(2 → 1)
Rebaudioside A	β-Glc	β-Glc-β-Glc(2→1) β-Glc(3→1)
Rebaudioside B	H	β-Glc-β-Glc(2→1) β-Glc(3→1)
Rebaudioside C	β-Glc	β-Glc-α-Rha(2→1) β-Glc(3→1)
Rebaudioside D	β-Glc-β-Glc(2 → 1)	β-Glc-β-Glc (2→1) β-Glc (3→1)
Rebaudioside E	β-Glc-β-Glc(2 → 1)	β-Glc-β-Glc(2 → 1)
Rebaudioside F	β-Glc	β-Glc-β-Xyl(2→1) β-Glc(3→1)
Stevioside	β-Glc	β-Glc-β-Glc (2 → 1)
Steviolbioside	H	β-Glc-β-Glc (2 → 1)
Steviol	H	H

Key: Glc: glucose; Rha: rhamnose; Xyl: xylose [2].

extraction of steviol glycosides such as dulcoside A, revaudioside C, and rebaudioside A using subcritical fluid extraction (Sub FE). Liu et al. (1997) devised a simple Sub FE efficient method and at least 88% efficiency was attainable using methanol modifier.

Pol et al. (2007) reported that stevioside is commonly extracted using hot water, leaching, or supercritical fluid extraction (SFE), followed by a quantitative analysis of extracts to examine its purity using chromatographic techniques such as recrystallization coupled with preparative reversed phase-high-performance liquid chromatography (RP-HPLC) (Nathalie et al., 2019). The above method is slower as to the SFE method that utilizes carbon dioxide as a medium for extraction. The method has supercritical carbon dioxide physicochemical advantages like lower viscosity and higher diffusivity properties as compared to conventional liquid solvents. Notwithstanding, carbon dioxide in its pure form is destitute of suffice solvation strength for stevioside, a polar organic compound. Consequently, addition of a polar cosolvent is imperative. Probed copolar solvents include water, methanol, ethanol, and mixtures of diverse proportions of these solvents (Yoda et al., 2003; Choi *et al*., 2002, Pasquel et al., 2002 and Abau-Arab *et al*., 2010). An alternative approach is the method reported by Jimenez et al. that separates glycosidic compounds, following aqueous extraction, on the basis of molecular weight. The process was done through an amino column using HPLC, where findings were reported in percentage relative standards (Lemus-Mondaca et al., 2012). Afandi et al. (2013) devised a solvent extraction method to isolate stevioside from *S. rebaudiana* leaf powder. The team used solvents such as diethyl-ether, petroleum ether, methanol, and butanol. The purification stage was performed using HPLC to get rebaudioside, a bioactive compound. Interestingly, Rao et al. (2012) carried out the isolation and purification of steviosides from a different angle. They ground the dried leaves, removed all fats, and then carried out the extraction process using pressurized hot water extractor (PHWE). The final stage which required concentration and purification of sweet glycosides was conducted using nano- and ultramembrane filtration. Rao and colleagues managed to achieve 98.2% purity of the steviosides.

3.2. Phenols. Chlorogenic acids, which fall under polyphenol esters family, are the major constituents of polyphenols found in *Stevia rebaudiana*. Examples are hydrocinnamic acids and quinic acids (Myint et al., 2020). Pacifico et al. (2019) reported isochlorogenic acids and hyrocinnamic acids as part and parcel of polyphenols present in *Stevia* leaves. Generally, phenolic compounds are vital for plant growth and defend against injuries and infections, rendering oxidative stability (Pacifico et al., 2019; Arriola et al., 2019). Singh et al. (2008) and Hanhineva et al. (2010) defined polyphenols as dietary antioxidants, which include polyphenols from grape seeds tea and apples. Can and Baltas (2016), Lemus-Mondaca et al. (2018), Kim et al. (2011), Zheng et al. (2017), and Pacifico et al. (2019) confirmed the presence of the following polyphenols in *Stevia rebaudiana* (Bertoni) leaves: caffeic acid; 4-coumaric acid; cinnamic acid; syringic acid; vanillic acid; 4-methoxybenzoic acid; 4-methylcatechol; gallic acid; pyrogallol; tricaffeoylquinic acid; 3,4,5-tricaffeoylquinic acid; 1,3,5-tricaffeoylquinic acid; rutin; 3-feruloyl-5-caffeoylquinic acid; 4-caffeoyl-5-feruloylquinic acid; 3.5-dicaffeoylquinic acid (isochlorogenic acid A); 1,4-dicaffeoylquinic acid; 3,4-dicaffeoylquinic acid (isochlorogenic acid B); 1,3-dicaffeoylquinic acid; 4,5-dicaffeoylquinic acid (isochlorogenic acid C); quercetin-3-O-glycoside; galuteolin; quercetin; roseoside; 3-feruloylquinic acid; 5-feruloylquinic acid; 4-caffeoylquinic acid (cryptochlorogenic acid); 3-caffeoylquinic acid (chlorogenic acid); 4-caffeoylshikimic acid; 3-caffeoylshikimic acid; 5-caffeoylquinic acid (neochlorogenic acid); 5-p-coumaroylquinic acid; 5-caffeoylshikimic acid; catechin; luteolin, sinapic acid, and *trans*-ferulic acid (Myint et al., 2020).

The methods employed for the extraction and determination of polyphenols varied from researcher to researcher. On one end of the spectrum, Wolwer-Rich (2012), Kim et al. (2011), and Pacifico et al. (2019) regarded liquid chromatography-tandem mass spectrometry (LC-MS/MS) as the most reliable and effective method for the determination of polyphenols. Oppositely, Myint et al. (2020) observed that LC-MS/MS analysis was not that much reliable when it comes to quantification of phenols. The reason is that the method requires many chemicals as standards since there are many polyphenolic isomers. Consequently, other methods were needed to accomplish the quantification and characterization of phenols. These methods included NMR (nuclear magnetic resonance) and purification processes. Nowadays, Folin-Ciocalteu assay had been widely used for the total phenolic content (TPC) analysis.

The assay works on the basis of calorimetric redox reactions performed by phenols. Folin-Ciocalteu is the frequently used assay owing to its ease of use and cost. The total phenolic content (TPC) may be reported as the equivalent standard chemical, like gallic acid (GA), catechin (CE), and tannic acid

(TA), with the unit of milligrams or micrograms equivalents per gram of dried extract. The extracts can be 'named' catechin equivalent, gallic acid equivalent, etc. (Myint et al., 2020). Notwithstanding, the assay has its drawbacks. One of the major disadvantages is that the assay has an inability to select polyphenols with respect to equivalent standard chemicals. A subtle task to choose the rightful reference chemicals as standards is crucial due to the discrepancies in polyphenolic molecular weights and standard molecular weight equivalent. Myint et al. (2020) illustrated the major disadvantage of the assay by analyzing a sample that was from Zhucheng Hao Tian Pharm Co. Ltd., Shandong, China. The sample was labelled 'no chlorogenic acid' and 58.92% TPC. Now, upon analysis and chemical composition determination by the HPLC method, the sample contained 36.98% isochlorogenic acid A, 16.50% isochlorogenic acid C, 4.50% isochlorogenic acid B, 0.69% chlorogenic acid, 0.15% neochlorogenic acid, and 0.10% cryptochlorogenic acid. The sample could be labelled 771 mg GAE/g TPC. The same sample could be also 1.076 mg chlorogenic acid equivalents per gram extract. The 1.076 mg anomaly is explained by the fact that chlorogenic acid offers much lower molecular weight. In addition to the above reported chemical composition, the sample was found to contain 31.64% polysaccharides which were detected by phenol-sulphuric acid assay, 0.44% total flavonoid, and 0.82% protein, determined by the Kjeldahl method. Another striking example to shed some light on how scientists ought to be careful when conducting the Folin-Ciocalteu assay is the discrepancies in TPC reported by Karakose et al. (2011) and Kim et al. (2011). Karakose and colleagues extracted chlorogenic acids using chloroform-methanol solvent. After that, further determination process was carried out using the LC-MS method. The team reported twenty-four chlorogenic acids which were mainly hydoxycinnamic acid derivatives of shikimic and quinic acid. Altogether, chlorogenic acids amounted to 370 μg GAE/g of dry extract. Kim et al. (2011) used a water extract and observed that the major phenolic compound in both callus and leaf was pyrogallol, 0.04 mg/g extract in callus, and 9.51 mg/g in leaf extracts. The team reported a sum of 130.76 mg catechin (CE).

As illustrated above, the unwanted substances act as impurities during the quantification and characterization of polyphenols. Substances like sugars, ferrous ion, organic acids, reductones, other enediols, ascorbic acid, sulphur dioxide, and aromatic amines react with the Folin-Ciocalteu reagent giving rise to biased results (Prior, Wu & Schaich, 2005). Consequently, such substances should be removed using a broad spectrum of purification methods for more accurate results.

4. Health-Promoting Activity of *Stevia* Phenolic Compounds

According to Zhang et al. [4], *Stevia* leaves are safe to eat. Majority of polyphenols therein have antioxidant activity (Lemus-Mondaca et al., 2018). In addition to that, anticancer, antilipidemic, anti-inflammatory, and antidiabetic properties are reported (Liang & Kitts, 2016; Gouthamchandra et al., 2017; Ong, Hsu & Tan 2013; Pacifico et al., 2019; [3]; Zaidan et al., 2018). Phenolic compounds come in different classes. Among the different classes, phenolic acid derivatives, anthocyanins and flavonoids are the major ones in terms of abundancy. The trio is synthesized in the chloroplasts via a pathway known as the phenylpropanoid synthetic pathway (Santiago et al., 2000; [5]; Khoddami et al., 2013). The chemical compounds are known for protecting the plants from insects, viral, and bacterial invasion (Nicholson & Hammerschmidt, 1992; [6]; Lee et al., 2004; Baidez *et al*., 2007, Eyles *et al*., 2010; [7]). Not only that, the phenolic compounds have the ability to safeguard the plant deoxyribonucleic acid (DNA) by protecting it from oxidative reactions. Mitigation of photooxidative harm in photosystems is executed by the phenolic compounds (Zhang et al., 2018). Many published papers report that increased light intensity correlates with an upregulation of phenolic compounds [4, 8].

4.1. Antioxidant Activities. Biological systems have complicated metabolic processes. Reactive oxygen species (ROS) such as hydrogen peroxide and superoxide anion are produced along with the metabolic processes. If a body experiences an imbalance between free radicals produced and the ability of the body to get rid of the radicals, serious health conditions arise due to oxidative stress. For example, cardiovascular pathologies and cancer arise if the ROS persist in the biological systems. The biological systems are loaded with mechanisms meant to prevent any harm that might be caused by ROS. The mechanisms can be categorized into two: enzymatic and nonenzymatic systems. Biological systems have enzymes such as catalase (CAT), superoxide dismutase (SOD), and glutathione peroxidase which demolish ROS and other free radicals. Albumin and bilirubin are endogenous nonenzymatic antioxidants which serve the same purpose as that of the aforementioned enzymes. Nonetheless, phenomena where the ROS outpower the endogenous antioxidant systems occur. Exogenous antioxidants are in such times imperative. Sources of exogenous antioxidants include supplements, pharmaceuticals, and food. Among exogenous antioxidants are ascorbic acid, phenolic compounds, carotenoids, and minerals like zinc and selenium (Santos-Sanchez et al. 2019).

4.1.1. Oxidative Stress. Oxygen molecule is crucial. It is involved in aerobic cell metabolism to produce energy needed to sustain life. The downside of the molecule is that it can pose serious harm in the body due to its paramagnetic properties. Partly oxidized intermediates, which are highly reactive, are formed due to the paramagnetic properties of the molecule. Such intermediates are referred to as reactive oxygen species (ROS). Exogenous factors like ultraviolet radiation contribute to the formation of ROS. The ultraviolet (UV) light has potency to lyse molecules. In case of the oxygen molecule, homolysis occurs, giving rise to oxygen radicals. ROS can be formed during the course of an ailment. Progression of diseases like myocardial infarction produces free radicals. Biotransformation of xenocompounds carried out in the body by a concert of defense molecules also forms free radicals reluctantly, following chemical intoxication. The purpose of biotransformation is to mitigate the toxicity

of the foreign compound hence rendering it ineffective. Nonetheless, the unexpected happens (Santos-Sanchez et al., 2019).

The immune system carries out inflammatory response upon the invasion by foreign bodies. There is a production of free radicals which destroy foreign bodies. However, detrimental results ensue when the inflammatory response last longer than expected. Immune cells like macrophages and neutrophils make use of the NADH oxidase system to get rid of foreign bodies. The cells, in doing so, produce superoxide ion, a free radical. The superoxide ion is regarded as a primary ROS. The ion can then undergo some reactions to form a secondary ROS. Enzymatic reactions and metal ions are examples of two systems that are capable of reaction with a primary superoxide ion, forming a secondary superoxide ion ROS. Photolysis of water is one the reactions known for the generation of a superoxide ion. When the superoxide ion undergoes reactions like protonation, H_2O_2, and HO_2·, ROS are produced (Santos-Sanchez et al., 2019).

The action of nitric oxide synthase on intracellular arginine, as a defense mechanism executed by immune system cells, leads to the formation of .NO radical. If the formed radical merges with O_2, the ONOO· radical is formed. It is the ONOO· radical that induces lipoprotein peroxidation. Individuals suffering from the following autoimmune diseases have significant lipoprotein oxidation rate once occurring: vitiligo, psoriasis, multiple sclerosis, scleroderma, inflammatory bowel disease, Hashimoto's disease, Grave's disease, celiac disease, type 1 diabetes, primary biliary cirrhosis, systemic lupus erythematosus, and rheumatoid arthritis (Santos-Sanchez et al., 2019).

Sometimes free radical production is good and crucial in some biochemical reactions. Giving examples, production of polypeptides requires free radicals. The free radicals aid in formation and chain elongation of proteins during amino acid polymerization. Also, glycogenesis requires free radicals. A number of enzymes that are responsible for the formation of intermediary molecules require free radicals for activation. Examples of such enzymes are lipoxygenase, cyclooxygenase, monoamine oxidase, aldehyde oxidase, xanthine oxidase, and hypoxanthine (Santos-Sanchez et al., 2019).

Structural changes in critical biomolecules, like lipids, proteins, and deoxyribonucleic acid caused by irreversible reactions, lead to the production of free radicals. Such chemical reactions cause the formation of hydroperoxides and monoaldehyde derivatives that propagate oxidative damage. Apart from ROS, there are reactive nitrogen species (RNS). RNS are generated in small amounts during cellular processes like regulation of cell growth, production of cellular energy, phagocytosis, immune system control, blood pressure modulation, platelet aggregation, peristalsis, muscle relaxation, neurotransmission, and cell signaling. Examples of RNS are NO· (nitrogen oxide), NO_2. (Nitrogen dioxide), $ONOO^-$ (peroxynitrite), $ONOOCO_2^-$ (nitrosoperoxycarbonate), NO_2^+ (nitronium ions), peroxynitrous acid (ONOOH), and dinitrogen trioxide (N_2O_3) (Santos-Sanchez et al., 2019).

Below is Table 2 that sums up the sources and potential harm that might occur to biomolecules in the body.

4.1.2. Assays and Mechanisms of Antioxidant Action. There is a very thin line between oxidant capacity and activity. Majority of scientists use the two terms interchangeably yet they do not mean the same thing. When studying mechanisms and antioxidants assays, great care ought to be taken concerning the confused two terms. A rate constant of reaction between an antioxidant and an oxidant is called antioxidant activity. Antioxidant capacity is defined as the measure of how much free radicals an antioxidant sample can capture. When selecting method, the consideration of response parameter is crucial in terms of evaluating the antioxidant properties of a sample. The responses parameter could be a function of the substrate's concentration, or the concentration and time required for the inhibition of ROS with defined concentration. For the environment in which the free radical (FR) is, its structure and reactivity govern the antioxidation reaction mechanism to be employed for such particular FR. It is imperative therefore to describe ROS and the reactive nitrogen species (RNS), to a lesser extent, which include both free radicals and precursors (Santos-Sanchez et al. 2019).

The phenolic-compound measurement of antioxidant potency can be categorized into two: (a) electron transfer ability as like ferric-reducing antioxidant power, radical scavenging of 2,2′-azino-bis-ethylbenzo-thiazoline-6-sulphonic acid (ABTS) and 2,2-diphenyl-1-picrylhyrazyl (DPPH) assay (Huang et al., 2005), and (b) hydrogen atom transfer ability as like oxygen radical absorbance capacity (ORAC) (Barba et al., 2014; [9], Lemus-Mondaca et al., 2016; Prior et al., 2005; Huang, Ou & Prior, 2005). Frequently, ascorbic acid is the reference antioxidant used. Needless to say, for comparison studies, the *Stevia* leaf extracts purity and composition ought to be taken note of (Myint et al., 2020). Shuckla *et al.* (2009) and Shuckla *et al.* (2011) reported similar antioxidant properties in *Stevia* leaf extracts to that of ascorbic acid. Ethanolic extract (61.50 mg GAE/g) and aqueous extract (56.73 mg GAE/g) of *Stevia* leaf extracts showed an antioxidant activity of up to 200 μg/mL dose dependently in a DPPH assay. The rate at which oxidation was inhibited in aqueous extract and ethanolic extract ranged 40.00-72.30% and 36.93-68.76%, respectively. The antioxidant reference (ascorbic acid) range was 64.26-82.58%. Ascorbic acid, aqueous leaf extract, and ethanolic leaf extract scored 26.75, 83.45, and 93.46 μg/mL IC_{50} values, respectively, in a DPPH assay (Myint et al., 2020).

Antioxidant activity of ethanolic leaf extract against superoxide anions, nitric oxide, and hydroxyl radicals scored IC_{50} values of 100.86 (81.08) μg/mL, 93.73 (132.05) μg/mL, and 100.86 (93.46) μg/mL, respectively. The ascorbic acid standard IC_{50} values were observed to be 71.41, 66.01, and 26.75 μg/mL, respectively. Consequently, one can infer that Shuckla et al. (2009) and Shuckla et al. (2011) results do not agree with the notion that *Stevia* leaf extracts do exhibit similar antioxidant activities as ascorbic acid. Considering IC_{50} values, ascorbic acid outweighed *Stevia* leaf extracts in terms of antioxidant activity. According to the Gawel-Beben et al. (2015) experiment, in which glycol-aqueous extracts, ethanolic, and aqueous extracts were analyzed for antioxidant activity against DPPH and ABTS radicals,

Table 2: Some of the free radicals' potential harm to biomolecules in the body.

Species	Source	Reaction(s) with biomolecules
$O_2^{\cdot -}$	Enzymatic process, autoxidation reaction, and nonenzymatic electron transfer reactions	It can act as reducing agent of iron complexes such as cytochrome-c or oxidizing agent to oxidize ascorbic acid and α-tocopherol
$HO_2\cdot$	Protonation of $O_2\cdot$	Initiates fatty acid peroxidation
HO·	H_2O_2 generates HO· Through the metalcatalyzed Fenton reaction	HO· reacts with both organic and inorganic molecules including DNA, proteins, lipids, and carbohydrates
NO·	Action of nitric oxide synthase using arginine as a substrate and NADPH as an electron source	NO· is an intracellular second messenger stimulates guanylate cyclase and protein kinases and helps in smooth muscle relaxation in blood vessels
$NO_2\cdot$	Protonation of ONOO· Or homolytic fragmentation of $ONOOCO_2\cdot$	This radical acts on the antioxidative mechanism decreasing ascorbate and α-tocopherol in plasma
ONOO·	Reaction of $O_2\cdot$ With NO.	ONOO. is a strong oxidizing and nitrating species of methionine and tyrosine residues in proteins and oxidizes DNA to form nitroguanine
$CO_3^{\cdot -}$	The intermediate of reaction superoxide dismutase (SOD)-Cu_2^{+}-OH· react with bicarbonate to generates $CO_3^{\cdot -}$	Oxidizes biomolecules such as proteins and nucleic acids
$ONOOCO_2^{-}$	The peroxynytrite-CO_2 adduct is obtained by reaction of $ONOO^{-}$ with CO_2	This anion promotes nitration of tyrosine fragments of the oxyhemoglobin via free radicals

glycol-aqueous and ethanolic extracts exhibited the highest activity with the IC_{50} values 0.38 and 0.71 μg flavonoids/mL and 2.08 μg flavonoids/mL. Ethanolic extracts showed the highest potency to chelate the ferrous ion (Myint et al., 2020). Generally, the higher the TPC, the stronger the antiradical activity. Nonetheless, one ought to bear in mind that the *Stevia* leaf extract antiradical activity is 'water-loving,' just like that of ascorbic acid. *Stevia* leaf extract is more thermostable than ascorbic acid (Myint et al., 2020).

In addition, antioxidant modes of action vary from one antioxidant to another. A number of such mechanisms are reported. Among such mechanisms are singlet oxygen quenching, potency to chelate metal ions, singlet electron transfer (SET), mechanisms that mitigate tocopherol radicals, hydrogen atom transfer (HAT) mechanisms, suppression of oxidases mechanisms, and some which activate antioxidant enzymes. There is a need, therefore, to carry out many assays for antioxidant activities (Myint et al., 2020; Santos-Sanchez *et al.* 2019). Many polyphenols found in *Stevia* are basically the same as those found in other plants. Antioxidant properties in *Stevia* are therefore expected. Yu et al. (2017) observed that a *Stevia* extract of total phenolic compound 71.46 mg GAE/g inhibited the formation of hydroperoxide in fish oil. According to Ortiz-Viedma et al. (2017), 23.97 mg GAE/g DW improved the shelf-life and quality of salmon paste by presenting a lipid oxidation inhibition activity and suppression of pathogenic microorganism development in the salmon paste that was kept under refrigeration conditions.

Notably, the geographical place from where the *Stevia* samples are taken affects the antioxidant activity. Also, different parts of the herb give different antioxidant activities. Leaves, stems, and roots, for example, do not produce antioxidants of same activity ([10]; Zayova *et al.*, 2013). Singh and colleagues observed that the highest ABTS radical scavenging activity was scored by a methanolic root extract (64.23 mM). The flower, stem, and leaf extracts showed 46.49, 49.28, and 56.26 mM ABTS radical scavenging activity (Myint et al., 2020).

Unfortunately, antioxidant assays done *in vitro* do not represent the true *in vivo* biochemical reactions. One of the reasons is that free radicals easily spread. Also, majority of free radicals have a short life span. As a result, the chances of an antioxidant capturing the radical(s) are very slim. Worse still, the free radical-antioxidant reaction is a second-order reaction. Consequently, factors like concentration of antioxidants and free radicals are not enough considerations. Further considerations like the medium in which the free radical-antioxidant reaction is occurring, reaction conditions and chemical structures of both reactants need to be assessed too (Santos-Sanchez et al., 2019).

The reaction mechanism of phenolic compounds with the peroxy radical involves a proton transfer from phenol to the radical, leading to the formation of transition state H-O bond with one electron. If a phenolic antioxidant reaction occurs in an environment that favors the formation of hydrogen bonds, the antioxidant capacity is reduced. Alcohols were observed to have a dual effect on the reaction rate between peroxy radical and phenol. On one end of the spectrum, alcohols accept hydrogen bonds. On the other end, alcohols make a conducive environment for the phenol's ionization, forming phenoxide ions. The phenoxide ions formed quickly react with the peroxy radicals via an electron transfer mechanism (Santos-Sanchez et al., 2019).

Leopoldini et al. (2004) determined a theoretical dissociation bond energy of the O-H bonds in several phenolic compounds and their adiabatic ionization potentials. The compounds possessed different structures and polarities. The team simulated solvated and vacuum conditions. Individual compounds exhibited different mechanisms and reaction rates. Among these compounds were tyrosol, caffeic acids, hydroxytyrosol, and gallic acids. The compounds that exhibited hydrogen electron transfer (HAT) mechanism

were tocopherol, followed by hydroxytyrosol, gallic acid, caffeic acids, and epicatechin. Kaempferol and resveratrol exhibited a singlet electron transfer (SET) mechanism (Santos-Sanchez et al., 2019).

4.2. Anti-Inflammatory Activities. The body undergoes a natural response whenever foreign bodies invade or when injuries occur. Such a response is carried out by the immune system. Inflammation, however, is the cause of a number of serious diseases (Zou et al.,2020). Inflammation mobilizes immune cells to attack the inflammation rendezvous by producing special chemicals known as proinflammatory mediators (Al-Kharashi, 2018). Such mediators include interleukins (ILs). Interleukins are known for recruiting immune cells to aid warring against cancer, pathogens, and foreign bodies. Nonetheless, overproduction of the proinflammatory mediators is capable of inducing several acute and chronic ailments like arthritis, inflammatory bowel disease, and atherosclerosis [11–13]. The most commonly used anti-inflammatory drugs come with serious side effects like gastrointestinal toxicity, addiction, and drug tolerance. Therefore, a search for natural resources which exhibit anti-inflammatory activities with ideally no toxicity is on [14].

Natural product development like steviol glycosides, with an intention to prevent proinflammation is regarded as an efficient, safe, and cost-effective pharmaceutical invention (Auyeng et al., 2016; [15]). Many studies showed that *Stevia* extracts have anti-inflammatory properties. Among those studies, a few of them reported that hydroalcohol *Stevia* extracts (500 mg/kg) mitigated oxidative damage in the liver by changing levels of cytokines like TNF-α, IL-6, and IL-1β. Also, the extract exhibited the ability to stop inflammation (Holvoet et al., 2015; Latha *et al*., 2017).

Cytokines are signaling molecules that are secreted during pathological and physiological processes by the immune cells such as lymphocytes, macrophages, and various stroma cells. Stevioside is capable of restraining the secretion of proinflammatory cytokines in macrophages following being challenged with lipopolysaccharides in a dose-dependent manner [16]. Meng et al. [17] also had similar observations that 200 μM stevioside restrained an inflammatory response that was induced by titanium particles in bone marrow-derived macrophages. In addition to that, stevioside prevented osteolysis in titanium particles-treated mice with doses of 10 or 30 mg/kg (Zou et al., 2020).

Basically, stevioside exhibits anti-inflammatory properties by downregulating the major two pathways, namely, nuclear factor kappa B (NF-κB) and mitogen-activated protein kinase (MAPK) signaling pathways [17]. Mitigation of inflammation in a mouse that was treated infected with *Staphylococcus aureus* (*S. aureus*) was reported by Wang et al. [18]. The downregulation of MAPK and NF-κB pathways' mechanism was exhibited in the mouse. Wang and colleagues started by conducting an experiment on primary mouse mammary epithelial cells (MMECs) that were infected with *S. aureus*. They noted that stevioside inhibited the production of cytokines like IL-6, IL-1β, and TNF-α. Stevioside also prevented necrosis of the *S. aureus*-infected MMECs by downregulating the gene expression for type 2 Toll-like receptors (TLRs) (Zou et al., 2020).

Wang and colleagues advanced their research. They administered the *S. aureus* in the mouse's mammary gland intraperitoneally. The team observed that stevioside reduced inflammatory cell infiltration and maintained the histological mammary gland structure. Exact findings were noted when the mammary gland primary cultures were used for the experiment in lieu of the whole mouse. The cells were infected with *S. aureus*; however, stevioside protected the cells from death and inflammatory hazards by controlling the actions of TLR2 expression, NF-κB, MAPK, and cytokines (Zou et al., 2020).

Reduction of both inflammation and oxidative stress by stevioside is reported by a number of scientists. Many mechanisms had been reported. One of the mechanisms by which oxidative stress is quenched is activating nuclear factor erythroid 2-related factor 2 (Nrf2). The protein, Nrf2, is capable of preventing inflammation process. Casas-Grajales (2019) observed that rebaudioside A inhibited the expression of the Nrf2. It also downregulated the expression of proinflammatory genes like MMP-13 protein, Smad7, NF-κB, and TGF-β1 (Zou et al., 2020).

The notion that there is communication between Nrf2 antioxidant response and NF-κB-inflammatory response had been reported (Li et al., 2008; [19]). Substances that activate Nrf2 are capable of inhibiting the phosphorylation of IKK and p65 NF-κB subunit nuclear translocation, therefore preventing inflammation suppression (Zou et al., 2020).

4.3. Antidiabetic Properties. If insulin action, secretion, or both are not normal, one suffers from a group of carbohydrate metabolism disorders, namely, diabetes mellitus after some time. The ailments are chronic. Challenges like side effects rendered by diabetes mellitus therapeutic drugs make them less likely the favorable solution. Also, a few individuals can afford to buy such drugs. Therefore, an alternative way which is cheaper, effective, and affordable is needed. Many folks resort to the traditional herbs. Among those traditional plants is Stevia rebaudiana [20].

Ahmad and Ahmad [20] designed an experiment to examine the antidiabetic properties of aqueous extract of *Stevia rebaudiana* Bertoni leaves in streptozotocin- (STZ-) induced diabetes in albino rats. The duo injected 40 mg/kg body weight STZ intraperitoneally. The STZ was prepared in a citrate buffer (0.1 M, pH 4.5). The scientists injected STZ into the femoral vein of rats following an overnight fast. Initial drug-induced hypoglycemia mortality was circumvented by the administration of 20% glucose solution to the rats for twenty-four hours. The rats that served as normal during the experiment course were given standard diet and distilled water.

The biochemical serum at the end of the experiment was then analyzed for liver glycogen, glycosylated hemoglobin (HbA1c), insulin levels, and random and fasting blood glucose levels. Blood glucose levels were quantified using the GOD PAP Enzymatic Calorimetric Test Method according to Trinder (1969). The method reported by Nayak and Pattabiraman (1981) was used to quantify HbA1c levels in the

rats' serum. Liver glycogen levels were determined according to Babu et al.'s (2003) protocol. Finally, insulin levels were determined by ELISA (enzyme-linked immunosorbent assay) using the Boehringer-Mannheim kit (Andersen et al., 1993).

Ahmad and Ahmad [20] observed that administration of aqueous *Stevia* extract orally at different concentrations (200, 300, 400, and 500 mg/kg) for a period of 8 weeks markedly reduced the feed and water intakes of the diabetic albino rats. One can then infer that *Stevia* reduces the water and feed intake; therefore, weight gain is prohibited. This is simply because *Stevia* does not induce appetite (Robarts & Wright, 2010). The same results were reported for female Wistar strain rats at doses of 25, 250, 500, and 1000 mg/kg body weight (Abo et al., 2010).

The results reported by Ahmad and Ahmad [20] showed that *Stevia rebaudiana* leaf aqueous extract produced a significant dose-dependent reduction in body weight and body weight gain percentage of rats treated with the *Stevia* extract. The reduction in blood glucose levels is explained by the stevioside present in the extract. The rats lost weight probably because the diet glucose metabolism reduced or maybe the rats decreased rate of food consumption [21]. Reduction in weight of rats that were administered *Stevia* extract might be due to the large amount of stevioside (Awney et al., 2010). The finding is supported by a number of previous research studies (Bernal et al., 2011; Abd-El-Razek & Massoud, 2012; [22]).

Not only that, Ahmad and Ahmad [20] observed that a spectrum of different aqueous *Stevia* extract controlled random and fasting glucose levels with a significant good efficacy. It was observed that stevioside capably controlled glucose levels by enhancing insulin secretion, insulin sensitivity, and insulin utilization in insulin-deficient rats due to downregulation in phosphoenolpyruvate carboxykinase (PEPCK) gene in a rat liver [23]. *Stevia* is thought to contain biomolecules that are able to make the insulin receptor more sensitive to insulin or stimulate β-cells of islets of Langerhans leading to the insulin secretion. This favors biochemical reactions like glycolysis and glycogenesis that aid in lowering blood glucose levels ([1]; Abo Elnag *et al*., 2016; Awney *et al*., 2010).

The HbA1c levels of the rats treated with aqueous *Stevia* extract were almost normal ($\geq$6.5%, 48 mmol/mol). The explanation is that glycemic control mechanisms were mobilized to do the work successfully. The results found by Ahmad and Ahmad [20] are in agreement with Prasal et al. and Rao et al. (Prasad *et al*., 2016; Rao & Najam 2016).

The serum insulin levels in control rates were found to decrease because of the STZ injected. Consequently, β cells decreased, causing insulin secretion to fall as well. Insufficient insulin secretion causes hyperglycemia. Once hyperglycemia occurs, oxidative damage ensues due to ROS and diabetic complication development (Kangralkar et al., 2010; [20]). When the diabetic albino rats were given different concentrations of aqueous *Stevia* extracts, a significant improvement in insulin levels was noted. Stevioside inhibited hepatic PEPCK and gluconeogenesis and, at the same time, enhanced hepatic glycogenesis that led to insulin sensitivity and insulin secretion (Yang et al., 2009). Stevioside in the extract acted upon pancreatic tissue, exerting a beneficial antihyperglycemic effect through the PPARγ-dependent mechanism. Other researchers reported the same mechanism ([22]; Akbarzadeh *et al*., 2015).

Stevioside is capable of inhibiting gluconeogenesis simply by inhibiting the glucagon action. Steviol glycosides modulate pancreatic beta cell function by enhancing TRPM5 (transient receptor potential cation channel subfamily M member 5). TRPM5 is an activated calcium cation channel protein that is expressed on beta cells and gut peripheral enteroendocrine cells by speeding up the rate of insulin production in response to glucose stimulation. One should bear in mind that rebaudioside, stevioside, and steviol are not the ones that have a direct interaction with the TRPM5 but the steviol moiety (Scaria et al., 2017; Prata *et al*., 2017). Steviol glycosides have the capability to act as the insulin receptor ligands (IR or IGF-IR) potentiating the P13k/Akt pathway. The biochemical pathway results in the translocation of glucose transporter 4 (GLUT-4) from an intracellular pool to the plasma membrane. Consequently, glucose enters into the cells and thus mimics the action of insulin (Fasiha et al., 2020).

4.4. Antihyperlipidemic and Hypotensive Effect. Aqueous *Stevia rebaudiana* extracts decrease fatty acid and cholesterol synthesis, mitigating LDL, total cholesterol, and triglycerides. Simultaneously, the extracts elevate HDL cholesterol (Scaria et al., 2017). The mechanism by which *Stevia leaves* aid in controlling blood pressure is relaxation of arteries and prevention of calcium accumulation on the arterial walls that favors vasodilation and reduction of total peripheral resistance and extracellular fluid volume. Hypolipidemia and hypotension causes a cardioprotective effect (Fasiha, Shahid & Faiz-ul-Hassan, 2020).

4.5. Antitumor Effect. Different types of cancers such as breast cancer, skin cancer, and ovarian cancer were found to be stopped and cured by stevioside. The stevioside induces apoptosis biochemical pathways. The cascade of the biochemical events leads to the upregulation of apoptotic proteins such as Bax, Bc1, and caspase-9. Cancer cell viability is mitigated by DNA synthesis inhibition and induced cell apoptosis. Stevioside metabolite, isosteviol, exhibited an inhibitory property against DNA topoisomerase II and DNA polymerase. The metabolite is capable of inactivating the P13/AKT signaling pathway by blocking P13 and AKT phosphorylation. There is an antimitotic compound extracted from *Stevia* called centaureidin. The compound has a potential use in tumor therapy (Mohammad, 2018; [24]; Fasiha, Shahid & Faiz-ul-Hassan, 2020).

4.6. Antibacterial and Antifungal Activity. Plant infections are a global challenge faced. Multidrug resistance (MDR) is rapidly skyrocketing due to an increase in number of microorganisms that resist a lot of drugs (Sundin & Bender, 1996). Dimaguga (1991) mentioned that scientists frequently screen for the active chemical components in herbs and plants. This is done to find solutions to a number of

microbial diseases and other diseases. *Stevia* is full of chemical components namely, flavonoids, phenols, and terpenes, which have the antimicrobial activity (Taware, 2010). Reports revealed that *Stevia* is capable of inhibiting microbial growth. Therefore, it had found many applications in wound healing and gum diseases. Diseases like yeast infections and recurring streptococcal infections can also be cured using *Stevia* [25].

Muradashvili et al. (2019) designed an experiment to probe the antibacterial and antifungal activities of the *Stevia* extract against microbials that cause plant diseases. The team extracted the desired phytochemicals using different solvents. Antimicrobial assay was investigated using the Agar-well bioassay (Lindsay, 1962). The team made each extract of 10 mg/mL final concentration. All extracts were then analyzed for antimicrobial activity by measuring the diameter of zone of inhibition using the disc diffusion method (Valgas, 2007). The detailed methodology is expounded in Muradashvili et al.'s (2019) article.

The team observed that chloroform and ethyl alcohol extracts had highest inhibitory effects on bacterial strains. Chloroform extract inhibited the growth of *Ralstonia solanacearum* culture by scoring 15 mm diameter zone of inhibition after 24 hours. Ethyl alcohol scored 18 mm and lastly acetone which scored 6 mm diameter zone of inhibition. Detailed results are available in Muradashvili et al.'s (2019) article. Nonetheless, the take home point is that *Stevia* has antibacterial and antifungal properties (Muradashvili et al., 2019).

4.7. Hepaptoprotective Properties. Das and Khathiriya [26] designed an experiment to examine the hepatoprotective properties of *Stevia rebaudiana*. The duo used thioacetamide (TAA) to induce hepatotoxicity in healthy Wister-Albino rats which weighed about 150-250 g. The duo then went on to evaluate 200 and 400 mg/kg/day doses on the rats following induced liver damage. An observation made concerning 400 mg/kg dose of aqueous *Stevia* extract administered orally was that it reduced levels of the liver enzymes like aspartate transaminase (AST, 131 ± 3.0 IU/L), alanine aminotransferase (ALT, 62.2 ± 1.8 IU/L), gamma glutamyl transpeptidase (GGT, 13.0 ± 0.3 IU/L), alkaline phosphatase (ALP, 197.4 ± 3.2 IU/L), and total bilirubin levels as compared to the controls used.

TAA has been commonly used to induce a variety of hepatoxicity ailments in experimental animals. Levels of hepatoxicity range from nodular cirrhosis, liver cell proliferation, parenchymal cell necrosis, and pseudolobule formation. A number of researches done reported that a single dose of TAA is capable of causing centrilobular hepatic necrosis. Chronic administration of the hepatotoxin gives rise to liver cirrhosis in the rats. The mechanism by which the hepatotoxin works is that it forms thioacetamide-5-oxide which causes changes cell permeability, increase in Ca^{2+} intracellular concentration, increase in nuclear volume, and nucleoli enlargement. The TAA also inhibits mitochondrial activity leading to necrosis (Mitra et al., 1998; Fort *et al*., 2008; Ahmad et al., 2002).

A number of scientists suggested that part of hepatotoxicity caused by TAA is mediated via oxidative stress which is caused by the action of cytokines through lipid oxidation (So et al., 2002; Okuyama *et al*., 2004). Another suggested mechanism by which TAA causes liver damage is by reducing the antioxidant properties of the liver [27]. Cirrhosis induced by TAA in animal models resembles vital features of human diseases [28]. Transaminases are good biomarkers of hepatocellular damage. The enzymes levels are naturally higher in the intracellular compartments than in the counterpart compartments. Escalated levels in the serum indicate liver damage. In the Das and Khathiriya [26] study, TAA was observed to increase serum levels of AST, ALP, GGT, ALT, and total bilirubin. Pretreatment of the rats with the aqueous *Stevia* leaf extract reduced the abnormal serum levels of the above enzymes. Membrane integrity was under restoration. It is thought that flavonoids present in the *Stevia* are responsible for the hepatoprotective properties [26].

4.8. Nephroprotective Properties. Stevia is capable of carrying out inhibition of apoptosis, oxidative stress, and inflammation, hence exhibiting nephroprotective properties. Initial stages of diabetes mellitus are characterized by two major kidney complications, namely, glomerular hyperfiltration and renal hypertrophy. It is reported that a mechanism by which renal hypertrophy and glomerular hyperfiltration occur is production of transforming growth factor β (TGF-β) by mesangial components and overproduction of free radicals after hyperglycemia. *Stevia* being able to carry out antioxidation activities is able to alleviate and treat the renal diseases. Glycosides do not only mitigate kidney-injury-related diabetes, but also cisplatin-induced nephrotoxicity (Fasiha, Shahid & Faiz-ul-Hassan, 2020). According to Ramos-Tovar et al. [29], aqueous extract of *Stevia* prevented liver cirrhosis in rats that was induced by administering carbon tetrachloride for 12 weeks, 3 times a weak giving a dose of 400 mg/kg i.p. The crew observed that chronic administration of carbon tetrachloride elevated nuclear factor kappa B (NF-κB), proinflammatory cytokine production, and oxidative parameters such as lipid peroxidation whereas nuclear factor-E2-related factor 2 (Nrf2) and glutathione levels decreased. Hepatic stellate cell activation and profibrogenic mediator expression induction were reported. As a result, extracellular matrix production followed. The authors reported that aqueous stevia extract exhibited antifibrotic properties. The mechanism is not known but the authors suggest that it might be due to the extract's ability to block the profibrogenic signaling pathway.

4.9. Cardioprotective Properties. In developing countries, cardiovascular diseases and resultant cardiotherapeutic regimens are the major causes of deaths. A calcium channel blocker, diltiazem, is primarily used to treat hypertrophic cardiomyopathy, systemic hypertension, and supraventricular arrythmias. Stevioside, a chemical component found in *Stevia*, has a synergic pharmacological activity. Bhatt et al. [30] designed an experiment to evaluate the cardioprotective properties of stevioside and possible synergistic effects upon coadministration with diltiazem. The team made use of standard cardiotoxicity models to test the hypothesis: ischemia-reperfusion injury (IRI) and isoproterenol-induced myocardial infarction through Langendoff set up. Rats were

Table 3: Some of the *stevia* species and their properties.

Species	Properties
S. eupatoria (Spreng.) wild	Analgesic, anti-inflammatory, antihypertensive.
S. pilosa Lag.	Antimalarial, antipyretic, cathartic, diuretic.
S. cardiatica Perkins	Heart diseases.
S. lucida Lag	To cure wounds, to soothe pains, rheumatism treatment, anti-inflammatory
S. nepetifolia HBK	Dysmenorrhea treatment.
S. petiolata (Cass) Sch. Bip.	Meat-flavouring agent
S. salicifolia Cav	Rheumatism treatment, cathartic, treatment for intestinal upset due to parasites, purgative. Treatment for fevers and colds.

grouped randomly into control animals (normal: physiological saline and toxic: isoproterenol, 150 mg/kg, s.c., and IRI-induced normal control animals) and treatment groups (diltiazem: 17.5 mg/kg, p.o., stevioside: 100 and 200 mg/kg, p.o. and combination of groups). The animals (female Wistar rats) were sacrificed at the end of the treatment period and histopathological, electrocardiographic, and biochemical analyses were done.

Bhatt et al. [30] observed that pretreatment with the stevioside prevented cardiac biomarkers from leaking into the extracellular compartments hence normalizing perfusate and serum levels of CK-MB, ALT, AST, LDH, and CK-NAC enzymes. Antihyperlipidemic effects were observed on total cholesterol and triglycerides levels dose dependently. Stevioside also exhibited a protective action on SOD and catalase. A combination of stevioside and diltiazem (200 mg/kg and 17.5 mg/kg, respectively) was found to be more powerful in terms of pharmacodynamic response by significantly normalizing electrocardiographic parameters, myocardial histology, antioxidants levels, and biomarker levels.

5. Anticancer Properties

Martínez-Rojo et al. [31] conducted an experiment on *Stevia pilosa* and *Stevia eupatoria* methanolic extracts to observe their effects on prostate cancer cells. The team further probed the effects of each extract combined with enzalutamide. The team used 1000 μg/mL of each extract and 40 μM enzalutamide. The wound healing assay was performed for PC-3 cells treated with combinations of each extract and enzalutamide. It was observed that the combinations were stronger than extracts alone in increasing the inhibition closure of the wound. According to the authors, the extracts alone (concentration range 250 to 1000 μg/mL) have no cytotoxic effects on human fibroblastic cells. The finding is supported by Panagiotou et al. [32] who exposed peripheral blood mononuclear cells to *Stevia rebaudiana* extract. Howbeit, in Martínez-Rojo et al.'s [31] project, the *Stevia* extracts were able to retard PC-3 and LNCaP cancer cell viability at all concentrations assessed. The result is supported by López et al. [33] and Vaško et al. [34] when breast cancer (MCF-7 and MDA), colon cancer (Caco2 and HCT116), lung cancer (A-549), cervical cancer (He-La), and pancreatic cancer cells (MiaPaCa-2) were exposed to *Stevia rebaudiana* extracts.

Šic Žlabur et al. [35] identified luteolin in *Stevia rebaudiana*. The following year, Martínez-Rojo et al. reported that luteolin showed cellular arrest and could induce apoptosis in a broad spectrum of cancer cell lines like prostate cancer (PC-3), liver cancer (SMMC7721), colon cancer (COLO205), and cervical cancer (HeLa) (Lu, Li and Li, 2017). Quercetin, another compound present in the herb, is capable of retarding cell proliferation and viability in MCF-7 breast cancer cells. It is reported that the mechanism behind is apoptosis activation which is achieved through elevation of BAX (Bcl-2-associated X protein) and caspace-3 expression levels while lowering Bcl-2 expression. Also, quercetin activates necroptosis via elevation of receptor-interacting serine/threonine-protein kinase 1 (RIPK1) and receptor-interacting serine/threonine-protein kinase 3 (RIPK3) expressions [4, 36]. Different compounds found in the herb seem to have different mechanisms of arresting cell viability and proliferation.

5.1. Safety. The paper highlights mainly the medicinal properties of the herb. Notwithstanding, there are documented papers that reveal toxicity of the herb. The acceptable daily intake of *Stevia* dry extract defined by the Scientific Committee on Food of the European Food Safety Authority and Food and Drug Administration is 4 mg/kg body mass. One animal study revealed that the herb has a potential to cause allergy. In addition, it was observed that the *Stevia* extract reduced fertility in rats by up to 21% as compared to control rats. It is reported that fertility remained reduced by 47% even following 50 to 60 days recovery time frame (Lohner et al., 2017). The rats that were treated with the *Stevia* extract were found to have a decrease in the relative weight of seminal vesicle and testis as well as a significant decrease in the number of spermatozoa stored (Mazzei-Planas & Kuc, 1968; Melis, 1999). One study revealed that steviol is a mutagen although there is no supporting evidence as of late ((Pezzuto et al., 1985). The primary evidence of *Stevia* safety is that since its use about 1500 years ago by the Paraguayans, there have been no reports of adverse effects. Also, the Japanese consumed the herb in large quantities and no reports are available on the herb toxicity [37]. Moreover, a number of studies that probed *Stevia* effects on the human body

revealed no toxicity (Roy et al., 2010; Nikiforov *et al*., 2013; Uçar *et al*., 2017) [38] are shown in Table 3 [39].

5.2. Conclusion. One can confidently infer that *Stevia rebaudiana* is a versatile useful herb in the world. The herb is capable of treating renal diseases, liver pathologies, diabetes, hyperglycemia, hypoglycemia, hypertension, tumors, microbial diseases, and obesity. Nonetheless, researches are still going on to understand fully the herb. Therefore, the conclusion made is not everything known about the herb. This work highlights chemical composition of *Stevia rebaudiana* and its medicinal properties like antioxidant, antidiabetic, anti-inflammatory, antihypoglycaemic, anticancer, renal-healing, cardiac-healing, antilipidemic, and hepatoprotective effects.

Data Availability

The data supporting this review are from previously reported studies and datasets, which have been cited.

Conflicts of Interest

The authors declare that they have no conflicts of interest.

Supplementary Materials

Stevia extracts are obtained via a plethora of extraction techniques like solvent extraction, selective precipitation, supercritical fluids, and chromatographic adsorption among others. The extracts are then concentrated and purified using purification techniques like ion exchange chromatography and high-pressure liquid chromatography. The constituencies separated include amino acids, fats, mineral ions, terpenes, flavonoids, steviols, steviol glycosides, phenols, and polyphenols. Phenols and vitamins are antioxidants. These antioxidants play a crucial role as anticancer molecules. Anticancer properties were reported in a number of papers. The DNA synthesis of cancerous cells is lowered when subjected to Stevia extracts. Steviol glycosides have an anti-inflammatory property (proinflammatory factors production decreases) and steviosides have an antidiabetic (insulin sensitivity increased). Stevia extracts were reported to have antihyperlipidemic and hypotensive effects (fatty acid and cholesterol synthesis lowered; vascular diameter increased, respectively). Plant secondary metabolites in Stevia were found to have antibacterial and antifungal activities. Flavonoids in Stevia are thought to be responsible for hepatoprotective properties. *(Supplementary Materials)*

References

[1] F. Hossain, M. T. Islam, M. A. Islam, and S. Akhta, "Cultivation and uses of *Stevia (Stevia rebaudiana* Bertoni): a review," *African Journal of Food, Agriculture, Nutrition and Development*, vol. 17, no. 4, pp. 12745–12757, 2017.

[2] J. M. Geuns, "Stevioside," *Phytochemistry*, vol. 64, no. 5, pp. 913–921, 2003.

[3] J.-Y. Wang, C.-P. Chen, and S.-W. Tan, "A review of stevia as a potential healthcare product: up-to-date functional characteristics, administrative standards and engineering techniques," *Trends in Food Science & Technology*, vol. 103, pp. 264–281, 2020.

[4] Q. Zhang, G. Cheng, H. Qiu et al., "Expression of prostate stem cell antigen is downregulated during flavonoid-induced cytotoxicity in prostate cancer cells," *Experimental and Therapeutic Medicine*, vol. 14, no. 2, pp. 1795–1801, 2017.

[5] A.-M. Boudet, "Evolution and current status of research in phenolic compounds," *Phytochemistry*, vol. 68, no. 22-24, pp. 2722–2735, 2007.

[6] N. H. Aziz, S. E. Farag, L. A. Mousa, and M. A. Abo-Zaid, "Comparative antibacterial and antifungal effects of some phenolic compounds," *Microbios*, vol. 93, no. 374, pp. 43–54, 1998.

[7] M. Daglia, "Polyphenols as antimicrobial agents," *Current Opinion in Biotechnology*, vol. 23, no. 2, pp. 174–181, 2012.

[8] N. M. Hughes, H. S. Neufeld, and K. O. Burkey, "Functional role of anthocyanins in high-light winter leaves of the evergreen herb Galax urceolata," *The New Phytologist*, vol. 168, no. 3, pp. 575–587, 2005.

[9] C. Bender, S. Graziano, and B. F. Zimmermann, "Study of *Stevia rebaudiana* Bertoni antioxidant activities and cellular properties," *International Journal of Food Sciences and Nutrition*, vol. 66, no. 5, pp. 553–558, 2015.

[10] S. Singh, V. Garg, and D. Yadav, "Antihyperglycemic and antioxidative ability of *Stevia rebaudiana* (Bertoni) leaves in diabetes induced mice," *International Journal of Pharmacy and Pharmaceutical Sciences*, vol. 5, no. 2, pp. 297–302, 2013.

[11] A. B. Kunnumakkara, B. L. Sailo, K. Banik et al., "Chronic diseases, inflammation, and spices: how are they linked?," *Journal of Translational Medicine*, vol. 16, no. 1, p. 14, 2018.

[12] R. Medzhitov, "Inflammation 2010: new adventures of an old flame," *Cell*, vol. 140, no. 6, pp. 771–776, 2010.

[13] S. E. Shoelson, J. Lee, and A. B. Goldfne, "Inflammation and insulin resistance," *The Journal of Clinical Investigation*, vol. 116, no. 7, pp. 1793–1801, 2006.

[14] Q. Xin, B. Bai, and W. Liu, "The analgesic effects of oxytocin in the peripheral and central nervous system," *Neurochemistry International*, vol. 103, pp. 57–64, 2017.

[15] A. Roberts and I. Munro, "Stevioside and related compounds: therapeutic benefits beyond sweetness," *Pharmacology & Therapeutics*, vol. 122, no. 3, pp. e1–2; author reply e3, 2009.

[16] L. Fengyang, F. Yunhe, L. Bo et al., "Stevioside suppressed inflammatory cytokine secretion by downregulation of NF-κB and MAPK signaling pathways in LPS-stimulated RAW264.7 cells," *Inflammation*, vol. 35, no. 5, pp. 1669–1675, 2012.

[17] J. Meng, C. H. Zhou, B. Hu et al., "Stevioside prevents wear particle-induced osteolysis by inhibiting osteoclastogenesis and inflammatory response via the suppression of TAK1 activation," *Frontiers in Pharmacology*, vol. 9, p. 1053, 2018.

[18] T. Wang, M. Guo, X. Song et al., "Stevioside plays an Anti-inflammatory role by regulating the NF-κB and MAPK pathways in *S. aureus*-infected mouse mammary glands," *Inflammation*, vol. 37, no. 5, pp. 1837–1846, 2014.

[19] Q. Ma, "Role of nrf2 in oxidative stress and toxicity," *Annual Review of Pharmacology and Toxicology*, vol. 53, pp. 401–426, 2013.

[20] U. Ahmad and R. S. Ahmad, "Anti diabetic property of aqueous extract of *Stevia rebaudiana* Bertoni leaves in streptozotocin-induced diabetes in albino rats," *BMC Complementary and Alternative Medicine*, vol. 18, no. 1, p. 179, 2018.

[21] J. C. Chang, M. C. Wu, I. M. Liu, and J. T. Cheng, "Increase of insulin sensitivity by stevioside in fructose-rich chow-fed rats," *Hormone and Metabolic Research*, vol. 37, no. 10, pp. 610–616, 2005.

[22] R. Assaei, P. Mokarram, S. Dastghaib et al., "Hypoglycemic effect of aquatic extract of stevia in pancreas of diabetic rats: PPARγ-dependent regulation or antioxidant potential," *Avicenna Journal of Medical Biotechnology*, vol. 8, no. 2, pp. 65–74, 2016.

[23] J. M. Geuns, J. Buyse, A. Vankeirsbilck, and E. H. Temme, "Metabolism of stevioside by healthy subjects," *European Journal of Clinical Investigation*, vol. 232, no. 1, pp. 164–173, 2007.

[24] C. L. Li, L. H. Tan, Y. F. Wang et al., "*Comparison of anti-inflammatory effects of berberine, and its natural oxidative and reduced derivatives from Rhizoma Coptidis _in vitro_ and _in vivo_*," *Phytomedicine*, vol. 52, pp. 272–283, 2019.

[25] T. Tomita, N. Sato, T. Arai et al., "Bactericidal activity of a fermented hot-water extract from *Stevia rebaudiana* Bertoni towards enterohemorrhagic *Escherichia coli* O157: H7 and other foodborne pathogenic bacteria," *Microbiology and Immunology*, vol. 41, no. 12, pp. 1005–1009, 1997.

[26] K. Das and A. N. Kathiriya, "Hepatoprotective activity of *Stevia rebaudiana* Bert. leaves against thioacetamide induced toxicity," *Turk Journal of Pharmaceutical Sciences*, vol. 9, no. 3, pp. 343–352, 2012.

[27] H. Wang, R. Peng, R. Kong, and Y. Li, "Serum glutathione S-transferase activity as an early marker of thioacetimide-induced acute hepatotoxicity in mice," *Wei Sheng Yan Jiu*, vol. 28, no. 3, pp. 179-180, 1999.

[28] M. I. Torres, I. Fernandez, L. Fontana, A. Gil, and A. Rios, "Influence of dietary nucleotides on liver structural recovery and hepatocyte binuclearity in cirrhosis induced by thioacetamide," *Gut*, vol. 38, no. 2, pp. 260–264, 1996.

[29] E. Ramos-Tovar, R. E. Flores-Beltrán, S. Galindo-Gómez, J. Camacho, V. Tsutsumi, and P. Muriel, "An aqueous extract of *Stevia rebaudiana* variety Morita II prevents liver damage in a rat model of cirrhosis that mimics the human disease," *Annals of Hepatology*, vol. 18, no. 3, pp. 472–479, 2019.

[30] L. Bhatt, J. Amraita, M. Chakraborty, and J. Kamath, "Evaluation of cardioprotection and bio-efficacy enhancement of stevioside and diltiazem in rats," *Future Journal of Pharmaceutical Sciences*, vol. 6, no. 1, p. 34, 2020.

[31] E. Martínez-Rojo, R. Cariño-Cortés, L. C. Berumen, G. García-Alcocer, and J. Escobar-Cabrera, "*Stevia eupatoria* and *Stevia pilosa* extracts inhibit the proliferation and migration of prostate cancer cells," *Medicinia*, vol. 56, no. 2, p. 90, 2020.

[32] C. Panagiotou, C. Mihailidou, G. Brauhli, O. Katsarou, and P. Moutsatsou, "Effect of steviol, steviol glycosides and *stevia* extract on glucocorticoid receptor signaling in normal and cancer blood cells," *Molecular and Cellular Endocrinology*, vol. 460, pp. 189–199.

[33] V. López, S. Pérez, A. Vinuesa, C. Zorzetto, and O. Aban, "*Stevia rebaudiana* ethanolic extract exerts better antioxidant properties and antiproliferative effects in tumour cells than its diterpene glycoside stevioside," *Food & Function*, vol. 7, no. 4, pp. 2107–2113, 2016.

[34] L. Vaško, J. Vašková, A. Fejerˇcáková, G. Mojžišová, and J. Poráˇcová, "Comparison of some antioxidant properties of plant extracts from Origanum vulgare, Salvia officinalis, Eleutherococcus senticosus and *Stevia rebaudiana*," *In Vitro Cellular & Developmental Biology. Animal*, vol. 50, no. 7, pp. 614–622, 2014.

[35] J. Šic Žlabur, N. Dobričević, M. Brnčić et al., "Evaluation of the behavior of phenolic compounds and steviol glycosides of sonicated strawberry juice sweetened with stevia (Stevia *rebaudiana* Bertoni)," *Molecules*, vol. 24, no. 7, p. 1202, 2019.

[36] L. Khorsandi, M. Orazizadeh, F. Niazvnd, M. R. Abbaspour, E. Mansouri, and A. Khodadadi, "Quercetin induces apoptosis and necroptosis in MCF-7 breast cancer cells," *Bratislavské Lekárske Listy*, vol. 118, no. 2, pp. 123–128, 2017.

[37] S. D. Singh and G. P. Rao, "Stevia: the herbal sugar of 21st century," *Sugar Tech.*, vol. 7, no. 1, pp. 17–24, 2005.

[38] V. Peteliuka, L. Rybchuka, M. Bayliaka, K. B. Storey, and O. Lushchaka, "Natural sweetener *stevia rebaudiana*: functionalities, health benefits and potential risks," *EXCLI Journal*, vol. 20, pp. 1412–1430, 2021.

[39] J. Borgo, L. C. Laurella, F. Martini, C. A. N. Catalán, and V. P. Sülsen, "*Stevia genus*: phytochemistry and biological activities update," *Molecules*, vol. 26, no. 9, pp. 2733–2745, 2021.

Hindawi
Journal of Nanomaterials
Volume 2022, Article ID 1982554, 7 pages
https://doi.org/10.1155/2022/1982554

Research Article

Application of Health Education Model Based on Theory of Behavior Change in Nursing Care of Patients with Chronic Hepatitis B

Ying Luo,[1] Zhenhua Dong,[2] and Suying Qi[1]

[1]*Department of Digestive Liver Oncology, Third People's Hospital of Changzhou, Jiangsu 213001, China*
[2]*Department of Orthopedics and Neurosurgery, Third People's Hospital of Changzhou, Jiangsu 213001, China*

Correspondence should be addressed to Suying Qi; syqi211@126.com

Received 20 February 2022; Accepted 14 March 2022; Published 28 March 2022

Academic Editor: Weiguo Li

Chronic hepatitis B (CHB) is a lifelong disease that harms human health. Bad lifestyle can induce and aggravate liver dysfunction of patients with CHB and even cause liver cirrhosis and liver cancer. Therefore, it is very important to help patients with CHB establish a good lifestyle to control their liver function deterioration. In this study, the theory of behavior change was applied to the nursing process of patients with CHB. The results showed that this method could help to improve liver function of patients with CHB, improve patients' compliance behavior, and promote the development of self-management behavior ability and then improve patient satisfaction, which was worthy of promotion.

1. Introduction

Chronic hepatitis B (CHB) is a systemic infectious disease caused by hepatitis B virus infection, with clinical manifestations of liver inflammation and necrotizing lesions [1]. To control the adverse effect of disease progression on prognosis, patients with CHB often require long-term medication to nourish and protect the liver. However, clinical investigations have revealed that disease cognition deficiency is common in patients with CHB [2]. In addition, the disease needs long treatment period and high cost, which may result in low self-management ability and insufficient medication compliance and affect the prognosis [3]. Therefore, it is necessary to adopt effective means of health education in order to improve the self-management ability of this group of patients.

Health education is not only the main way to improve CHB patients' understanding of the disease, but also the key step in clinical nursing of CHB [4]. The theory of behavior change is an intervention model that provides targeted behavioral support and helps those in need to change or establish healthy behaviors according to needs [5]. At present, there is no literature report that health behavior change theory is applied to health education of CHB patients. This study analyzes the application effect of health education model based on theory of behavior change in the nursing of patients with chronic hepatitis B, aiming at providing theoretical support for broadening the health education methods in CHB nursing, which is reported as follows.

2. Information and Methods

2.1. General Information. A total of 110 patients with CHB who visited our hospital from January 2020 to January 2021 were selected as the research subjects, including 59 males and 51 females. Their age ranged from 43 to 70 years old, and the average age was 59.84 ± 6.33 years old. According to the difference in nursing methods, the patients were divided into study group and control group, 55 cases in each group. There were 30 males and 25 females in the research group. Their age ranged from 44 to 70 years old, with an average age of 59.51 ± 6.74 years old. There were 29 males

and 26 females in the control group. Their age ranged from 43 to 69 years old, with an average age of 59.52 ± 6.46 years old. There was no statistically significant difference in general information between the two groups, and they were comparable ($P > 0.05$).

2.2. Inclusion Criteria. The inclusion criteria are as follows: (i) serological indicators HBsAg-HBc positive, diagnosed as CHB; (ii) the patients' consciousness and thinking are clear; (iii) the patient himself/herself agreed to participate in this trial; (iv) the patients with primary school education or above were able to cooperate with the trial; and (v) the patients are over 18 years of age.

2.3. Exclusions Criteria. The exclusion criteria are as follows: (i) patients with combined cardiopulmonary insufficiency; (ii) patients with severe hearing impairment or aphasia; (iii) patients with psychiatric disorders; (iv) patients with diseases of immune system; and (v) patients with hematological diseases and other chronic or acute infectious diseases.

2.4. Methodology. The patients in the control group received routine nursing intervention. The causes, transmission routes, relevant protective measures, treatment methods, possible complications, and prognosis of CHB were explained in detail to patients by PPT, short video, animation, and other methods. Carry out psychological nursing to help patients maintain a stable mood. Inform them of the adverse effects of bad emotions on disease recovery, and urge them to actively cooperate with treatment. The patients were guided to establish regular living habits and maintain adequate sleep. It is suggested that the patients should take easily digested and light food as their main dietary habit, eat more fresh fruits and vegetables, strictly prohibit spicy and excitant food, and give up smoking and drinking. The nursing staff should always keep ward environment clean and tidy. Explain the harmfulness of irrational drug use to patients, ask them to take drugs on time and according to the amount, and explain the adverse reactions of various drugs and the corresponding treatment measures. After the patient's condition is stable, he can be assisted to carry out appropriate amount of exercise. After discharge, patients were followed up by telephone to strengthen their ability to cope with adverse events.

The patients in study group were intervened by adding the theory of behavior change on the basis of routine nursing. (i) Set up a nursing intervention group: Set up a nursing intervention group including one attending physician, one head nurse, one dietitian, and several responsible nurses. Organize all members to learn the clinical treatment and nursing knowledge of CHB and behavior change theory, and develop health education programs for CHB patients on the basis of behavior change theory. When the patients were admitted to the hospital, they were evaluated by the CHB behavioral stage change questionnaire made by the hospital, and the behavioral stages of the patients were comprehensively analyzed, and then targeted nursing, health education and behavioral guidance were provided to the patients at different stages. (ii) Intervention during the prethinking: The patients in the prethinking stage had no intention of changing their health behaviors and did not understand the role of behavior change. Therefore, upon admission, nursing staff could issue targeted self-management cards to let them understand that the recovery of the disease was closely related to their management abilities. The contents of the card include knowledge about chronic hepatitis, exercise advice, dietary guidance, psychological care, regular check-ups, and other aspects. Subsequently, the patients were followed up for more than 15 minutes once or twice a week to consolidate their understanding of chronic hepatitis. (iii) Intervention during the thinking period: The patients in this stage have the idea to changing their behaviors and are willing to accept the related changes but did not take action. At this point, the nursing staff should formulate daily behavior management requirements according to the patient's situation, explain and demonstrate when necessary, and standardize its code of conduct. (iv) Intervention during the preparation period: The patients at this stage made some preparations for the paying action. At this stage, the nurse needs to formulate daily behavior management requirements according to the patient's situation. Explain and demonstrate the rules when necessary to regulate patient behavior. (v) Intervention during the action period: The patients at this stage have taken certain actions, but the state is not stable and may return to the previous state. And the nursing staff needs to strengthen the patient's ability at this time. In the nursing work, the patients' changes can be recognized and encouraged through regular lectures or communication meetings. At the same time, the patients with good therapeutic effects are encouraged to share their experiences, so as to help patients learn how to overcome the problems encountered in self-management. At the same time, the nurses should also guide the patients' failed behaviors to improve the patients' enthusiasm to maintain change. (vi) Intervention during the maintenance period: The patients at this stage have changed their behavior into habits and have confidence, and the possibility of returning to the original stage is reduced. The doctors and nurses can regularly hold seminars and other activities to supplement the knowledge of patients and inform them of the various hazards of chronic hepatitis. At the same time, the patient's family members can also be encouraged to participate so that the family members can have more understanding and confidence in the patient and inform the family members to urge the patient to take medicine on time and develop good living habits. In addition, the medical staff can use the relevant WeChat groups or WeChat official account to prevent patients from being unable to maintain established healthy behaviors due to environmental changes or insufficient self-efficacy and urge them to return to society.

The patients in both groups received nursing intervention for 6 months.

2.5. Observation Indicators

(i) To evaluate the changes of liver function indexes of all patients before and after six months of

Table 1: Comparison of liver function indicators between the two groups before and after intervention ($\bar{x}$±s).

Group	ALT (U/L)		TBIL (μmol/L)		DBIL (μmol/L)		ALB (g/L)		HBV-DNA (cps/mL)	
	Before intervention	After intervention	Before intervention	After intervention	Before intervention	After intervention	Before intervention	After intervention	Before intervention	After intervention
Study group ($n = 55$)	79.18 ± 4.66	43.59 ± 5.41[a]	26.57 ± 3.49	16.55 ± 2.17[a]	7.59 ± 1.82	4.31 ± 1.08[a]	40.72 ± 8.51	65.18 ± 7.65[a]	1019.25 ± 96.46	1006.45 ± 90.88[a]
Control group ($n = 55$)	78.83 ± 4.71	49.94 ± 5.27[a]	26.74 ± 3.51	19.94 ± 3.24[a]	7.64 ± 1.71	5.26 ± 1.17[a]	41.08 ± 8.44	60.17 ± 7.33[a]	1020.87 ± 97.58	1015.98 ± 91.65[a]
t	0.392	6.235	0.255	6.447	0.148	4.425	0.223	3.507	0.088	0.548
P	0.696	<0.001	0.799	<0.001	0.882	<0.001	0.824	0.001	0.930	0.585

Note: comparison with before intervention, [a]$P < 0.05$.

intervention, including alanine amino transferase (ALT), serum total bilirubin (TBIL), serum direct bilirubin (DBIL), albumin (ALB), and HBV-DNA. 3 ml fasting venous blood was taken from all patients before admission and after treatment, and supernatant was taken after centrifugation. Architectc-8000 automatic biochemical analyzer (made by ABBOTT) was used to measure the level of each indicator, strictly following the instructions.

(ii) Medication compliance: The self-made medication compliance questionnaire was used to investigate the medication compliance of the two groups before and after intervention. There were seven questions in the questionnaire, and the answer "Yes" was 0 point, and the answer "No" was 1 point, with full scores of 8. The score below 6 points was low compliance, 6–7 points was medium compliance, and 8 points was high compliance [6].

(iii) Self-management ability: The health self-management ability scale (AHSNSRS) was used to assess the self-management ability of patients in two groups before and after intervention. The scale totally included three contents: self-management cognition (14 items), self-management behavior (14 items), and self-management environment (40 items), which was scored according to the Likert5-level scoring method. A higher score means more self-management [7].

(iv) Self-efficacy: Self-efficacy was assessed using the General Self-Efficacy Scale (GSES) and Likert 4-level scoring system. Each item was rated as L–4, and there were 10 items in total as 10–40 points. The higher the score was, the stronger the self-efficacy was [8].

(v) Hope level: The Herth Hope Scale (HHI) [9] was used to assess the change of hope level before and after intervention in the two groups. The 12 items included three dimensions: maintaining close relationship with others (I), positive attitude towards reality and the future (T), and taking positive action (P). According to the Likert4-level scoring system, the higher the score was, the higher the desired level would be.

(vi) Nursing satisfaction: The nursing service satisfaction was evaluated for all patients by self-made nursing satisfaction questionnaire. The total score of this scale is 100 points, with the score ≥90 points was considered as satisfactory, with the score of 90–70 points as basic satisfactory, the score of 69–50 points as general satisfaction, and the score of <50 points as unsatisfactory. The total satisfaction is the sum of satisfaction rate and basic satisfaction rate [10].

2.6. Statistical Methods. SPSS22.0 software was used for processing. The continuous variable data of experimental data were expressed as mean standard deviation ($\bar{x}\pm s$) and adopted t test. The classified variable data and descriptive analysis were expressed as (%) and adopted χ^2 test.

Table 2: Comparison of medication compliance between the two groups after intervention [n (%)].

Group	Low compliance	Medium compliance	High compliance
Study group ($n = 55$)	2 (3.64)	18 (32.73)	35 (63.63)
Control group ($n = 55$)	8 (14.55)	21 (38.18)	26 (47.27)
χ^2		3.960	
P		0.047	

3. Results

3.1. Comparison of Liver Function Indicators between the Two Groups before and after Intervention. ALT, TBIL, DBIL, ALB, and HBV-DNA in patients between the two groups before intervention were not statistically significant ($P > 0.05$). ALT, TBIL, and DBIL in the two groups after intervention were lower than those before intervention, while ALB was higher than that before intervention ($P < 0.05$). After intervention, ALT, TBIL, and DBIL of the treatment group were lower than those of the control group, while ALB was higher than those of the control group ($P < 0.05$). There was no significant difference in HBV-DNA level between the two groups before and after intervention ($P > 0.05$, Table 1).

3.2. Comparison of Medication Compliance between the Two Groups after Intervention. The patients with high compliance in the study group were significantly higher than those in the control group, and the medication compliance between the two groups was statistically significant ($P < 0.05$, Table 2).

3.3. Comparison of Self-Management Ability and Self-Efficacy between the Two Groups before and after Intervention. There was no significant difference in self-management cognition, self-management behavior, self-management environment, and self-efficacy between the two groups before the intervention ($P > 0.05$). After the intervention, the self-management cognition, self-management behavior, self-management environment, and self-efficacy of the two groups increased compared with those before the intervention ($P < 0.05$). And the study group was higher than the control group ($P < 0.05$, Table 3).

3.4. Comparison of Self-Efficacy between the Two Groups before and after Intervention. There was no significant difference in self-efficacy between the two groups before intervention ($P > 0.05$), but the self-efficacy of the two groups increased after intervention as compared with that before intervention ($P < 0.05$). And the level in the study group was higher than that in the control group ($P < 0.05$, Table 4).

Table 3: Comparison of self-management ability and self-efficacy between the two groups before and after intervention ($\bar{x}$±s, score).

Group	Self-management cognition		Self-management behavior		Self-management environment		Self-efficacy	
	Before intervention	After intervention	Before intervention	After intervention	Before intervention	After intervention	Before intervention	After intervention
Study group (n = 55)	40.19 ± 7.54	67.59 ± 5.63[a]	46.81 ± 5.97	66.12 ± 6.17[a]	38.58 ± 6.19	47.99 ± 7.14[a]	21.59 ± 6.43	35.14 ± 3.75[a]
Control group (n = 55)	41.85 ± 7.43	60.11 ± 5.76[a]	47.18 ± 5.66	61.08 ± 6.25[a]	39.23 ± 6.21	41.84 ± 6.52[a]	22.25 ± 6.17	30.39 ± 3.87[a]
t	1.163	6.887	0.334	12.700	0.550	4.717	0.549	6.537
P	0.247	<0.001	0.739	<0.001	0.584	<0.001	0.584	<0.001

Note: comparison with before intervention, [a]$P < 0.05$.

Table 4: Comparison of self-efficacy between the two groups before and after intervention ($\bar{x}$±s, score).

Group	Before intervention	After intervention
Study group (n = 55)	21.59 ± 6.43	35.14 ± 3.75[a]
Control group (n = 55)	22.25 ± 6.17	30.39 ± 3.87[a]
t	0.549	6.537
P	0.584	<0.001

Note: comparison with before intervention, [a]$P < 0.05$.

3.5. Comparison of Hope Levels between the Two Groups before and after Intervention. There was no significant difference in the desired level between the two groups before intervention ($P > 0.05$). After intervention, the hope levels of the two groups were higher than those before intervention, and the hope levels in the research group were higher than those in the control group ($P < 0.05$, Table 5).

3.6. Comparison of Nursing Satisfaction between the Two Groups. The nursing satisfaction degree in the research group was higher than that in the control group ($P < 0.05$, Table 6).

4. Discussion

CHB is a public health problem of global concern. Clinical data show that there are individual differences in the prognosis of CHB patients, and some studies have pointed out that such a variety of clinical manifestations are the result of the combined effects of environmental factors, genetic factors, viral factors, and individual factors [11]. Individual factors were mainly related to disease cognition, including unscientific eating habits, drinking alcohol, poor lifestyle such as long-term lack of sleep, and not taking drugs according to the doctor's advice. And these factors can induce a variety of psychological stress reactions, leading to a decrease in patients' hope level and negative treatment of the disease and treatment [12]. Therefore, in the long-term treatment of CHB, it is of great significance to promote the patients to develop self-management behavior ability, help them to correctly understand the disease, and maintain good compliance with the doctor's advice [13].

All the subjects in this study were in the active stage of hepatitis, so all the indexes of liver function were abnormal at admission. After the intervention, the ALT, TBIL, and DBIL of patients in the study group were lower than those before the intervention, and ALB was higher than those before the intervention ($P < 0.05$). This indicates that the health education model based on behavior change theory has a significant effect in improving the liver function of patients with CHB. The theoretical model of behavioral transformation in stages points out that the change of human behavior or the establishment of a healthy behavior is a dynamic and continuous process in stages [14]. In this study, the behavior changes of patients with CHB during clinical treatment were divided into five stages, i.e., prethinking stage, thinking stage, preparation stage, action stage, and maintenance stage. Through personalized and targeted care for patients, they can be promoted to advanced stages of transformation so that they establish a healthy lifestyle.

Previous findings found that most patients were in the prethinking stage and the thinking stage during hospitalization [15]. At this stage, some patients are not aware of their problematic behaviors, so they do not want to take action. Other patients have realized the positive benefits of behavior change, but they are still weighing the cost of behavior change. Therefore, for patients at this stage, it is necessary to strengthen the publicity of disease-related knowledge, so as to improve patients' awareness of lifestyle change and timely evaluation of patients' unhealthy lifestyle, according to the evaluation results to formulate reasonable nursing strategies [16]. For the patients in the preparation stage and the action stage, it is necessary to adjust the daily life precautions, diet, medication guidance, and emotional adjustment [17]. At the same time, the patients at this stage have not fully mastered the disease knowledge, and their compliance behavior is relatively poor. Therefore, at this stage, we should improve their sense of responsibility, strengthen their self-management ability, and make use of the liver function results with improved self-efficacy, so as to improve patients' confidence in treatment and promote patients to establish a healthy lifestyle [18]. At the initial stage after discharge, the patients' treatment environment changes, they will forget relevant knowledge, and the bad behavior may still recur [19]. Therefore, the nurses need to continue to urge and guide patients in outpatient follow-up, so as to prevent patients from returning to the previous stage of behavior. In the later stage, the patients have learned the importance of controlling and maintaining

Table 5: Comparison of hope levels between the two groups before and after intervention ($\bar{x}$±s, score).

Group	T		I		P	
	Before intervention	After intervention	Before intervention	After intervention	Before intervention	After intervention
Study group (n = 55)	8.43 ± 2.13	13.79 ± 1.74[a]	8.51 ± 1.96	13.28 ± 2.17[a]	8.47 ± 2.18	13.59 ± 1.66[a]
Control group (n = 55)	8.51 ± 2.14	10.44 ± 1.87[a]	8.66 ± 1.78	11.49 ± 1.94[a]	8.55 ± 2.14	10.38 ± 1.74[a]
t	0.197	9.726	0.420	4.555	0.194	9.899
P	0.845	<0.001	0.675	<0.001	0.846	<0.001

Note: comparison with before intervention, [a]P<0.05.

Table 6: Comparison of nursing satisfaction between the two groups [*n* (%)].

Group	Satisfactory	Basic satisfactory	General satisfaction	Unsatisfactory	Nursing satisfaction
Study group (*n* = 55)	26 (45.45)	20 (36.36)	7 (12.73)	2 (3.64)	83.64
Control group (*n* = 55)	21 (38.18)	16 (29.09)	14 (25.45)	4 (7.27)	67.27
χ^2			3.976		
P			0.046		

liver function, and a good lifestyle has become a habit, but there is still the possibility of insufficient self-efficacy and difficulty in resisting external temptation [20]. At this time, giving support and strengthening management can better help patients to maintain healthy behaviors [21]. The results showed that with the improvement of cognitive level, the self-management cognition, self-management behavior, self-management environment, and self-efficacy of patients in the study group were significantly higher than those in the control group. This further indicates that health education based on the integration theory of health behavior change is helpful to improve the self-management ability of CHB patients. In addition, this may also be the main reason for the improvement of patient satisfaction in the study group.

In summary, the addition of health education model based on the theory of behavior change in the care of patients with CHB contributes to the improvement of liver function, improves patients' compliance behavior, promotes the development of self-management behavior ability, and improves patient satisfaction, which is worthy of promotion.

Data Availability

The primary data to support the results of this study are available at reasonable request to the Corresponding Author.

Ethical Approval

This study was approved by the Ethics Committee of our hospital.

Conflicts of Interest

The authors declare no conflict of interest, financial or otherwise.

References

[1] T. Inoue and Y. Tanaka, "Novel biomarkers for the management of chronic hepatitis B," *Clinical and Molecular Hepatology*, vol. 26, no. 3, pp. 261–279, 2020.

[2] C. S. Coffin, K. Zhou, and N. A. Terrault, "New and old biomarkers for diagnosis and management of chronic hepatitis B virus infection," *Gastroenterology*, vol. 156, no. 2, pp. 355–368.e3, 2019.

[3] M. Belopolskaya, V. Avrutin, O. Kalinina, A. Dmitriev, and D. Gusev, "Chronic hepatitis B in pregnant women: current trends and approaches," *World Journal of Gastroenterology*, vol. 27, no. 23, pp. 3279–3289, 2021.

[4] A. Koffas, M. Kumar, U. S. Gill, A. Jindal, P. T. F. Kennedy, and S. K. Sarin, "Chronic hepatitis B: the demise of the 'inactive carrier' phase," *Hepatology International*, vol. 15, no. 2, pp. 290–300, 2021.

[5] Z. Meng, Y. Chen, and M. Lu, "Advances in targeting the innate and adaptive immune systems to cure chronic hepatitis B virus infection," *Frontiers in Immunology*, vol. 10, no. 35, p. 3127, 2019.

[6] N. E. Airewele and M. L. Shiffman, "Chronic hepatitis B virus in patients with chronic hepatitis C virus," *Clinics in Liver Disease*, vol. 25, no. 4, pp. 817–829, 2021.

[7] B. Testoni, F. Lebossé, C. Scholtes et al., "Serum hepatitis B core-related antigen (HBcrAg) correlates with covalently closed circular DNA transcriptional activity in chronic hepatitis B patients," *Journal of Hepatology*, vol. 70, no. 4, pp. 615–625, 2019.

[8] M. Tan, A. S. Bhadoria, F. Cui et al., "Estimating the proportion of people with chronic hepatitis B virus infection eligible for hepatitis B antiviral treatment worldwide: a systematic review and meta-analysis," *The Lancet Gastroenterology & Hepatology*, vol. 6, no. 2, pp. 106–119, 2021.

[9] Y. W. Shi, R. X. Yang, and J. G. Fan, "Chronic hepatitis B infection with concomitant hepatic steatosis: current evidence and opinion," *World Journal of Gastroenterology*, vol. 27, no. 26, pp. 3971–3983, 2021.

[10] J. Zhang, S. Lin, D. Jiang et al., "Chronic hepatitis B and non-alcoholic fatty liver disease: conspirators or competitors?," *Liver International*, vol. 40, no. 3, pp. 496–508, 2020.

[11] T. Cargill and E. Barnes, "Therapeutic vaccination for treatment of chronic hepatitis B," *Clinical and Experimental Immunology*, vol. 205, no. 2, pp. 106–118, 2021.

[12] Y. Liu, M. Jiang, J. Xue, H. Yan, and X. Liang, "Serum HBV RNA quantification: useful for monitoring natural history of chronic hepatitis B infection," *BMC Gastroenterology*, vol. 19, no. 1, p. 53, 2019.

[13] M. L. Shiffman, "Approach to the patient with chronic hepatitis B and decompensated cirrhosis," *Liver International*, vol. 40, no. S1, pp. 22–26, 2020.

[14] W. J. Rejeski and J. Fanning, " Models and theories of health behavior and clinical interventions in aging: a contemporary, integrative approach ," *Clinical Interventions in Aging*, vol. Volume 14, no. 35, pp. 1007–1019, 2019.

[15] S. Medlock and J. C. Wyatt, "Health behaviour theory in health informatics: support for positive change," *Studies in Health Technology and Informatics*, vol. 263, no. 14, pp. 146–158, 2019.

[16] E. Boulton, H. Hawley-Hague, D. P. French et al., "Implementing behaviour change theory and techniques to increase physical activity and prevent functional decline among adults aged 61-70: the PreventIT project," *Progress in Cardiovascular Diseases*, vol. 62, no. 2, pp. 147–156, 2019.

[17] R. Tapera, B. Mbongwe, M. Mhaka-Mutepfa, A. Lord, N. A. Phaladze, and N. M. Zetola, "The theory of planned behavior as a behavior change model for tobacco control strategies among adolescents in Botswana," *PLoS One*, vol. 15, no. 6, article 233462, 2020.

[18] R. Watakakosol, P. Suttiwan, S. T. Ngamake et al., "Integration of the theory of planned behavior and transtheoretical model of change for prediction of intentions to reduce or stop alcohol use among Thai adolescents," *Substance Use & Misuse*, vol. 56, no. 1, pp. 72–80, 2021.

[19] V. Klusmann, A. J. Gow, P. Robert, and G. Oettingen, "Using theories of behavior change to develop interventions for healthy aging," *The Journals of Gerontology. Series B, Psychological Sciences and Social Sciences*, vol. 76, Supplement_2, pp. S191–S205, 2021.

[20] M. R. Harrington, M. Ickes, K. Bradley, and M. Noland, "The theory of planned behavior and the USDA _summer food service program_," *Journal of Nutrition Education and Behavior*, vol. 52, no. 10, pp. 944–951, 2020.

[21] T. Baranowski, C. Ryan, A. Hoyos-Cespedes, and A. S. Lu, "Nutrition education and dietary behavior change games: a scoping review," *Games for health journal*, vol. 8, no. 3, pp. 153–176, 2019.

Hindawi
Journal of Nanomaterials
Volume 2022, Article ID 9000689, 10 pages
https://doi.org/10.1155/2022/9000689

Research Article

miR-622 Induces Breast Cancer Cell MCF-7 Proliferation, Migration, and Invasion by Directly Negatively Targeting EYA1

Pan Tang,[1] **Yanyan Shen**,[1] **Jihui Yang**,[2] **Nan Wen**,[1] **Ying Liu**,[1] **Qiqing Zeng**,[1] **and Tingting Yin**[1]

[1]*The Affiliated Nanhua Hospital, Department of Ultrasound Medicine, Hengyang Medical School, University of South China, Hengyang, Hunan 421001, China*
[2]*Department of Ultrasound Medicine, Hunan Provincial People's Hospital, Changsha, Hunan, China*

Correspondence should be addressed to Yanyan Shen; syybwk@163.com

Received 5 November 2021; Accepted 13 December 2021; Published 6 January 2022

Academic Editor: Weiguo Li

Breast cancer is the most common female cancer in the world. Breast cancer patients are currently treated with a combination of surgery, chemotherapy, radiotherapy, and targeted therapy, but the 5-year overall survival rate is still low. Therefore, we plan to explore the potential interaction mechanism between miR-622 and EYA1 in the breast cancer cells and their effect on proliferation, migration, and invasion of breast cancer, to lay a foundation for the gene therapy of breast cancer and improve the therapeutic effect. This study found that miR-622 was highly expressed in breast cancer cell lines, while EYA1 was poorly. In MCF-7 cell line, miR-622 had the highest expression level, while EYA1 had the lowest. Besides, the bioinformatics analysis showed that EYA1 possesses putative miR-622 binding sites within its 3′UTR. The increased miR-622 significantly enhanced the proliferation, migration, and invasion of MCF-7 cell line and inhibited luciferase reporter activity in the 3′UTR of EYA1-WT. When upregulating the expression of miR-622, the mRNA and protein expression levels of EYA1 were significantly decreased. We also found that the silencing of EYA1 promoted the proliferation, migration, and invasion of breast cancer MCF-7 cell line. These results indicate that miRNA-622 plays a tumor-promoting role in breast cancer through targeted negative regulation of EYA1, suggesting that miRNA-622 may become a potential target for breast cancer treatment.

1. Introduction

Breast cancer is a malignant tumor growing in the epithelial tissue of the breast. In recent years, the incidence of breast cancer among women in the world has been rising continuously, surpassing lung cancer for the first time and becoming the largest cancer in the world [1, 2]. It is estimated that by the end of 2020, there will be about 279,100 new confirmed cases of breast cancer in the United States alone [3]. It is the second leading cause of cancer-related deaths among women in the world [3, 4]. Many studies have made significant progress in early detection, diagnosis, surgery, radiotherapy, and chemotherapy of breast cancer, but there are still a large number of patients who have distant metastasis and become resistant to radiotherapy and chemotherapy [5]. Therefore, it is of great significance to further study the molecular mechanism and signal transduction pathway of breast cancer progression and find new targets for improving breast cancer treatment methods and improving patients' quality of life.

MicroRNAs (miRNAs), small RNA molecules composed of 17-22 nucleotide acids, are able to regulate their target genes directly by binding with their 3′ untranslated regions [6]. It has been estimated that over 30% of all protein-coding genes in humans are regulated by miRNAs [7]. Due to the difference of miRNA expression between tumor tissues and normal tissues, as well as its characteristics of endogenous, low toxicity, and multitarget, the value of miRNA in tumor diagnosis and treatment has attracted more and more attention. A large number of studies have shown that miRNA plays an important role in the process of breast cancer proliferation and metastasis. For example,

miR-98-5p regulates breast cancer proliferation by targeting Gab2 [8]. Moreover, miR-19, miR-136, miR-221/222, and other miRNAs have been proved to be related to the invasion and metastasis of breast cancer [9–11].

The miR-622 coding gene is mapped to chromosome 13q31.3. Studies have shown that the expression of miR-622 is downregulated in uveal melanoma, human colon cancer, papillary thyroid carcinoma, and other tumors; at the same time, acting as a tumor inhibitor in these types of cancer can inhibit the proliferation, migration, and invasion of a variety of tumor cells from achieving the effect of tumor inhibition by targeting G3BP1, UNC5B, and VEGFA genes [12–14]. Orlandella et al. [15] found that miRNA-622 could inhibit the invasion and migration of breast cancer cell lines MCF-7 and MDA-MB-231 through in vitro studies. Liu et al. [16] also proposed that miR-622 overexpression could inhibit breast cancer cells' epithelial-mesenchymal transition (EMT) by downregulating RNF8, thus inhibiting the migration and invasion of breast cancer cells. However, the exact function and underlying mechanisms of miR-622 in the development of breast cancer need further investigation.

EYA, a member of the retinal determinant gene network (RDGN) family, is a key regulator of eye morphogenesis in Drosophila [17]. Continuing research on the gene has revealed that members of the EYA family have become one of the "tumor markers" because of its overexpression, resistance to cell death, and promotion of angiogenesis, invasion, and metastasis [18]. As a member of its family, EYA1, by binding to SIX1, not only activated STAT3 signaling to promote the development of thyroid cancer but also played a key role in the progression of colorectal cancer [19, 20]. Wu et al. [21] studied the expression of EYA1 and found that EYA1 was upregulated in both breast cancer tissues and cell lines. EYA1 promoted the growth of cancer cells by promoting cell proliferation and DNA synthesis and reduced apoptosis. Guan et al. [22] proposed that miR-101 can directly target EYA1 to inhibit the proliferation and induce apoptosis of breast cancer cell [22]. Our bioinformatics analysis showed that EYA1 possesses putative miR-622 binding sites within its 3′UTR. Therefore, we intend to study the expression of EYA1 and miR-622 in breast cancer cell lines and their interaction mechanism through in vitro experiments to find new targets for breast cancer treatment.

2. Materials and Methods

2.1. Cell Culture. Human breast cancer BT474 cell line and the normal human breast epithelial cell line MCF-10A were purchased from Yuchun Biotech, Shanghai, China. MCF-7 and MDA-MB-231 cell lines were acquired from the Clinical Research Institute of the First Affiliated Hospital of University of South China. MCF-7, BT474, and MDA-MB-231 cell lines were cultured in DMEM medium (Gibco, USA) supplemented with 10% fetal bovine serum (FBS, Gibco, USA) and 1% penicillin-streptomycin solution (P/S, Gibco, USA). MCF-10A cell line was cultured in the MCF-10A special medium (Yaji Biotech, Shanghai, China, DMEM/F12 (PM150312)+5%HS (164215-100)+20 ng/mL EGF+0.5 μg/mL hydrocortisone+10 μg/mL insulin+1% NEAA (PB180424)+1% P/S (PB180120)). All cell lines were maintained at 37°C in a 5% CO_2 atmosphere. Exponentially growing cell lines were used for the experiments.

2.2. RNA Extraction and Quantitative Reverse Transcriptase-Polymerase Chain Reaction (qRT-PCR) Analysis. Total RNA was extracted from the cell lines according to the instructions of the RNA extraction kit (Jin Baite Biotech, Beijing, China), and the RNA was reverse-transcribed into cDNA by using the reverse transcription kit (Nuo Weizan Biotech, Nanjing, China). The U6 and GAPDH mRNA were used as internal references. The specific primers of miR-622, EYA1, and U6 were synthesized (Table 1). The qRT-PCR kit (Nuo Weizan Biotech, Nanjing, China) was used for testing. Reaction procedure: predenaturation at 95°C 10 sec; 95°C 5 sec, 40x; dissolution curve program: 95°C 60 sec; 55°C 30 sec; 95°C 30 sec. After the quantification, the relative quantitative analysis ($2^{-\triangle\triangle Ct}$) was used to measure the relative expression levels of miR-622 and EYA1 mRNA. All the reactions were performed three times.

2.3. Target Prediction. To determine whether EYA1 is a direct target of miR-622, we searched for the potential targets of miR-622 using the prediction programs, TargetScan (http://www.targetscan.org/), miRDB (http://www.mirdb.org/), and microbase (http://www.mirbase.org/).

2.4. Cell Transfection and Small RNA Interference. Take the cells in good condition in the logarithmic growth phase, digest them with pancreatin to make the single-cell suspension, inoculate them into a Petri dish, put them in an incubator overnight, and transfect them when the convergence of cells reaches 30%-50%. miR-622 mimic or its negative control (miR-NC) was transfected into the MCF-7 cells using Ribofactamine transfection reagent (Ruibo Biotech, Guangzhou, China) according to the instructions provided by the manufacturer. After transfection for 6 h, it was changed into a new complete medium and cultured under normal conditions for subsequent experiments. The transfection efficiency was examined according to the green fluorescence detected by a microscope.

To knockdown EYA1 expression, EYA1 siRNA (si-EYA1) and its negative control (siRNA-NC) (Ruibo Biotech, Guangzhou, China) were transfected into the MCF-7 cells. Following culture for 48 h, the cells were harvested and the expression level of EYA1 mRNA and protein was measured by qRT-PCR and western blot experiments.

2.5. Western Blot Analysis. Western blot kit (Dingguo Changsheng, Beijing, China) was used to detect the protein expression level of EYA1. Cells in each group were collected, the total protein was extracted with radioimmunoprecipitation assay buffer (RIPA, Yaji Biotech, Shanghai, China), and the protein concentration was detected by BCA Kit (Dingguo Changsheng, Beijing, China). Total protein samples were subjected to electrophoretic separation in an SDS polyacrylamide gel and then were electrotransferred to a PVDF membrane (GE, USA). The membranes were subsequently blocked with blocking fluid (Dingguo Changsheng, Beijing, China). Primary antibodies EYA1 (1 : 5000,

Table 1: Primer sequences for qRT-PCR.

Name	Sequences
Stem loop	GTCGTATCCAGTGCAGGGTCCGAGGTATTCGCACTGGATACGACGCTCCA
miR-622	Forward primers: 5′-GGGTCCGAGGTATTCGCACT-3′ Reverse primers: 5′-GCACAGTCTGCTGAGGTTGGA-3′
U6	Forward primers: 5′-CTCGCTTCGGCAGCACA-3′ Reverse primers: 5′-AACGCTTCACGAATTTGCGT-3′
EYA1	Forward primer: TTTGGCAACTGGTGTACGGG Reverse primer: GGAGTCGGTCAGGGCTTCA
GAPDH	Forward primer: CTGCCAACGTGTCAGTGGTG Reverse primer: TCAGTGTAGCCCAGGATGCC

ABclonal, USA, 55 kDa) and GAPDH (1 : 5000, ABclonal, USA, 36 kDa) were incubated at 4°C 14 h, and then, the membrane was incubated in the secondary antibody (goat anti-rabbit IgG labeled with horseradish peroxidase, 1 : 5000, ABclonal, USA) for 1 h at 25°C. The bands were detected by ECL high-efficiency chemiluminescence kit (Genview, USA), and analyzed by ImageJ software. The absorbance of protein bands in each group was determined, and the ratio of target band to GAPDH band was used as the protein expression. The experiment was carried out three times independently.

2.6. CCK-8 Cell Proliferation Assay. According to the manufacturer's instructions, the cell proliferation assay was performed with Cell Counting Kit-8 (CCK-8, Genview, USA). In brief, stably transfected MCF-7 cells were harvested and seeded onto 96-well plates at a density of 5.0×10^3 cells per well, continued to be cultured in a 5% CO_2 incubator at 37°C. After 12, 24, 48, and 72 hours, the cells were treated with 20 μL CCK-8 reagent and incubated for 2 h. The OD value at 450 nm was measured using a microplate imaging system. All experiments were repeated three times.

2.7. Wound Healing Assay. Cell migration was assessed by wound healing assay. After transfection for 48 h, MCF-7 cells in the logarithmic growth stage were inoculated into 6-well plates, and the cell concentration was adjusted to 2×10^5 cells/well. When the cells grew to 80-90% fusion, a sterile 10 μL pipet tip was used to lacerate the center of each hole. After scratching the cells for 0 h, the detached cells were washed with phosphate-buffered saline (PBS), and the remaining cells were cultured at 37°C for 12 h. Photographs were taken with the microscope at 0 h and 12 h. The percentage of wound healing between the two sides of the scratch for each image was measured using ImageJ software (National Institutes of Health). The cell migration assays were performed three independent times.

2.8. Transwell Assay. MCF-7 cell invasion was assessed in transwell chambers (Becton, Dickinson and Company, USA) following the manufacturer's instructions. Matrigel was coated on the upper chamber of transwell in advance, and then, cells of each group in the logarithmic growth phase after transfection for 48 h were resuspended in a serum-free medium and inoculated on Matrigel with 1×10^4 cells/well. The medium containing 20% FBS was added into the lower chamber and placed in a 5% CO_2 cell incubator at 37°C for 24 h. Cotton swabs wiped the noninvading cells and Matrigel matrix. After fixing with 4% formaldehyde for 10 min, wash with PBS 3 times, and stain with hematoxylin-eosin (HE, Dingguo Changsheng, Beijing, China). After PBS cleaning, 5 microscopic fields were randomly selected to observe the number of invaded cells (200x). All experiments were duplicated three times.

2.9. Dual-Luciferase Reporter Assay. To construct the wild-type luciferase reporter vector of PGL3-EYA1-WT containing the EYA1 3′UTR binding site and the mutant luciferase reporter vector of PGL3-EYA1-MUT without the EYA1 3′ UTR binding site, PGL3-EYA1-WT and PGL3-EYA1-MUT were cotransfected into cells with miR-622 mimic and miR-NC, respectively. Firefly and Renilla luciferase activities were determined at 24 h posttransfection by using the Dual-Luciferase Reporter Assay Kit (Thermo Fisher, USA). Calculation formula: relative fluorescence value = firefly luciferase fluorescence value/Renilla luciferase fluorescence value. The assay was carried out three times independently.

2.10. Statistical Analysis. All of the statistical data were analyzed by SPSS 21.0 software. The mean ± SD presented the results from 3 independent experiments. The *t*-test and one-way analysis of variance was used to determine whether the comparison between two or more groups was statistically significant. $P < 0.05$ was considered statistically significant.

3. Results

3.1. miR-622 Is Upregulated in Breast Cancer Cell Lines, While EYA1 Is Downregulated. The relative expression level of miR-622 and EYA1 between breast cancer cell lines and normal epithelial cell line was measured by qRT-PCR and western blot. The result showed that miR-622 in BT474, MDA-MB-231, and MCF-7 was upregulated (Figure 1(a)), while EYA1 was downregulated (Figure 1(b)), compared with MCF-10A (miR-622: BT474 vs. MCF-10A, $P = 0.010$; MDA-MB-231 vs. MCF-10A, $P = 0.001$; MCF-7 vs. MCF-10A, $P < 0.0001$; EYA1: BT474 vs. MCF-10A, $P = 0.028$;

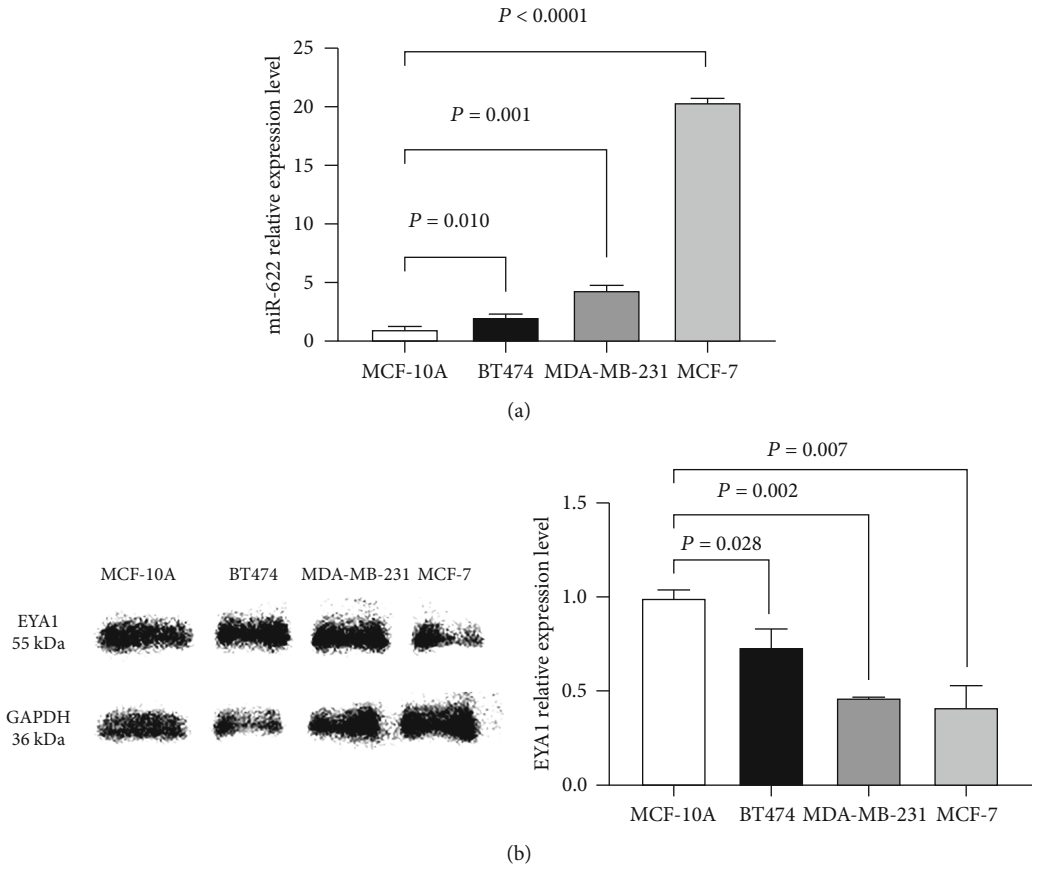

Figure 1: Expression levels of miR-622 and EYA1 in MCF-10A, BT474, MDA-MB-231, and MCF-7 cell lines. (a) The expression of miR-622 was increased in three breast cancer cell lines (BT474, MDA-MB-231, and MCF-7) compared to breast normal epithelial cell line MCF-10A, detected by using qRT-PCR. The expression level was the highest in MCF-7 (BT474 vs. MCF-10A, $P = 0.010$; MDA-MB-231 vs. MCF-10A, $P = 0.001$; MCF-7 vs. MCF-10A, $P < 0.0001$). (b) The expression of EYA1 was decreased in three breast cancer cell lines (BT474, MDA-MB-231, and MCF-7) compared to breast normal epithelial cell line MCF-10A, detected by using qRT-PCR and western blot. The expression level was the lowest in MCF-7 (EYA1: BT474 vs. MCF-10A, $P = 0.028$; MDA-MB-231 vs. MCF-10A, $P = 0.002$; MCF-7 vs. MCF-10A, $P = 0.007$).

MDA-MB-231 vs. MCF-10A, $P = 0.002$; MCF-7 vs. MCF-10A, $P = 0.007$). MCF-7 cell line was selected for the following experiment due to the expressions of miRNA and EYA1, in which miR-622 was much higher while EYA1 was lower than that of other breast cancer cell lines.

3.2. Overexpression of miR-622 Promotes Breast Cancer Cell Proliferation, Migration, and Invasion. In order to investigate the role of miR-622 in breast cancer, an experiment in vitro was conducted. miR-622 mimic or miR-NC was transfected into MCF-7 cell line, respectively, for further culture. The result showed that the expression of miR-622 was promoted by mimic compared with the miR-NC or control group after the transfection for 48 h (Figure 2(a)) (miR-622 mimic vs. miR-NC, $P = 0.007$; miR-622 mimic vs. control group, $P = 0.011$). Furthermore, CCK-8 assay, wound healing assay, and transwell chamber assay was conducted to reveal the roles of miR-622 in proliferation, migration, and invasion of MCF-7 cells. We found that the overexpression of miR-622 significantly promoted cell proliferation, migration, and invasion compared with the miR-NC or control group (Figures 2(b)–2(f)) (proliferation: miR-622 mimic vs. miR-NC, $P = 0.009$; miR-622 mimic vs. control group, $P = 0.030$; migration: miR-622 mimic vs. miR-NC, $P = 0.023$; miR-622 mimic vs. control group, $P = 0.011$; invasion: miR-622 mimic vs. miR-NC, $P = 0.033$; miR-622 mimic vs. control group, $P = 0.032$), which indicates that miR-622 might serve as a tumor promoter in regulating breast cancer biological process.

3.3. EYA1 Was the Direct Target of miR-622 in Breast Cancer. Here, we explored the molecular mechanisms of the tumor-promoting effect of miR-622 on breast cancer. Firstly, through TargetScan (http://www.targetscan.org/), miRDB (http://www.mirdb.org/), and microbase (http://www.mirbase.org/) software database screening, we found that EYA1 was a predicted target of miR-622 and that there were two binding sites of miR-622 in the 3′UTR of EYA1 (Figures 3(a) and 3(b)). According to the context++ score and the context++ score percentile, position 1779-1786 was selected for further analysis, suggesting that EYA1 may be a potential target of miR-622. Further luciferase reporter assay proved miR-622 could directly target EYA1. When we cotransfected the reporter vectors containing wild-type

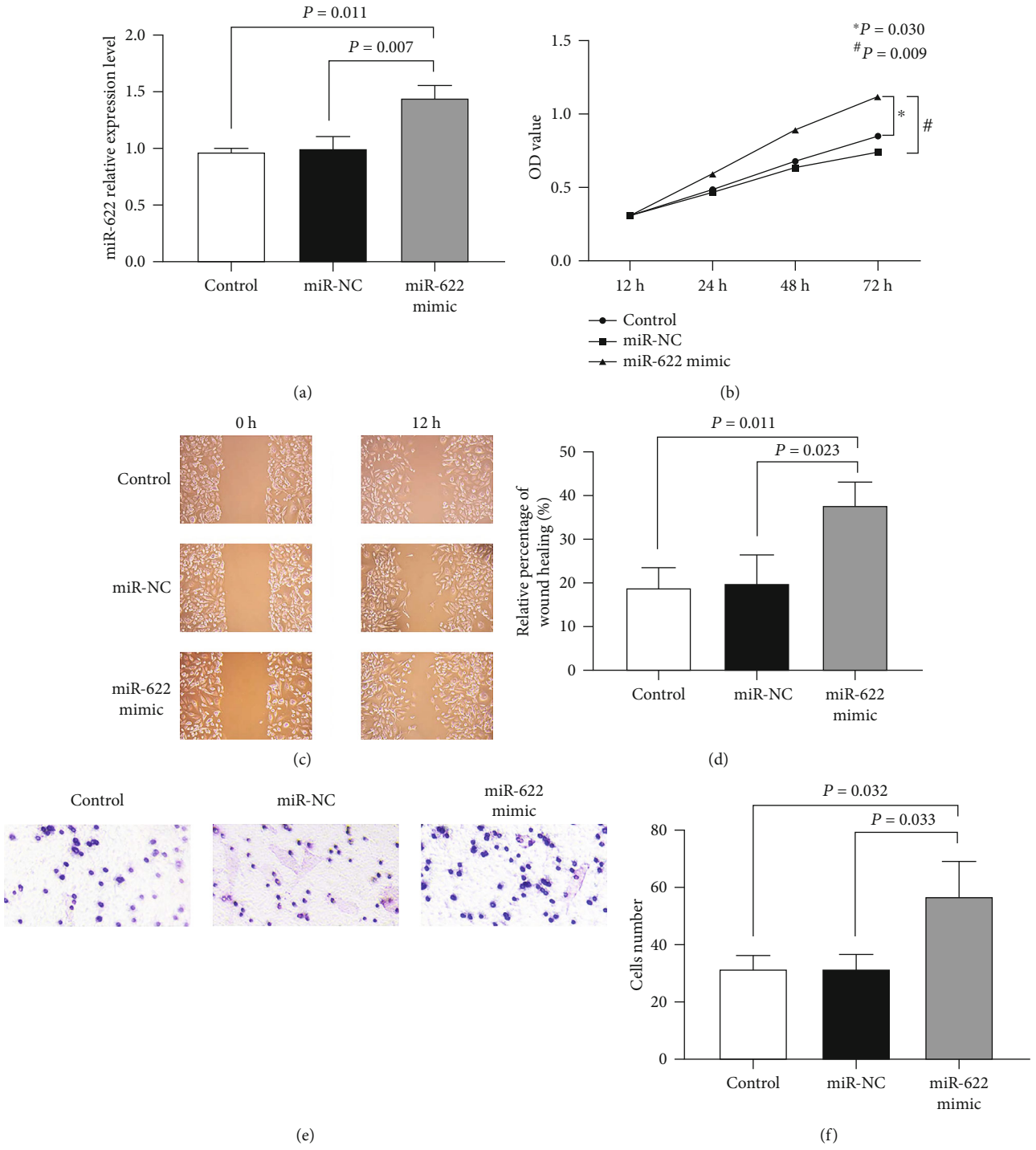

Figure 2: Overexpression of miR-622 could promote breast cancer cell proliferation, migration, and invasion. (a) After transfection of miR-622 mimic, the relative expression level of miR-622 in the miR-622 mimic group was higher than that in the miR-NC and control group (miR-622 mimic vs. miR-NC, $P = 0.007$; miR-622 mimic vs. control group, $P = 0.011$). (b) After transfection of miR-622 mimic for 24 hours, the proliferation of the miR-622 mimic group was stronger than that of the miR-NC and control group (miR-622 mimic vs. miR-NC, $P = 0.009$; miR-622 mimic vs. control group, $P = 0.030$). (c, d) The mobility in the miR-622 mimic group ($37.79\% \pm 5.42\%$) was higher than that in the miR-NC group ($19.96\% \pm 6.53\%$) and the control group ($18.95\% \pm 4.53\%$) (miR-622 mimic vs. miR-NC, $P = 0.023$; miR-622 mimic vs. control group, $P = 0.011$). (e, f) The number of invasive cells in the miR-NC and control group was lower than that in the miR-622 mimic group (miR-622 mimic vs. miR-NC, $P = 0.033$; miR-622 mimic vs. control group, $P = 0.032$).

EYA1 3′UTR (PGL3-EYA1-WT) and miR-622 mimics into MCF-7 cells, luciferase activity was significantly reduced (miR-622 mimic vs. miR-NC, $P = 0.002$). On the contrary, when we cotransfected the reporter vectors containing mutant EYA1 3′UTR (PGL3-EYA1-MT) and miR-622 mimics, luciferase activity was not changed (Figure 3(c))

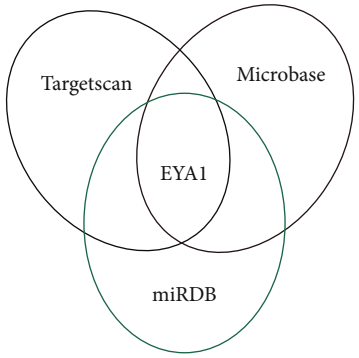

(a)

	Predicted consequential pairing of target region (top) and miRNA (bottom)	Site type	Context++ score	Context++ score percentile
Position 376-382 of EYA1 3' UTR	5' ...CUAAUUGCACAACAGAGACUGAA...	7mer-A1	−0.14	84
hsa-miR-622	3' CGAGGUUGGAGUCGUCUGACA			
Position 1779-1786 of EYA1 3' UTR	5' ...UGUUUUUGUACUCUGCAGACUGA...	8mer	0.32	97
hsa-miR-622	3' CGAGGUUGGAGUCGUCUGACA			

(b)

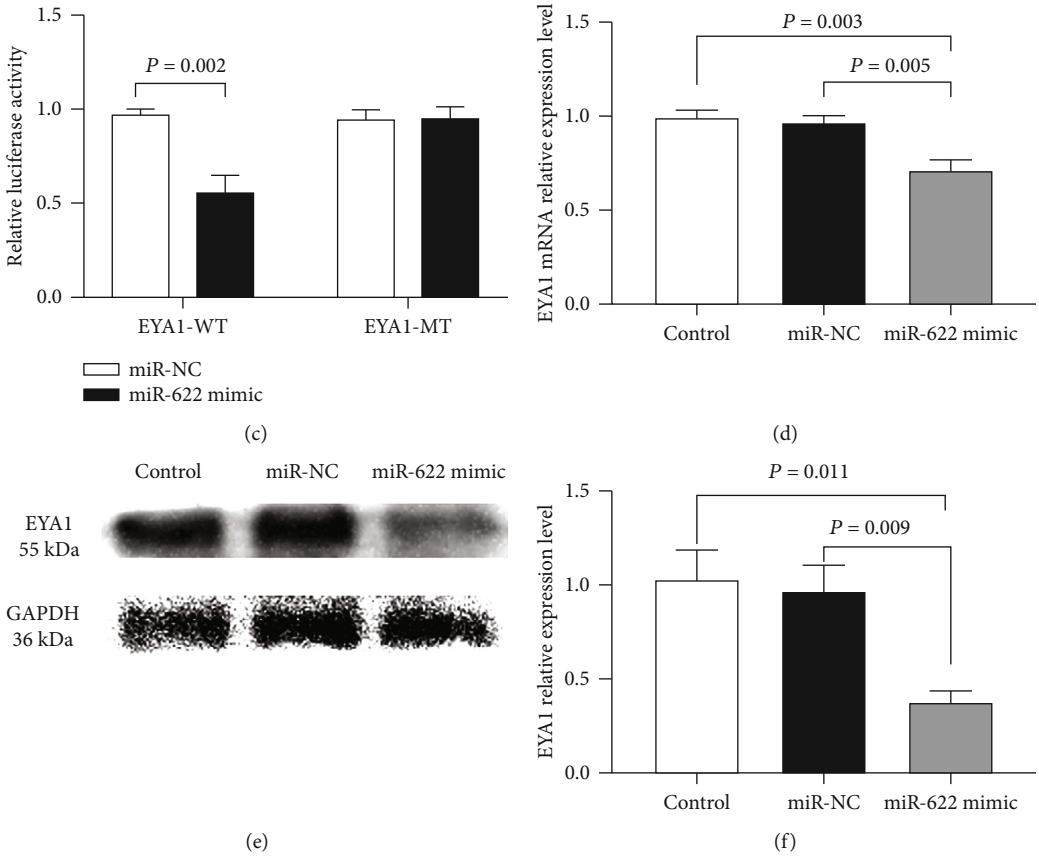

Figure 3: EYA1 was the direct target of miR-622 in breast cancer. (a, b) through TargetScan, miRDB, and microbase software database screening, we found that EYA1 was a predicted target of miR-622 and that there were two binding sites of miR-622 in the 3′UTR of EYA1. (c) miR-622 only affects the wild-type 3′UTR of EYA1, but not the mutant-type, as determined by the luciferase assay (EYA1-WT: miR-622 mimic vs. miR-NC, $P = 0.002$; EYA1-MT: miR-622 mimic vs. miR-NC, $P > 0.05$). (d–f) After transfection of miR-622 mimic, the relative expression levels of EYA1 mRNA and protein in the miR-622 mimic group were lower than those in the miR-NC and control group (EYA1 mRNA: miR-622 mimic vs. miR-NC, $P = 0.005$; miR-622 mimic vs. control group, $P = 0.003$; EYA1 protein: miR-622 mimic vs. miR-NC, $P = 0.009$; miR-622 mimic vs. control group, $P = 0.011$).

(miR-622 mimic vs. miR-NC, $P > 0.05$). In addition, after transfection for 48 hours, we found that the overexpression of miR-622 significantly decreased the expression of EYA1 mRNA and protein compared with miR-NC or the control group (Figures 3(d)–3(f)) (EYA1 mRNA: miR-622 mimic vs. miR-NC, $P = 0.005$; miR-622 mimic vs. control group, $P = 0.003$; EYA1 protein: miR-622 mimic vs. miR-NC, $P = 0.009$; miR-622 mimic vs. control group, $P = 0.011$).

3.4. Roles of EYA1 in Proliferation, Migration, and Invasion of Breast Cancer Cells. In order to further investigate the role of EYA1 in breast cancer, an experiment in vitro was conducted. si-EYA1 or siRNA-NC was transfected into MCF-7 cell line, respectively, for further culture. The result showed that si-EYA1 inhibited the expression of EYA1 mRNA and protein expression compared with the siRNA-NC or control group (Figures 4(a)–4(c)) (EYA1 mRNA: si-EYA1 vs. siRNA-NC, $P = 0.011$; si-EYA1 vs. control group, $P = 0.012$; EYA1 protein: si-EYA1 vs. siRNA-NC, $P = 0.033$; si-EYA1 vs. control group, $P = 0.004$). Furthermore, CCK-8 assay, wound healing assay, and transwell chamber assay were conducted to reveal the roles of EYA1 in proliferation, migration, and invasion of MCF-7 cells. The results showed that the silencing of EYA1 significantly promoted cell proliferation, migration, and invasion compared with the siRNA-NC or control group (Figures 4(d)–4(h)) (proliferation: si-EYA1 vs. siRNA-NC, $P = 0.004$; si-EYA1 vs. control group, $P = 0.001$; migration: si-EYA1 vs. siRNA-NC, $P = 0.046$; si-EYA1 vs. control group, $P = 0.049$; invasion: si-EYA1 vs. siRNA-NC, $P = 0.003$; si-EYA1 vs. control group, $P = 0.003$).

4. Discussion

Breast cancer is the most common cancer among women. According to the latest global cancer data in 2020, breast cancer has replaced lung cancer as the most common cancer in the world [1]. Distant organ metastases account for 90% of breast cancer deaths [23]. Therefore, there is an urgent need to understand the biological mechanism of breast cancer and find new therapeutic targets to improve the disease treatment and patients' survival rates.

Molecular targeted therapy is a systemic treatment that can effectively improve disease-free survival in operable breast cancer [24]. Since its discovery in 1993, more and more evidence had shown that various miRNAs' abnormal expression is involved in the occurrence and development of various tumors. Downregulated or upregulated miRNAs are advocated as new prognostic biomarkers and therapeutic targets. For example, in metastatic breast cancer, the expression levels of miR-21 and miR-105 were significantly higher than those in healthy subjects [25, 26]. miR-21 was significantly associated with the advanced clinical stage, the metastasis of the cancer cells in a lymph node, and poor prognosis [27]. Therefore, the study of the biological role of miRNAs in cancer opens up a new approach for cancer diagnosis and treatment.

miR-622, a member of the miRNA family, has been presented in various cancers as an oncogene or tumor suppressor gene since its discovery in 2010 [28]. Our results showed that the expression level of miR-622 in breast cancer cell lines was higher than that in normal human breast epithelial cell line, and the expression level of miRNA-622 was the highest in MCF-7 cell line. In order to understand the effect of miR-622 on the proliferation, migration, and invasion of breast cancer, we transfected breast cancer MCF-7 cell line with miR-622 mimic and found that the proliferation, migration, and invasion ability of MCF-7 cell line was significantly enhanced, when miR-622 was overexpressed. Therefore, overexpression of miR-622 significantly promoted the proliferation, migration, and invasion of MCF-7 cells. These results suggest that miR-622 may play a promoting role in breast cancer progression. However, related studies have shown that in various cancers, including breast cancer, miR-622, as a tumor suppressor gene, can directly act on the corresponding targets to inhibit tumor proliferation, migration, and invasion, respectively. miR-622 can directly target CCL18/MAPK, c-myc, and E2F1 to inhibit the progression of renal carcinoma, cholangiocarcinoma, and human esophageal squamous cell carcinoma, separately [29–31]. Furthermore, miR-622 has been shown to target RNF8 and NUAK1 kinase in breast cancer to inhibit its progression [15, 16]. In addition, Orlandella et al. [15], in the study of patients with ductal breast carcinoma, found that miR-622 was low expressed in the plasma of these patients, and miR-622 expression was negatively correlated with advanced tumor grade and aggressive clinicopathological features with high levels of Ki67. These conclusions are contrary to our findings that miR-622 is a procancer factor. However, the bioinformatics identification of Liu et al. [16] supports our study, showing that high levels of miR-622 expression were inversely associated with patient survival in all breast cancer patients in TCGA data set. Therefore, miR-622 can act as both a tumor suppressor gene and an oncogene in breast cancer, which may be associated with the high heterogeneity of breast cancer or different tumor sources and cell line classifications. Similarly, miR-622 can be used as both oncogene and tumor suppressor gene in colorectal cancer. Wang et al. [32] reported that miR-622 was upregulated in colorectal cancer tissues and cells, and it was used as a promoter in colorectal cancer. When miR-622 expression was decreased, the migration and invasion of colorectal cancer cells were inhibited. However, Fang et al.'s [33] research found that miR-622 was downregulated in colorectal cancer tissues and cells; the increased miR-622 inhibited CRC cell proliferation and migration, while inhibition of miR-622 reversed this phenomenon in CRC cells. In addition, Liu et al. [16] pointed out that due to the difference in the tumor microenvironment, whether miR-622 is carcinogenic or anticancer cannot be generalized [16].

Through bioinformatics analysis, we found that the $3'$ UTR of EYA1 has putative binding sites of miRNA-622. Therefore, to explore the relationship between miR-622 and EYA1 and find out the related mechanism of miR-622 promoting breast cancer cell lines, we launched a study on EYA1.

As one of the four mammalian EYA homologous genes, EYA1 has attracted extensive attention in the role of oncogenesis and development in recent years. Studies have shown that EYA1 is overexpressed as a tumor promoter in various types of cancer, including breast cancer, glioblastoma, and

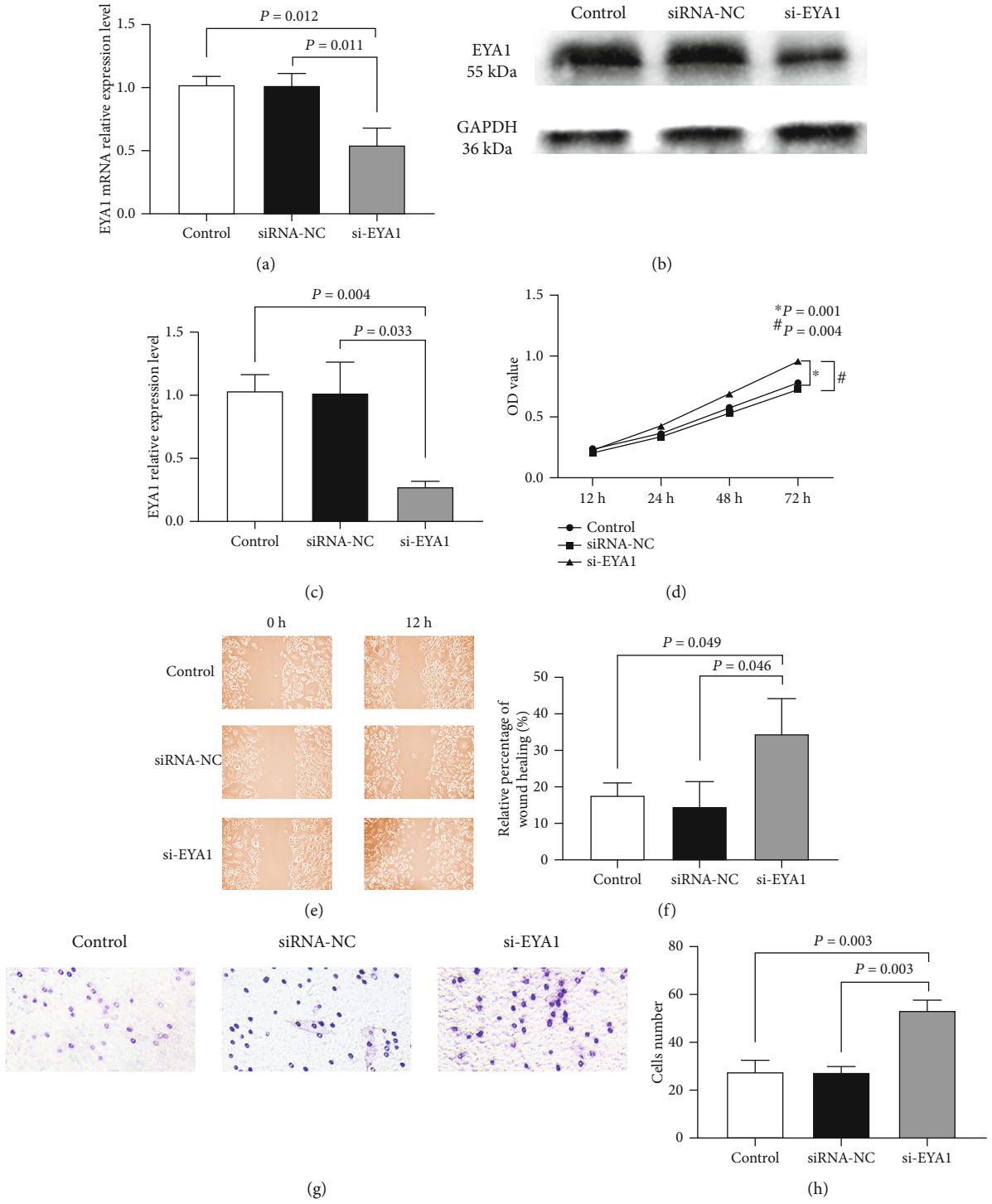

FIGURE 4: Roles of EYA1 in proliferation, migration, and invasion of breast cancer cells. (a–c) After transfection of si-EYA1, the relative expression levels of EYA1 mRNA and protein in the si-EYA1 group were lower than those in the siRNA-NC and control group (EYA1 mRNA: si-EYA1 vs. siRNA-NC, $P = 0.011$; si-EYA1 vs. control group, $P = 0.012$; EYA1 protein: si-EYA1 vs. siRNA-NC, $P = 0.033$; si-EYA1 vs. control group, $P = 0.004$). (d) After transfection of si-EYA1 for 48 hours, the proliferation of the si-EYA1 group was stronger than that of the siRNA-NC and control group (si-EYA1 vs. siRNA-NC, $P = 0.004$; si-EYA1 vs. control group, $P = 0.001$). (e, f) The mobility in the si-EYA1 group ($34.40\% \pm 9.81\%$) was higher than that in the siRNA-NC group ($14.60\% \pm 7.93\%$) and the control group ($17.63\% \pm 3.52\%$) (si-EYA1 vs. siRNA-NC, $P = 0.046$; si-EYA1 vs. control group, $P = 0.049$). (g, h) The number of invasive cells in the control group and the siRNA-NC group was lower than that in the si-EYA1 group (si-EYA1 vs. siRNA-NC, $P = 0.003$; si-EYA1 vs. control group, $P = 0.003$).

hepatocellular carcinoma [22, 34–36]. In addition, in breast cancer, related studies indicate that breast cancer with high levels of EYA1 has a poor prognosis, and EYA1 has been independently identified as a prognostic biomarker for breast cancer. Exogenous expression of EYA1 promoted the growth of breast tumors and induced the properties of tumor stem cells (CSCs) by activating cyclin D1 [21]. However, our results showed that the expression level of EYA1 in breast cancer cell lines was lower than that in normal human breast epithelial cell line, and the expression level of EYA1 was the lowest in MCF-7 cell line with the highest miRNA-622 expression level. Therefore, we chose MCF-7 cell line for subsequent experiments. In order to confirm the relationship between miR-622 and EYA1, we conducted a dual-luciferase reporter gene assay. The results showed that increased miR-622 level inhibited the activity of luciferase reporter in the 3′UTR of EYA1-WT. The overexpression of miRNA-622 inhibited EYA1 mRNA and protein expression level, which confirmed that EYA1 was a direct target of miRNA-622. At the same time, we silenced the expression of EYA1 gene and the result showed that the decreased expression of EYA1 had the same effect as miRNA-622, which is, in MCF-7 cells, overexpression of miRNA-622 or silencing of EYA1 significantly enhanced the proliferation, migration, and invasion of breast cancer cells. Therefore, we speculated that miR-622 might play a cancer-promoting role by inhibiting the expression of EYA1. This is consistent with decreased expression of EYA1 in gastric tumor samples, and EYA1 is inversely correlated with tumor size, lymphatic infiltration, and distant metastasis [37].

5. Conclusion

In conclusion, the results have shown that by targeting EYA1, miR-622 regulates breast cancer MCF-7 cell line proliferation, migration, and invasion, suggesting that miR-622 may become a potential target for breast cancer treatment. Reducing the production of miR-622 should be considered a promising strategy for targeted therapy of breast cancer.

Abbreviations

CCK-8:	Cell Counting Kit-8
EMT:	Epithelial-mesenchymal transition
FBS:	Fetal bovine serum
HE:	Hematoxylin-eosin
miRNAs:	MicroRNAs
miR-NC:	miRNA negative control
P/S:	Penicillin-streptomycin
qRT-PCR:	Quantitative reverse transcriptase-polymerase chain reaction
RDGN:	Retinal determinant gene network
RIPA:	Radioimmunoprecipitation assay lysate
siRNA-NC:	siRNA negative control
si-EYA1:	EYA1 siRNA.

Data Availability

The data used to support the findings of this study are available from the corresponding author upon request.

Conflicts of Interest

The authors declare that they have no conflicts of interest.

Acknowledgments

This work was supported by the Hunan Provincial Technology Innovation Guiding Plan-Clinical Medical Technology Innovation Guiding Project (2018SK51706).

References

[1] F. Bray, J. Ferlay, I. Soerjomataram, R. L. Siegel, L. A. Torre, and A. Jemal, "Global cancer statistics 2018: GLOBOCAN estimates of incidence and mortality worldwide for 36 cancers in 185 countries," *CA: a Cancer Journal for Clinicians*, vol. 68, no. 6, pp. 394–424, 2018.

[2] H. Sung, J. Ferlay, R. L. Siegel et al., "Global cancer statistics 2020: GLOBOCAN estimates of incidence and mortality worldwide for 36 cancers in 185 countries," *CA: a Cancer Journal for Clinicians*, vol. 71, no. 3, pp. 209–249, 2021.

[3] R. L. Siegel, K. D. Miller, and A. Jemal, "Cancer statistics, 2020," *CA: a Cancer Journal for Clinicians*, vol. 70, no. 1, pp. 7–30, 2020.

[4] R. L. Siegel, K. D. Miller, and A. Jemal, "Cancer statistics, 2018," *CA: a Cancer Journal for Clinicians*, vol. 68, no. 1, pp. 7–30, 2018.

[5] A. B. Hanker, D. R. Sudhan, and C. L. Arteaga, "Overcoming endocrine resistance in breast cancer," *Cancer Cell*, vol. 37, no. 4, pp. 496–513, 2020.

[6] J. Yang, A. Liu, I. He, and Y. Bai, "Bioinformatics analysis revealed novel 3′UTR variants associated with intellectual disability," *Genes*, vol. 11, no. 9, p. 998, 2020.

[7] X. Pan, Z. Li, L. Zhao et al., "microRNA-572 functions as an oncogene and a potential biomarker for renal cell carcinoma prognosis," *Oncology Reports*, vol. 40, no. 5, pp. 3092–3101, 2018.

[8] X. Y. Shi, H. Wang, W. Wang, and Y. H. Gu, "MiR-98-5p regulates proliferation and metastasis of MCF-7 breast cancer cells by targeting Gab2," *European Review for Medical and Pharmacological Sciences*, vol. 24, no. 21, p. 10914, 2020.

[9] Y. K. Liang, H. Y. Lin, X. W. Dou et al., "MiR-221/222 promote epithelial-mesenchymal transition by targeting Notch3 in breast cancer cell lines," *NPJ Breast Cancer*, vol. 4, no. 1, p. 20, 2018.

[10] A. X. Liu, F. Yang, L. Huang, L. Y. Zhang, J. R. Zhang, and R. N. Zheng, "Long non-coding RNA tubulin alpha 4B (TUBA4B) inhibited breast cancer proliferation and invasion by directly targeting miR-19," *European Review for Medical and Pharmacological Sciences*, vol. 23, no. 2, pp. 708–715, 2019.

[11] C. Han, Y. Fu, N. Zeng, J. Yin, and Q. Li, "LncRNA FAM83H-AS1 promotes triple-negative breast cancer progression by regulating the miR-136-5p/metadherin axis," *Aging*, vol. 12, no. 4, pp. 3594–3616, 2020.

[12] S. Liu, L. Chen, H. Chen, K. Xu, X. Peng, and M. Zhang, "Circ_0119872 promotes uveal melanoma development by regulating the miR-622/G3BP1 axis and downstream signalling pathways," *Journal of Experimental & Clinical Cancer Research: CR*, vol. 40, no. 1, p. 66, 2021.

[13] Y. Zhang, Z. Li, and Z. Lan, "Retracted article: Silencing UNC5B antisense lncRNA 1 represses growth and metastasis of human Colon cancer cells via raising miR-622," *Artificial Cells, Nanomedicine, and Biotechnology*, vol. 48, no. 1, pp. 60–67, 2020.

[14] R. Wang, Q. Ma, L. Ji, Y. Yao, M. Ma, and Q. Wen, "miR-622 suppresses tumor formation by directly targeting VEGFA in papillary thyroid carcinoma," *OncoTargets and therapy.*, vol. 11, pp. 1501–1509, 2018.

[15] F. M. Orlandella, R. M. Mariniello, P. Mirabelli et al., "miR-622 is a novel potential biomarker of breast carcinoma and impairs motility of breast cancer cells through targeting NUAK1 kinase," *British Journal of Cancer*, vol. 123, no. 3, pp. 426–437, 2020.

[16] C. Liu, L. Min, J. Kuang, C. Zhu, X. Y. Qiu, and L. Zhu, "Bioinformatic identification of miR-622 key target genes and experimental validation of the miR-622-RNF8 axis in breast cancer," *Frontiers in Oncology*, vol. 9, p. 1114, 2019.

[17] Y. Okabe, T. Sano, and S. Nagata, "Regulation of the innate immune response by threonine-phosphatase of eyes absent," *Nature*, vol. 460, no. 7254, pp. 520–524, 2009.

[18] M. A. Blevins, C. G. Towers, A. N. Patrick, R. Zhao, and H. L. Ford, "The SIX1-EYA transcriptional complex as a therapeutic target in cancer," *Expert Opinion on Therapeutic Targets*, vol. 19, no. 2, pp. 213–225, 2015.

[19] D. Kong, A. Li, Y. Liu et al., "SIX1 activates STAT3 signaling to promote the proliferation of thyroid carcinoma via EYA1," *Frontiers in oncology.*, vol. 9, p. 1450, 2019.

[20] J. Wu, B. Huang, H. B. He, W. Z. Lu, W. G. Wang, and H. Liu, "Two naturally derived small molecules disrupt the sineoculis homeobox homolog 1-eyes absent homolog 1 interaction to inhibit colorectal cancer cell growth," *Chinese medical journal.*, vol. 134, no. 19, pp. 2340–2352, 2021.

[21] K. Wu, Z. Li, S. Cai et al., "EYA1 phosphatase function is essential to drive breast cancer cell proliferation through cyclin D1," *Cancer Research*, vol. 73, no. 14, pp. 4488–4499, 2013.

[22] H. Guan, Z. Dai, Y. Ma, Z. Wang, X. Liu, and X. Wang, "MicroRNA-101 inhibits cell proliferation and induces apoptosis by targeting EYA1 in breast cancer," *International Journal of Molecular Medicine*, vol. 37, no. 6, pp. 1643–1651, 2016.

[23] C. L. Chaffer and R. A. Weinberg, "A perspective on cancer cell metastasis," *Science (New York, N.Y.)*, vol. 331, no. 6024, pp. 1559–1564, 2011.

[24] T. Shien and H. Iwata, "Adjuvant and neoadjuvant therapy for breast cancer," *Japanese Journal of Clinical Oncology*, vol. 50, no. 3, pp. 225–229, 2020.

[25] H. Wang, Z. Tan, H. Hu et al., "microRNA-21 promotes breast cancer proliferation and metastasis by targeting LZTFL1," *BMC Cancer*, vol. 19, no. 1, p. 738, 2019.

[26] B. Lin, C. Liu, E. Shi et al., "MiR-105-3p acts as an oncogene to promote the proliferation and metastasis of breast cancer cells by targeting GOLIM4," *BMC Cancer*, vol. 21, no. 1, p. 275, 2021.

[27] A. Rodríguez-Martínez, D. de Miguel-Pérez, F. G. Ortega et al., "Exosomal miRNA profile as complementary tool in the diagnostic and prediction of treatment response in localized breast cancer under neoadjuvant chemotherapy," *Breast Cancer Research: BCR*, vol. 21, no. 1, p. 21, 2019.

[28] X. Y. Wang, M. H. Wu, F. Liu et al., "Differential miRNA expression and their target genes between NGX6-positive and negative colon cancer cells," *Molecular and Cellular Biochemistry*, vol. 345, no. 1-2, pp. 283–290, 2010.

[29] T. Li, X. Sun, and K. Xu, "The suppressing role of miR-622 in renal cell carcinoma progression by down-regulation of CCL18/MAPK signal pathway," *Cell & Bioscience*, vol. 8, no. 1, p. 17, 2018.

[30] Y. F. Wu, Z. R. Li, Z. Q. Cheng, X. M. Yin, and J. S. Wu, "Decrease of miR-622 expression promoted the proliferation, migration and invasion of cholangiocarcinoma cells by targeting regulation of c-Myc," *Biomedicine & Pharmacotherapy = Biomedecine & Pharmacotherapie*, vol. 96, pp. 7–13, 2017.

[31] C. Song, P. Lu, W. Shi et al., "MiR-622 functions as a tumor suppressor and directly targets E2F1 in human esophageal squamous cell carcinoma," *Biomedicine & Pharmacotherapy = Biomedecine & Pharmacotherapie*, vol. 83, pp. 843–849, 2016.

[32] Y. Wang, J. Sun, X. Wei et al., "Decrease of miR-622 expression suppresses migration and invasion by targeting regulation of DYRK2 in colorectal cancer cells," *OncoTargets and Therapy*, vol. Volume 10, pp. 1091–1100, 2017.

[33] Y. Fang, B. Sun, Z. Li, Z. Chen, and J. Xiang, "MiR-622 inhibited colorectal cancer occurrence and metastasis by suppressing K-Ras," *Molecular Carcinogenesis*, vol. 55, no. 9, pp. 1369–1377, 2016.

[34] J. Li, Y. Rodriguez, C. Cheng et al., "EYA1's conformation specificity in dephosphorylating phosphothreonine in Myc and its activity on Myc stabilization in breast cancer," *Molecular and Cellular Biology*, vol. 37, no. 1, 2017.

[35] J. Kim, C. She, M. Potez et al., "Phage display targeting identifies EYA1 as a regulator of glioblastoma stem cell maintenance and proliferation," *Stem Cells*, vol. 39, no. 7, pp. 853–865, 2021.

[36] D. Kong, W. Ma, D. Zhang et al., "EYA1 promotes cell migration and tumor metastasis in hepatocellular carcinoma," *American Journal of Translational Research*, vol. 11, no. 4, pp. 2328–2338, 2019.

[37] P. Nikpour, M. Emadi-Baygi, E. Emadi-Andani, and S. Rahmati, "EYA1 expression in gastric carcinoma and its association with clinicopathological characteristics: a pilot study," *Medical Oncology (Northwood, London, England)*, vol. 31, no. 5, p. 955, 2014.